Composition and mechanical properties of osteoarthritic subchondral trabecular tibial bone

John Patrick Gleeson

A thesis submitted to the University of Dublin in partial fulfilment of the requirements for the degree of

Doctor in Philosophy

Trinity College Dublin

Supervisor
Dr. Kevin U. O'Kelly

External Examiner
Professor J.D. Currey

Internal Examiner
Professor T.C. Lee

November 2006

Declaration

I declare that I am the sole author of this thesis and that work presented within, unless otherwise referenced, is my own. I also declare that the work has not been submitted, in whole or in part, to any other university or college for a degree or other qualification.

I authorise the library of Trinity College Dublin to lend or copy this thesis on request.

John Patrick Gleeson
November 2006

Summary

Osteoarthritis is a disease that has been characterised historically by the focal destruction of cartilaginous tissue and hence, is defined as such. However, recent investigations have brought this pathology into contention. Numerous investigators have found significant evidence implicating subchondral bone in the disease's pathophysiology. Hence, a complete and accurate pathology is still elusive.

Early-stage primary osteoarthritic bone samples, clinically-defined using the Mankin scoring system, were harvested from both medial and lateral compartments of diseased human tibiae. Only the medial compartments exhibited clinical evidence of early-stage OA. Subchondral trabecular bone from both the medial and lateral compartments were dehydrated and embedded in PMMA and subsequently examined using nanoindentation and quantitative backscatter electron imaging (QBEI). Stiffness, hardness and mineralisation were measured as a function of depth below the sample surface. A novel calibration technique was developed to facilitate damage-free analysis using qbei.

Significant differences in intrinsic tissue stiffness and mineralisation were observed in all samples presenting with clinically-defined, early-stage OA. Non-presenting lateral samples also exhibited significant differences in stiffness and mineralisation but these were opposite in direction to those seen in their medial counterparts. Hence, the presence of an early, non-presenting stage of OA initiation was observed. Additionally, differences in the measured tissue properties were difficult to explain as secondary to changes in

the overlying cartilaginous matrix, implying an exclusively biological equilibrium breakdown within affected knee joints. No significant relationship between stiffness or hardness and corresponding mineralisation density was observed, disproving our hypothesis that changes in the intrinsic mechanical properties are predominantly linked with corresponding changes in tissue mineralisation density in primary knee OA, strongly implicating the contribution of collagen and/or its subsequent effect on cohesive mineralisation

In conclusion, subchondral bone plays a significant role in the pathogenesis of human primary knee OA, conclusively proving that the classic 'wear' and 'tear' definition of this disease is no longer applicable to human knee OA.

Acknowledgements

I wish to thank my supervisor, Dr. Kevin U. O'Kelly for all his help and support throughout this project. His approach to my supervision always found the right balance between guidance and intellectual freedom over the last four and a half years. For this I cannot thank him enough.

I would also like to thank Professor Clive Lee of the Royal College of Surgeons in Ireland for his continuing generosity and counsel initiated during my supervisor's sabbatical.

I am indebted to Dr. Anthony Staines of the School Of Public Health and Population Science, University College Dublin, Earlsfort Terrace. I am eternally grateful for his selfless and exhaustive help with the statistical analysis of the data accumulated throughout this present work.

Particular thanks is given to Dr. Cormac O'Connell and Mr. David Cottell of the Electron Microscope Laboratory, University College Dublin, for their hospitality, generosity and enthusiasm for the work.

I would like to express my thanks to both bioengineering research groups that I had the pleasure and privilege of being a part of, the Bioengineering group in the Trinity Centre for Bioengineering and the 'Bone for Life' group based in the Royal College of Surgeons in Ireland. I thank all my colleagues, past and present, for their input into my work. I owe you all a pint or two!

Finally, I would like to thank Elaine for sticking with me throughout my academic adventures (and moods!) and my parents, Ann and Martin for their unconditional support, both emotional and financial, throughout the last eight and a half years of academia.

Publications and presentations

J. P. Gleeson, C. O'Connell, K. U. O'Kelly, *The relationship between bone tissue properties and bone's microstructure in healthy and osteoarthritic bone*. In: *Proceedings of the 9th Annual Conference of the Section of Bioengineering of the Royal Academy of Medicine in Ireland*, Cavan 2003.

J. P. Gleeson, C. O'Connell, K. U. O'Kelly, *Composition and mechanical properties of healthy and osteoarthritic bone using 3-D QBEI*. In: *Proceedings of the 10th Annual Conference of the Section of Bioengineering of the Royal Academy of Medicine in Ireland*, Limerick 2004.

J. P. Gleeson, C. O'Connell, K. U. O'Kelly, *Comparison of composition and mechanical properties of healthy and osteoarthritic bone using 3-D QBEI*. In: *Proceedings of the 14th Conference of European Society of Biomechanics*, s-Hertogenbosch 2004.

Topics in Biomechanical Engineering. Chapter 3, pp 70-71. Ed. P. Prendergast and P. J. McHugh. Trinity Centre for Bioengineering (TCBE) and the National Centre for Biomedical Engineering Science (NCBES) 2004.

J. P. Gleeson, C. O'Connell, K. U. O'Kelly, *Composition and mechanical properties of osteoarthritic subchondral.* In: *Proceedings of the 11th Annual Conference of the Section of Bioengineering of the Royal Academy of Medicine in Ireland*, Killiney 2005.

J. P. Gleeson, C. O'Connell, K. U. O'Kelly, *Composition and mechanical properties of osteoarthritic subchondral human bone.* In: *Proceedings of the 2005 Summer Bioengineering Conference of the Bioengineering Division of the American Society of Mechanical Engineers*, Vail CO 2005.

J. P. Gleeson, C. O'Connell, K. U. O'Kelly, *OA subchondral bone changes precede overlying cartilage damage in the human knee.* In: *Proceedings of the 12th Annual Conference of the Section of Bioengineering of the Royal Academy of Medicine in Ireland*, Galway 2006.

J. P. Gleeson, C. O'Connell, K. U. O'Kelly, *A novel calibration technique facilitates damage-free, depth-specific QBEI.* Submitted to the Journal of Microscopy (under review), April 2006.

J. P. Gleeson, C. O'Connell, K. U. O'Kelly, *Bone tissue changes in early-stage osteoarthritis of the human knee precede overlying cartilage damage..* In: *Proceedings of the 5th World Congress of Biomechanics*, Munich 2006.

Contents

Nomenclature **xxi**

1 Introduction **1**

1.1 Osteoarthritis 1

1.2 Objectives of the Thesis 5

2 Literature Review **7**

2.1 Structural Hierarchy of Bone 8

2.1.1 Nanostructure 8

2.1.2 Ultrastructure 13

2.1.3 Microstructure 18

2.1.4 Sub-macrostructure 20

2.1.5 Macrostructure 22

2.2 Bone Cells 25

2.2.1 Osteoblasts 25

2.2.2 Osteoclasts 25

2.2.3 Osteocytes 26

2.2.4 Osteoprogenitor Cells 28

2.3 Ossification 28

2.4 Osteoarthritis 29

2.5 Nanoindentation 35

2.5.1 Theory 37

2.5.2 Continuous Stiffness Measurement (CSM) 40

2.5.3 Calibration and Tip Selection 43

2.6 Nanoindentation of Mineralised Tissue 52
2.6.1 Wet, Non-infiltrated Bone Tissue 53
2.6.2 Dry, Non-infiltrated Bone Tissue 53
2.6.3 Dry, Infiltrated Bone Tissue 54
2.7 Quantitative Backscatter Electron Imaging 56
2.7.1 QBEI of Mineralised Tissue 58
2.7.2 Theory 60
2.7.3 Depth-Specific Imaging 63
2.7.4 Quantitative Calibration 67
2.7.5 Beam Damage 69
2.7.6 Novel Damage Reduction Technique 72

3 Materials and Methods **75**
3.1 Materials 75
3.1.1 Sample Origins 75
3.1.2 Sample Preparation 77
3.1.3 Embedding Procedure 77
3.2 Nanoindentation Setup 79
3.2.1 Procedure 82
3.2.2 Analysis 86
3.3 QBEI Setup 88
3.3.1 QBEI Procedure 90
3.3.2 Analysis 94
3.4 Chromatography 97
3.4.1 High Pressure Liquid Chromatography 98
3.4.2 Chromatographic Quantification 100
3.4.3 Setup 101
3.4.4 Chromatographic Run 102
3.4.5 Results 103
3.5 Statistical Analysis 103

4 Results **105**
4.1 Population Analysis . . . 105
4.2 Mechanical Assessment . . . 108
4.2.1 1 μm Indentation Depth . . . 109
4.2.2 2 μm Indentation Depth . . . 115
4.2.3 3 μm Indentation Depth . . . 121
4.2.4 4 μm Indentation Depth . . . 126
4.2.5 Depth-Specific Behaviour . . . 132
4.3 Mineralisation Assessment . . . 138
4.3.1 1 μm Indentation Depth . . . 139
4.3.2 2 μm Indentation Depth . . . 141
4.3.3 3 μm Indentation Depth . . . 143
4.3.4 4 μm Indentation Depth . . . 145
4.3.5 Depth-Specific Behaviour . . . 147
4.4 Mechanical/Mineralisation Relationship . . . 149
4.4.1 1 μm Indentation Depth . . . 149
4.4.2 2 μm Indentation Depth . . . 153
4.4.3 3 μm Indentation Depth . . . 157
4.4.4 4 μm Indentation Depth . . . 161
4.4.5 Depth-specific Behaviour . . . 165
4.5 Transverse Mechanical/Mineralisation Relationship . . . 169
4.6 SEM Damage Calibration Results . . . 170
4.6.1 15keV Accelerating Voltage . . . 170
4.6.2 30keV Accelerating Voltage . . . 175

5 Discussion **180**
5.1 Population Analysis . . . 180
5.1.1 Pathological Definition . . . 180
5.1.2 Data Pre-Processing . . . 182
5.1.3 PMMA Embedding . . . 184
5.2 Nanoindentation Orientation . . . 186
5.3 Mechanical Properties . . . 187

5.3.1 Medial Stiffness 188
5.3.2 Lateral Stiffness 192
5.3.3 Hardness 196
5.3.4 E/H Relationship 198
5.4 Mineralisation 201
5.4.1 Medial Mineralisation 203
5.4.2 Lateral Mineralisation 205
5.5 Depth-Specific Behaviour 210
5.6 Mechanical/Mineralisation Relationship 211
5.7 Mechanical/Mineralisation Data Outliers 216
5.8 SEM Damage Calibration 217

6 Conclusion **221**
6.1 Main Results of the Thesis 221
6.2 Future Work 223

Bibliography **224**

List of Figures

1.1 X-ray image illustrating the location of an osteophyte within a osteoarthritic shoulder joint. [1] 2
1.2 An example of the large scale macroscopic damage due to complete cartilage erosion in an osteoarthritic femoral head. Image on the left shows a freshly excised, healthy femoral head, while the image on the right shows a late-stage osteoarthritic femoral head. [2] 3
1.3 A schematic diagram illustrating the final appearance of a knee joint in an advanced case of osteoarthritis. [3] 4

2.1 A schematic diagram illustrating the amino acid sequence and alpha chain configuration of a typical polypeptide chain. [4] . 10
2.2 A schematic diagram illustrating the tropocollagen helix. [4] . 10
2.3 A schematic diagram illustrating the assembly of tropocollagen and the resulting molecular domains. [5] 10
2.4 A schematic diagram illustrating the assembly of collagen fibrils and bone mineral crystals. [6] 13
2.5 A schematic diagram illustrating the assembly of collagen molecules into fibrils and, consequently, fibres. [7] 14
2.6 A schematic diagram illustrating the two dimensional arrangement of collagen molecules in quarter-stagger alignment. [5] . 15

2.7 A schematic diagram illustrating the quarter-stagger alignment of collagen molecules and the corresponding location of cross-links. A typical amino acid residue sequence is highlighted. [8] 15
2.8 Schematic diagram of mineral deposition within the collagen fibril gap regions. As the mineralisation process causes the fibril to swell, fibrils can eventually lose their individuality and merge. [9] 16
2.9 A schematic diagram illustrating the assembly and early mineralization of collagen molecules in a three-dimensional perspective. [10] 17
2.10 Schematic of a cross-section through a single collagen fibril showing mineral deposition throughout the fibril. [11] 17
2.11 A schematic diagram illustrating the proposed plywood structure of bone lamellae. [12] 19
2.12 A schematic diagram illustrating the proposed 'twisted' plywood structure of bone lamellae. [12] 19
2.13 A schematic diagram showing part of a trabecular network, where both trabecular struts and the connecting trabecular plates are evident. [13] 21
2.14 SEM image illustrating the non-parallel alignment of trabecular lamellae. [14] 21
2.15 Backscatter image of a trabecular bone plate transverse section, illustrating the non-parallel alignment of trabecular lamellae. Approximate lamellar direction denoted by black arrows. 22
2.16 Schematic illustrating cortical and cancellous tissue within the cross-section of a long bone diaphysis. [13] 24
2.17 Schematic illustrating the basic multicellular unit in both cortical and cancellous bone. [15] 26
2.18 Schematic of a trabecular strut cross-section, illustrating bone lacunae and their corresponding canalicular structure. 27

2.19 Schematic showing a bone osteocyte lacuna and its cell processes in the canalicular structure. 27
2.20 Indentations performed on a trabecular bone sample within the embedding medium (PMMA). 36
2.21 Typical load versus displacement curve for a typical nanoindentation. [16] 38
2.22 Contact geometry during indenter loading and unloading. [16] 39
2.23 Schematic of nanoindenter indentation head. 40
2.24 Indentation load as a function of indenter displacement into subchondral trabecular bone sample. 43
2.25 Typical elastic modulus versus indentation depth curve for bone. 43
2.26 Thermal drift as a function of time due to constant applied load. [17] 45
2.27 Effect of thermal drift on load versus displacement data. [17] . 46
2.28 Effect of compliance calibration on measured load versus displacement data. [17] 47
2.29 Schematic showing an exaggerated representation of pile-up as a result of a typical indentation. [17] 51
2.30 Schematic showing an exaggerated representation of sink-in as a result of a typical indentation. [17] 51
2.31 Schematic illustrating the basic components and function of a Scanning Electron Microscope (SEM). 57
2.32 Common electron specimen interactions due to an incident electron beam. 61
2.33 Image of alumina-nickel composite viewed using secondary electron emission. 64
2.34 Image of alumina-nickel composite viewed using backscatter electron emission. 64
2.35 Comparison of different emission depth penetration ranges for typical electron beam interactions. [18] 66
2.36 Interaction volume as a function of accelerating voltage. 67

2.37 Linear relationship between QBEI grey levels and wt% Ca. [19] 68
2.38 QBEI image of a trabecular bone sample exhibiting irreversible specimen damage in the form of a 'bright' patch. 70
2.39 Corresponding light microscope image of the damaged region in Figure 2.38. 71

3.1 Trabecular bone sample map cross-section through a typical trabecular network. 79
3.2 Sample stage with bone sample, aluminium standard and fused silica standard inserted. 81
3.3 Nanoindenter XP apparatus with sample stage removed. . . . 82
3.4 Indentation load as a function of indenter displacement into subchondral trabecular bone sample. 83
3.5 Indentation modulus as a function of indenter displacement. . 84
3.6 Indentation hardness as a function of indenter displacement. . 84
3.7 Trabecular bone sample showing insufficient depth of material, imaged using light microscopy with specimen embedded in PMMA. 86
3.8 Indentation set showing indentations performed close to embedding medium. Left-most indentation deemed too close to sample edge. 87
3.9 Typical plots of major experimental parameters as a function each other. 89
3.10 Embedded trabecular bone sample mounted on aluminium SEM stub with silver paint placed around the circumference. . 90
3.11 Backscatter image of trabecular bone. Nanoindentations are denoted 1 to 4 anti-clockwise from bottom left. 95
3.12 Selected ROI around nanoindentation 4 from Figure 3.11. . . . 96
3.13 Gaussian curve fitted to histogram data from the nanoindentation shown in Figure 3.12. 96
3.14 Sample chromatogram illustrating the most important parameters used to characterise a separation (Mackery-Nagel Inc) . . 100

4.1 Healthy versus OA medial average sample stiffness with 95% confidence intervals (1 μm). 110
4.2 Healthy versus OA lateral sample stiffness with 95% confidence intervals (1 μm). 110
4.3 Healthy versus OA sample hardness with 95% confidence intervals (1 μm). 111
4.4 Scatter plot of stiffness versus hardness in medial samples (1 μm). 112
4.5 Linear regression of stiffness versus hardness in medial samples (1 μm). 113
4.6 Scatter plot of stiffness versus hardness in lateral samples (1 μm). 114
4.7 Linear regression of stiffness versus hardness in lateral samples (1 μm). 114
4.8 Healthy versus OA medial sample stiffness with 95% confidence intervals (2 μm). 116
4.9 Healthy versus OA lateral sample stiffness with 95% confidence intervals (2 μm). 116
4.10 Healthy versus OA sample hardness with 95% confidence intervals (2 μm). 117
4.11 Scatter plot of stiffness versus hardness in medial samples. (2 μm). 119
4.12 Linear regression of stiffness versus hardness in medial samples. (2 μm). 119
4.13 Scatter plot of stiffness versus hardness in lateral samples. (2 μm). 120
4.14 Linear regression of stiffness versus hardness in lateral samples. (2 μm). 120
4.15 Healthy versus OA medial sample stiffness with 95% confidence intervals (3 μm). 122

4.16 Healthy versus OA lateral sample stiffness with 95% confidence intervals (3 μm). 122
4.17 Healthy versus OA sample hardness with 95% confidence intervals (3 μm). 123
4.18 Scatter plot of stiffness versus hardness in medial samples. (3 μm). 124
4.19 Linear regression of stiffness versus hardness in medial samples. (3 μm). 124
4.20 Scatter plot of stiffness versus hardness in lateral samples. (3 μm). 125
4.21 Linear regression of stiffness versus hardness in lateral samples. (3 μm). 126
4.22 Healthy versus OA medial sample stiffness with 95% confidence intervals (4 μm). 127
4.23 Healthy versus OA lateral sample stiffness with 95% confidence intervals (4 μm). 128
4.24 Healthy versus OA sample hardness with 95% confidence intervals (4 μm). 129
4.25 Scatter plot of stiffness versus hardness in medial samples. (4 μm). 130
4.26 Linear regression of stiffness versus hardness in medial samples. (4 μm). 130
4.27 Scatter plot of stiffness versus hardness in lateral samples. (4 μm). 131
4.28 Linear regression of stiffness versus hardness in lateral samples. (4 μm). 131
4.29 Comparative image of bone sample highlighting the extent of indentation depth relative to trabecular thickness. 133
4.30 Medial stiffness as a function of indentation depth in healthy and OA tissue. 133

4.31 Lateral stiffness as a function of indentation depth in healthy and OA tissue. 134
4.32 Hardness as a function of indentation depth in healthy and OA tissue. 135
4.33 Medial stiffness/hardness ratio as a function of increasing examination depth. 137
4.34 Lateral stiffness/hardness ratio as a function of increasing examination depth. 138
4.35 Healthy versus OA medial mineralisation assessed by QBEI at 15keV with 95% confidence intervals. 139
4.36 Healthy versus OA lateral mineralisation assessed by QBEI at 15keV with 95% confidence intervals. 140
4.37 Healthy versus OA medial mineralisation assessed by QBEI at 20keV with 95% confidence intervals. 141
4.38 Healthy versus OA lateral mineralisation assessed by QBEI at 20keV with 95% confidence intervals. 142
4.39 Healthy versus OA medial mineralisation assessed by QBEI at 25keV with 95% confidence intervals. 143
4.40 Healthy versus OA lateral mineralisation assessed by QBEI at 25keV with 95% confidence intervals. 144
4.41 Healthy versus OA medial mineralisation assessed by QBEI at 30keV with 95% confidence intervals. 145
4.42 Healthy versus OA lateral mineralisation assessed by QBEI at 30keV with 95% confidence intervals. 146
4.43 Medial mineralisation as a function of indentation depth in healthy and OA tissue with 95% confidence intervals. 148
4.44 Lateral mineralisation as a function of indentation depth in healthy and OA tissue with 95% confidence intervals. 149
4.45 Healthy and OA stiffness versus mineralisation in medial tissue samples (1 μm depth). 150

4.46 Healthy and OA hardness versus mineralisation in medial tissue samples (1 μm depth). 151
4.47 Healthy and OA stiffness versus mineralisation in lateral tissue samples (1 μm depth). 152
4.48 Healthy and OA hardness versus mineralisation in lateral tissue samples (1 μm depth). 153
4.49 Healthy and OA stiffness versus mineralisation in medial tissue samples (2 μm depth). 154
4.50 Healthy and OA hardness versus mineralisation in medial tissue samples (2 μm depth). 155
4.51 Healthy and OA stiffness versus mineralisation in lateral tissue samples (2 μm depth). 156
4.52 Healthy and OA hardness versus mineralisation in lateral tissue samples (2 μm depth). 157
4.53 Healthy and OA stiffness versus mineralisation in medial tissue samples (3 μm depth). 158
4.54 Healthy and OA hardness versus mineralisation in medial tissue samples (3 μm depth). 159
4.55 Healthy and OA stiffness versus mineralisation in lateral tissue samples (3 μm depth). 160
4.56 Healthy and OA hardness versus mineralisation in lateral tissue samples (3 μm depth). 161
4.57 Healthy and OA stiffness versus mineralisation in medial tissue samples (4 μm depth). 162
4.58 Healthy and OA hardness versus mineralisation in medial tissue samples (4 μm depth). 163
4.59 Healthy and OA stiffness versus mineralisation in lateral tissue samples (4 μm depth). 164
4.60 Healthy and OA hardness versus mineralisation in lateral tissue samples (4 μm depth). 165

4.61 Healthy and OA stiffness versus mineralisation as a function of examination depth (Medial). 167
4.62 Healthy and OA stiffness versus mineralisation as a function of examination depth (Lateral). 169
4.63 Histogram drift rates (Sample 1 to 5) using a novel CPS calibration (Low dosage setting) at 15keV. 171
4.64 Histogram drift rates (Sample 1 to 5) using visually optimum calibration (High dosage setting) at 15keV. 172
4.65 Boxplot illustrating linear regression slope values from figures 4.63 and 4.64 at 15keV. 173
4.66 Histogram drift due to a novel CPS calibration (Low dosage setting) at 15keV. 174
4.67 Histogram drift due to visually optimum calibration (High dosage setting) at 15keV. 174
4.68 Histogram drift rate using a novel CPS calibration (Low dosage setting) at 30keV. 177
4.69 Histogram drift rate using constant spot size calibration (High dosage setting) at 30keV. 178
4.70 Box plot illustrating linear regression slope values from figures 4.68 and 4.69 at 30keV. 178
4.71 Histogram drift due to a novel CPS calibration (Low dosage setting) at 30keV. 179
4.72 Histogram drift using constant spot size calibration (High dosage setting) at 30keV. 179

List of Tables

3.1 Mankin scoring system grades [20] 76
3.2 Embedding procedure and alcohol concentrations. 78

4.1 Total samples numbers divided by factor. 105
4.2 Three-factor ANOVA of nanoindentation stiffness data. * indicates factor interaction. 106
4.3 Three-factor ANOVA of nanoindentation hardness data. * indicates factor interaction. 106
4.4 Three-factor ANOVA of QBEI mineralisation data. * indicates factor interaction. 106
4.5 Healthy versus OA medial result summary (1 μm). 109
4.6 Healthy versus OA result summary (2 μm). 115
4.7 Healthy versus OA result summary (3 μm). 121
4.8 Healthy versus OA result summary (4 μm). 127
4.9 Average stiffness values as a function of indentation depth. ** indicates statistical significance ($p<0.05$) relative to the 1 μm value. 134
4.10 Average hardness values as a function of indentation depth. . . 136

Nomenclature

α	Nanoindentation power law fitting constant
β	Nanoindentation indenter geometry constant
ϵ	Nanoindentation indenter geometry constant
η	Backscatter electron coefficient
η_{BSE}	Number of backscattered electrons
η_B	Total number of incident electrons
ω	CSM force frequency
$\overline{\eta}$	Mean weighted backscatter coefficient
$\overline{Z}$	Sample mean atomic number
ϕ	CSM lag phase angle
ψ_1	Angle of rotation about fibril short axis
ψ_2	Angle of rotation about fibril long axis
ρ	Material density
A	Nanoindentation projected contact area
C_m	Nanoindentation machine compliance
C_s	Nanoindentation indenter-sample elastic compliance

C_t	Nanoindentation total compliance
D	CSM system damping rate
D_i	CSM indenter head damping rate
D_s	CSM sample damping rate
E_o	Electron beam accelerating voltage
E_r	Nanoindentation reduced modulus
F_o	CSM excitation amplitude
F_t	CSM force term
h	Nanoindentation total displacement
h_c	Nanoindentation contact depth
h_{max}	Maximum nanoindentation displacement
h_m	Nanoindentation machine displacement
h_s	Nanoindentation sink-in depth
K	CSM equivalent stiffness term
K_f	CSM machine load-frame stiffness
K_m	Nanoindentation machine stiffness
K_s	CSM support springs stiffness
m	Nanoindentation power law fitting constant
P	Nanoindentation load
P_{max}	Maximum nanoindentation load
S	Nanoindentation elastic unloading stiffness

t'_{R_1} Net retention time of chromatogram component 1

t'_{R_2} Net retention time of chromatogram component 1

t_0 Chromatographic column dead time

t_{R_1} Total retention time of chromatogram component 1

t_{R_2} Total retention time of chromatogram component 2

w Chromatogram peak band width

$w_{1/2}$ Chromatogram peak width at half peak height

Z Specimen atomic number

z CSM indenter displacement

z_o CSM displacement amplitude

(v/v) Volume per volume

ACC Articular calcified cartilage

ANOVA Analysis of variance

BMDD Bone mineralisation density distribution

BMU Basic multicellular unit

BSE Backscatter electron

CPS Counts per second

CSM Continuous stiffness measurement

E Stiffness

ECM Extra-cellular matrix

EDX Energy dispersive X-Ray analysis

FWHM Full width of distribution at half the maximum count

GAG Glycosaminoglycan

GL Image grey level

H Hardness

HCL Hydrochloric acid

HFBA Heptafluorobutyric acid

HPLC High pressure liquid chromatography

IGF Insulin-like growth factor

keV Kilo electron volts

MMP Matrix metalloproteinase

NSAID Non-steroidal anti-inflammatory drug

OA Osteoarthritis

OI Osteogenesis imperfecta

OIM Osteogenesis imperfecta murine

OP Osteoporosis

PAI Plasminogen activator inhibitor

PMMA Polymethylmethacrylate

PTFE Polytetrafluoroethylene

QBEI Quantitative backscatter electron imaging

ROI Region of interest

SEM Scanning electron microscopy

TENS Transcutaneous electrical nerve stimulation

TGF Transforming growth factor

THA Total hip arthroplasty

TKA Total knee arthroplasty

uPA urokinase-type plasminogen activator

wt% Ca Weight percentage calcium

X Human bone mineral non-stoichiometric coefficient 1

Y Human bone mineral non-stoichiometric coefficient 2

Chapter 1

Introduction

1.1 Osteoarthritis

In 1997, in a population of North Americans and Northern Europeans, approximately one third of the 25 to 74 year old population were found to present with radiographic features of osteoarthritis (OA), involving at least one peripheral joint group [21]. More recent studies conducted in the United Kingdom (UK) have specifically targeted knee osteoarthritis and one in particular, published in 2001, found that approximately 10% of the population greater that 55 years of age exhibited symptomatic radiographic knee OA, with 2.5% severely disabled as a result [22]. With the increasing average age of Western populations expected to occur over the next thirty years, OA will become a much more prevalent problem. These changes have already been seen in work published in 2005. In the UK, Bedson *et al.* [23] found an average knee OA incidence of approximately 12.5% in a population greater than 45 years of age, a significant increase over that found by Peat *et al.* in 2001 [22].

Although the initiating factors involved in this disease are still contentious, long term effects due to the presence of this condition within a major joint are well established in both the bone and cartilage tissues. Osteoarthritis results in the eventual but total destruction of a joint's constituents in severe

Figure 1.1: X-ray image illustrating the location of an osteophyte within a osteoarthritic shoulder joint. [1]

cases. Initial clinical symptoms include increased water content within the cartilage and degeneration of the protein make-up of the tissue. Localised bony outgrowths or osteophytes are also common (Figure 1.1). Repetitive use of the joint over time irritates and inflames the cartilage, causing joint pain and swelling. Eventually, the cartilage breaks down, initially evidenced by flaking or small crevasse formation within the superficial zone. This damage proceeds down through the middle and deep zones of the cartilaginous layer. Complete destruction of the cartilaginous layer can occur and results in macroscopic damage to the newly exposed bony ends of the *in situ* joint surfaces, illustrated clearly in Figure 1.2. Over time, the overall shape of the joint can change, with bone or cartilage debris floating around inside the joint space, causing subsequent pain and damage (Figure 1.3).

Figure 1.2: An example of the large scale macroscopic damage due to complete cartilage erosion in an osteoarthritic femoral head. Image on the left shows a freshly excised, healthy femoral head, while the image on the right shows a late-stage osteoarthritic femoral head. [2]

Osteoarthritis is a disease that has received much academic and scientific interest in recent years and the complete understanding of its pathogenesis is seen as somewhat of a 'Holy Grail' to many researchers intimately involved in contemporary arthritis research. The implied importance of this analogy is quite apt since the answer to this pathological problem would facilitate treatment of the origin, not the symptoms, of a condition that has reputedly plagued our species as far back as the middle paleolithic era (30,000 to 300,000 years ago) [24]. However, this answer remains elusive long after the solution of seemingly more intricate medical conditions. It is a disease that has long been presented as an apparently simple condition of joint wear and consequent joint tear. The characteristic feature of this disease is a loss of articular cartilage quality or physical integrity, initially in the form

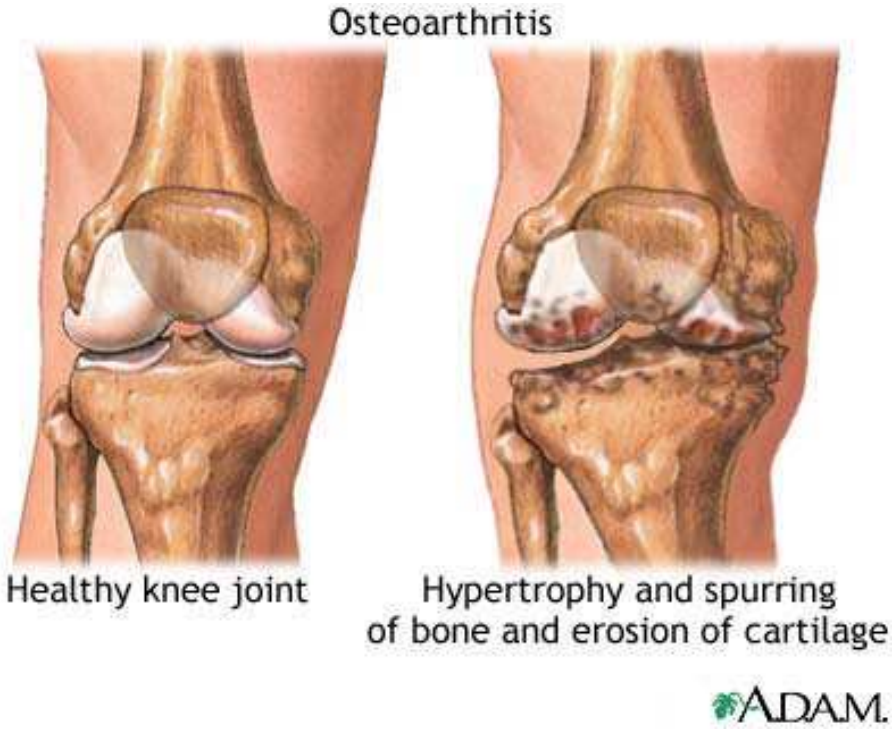

Figure 1.3: A schematic diagram illustrating the final appearance of a knee joint in an advanced case of osteoarthritis. [3]

of surface crevasses or fissures. As the condition develops, roughening of the cartilage continues to worsen and the synovium begins to swell and inflame. These clinical symptoms, coupled with a strong relationship with age and obesity lead to the classification of the condition as a rheumatic disease, a rather broad classification including approximately one hundred inflammation-related diseases.

The origin of this debilitating disease was thought to be in the first clinically-observed tissue affected, namely the cartilage. Bone changes were seen as responsive to the altered mechanical equilibrium within the joint, due to cartilage degradation. As predicted by Wolff's Law (or Roux's Law to be historically accurate [25]), bone adaptations were apparently secondary and unrelated to the initiation of the disease. Consequently, the current state

of the art with regard to disease treatment and management regarding the *in situ* tissues (bone or cartilage) is arthroscopic surgery, an invasive procedure which serves only to retard disease development and alleviate joint inflammation and pain. The majority of non-invasive disease treatments specifically target the painful inflammatory symptoms of this disease as opposed to its cause or development. Examples include exercise, weight control, rest, hot/cold treatments, non-steroidal anti-inflammatory drugs (NSAID's) and transcutaneous electrical nerve stimulations (TENS) [26, 27]. In severe cases, treatment involves arthroscopic surgery. Significant developments in our understanding of the pathogenesis of this disease must occur to allow any significant improvements over these currently available techniques.

Contemporary scientific investigations into the nature of this disease have questioned this classic view of OA, bringing into contention the main tissue of initiation. Subchondral bone has been implicated in numerous studies as having a primary role in the development of this disease [28, 29, 30, 31, 32, 33, 34, 35, 36, 37, 20, 38, 39, 40] and consequently may be its root cause. These studies have produced strong evidence that the cartilage can no longer be considered exclusively in the pathogenesis of this disease.

1.2 Objectives of the Thesis

Previous research in this field has exhibited major analytical shortcomings with a number of notable exceptions. Lack of consistency and agreement in the findings of most contemporary studies are unsurprising given the level of ambiguity and heterogeneity in the classification of the severity of the disease. Interpretation of results and subsequent conclusions regarding the intricacy of the pathology of this disease are impossible without a quantitative description of disease severity or stage of progression within an investigated sample set.

The aim of this thesis is to quantitatively investigate clinically-defined early-stage primary osteoarthritis in subchondral cancellous bone from hu-

man knee joint tibiae, specifically knee joints exhibiting medial compartment OA only. It is hypothesised that examination of the faster metabolising cancellous tissue would facilitate the measurement of the earliest changes occurring within the bone tissue. A quantitative classification (Mankin scoring system) of the disease's progression is employed to identify early-stage OA samples exclusively. This facilitates the investigation of the bone tissue at the earliest, clinically definable stage of the disease, reducing the influence of a secondary bone response on the measurements. Changes in the subchondral trabecular bone's mechanical properties will be determined and correlated with corresponding measurements of tissue mineralisation.

The secondary objective of this thesis is to evaluate bone samples originating from adjacent, non-presenting lateral tibial compartments. Evidence of a possibly earlier stage in the development of this disease within the joints *in situ* bone tissue will be investigated, with a view to characterise mechanical and compositional properties. A tertiary objective of this thesis is the development of a novel scanning electron microscopy technique, facilitating damage-free, depth-specific mineralisation assessment. This allows direct comparisons between depth-specific mineralisation data and depth-specific nanoindentation data within our sample set.

This study offers a novel insight into primary OA of human subchondral trabecular bone at its earliest developmental stage currently known to exist. Contemporary analysis techniques such as nanoindentation and quantitative backscatter electron imaging (QBEI) will be employed within a defined depth range at the tissue level, offering new insight into the pathophysiology of this deceptively complicated disease.

Chapter 2

Literature Review

The purpose of the literature review is to supply a concise and relevant description of the current state of knowledge, specifically with regard to this investigation. This will include bone tissue and structure, changes at all relevant structural levels due to osteoarthritis, and relevant contemporary work conducted on healthy and osteoarthritic bone tissue using the methodologies employed and described within this thesis.

A detailed description of the hierarchical structure of healthy bone is presented, with specific focus on the architectural levels identified as most important with regard to the pathogenesis of osteoarthritis. At the tissue level, morphological changes with a large influence on the strength of the resulting macrostructure will be identified and their observed influence in this pathology described. The mineralisation process is summarised, with particular emphasis on the constituents identified as intrinsic to the pathogenesis of osteoarthritis.

The current extent of knowledge regarding the pathology of osteoarthritis will also be discussed. The classic view of this disease is presented, as are the findings of contemporary and relevant investigations that challenge this approach to the disease and its initiation. The measurement methods employed throughout this research can influence the final results [41] and consequently the state of research in both nanoindentation and QBEI

is reviewed. Additionally, relevant contemporary investigations concerning healthy and diseased bone tissue, using similar experimental protocols to those used throughout this present work, are also described.

2.1 Structural Hierarchy of Bone

The hierarchical structure of bone is split into five main levels within this thesis for descriptive purposes. These hierarchical levels are discussed in detail in the following subsections and described as follows;

- Nanostructure (<500 nm) e.g. collagen molecules, bone mineral crystals
- Ultrastructure (≈500-1000 nm) e.g. collagen fibrils and fibres
- Microstructure (≈1-10 μm) e.g. bone lamellae
- Sub-macrostructure (≈10-500 μm) e.g. Haversian systems, trabeculae
- Macrostructure (>0.5 mm) e.g. cortical and cancellous bone

2.1.1 Nanostructure

Collagen Molecule

The term collagen is used to refer generally to the group of proteins forming a characteristic triple helix of three polypeptide chains [5]. Currently, at least nineteen genetically distinct collagen types have been discovered and isolated [42]. Collagen type classification is based on molecular size or method of assembly. Collagen types are usually divided into two main groups: fibrillar (e.g. types I, III, V) and non-fibrillar (e.g types VI) [42]. Human bone tissue is predominantly composed of type I collagen with trace amounts of type V. This review will focus entirely on type I collagen based on empirical evidence of its primary role in the determination of bone stiffness and toughness [43, 44, 45].

Collagen is secreted by osteoblasts in the form of bone organic matrix. Type I collagen is the primary organic component of bone's organic matrix, a highly vascular domain containing various growth factors such as glycosaminoglycans (GAGs), osteocalcin and osteonectin. Quantitatively, type I collagen makes up approximately 85 to 90% of the organic matrix in bone [46]. In humans, this predominantly type I collagen matrix forms the essential framework on which intramembranous ossification occurs. The type I collagen molecule or 'tropocollagen' is made up of three entwined polypeptide chains. Each polypeptide chain is composed of approximately 1050 amino acid residues, such as glycine, lysine and hydroxyproline [42]. The central region of each polypeptide chain consists of a sequence of 338 contiguous, repeating triplets. In healthy type 1 tropocollagen, every third residue within these repeating triplets must be a glycine residue (Figure 2.1) [46, 42, 4]. Additionally, investigations into the residual profile of the molecule have shown that in approximately one-third of all these 338 sequence triplets, at least one of the residues adjacent to the requisite glycine residue (X and Y in Figure 2.1) is either proline or hydroxyproline [46, 47].

Tropocollagen contains more than one genetically distinct type of polypeptide chain. Healthy type I collagen is comprised of three polypeptide chains in total (Figure 2.1), specifically two $\alpha 1$(I) chains and one $\alpha 2$(I) chain [5]. These helical polypeptide chains differ in terms of their amino acid sequence which has subsequent important structural consequences, primarily an extremely residue-specific intrinsic strengthening system [5, 37, 48, 42]. Each polypeptide chain takes the form of a left-handed helix. These three left-handed helixes are entwined together to form a single right-handed triple helix [4, 42, 46] or 'supercoil' (Figure 2.2) [4]. Tropocollagen is approximately 300 nm long and 1.5 nm in diameter (Figure 2.3) [46]. The molecule is comprised of a central helical section with an adjacent telopeptide section at each end. Formation of the triple helix proceeds from the C-telopeptide side to the N-telopeptide side (Figure 2.3). As mentioned previously, preservation of the repeating glycine-based triplet sequence is extremely important

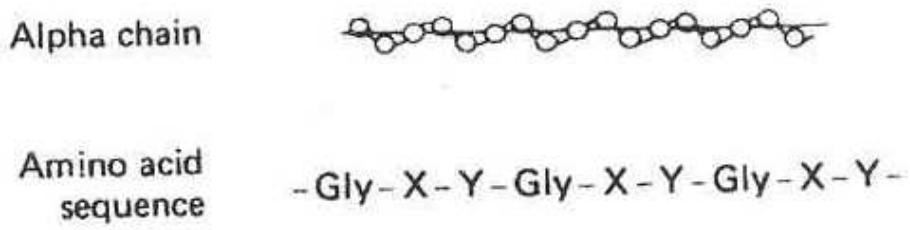

Figure 2.1: A schematic diagram illustrating the amino acid sequence and alpha chain configuration of a typical polypeptide chain. [4]

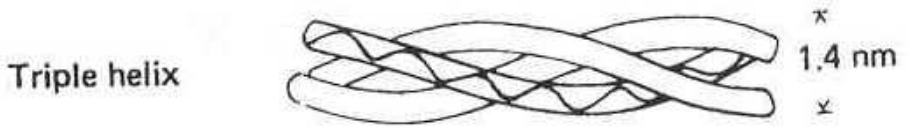

Figure 2.2: A schematic diagram illustrating the tropocollagen helix. [4]

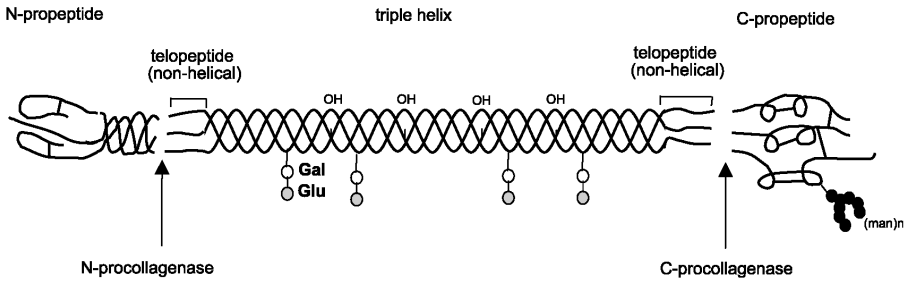

Figure 2.3: A schematic diagram illustrating the assembly of tropocollagen and the resulting molecular domains. [5]

but residue mutations can be tolerated with the exception of this glycine amino acid located at the critical third position. The glycine residue is the only amino acid small enough to be accommodated within the particularly small triple helical centre [47], hence its importance in molecular assembly. Healthy helical formation is impaired by the presence of any other residue at this point [5].

An additional stabilisation or strengthening process occurs within the triple helix. This method relies on the repeated presence of proline and hydroxyproline within each polypeptide chain. Hydroxyproline in particular has been seen to be a specific attachment site for the intra-molecular covalent bonds formed within healthy tropocollagen. These covalent bonds confer an additional helical stability to the structure [47].

The system of opposing helical twists in tropocollagen gives the resulting tropocollagen molecule a significant structural advantage. The opposing twists reduce subsequent twisting of the supercoil when subjected to externally applied tensile forces [42]. Twisting of the helical supercoil, caused by an externally applied tensile force, creates a residual stress within the structure, reducing the effective amount of load the coil can carry prior to failure. The overall result is the reduction of the coil's breaking or yield strength due to the presence of this residual stress caused by unnecessary supercoil twisting [49]. This is of particular relevance with regard to current investigations regarding the mutated form of collagen present in osteoarthritic bone tissue which exhibits a mutation of an entire polypeptide chain within the molecule [37]. This is discussed in detail in Section 2.4.

Mineral Crystal

Human bone mineral is primarily composed of calcium phosphate and is intimately associated with bone's organic matrix [50, 51, 11, 52]. Bone mineral belongs to the apatite series of minerals. Its actual crystal structure is based on, but not identical to, pure hydroxyapatite [42]. The chemical formula for pure hydroxyapatite is $Ca_{10}(PO_4)_6(OH)_2$ [46]. However, human bone mineral deviates from this stoichiometric relationship as it contains additional impurities, such as approximately 4 to 6% by weight of carbonate. The stoichiometric amount of phosphate also differs as some of this is replaced by either sulphates or silicates [42]. Any subsequent references to bone hydroxyapatite within this thesis refer to the actual, non-stoichiometric form found in bone tissue, unless explicitly stated otherwise.

Human bone mineral's actual composition can be written as

$$Ca_{8.3}(PO_4)_{4.3}(CO_3)_X(HPO_4)_Y(OH)_{0.3} \tag{2.1}$$

where subscripts X and Y in the chemical equation can vary indefinitely. The only requirement is that their sum must equal 1.7 in order to balance the chemical equation [46]. Due to its non-stoichiometry, bone mineral is poorly crystalline and the resulting mineral platelets can vary quite significantly in size across a range of different tissue types [42]. Mineral precipitation can occur spontaneously due to the mineral's relative insolubility in water and this is obviously advantageous throughout the mineralisation process *in vivo*. The mineralisation process is also known as calcification and, in the past, was considered a process involving only mineral precipitation dynamics. This simple mineral precipitation model assumed that the product of the two necessary mineral ions within the body, $[Ca^{2+}]\times[PO_4^{3-}]$, was insufficient for precipitation, hence the importance of the organic matrix as a catalytic substrate. However, this was subsequently shown to be too simplified a model of the actual process. Instead, a process known as epitactic nucleation was proposed. This method is based on the seeding of the non-stoichiometric hydroxyapatite mineral crystals on the nucleus of a mineral of similar composition or crystalline structure. This initial, base mineral crystal would be located within the gap region loci of the collagen fibrils [13].

Extensive investigations have been conducted in both human and animal models to conclusively characterise the mineral crystal morphology [53, 12, 50, 51, 11]. Bone mineral crystals taken from numerous species tend to form irregularly-shaped thin platelets. More recent investigations have shown that these platelets have an average length of approximately 50 nm and an average width of about 25 nm [50, 51]. The average platelet thickness has been found to be about 3 nm thick. These dimensions are of great significance as they are of similar dimension to the amount of space available on and within healthy mineralising collagenous structures within the bone matrix, such as collagen fibrils (Figure 2.4) [50, 51]. Their relationship with diseased OA

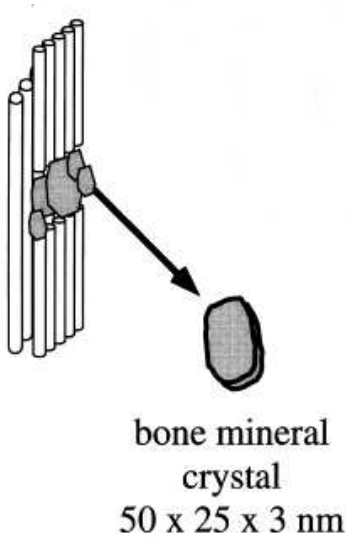

Figure 2.4: A schematic diagram illustrating the assembly of collagen fibrils and bone mineral crystals. [6]

bone tissue is still undetermined and of significant importance with regard to the pathogenesis of the disease.

2.1.2 Ultrastructure

The ultrastructure of bone tissue is based on structures formed as a direct result of the intimate physical relationship between the two main nanostructural constituents, tropocollagen and the mineral crystal. At this structural level, groups of collagen molecules aggregate to form mineralised collagen fibrils (≈100 nm in diameter [9]), which group together with other fibrils to eventually form mineralised collagen fibres (Figure 2.5) [6].

Fibril formation is inherent in the nature of tropocollagen. Tropocollagen is a highly reactive molecule which easily undergoes spontaneous fibrillogenesis to create a supramolecular structure [54]. The formation of these fibrillar structures is inherently linked with collagen cross-linking [6, 8]. The longitudinal distribution of polar and hydrophobic residues along the length of the tropocollagen helix results in a staggered, lateral intermolecular interac-

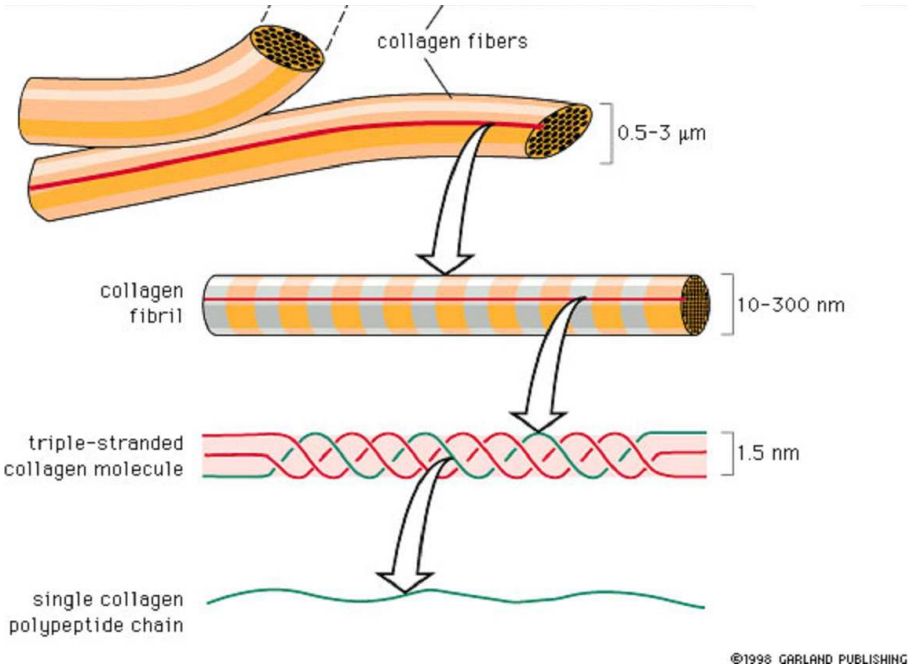

Figure 2.5: A schematic diagram illustrating the assembly of collagen molecules into fibrils and, consequently, fibres. [7]

tion through the process of cross-linking during fibrillogenesis. This method of self-assembly results in the frequently observed molecular axial stagger within collagen fibrils, approximately 67 nm in magnitude. The axial stagger results in the 40 nm wide gap regions between the tropocollagen ends that are vital for the healthy mineralisation process (Figure 2.6) [54]. Initial fibril formation is stabilised by polar, hydrophobic, non-covalent interactions. These are commonly referred to as immature cross-links [55] and these chemical interactions bond specific amino acid residues within adjacent collagen molecules. One side of this bond is created within the tropocollagen telopeptide and the other lies within the helical region of the molecule (Figure 2.7) [55]. The importance of collagen cross-linking on the overall strength of bone tissue has been studied by a number of investigators [43, 56]. These immature non-covalent bonds are eventually superceded by stronger, mature covalent cross-links. These form by spontaneous reaction with the existing

intermolecular immature cross-links to form this more stable mature form of cross-link [8, 55, 48, 37].

As alluded to earlier within this Section, the gap regions formed between the telopeptide ends of the collagen molecules are of significant importance with regard to the process of mineralisation. These gap regions become centres for ossification [9]. The specific nature of these residue sequences is believed to encourage the spontaneous precipitation of mineral out of the

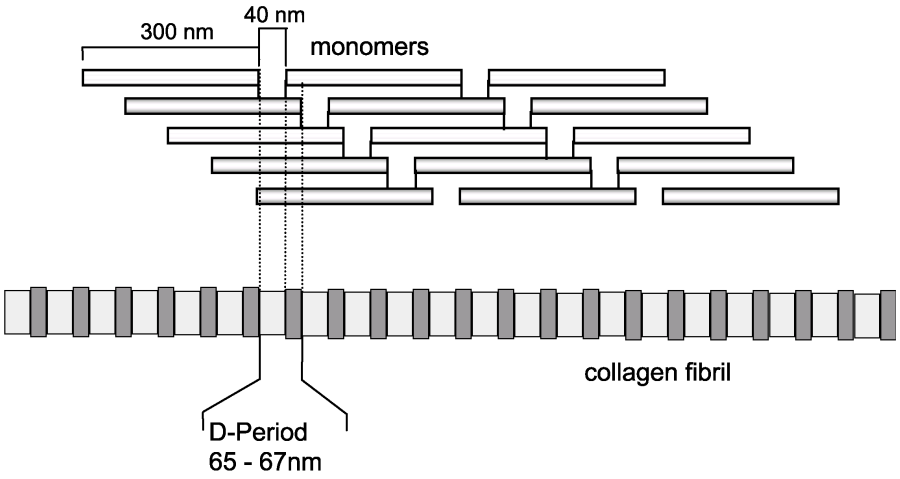

Figure 2.6: A schematic diagram illustrating the two dimensional arrangement of collagen molecules in quarter-stagger alignment. [5]

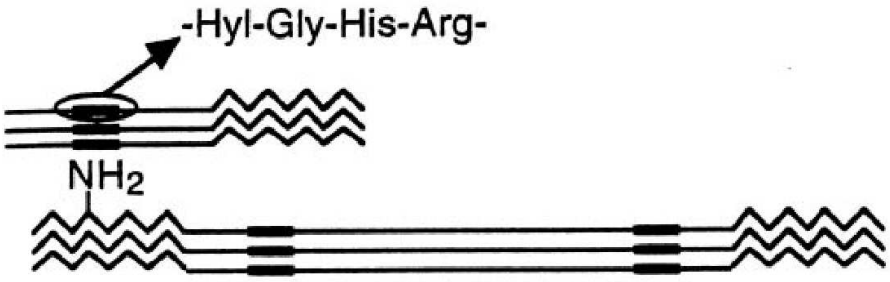

Figure 2.7: A schematic diagram illustrating the quarter-stagger alignment of collagen molecules and the corresponding location of cross-links. A typical amino acid residue sequence is highlighted. [8]

extracellular matrix onto an existing mineral nucleus (epitactic nucleation). The mineralisation process is predominantly intrafibrillar [54, 11] and begins with the appearance of multiple simultaneous independent nucleation sites based at the ossification centres. The mineral crystal platelets formed at these sites eventually grow to form the observed mineral plates and extend along the fibril surface (Figure 2.8) [54].

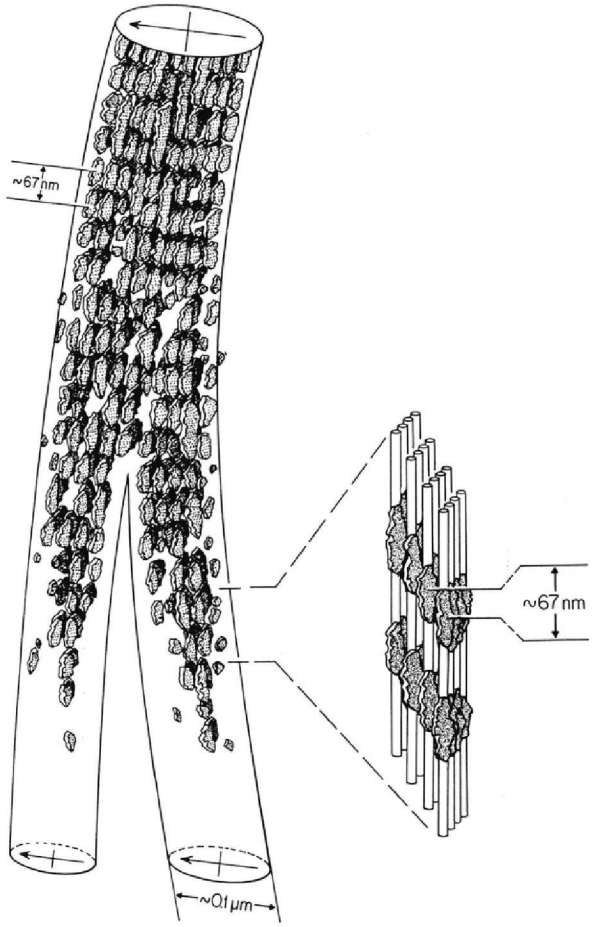

Figure 2.8: Schematic diagram of mineral deposition within the collagen fibril gap regions. As the mineralisation process causes the fibril to swell, fibrils can eventually lose their individuality and merge. [9]

The mineral crystals that form on and within these fibrils tend to grow exhibiting a specific crystalline orientation. The c-axes of the mineral crystals tend to run approximately parallel with the long axis of the associated fibrils (Figure 2.9) [11, 6]. The crystals also tend to be distributed evenly throughout the fibril (Figure 2.10) [11]. The consequence of OA on the fibril formation and subsequent mineralisation process has yet to be conclusively determined but based on the specific nature of these processes, serious consideration must be given to this area of bone synthesis when examining a disease such as OA.

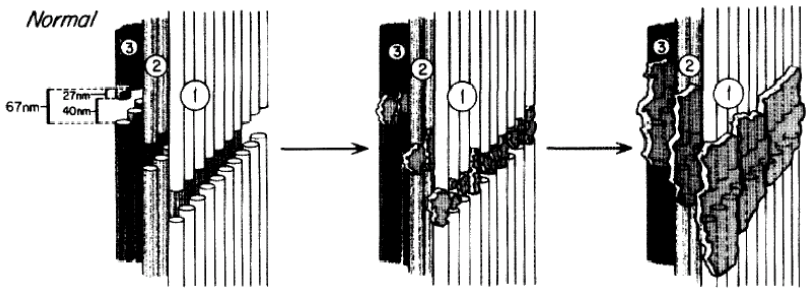

Figure 2.9: A schematic diagram illustrating the assembly and early mineralization of collagen molecules in a three-dimensional perspective. [10]

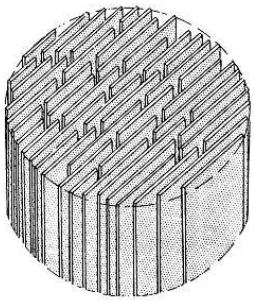

Figure 2.10: Schematic of a cross-section through a single collagen fibril showing mineral deposition throughout the fibril. [11]

2.1.3 Microstructure

The next structural level of bone is formed when individual mineralised collagen fibres are aligned over large distances and consequently form what are known as a lamellae [46]. These mineralised collagen fibres combine to form lamellae with an average thickness range of approximately 3 to 7 μm [6]. Definitive information about lamellar structure is still in contention and most of our knowledge about this structure is based on a number of contemporary hypotheses. Very little is definitively known about the detailed intra-lamellar structure due to empirical difficulties. The investigation or determination of the exact nature of this level of bone tissue structure is beyond the relevant scope of this study and, consequently, literature review. However, the most commonly accepted hypothesis will be described.

The prevalent model regarding intra-lamellar structure is known as the 'rotated' or 'twisted' plywood model, proposed by Giraud-Guille *et al.* in 1988 specifically for osteonal bone [57]. In this model, the mineralised fibril axes are all roughly parallel to the lamellar boundary plane [52, 12]. Adjacent lamellae differ with respect to the orientations of these fibril arrays, hence a 'plywood structure' (Figure 2.11) [12, 58]. The 'twisted' or 'rotated' proportion of the model refers to the twisting or rotating of the crystal layers within an individual fibril about the long axis of that fibril. This can be illustrated schematically as rotation about ψ_2 in Figure 2.12

Further complications to this model have been proposed [58, 59, 60], some of which were subsequently dismissed [61], but little empirical evidence has been found to conclusively define the actual structure. This has consequences regarding correct interpretation of subsurface data recorded throughout the course of this present work. The proportion of tissue level changes in mechanical properties and composition, associated with this level of bone's structure, will have a significant influence on the conclusions of the subsurface analysis conducted throughout the course of this present work.

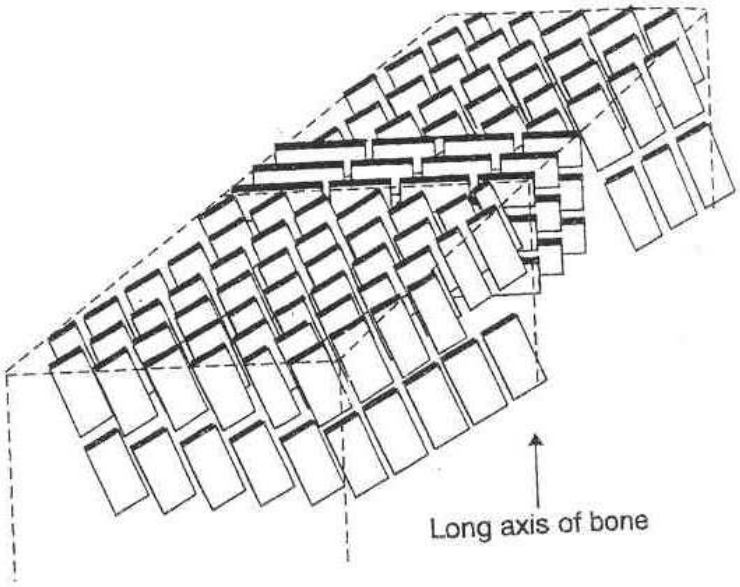

Figure 2.11: A schematic diagram illustrating the proposed plywood structure of bone lamellae. [12]

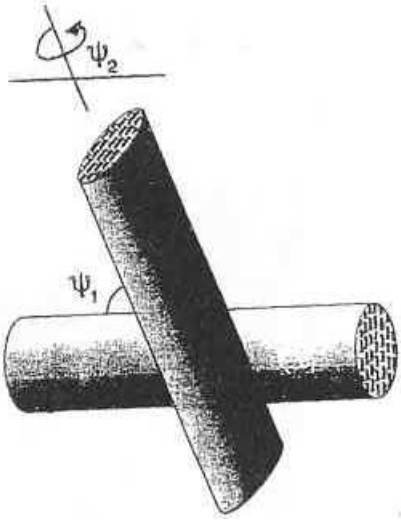

Figure 2.12: A schematic diagram illustrating the proposed 'twisted' plywood structure of bone lamellae. [12]

2.1.4 Sub-macrostructure

At this structural level, two main types of distinct tissues exist, both of which are composed of lamellar layers grouped together. The first tissue is known as a Haversian system or osteon while the other is known as trabecular tissue. Haversian systems are made up of lamellar groups (between approximately three and eight) wrapped in a concentric fashion around a central Haversian canal. Trabecular tissue is of greater relevance within the scope of this thesis and will be examined in more detail.

Trabecular tissue is more random in terms of its lamellar structure and hence harder to characterise. Trabecular tissue can take one of two forms. The first is known as a trabecular strut, a long, thin structure ranging in size from approximately 50 to 300 μm in diameter [6]. The second form of trabecular tissue is known as a trabecular plate and has a more irregular and random shape. This tissue is best described figuratively (Figure 2.13) where the struts are evident as long thin spicules and the trabecular plates are the jointing sections connecting the trabecular struts.

The major difference between Haversian systems and trabecular tissue, specifically with regard to the work presented in this thesis, is their different lamellar structures. Haversian systems are composed of effectively parallel lamellae, either in a concentric or longitudinal direction while trabecular tissue exhibits a more random lamellar layer orientation. Lamellar layers located within trabecular struts do not always run parallel with the trabecular surface [62]. However, as is generally evident, the lamellar layers closest to the trabecular surface tend to follow the surface approximately. The magnitude of the non-parallel alignment within a trabecula can become much more pronounced within the trabecular central core (Figure 2.14). The lamellar orientation within trabecular plates is more random in nature and can show no predominant orientation or partial orientation corresponding with the trabecular plates surface (Figure 2.15). This information is of paramount importance when the findings presented within this thesis are considered.

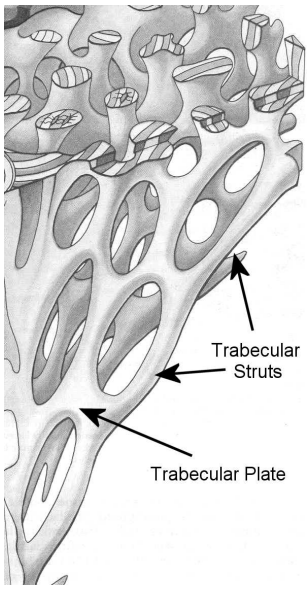

Figure 2.13: A schematic diagram showing part of a trabecular network, where both trabecular struts and the connecting trabecular plates are evident. [13]

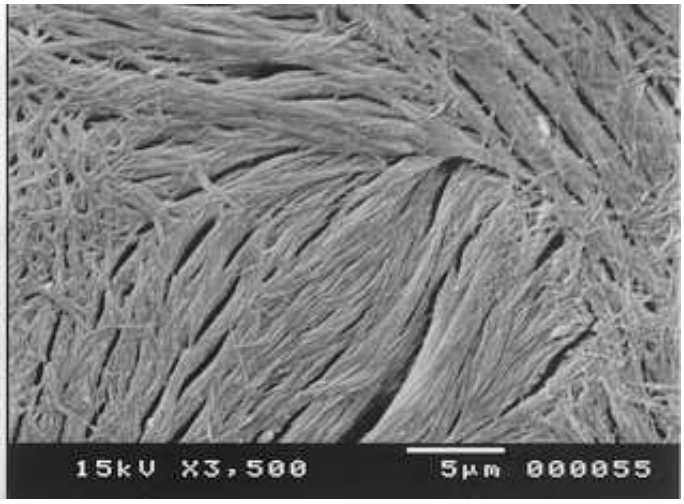

Figure 2.14: SEM image illustrating the non-parallel alignment of trabecular lamellae. [14]

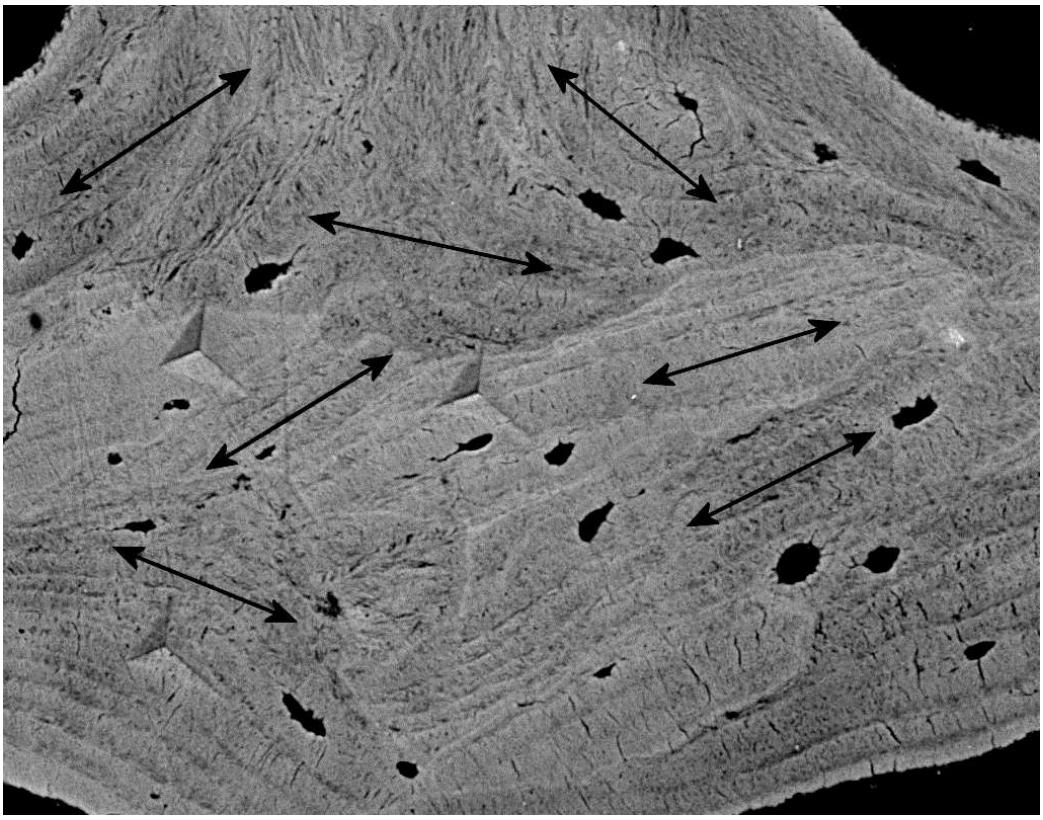

Figure 2.15: Backscatter image of a trabecular bone plate transverse section, illustrating the non-parallel alignment of trabecular lamellae. Approximate lamellar direction denoted by black arrows.

2.1.5 Macrostructure

At this level within the structural hierarchy, once again two main structures exist, each evolved from the two main constituents of the previous sub-macrostructural level, cortical and cancellous bone. Haversian systems develop within primary bone, resulting in secondary bone. Haversian systems form the basic fundamental unit in cortical bone. Cortical bone tissue is a solid material, with the only spaces in it being for osteocytes, canaliculi, blood vessels and erosion cavities [62]. Trabeculae fuse together to form a

porous, interconnected network known as cancellous tissue, seamlessly attached to the adjacent cortical bone (Figure 2.16). Most empirical evidence regarding the development and consequent effects of OA have been at this level of investigation. Many significant changes in bone's macrostructure due to the presence of primary OA have been recorded and are still of particular interest due to enduring contradictions between the findings, at both the macrostructural and sub-macrostructural levels. Tibial subchondral bone thickness has been seen to increase in OA samples, a scenario not mirrored in femoral subchondral bone examined within the same study [63]. Earlier studies conducted on femoral bone resulted in findings contrary to the previous example, specifically a significant increase in subchondral femoral head thickness in OA samples [28]. Additional empirical contradictions include bone stiffness measurements, which have been seen to both increase and decrease. Iliac crest trabecular bone specimens tested in compression were found to be stiffer with increased compressive strength relative to healthy controls [64]. Subsequent work found the opposite to be true in femoral head subchondral bone [31]. It is of paramount importance that these large scale changes are included in the overall assessment of the pathogenesis of this disease, particularly due to the level of disagreement in empirical conclusions. Additionally, empirical data at all architectural levels supports accurate speculation regarding the level of ubiquity of this disease throughout the tissue's macrostructure, a vital diagnostic tool with regard to disease initiation.

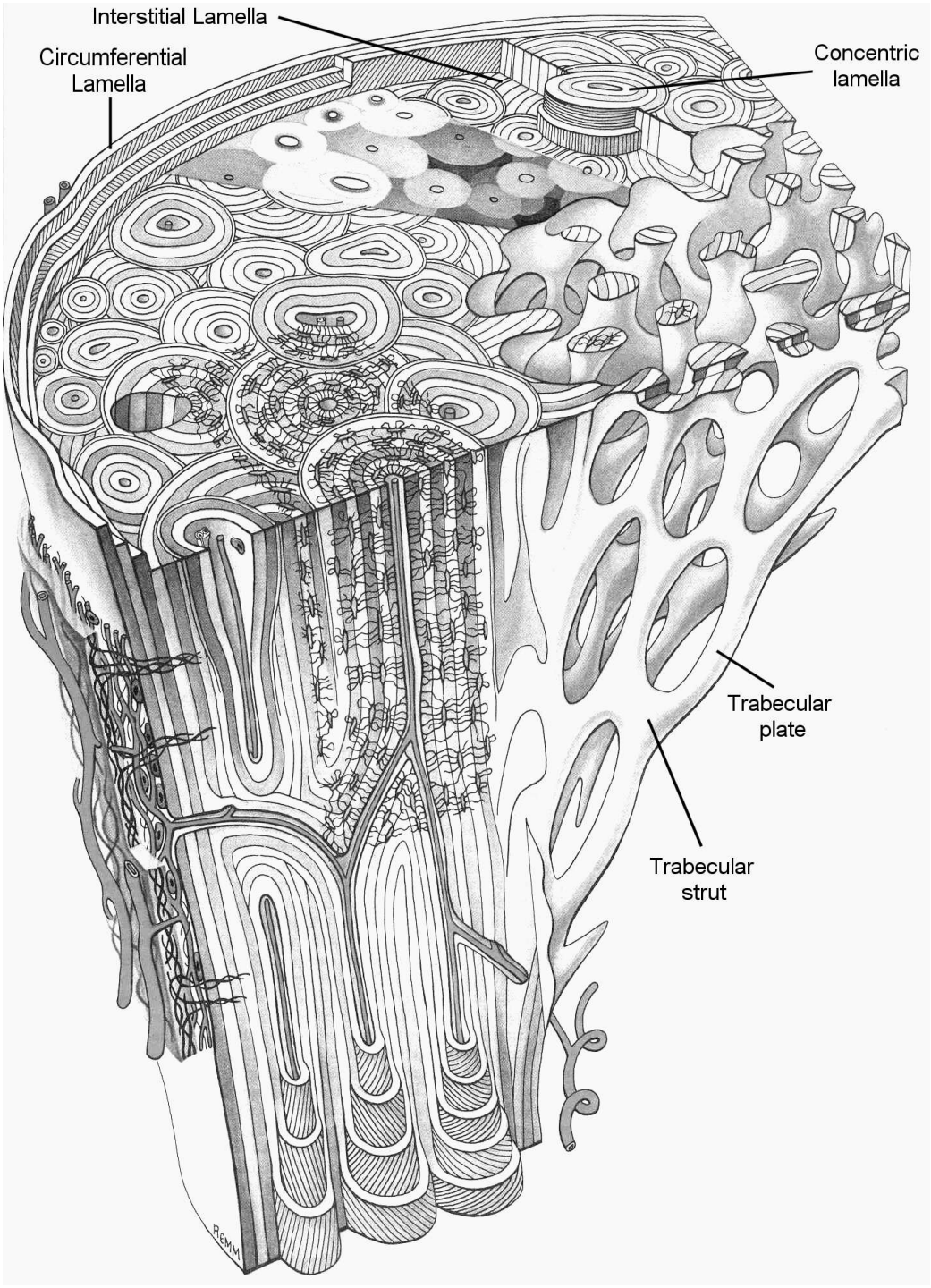

Figure 2.16: Schematic illustrating cortical and cancellous tissue within the cross-section of a long bone diaphysis. [13]

2.2 Bone Cells

There are four main types of bone cell of particular interest with regard to any pathological investigation conducted, namely osteoprogenitor cells, osteoblasts, osteoclasts and osteocytes. These cells are responsible not only for the initial mineralisation of the highly vascular osteoid matrix but also for the delicate balance of bone remodelling and repair that exists in healthy bone tissue. Significant changes in the function or phenotype of these cell types can affect the structure and integrity of the mineralised end product and have been implicated in the development of this condition [35, 37, 65, 66, 67].

2.2.1 Osteoblasts

Osteoblasts are primarily concerned with the formation of new bone matrix, a process known as osteogenesis. This function includes the synthesis and release of certain proteins and other organic components of the osteoid matrix, such as collagen or glycosaminoglycan. Osteoblasts play a crucial role in the mineralisation process by elevating local calcium phosphate levels and promoting the deposition of calcium salts within the organic matrix.

2.2.2 Osteoclasts

Osteoclasts are large cells involved in the removal of bone matrix, wherever necessary. They secrete acids and proteolytic enzymes which dissolve bone matrix, in a process known as osteolysis. Osteoclasts have a highly coupled relationship with osteoblasts [68]. Together, groups of osteoclasts form what is commonly referred to as a 'cutting cone', part of a basic multicellular unit (BMU). The BMU is a bone remodelling unit, maintaining the delicate balance of bone turnover within mineralised tissues. The front of a BMU is populated by osteoclasts which move along a surface of bone matrix, dissolving the existing material. The rear of a BMU is made up of osteoblasts which lay down new bone matrix (Figure 2.17). It has been estimated that

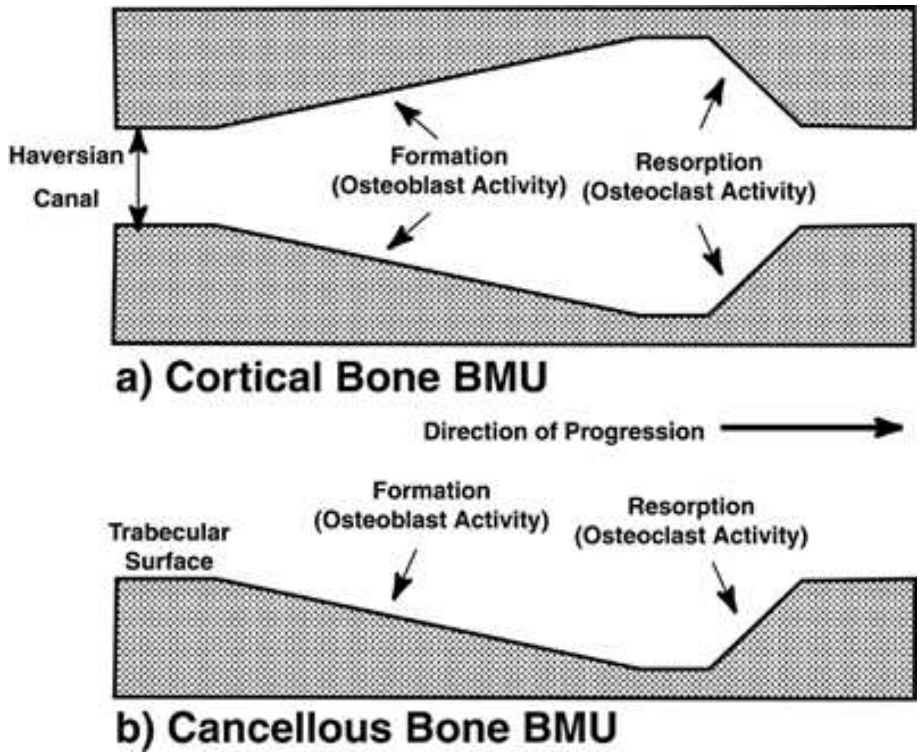

Figure 2.17: Schematic illustrating the basic multicellular unit in both cortical and cancellous bone. [15]

approximately one million BMU's can be operating at any given moment within an average skeleton, resulting in a total skeletal renewal occurring, on average, every ten years [69].

2.2.3 Osteocytes

Osteocytes are mature bone cells within bone matrix. The are formerly osteoblastic in nature and become osteocytes when they become surrounded by newly formed bone matrix in enclosures known as lacunae (Figure 2.18). Osteocytes are connected throughout the bone matrix by cellular processes which lie in small channels known as canaliculi (Figure 2.19). Their accepted primary function is transmission of fluid throughout the tissue [13]. However, the exact method and chronology of the formation of canaliculi is still in

contention, as is their relative importance in remodelling [70, 71]. Recent theoretical studies have proposed a vital role for these channels in the repair of bone microdamage detection and consequent repair signalling.

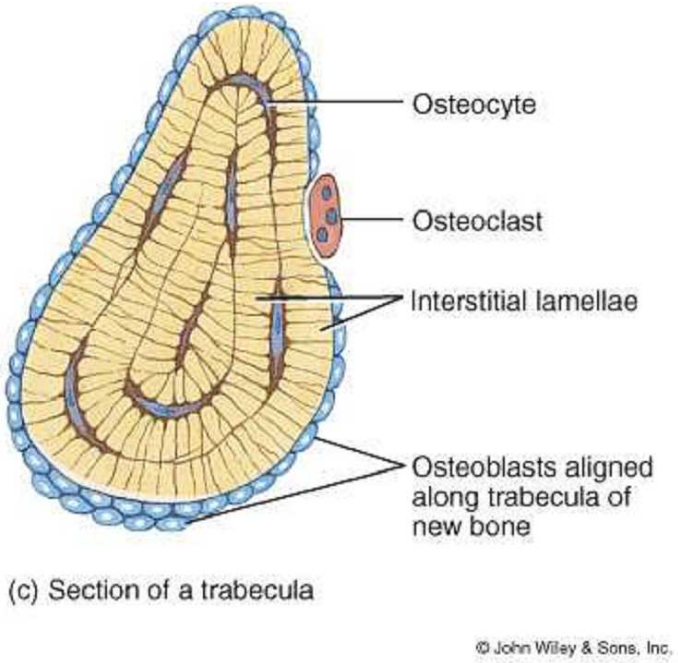

Figure 2.18: Schematic of a trabecular strut cross-section, illustrating bone lacunae and their corresponding canalicular structure.

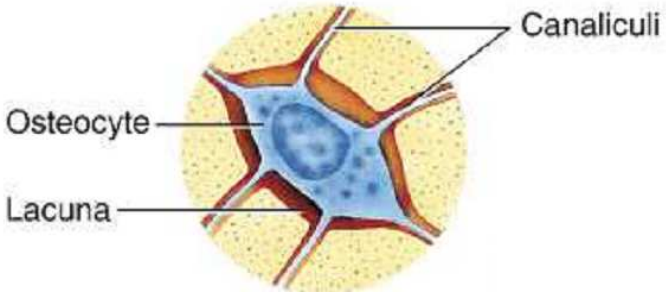

Figure 2.19: Schematic showing a bone osteocyte lacuna and its cell processes in the canalicular structure.

2.2.4 Osteoprogenitor Cells

Osteoprogenitors are a small group of mesenchymal cells that are located within the endosteum, an inner layer that lines vascular passages within bone matrix. Their primary function is to maintain the osteoblast population by producing daughter cells that differentiate into osteoblasts.

2.3 Ossification

The process of bone development or ossification is best understood with prior knowledge of the hierarchical structure of bone. There are two main types of ossification, namely intramembranous and endochondral ossification. Endochondral ossification is concerned with the process of bone growth through the ossification of cartilaginous tissue. Intramembranous ossification is the direct mineralisation of a highly vascularised connective tissue and occurs during bone remodelling. This literature review focuses exclusively on the process of intramembranous ossification based on the proposed relationship between OA pathological severity and bone remodelling [35, 32] on an altered collagenous substrate [37].

Intramembranous ossification is site-specific. Mesenchymal cells proliferate and condense around a profuse capillary network, becoming osteoblasts. They begin to form osteoid matrix, containing primarily collagenous tissue, proteoglycans and other important growth factors. Osteoblasts have the principle role of secreting this matrix framework. This osteoid matrix is rapidly calcified with minute deposits of calcium phosphate. These calcium phosphate deposits eventually form the non-stoichiometric hydroxyapatite crystals at ossification sites intimate with the collagen molecules and fibrils.

The resulting collagen network is coarse with interweaving collagen fibres. The mineralised form of this structure is commonly referred to as woven bone. This calcifying network is the initial and delicate basis for trabecular structure. Layers of calcifying matrix are added to these initial trabeculae while osteoblasts get concurrently trapped within the layers in primitive lacunae

(Figure 2.18). Contact between these lacunae and subsequent cells are retained using interconnected tubes known as canaliculi (Figure 2.19).

The ossification process proceeds by an overall thickening of trabecular tissue. At this point, the mineralising tissue can either remain as an interconnected trabecular network or through subsequent remodelling around trapped blood vessels, become the more densely packed cortical tissue. In cortical bone regions, the thickening process continues. In cancellous tissue, the process of trabecular thickening slows. Finally the surrounding mesenchyme condenses to form a fibro-vascular endosteum around the trabecular surfaces [13].

2.4 Osteoarthritis

Osteoarthritis is a disease with significant worldwide prevalence. Contemporary statistics are predominantly based on the United States of America, with the approximate U.S. prevalence rate calculated and applied worldwide. This results in an approximate estimate based on the total population of a given country. It is currently estimated that approximately 40 million Americans (or 1 in every 13 people) are affected by OA [27], with a cost of approximately $65 billion to their economy per annum [72].

The classic view of OA has been of a degenerative joint disease. It is a pathology primarily associated with damage to articular cartilage within an affected joint. Initiation was always assumed to be as a direct result of an initial biological or mechanical disruption to the joint. This would detrimentally affect the joint's mechanical equilibrium leading to macroscopic damage to both the articular cartilage and *in situ* subchondral bone. Degenerative changes would proceed over time, leading to a physical breakdown of the joint's constituents. This breakdown would present clinically as condylar damage, destruction of articular cartilage and the formation of osteophytes [21]. This is no longer the accepted aetiology. The characteristic feature of

this disease is still the destruction of cartilage but changes have been observed throughout the entire joint [55, 33, 34, 32, 35, 31].

One of the earliest studies to focus specifically on the bone tissue was conducted by Grynpas *et al.* [28]. They looked at subchondral human bone taken from the femoral heads of 60 to 80 year old donors with clinically diagnosed, moderate to severe OA, requiring Total Hip Arthroplasty (THA). Evidence of subchondral involvement was discovered when they measured a significant decrease in mineralisation level, a symptom hard to describe as a secondary consequence of articular cartilage damage. Dequeker *et al.* [30] investigated the effect of OA on local growth factors within transiliac biopsies. The grading of the pathology was conducted using remote assessment of the disease within the hands of donor subjects. Bone factors known to have strong links with bone growth and metabolism were significantly elevated in the OA transiliac samples. These included the specific growth factors IGF-I, IGF-II and TGF-β. This provides a possible explanation for the lack of OA symptoms in osteoporotic (OP) patients and vice versa. All these studies provided strong preliminary evidence of the integral part played by *in situ* bone tissue in the development of OA.

A number of years later, Li and Aspden [31] published an important paper describing initial evidence of a materially weaker bone tissue in OA samples. Using ultrasonic techniques, they looked at subchondral bone taken from human femoral heads and found an intrinsically less stiff bone tissue, as well as seeing hypomineralisation of the tissue. Within the same year, another study examined the cellular aspects of the disease. Westacott *et al.* [32] examined bone cell cultures established using explants obtained from both hip and knee joints with OA. The study found that osteoblast-like cells from OA patients were able to influence cartilage metabolism. Specifically, these osteoblast-like cells exhibited an altered function *in vitro* as they were found to be unusually capable of degrading cartilage glycosaminoglycans (GAGs). The following year, Hilal *et al.* [35] looked at similar osteoblast-like cell explants from subchondral bone harvested from the tibial plateaus of To-

tal Knee Arthroplasty (TKA) patients. These cells were found to express themselves differently *in vitro* when compared with healthy controls. Specifically, they expressed significantly elevated levels of uPA, IGF-I and PAI-I. Alkaline phosphatase and osteocalcin release were also elevated relative to controls. In essence, these cells exhibited an altered phenotype *in vitro*. At this stage, it was obvious that major tissue level changes occur in the disease that significantly affect the intrinsic strength of the tissue and its basic cellular components.

Changes in bone's metabolism in OA tissue were subsequently investigated by Mansell *et al.* in 1997 and 1998 [33, 34]. In general agreement with previous work, Mansell and his colleagues found an increased bone metabolism in OA human femoral heads, specifically significant increases in matrix metalloproteinase 2 (MMP-2) and alkaline phosphatase. Additionally, in a study reported the following year [34], collagen metabolism was specifically investigated and found to be significantly increased, with the greatest activity within the subchondral zone. Mineralisation levels and cross-linking profiles were also central parameters of interest. No significant alteration to the cross-linking profile was observed but hypomineralisation of the bone tissue was measured. With bone metabolism in mind, Li *et al.* [36] used the electron microscope to qualitatively assess the effect of OA on bone tissue structure. For this study, late-stage OA samples from human femoral heads were investigated. In general the tissue was seen to be more porous in the presence of the disease. Considerable thickening of both the trabecular struts and the subchondral bone plate was seen, suggesting a larger amount of a less tightly compacted bone mineral compared with healthy controls. Additional measurement of the bone's composition was carried out using Energy Dispersive X-ray Analysis (EDX) but no deviation from healthy bone's stoichiometry was observed due to presence of the disease. Summarising these studies, it is evident that the metabolism and consequent amount of bone mineral produced are affected by the presence of OA.

However, arguably the most significant work to date was carried out by Bailey *et al.* in 1999 [48]. Bailey and colleagues examined human OA collagen and discovered that the nature of the synthesised collagen in OA bone is distinct from that found in healthy controls. Specifically, overhydroxylation of either the helical or telopeptide lysine residues was observed, resulting in an altered collagen cross-link profile, specifically an overall reduction in lysine hydroxylation but with an increase in the hydroxylated collagen cross-links [48, 73]. The subsequent effect of this mutation and consequent disruption to the cross-linking profile is unknown but some forms of osteogenesis imperfecta (OI) are caused by similarly isolated and apparently minor mutations [47]. This gives some indication of the probable severity of such alterations within the collagen. Their investigation resulted in a subsequent discovery relating to the inherent nature of the collagen synthesised. A genetically distinct form of the collagen molecule was discovered in OA bone tissue, known as the homotrimer. This is an alternate form of type I collagen, composed of three identical $\alpha 1$(I) chains. This deviation from the normal heterotrimer molecule, tropocollagen, is very likely to have a deleterious effect on the tissue, primarily due to the precision of type 1 collagen orientation and its post-translational modifications [47, 42, 4, 8, 55]. The effect of an altered crosslink profile was seen previously in a study examining the relationship between collagen crosslinking and the mechanical strength of osteoporotic avian bone [56]. In a subsequent study a number of years later [37], the homotrimer was investigated again and significant quantities were measured in human OA tissue. Additionally, Bailey *et al.* tested the inherent strength of the molecule by assessing its enthalpy of formation. They found a significantly lower enthalpy in the homotrimer and concluded that it was easier to denature when compared with the healthy heterotrimer found in controls. This was consistent with an earlier study [67], using the osteogenesis imperfecta murine model (OIM) of the type 1 homotrimer.

A significant number of investigations into the nature of the type 1 collagen homotrimer have focused on this OIM murine model as an alternative

to the more difficult task of human homotrimer isolation. This specific form of OI animal model is known to exhibit the presence of the type 1 collagen homotrimer. McBride and his colleagues [66] investigated the function of the α2(I) chain in healthy tropocollagen and found that it is a vital component of tropocollagen with regard to the molecule's resistance to proteolytic degradation. It has also been shown to aid the self-assembly process of tropocollagen [74]. The OIM murine model was also looked at in a relevant study conducted in 2001 [75]. Grabner *et al.* looked at the end result of homotrimic collagen on bone's tissue properties. They found a significantly elevated microhardness and mineralisation in the OIM samples. An earlier study had suggested that the tensile strength of the modified collagen may also be reduced [76] while another [53] found the mineral crystals in OIM homotrimers to be thinner than normal and less aligned relative to healthy controls. It is evident from this body of work that the presence of the homotrimer is unlikely to be advantageous to bone tissue or its mineralisation. It could result in changes to the macroscale tissue of equal severity to those seen in OI, given the much more extreme process of complete molecular α-helix replacement in tropocollagen.

A number of more recent investigations have focused the current pathology of this disease even further. OA tends to favour medial side changes before lateral symptoms. This has been observed in a number of independent studies [77, 78, 79]. Bank *et al.* [40] looked at the question of disease initiation and found that collagen changes within the overlying cartilaginous tissue preceded gross cartilage fibrillation. Anderson-MacKensie and colleagues [20] examined the Dunkin-Hartley guinea pig model of spontaneous primary OA. They found a significant increase in density and bone thickness. The observed bone changes occurred prior to any gross cartilage symptoms but were at least coincident with histopathological cartilaginous symptoms. Bobinac *et al.* [38] found trabecular bone volume and thickness were significantly increased in OA samples and these observed increase were correlated with the severity of cartilage degradation. Consequently, trabecular number

and separation were seen to decrease. Of particular relevance to this thesis is work carried out by Professor Alan Boyde's research group in 2003 [39]. Ferguson *et al.* [39] investigated late-stage OA in human subchondral cortical bone tissue samples, harvested from femoral heads. They observed a significant decrease in intrinsic tissue stiffness using nanoindentation with a corresponding decrease in bone mineralisation level using QBEI. However, some caution must be exercised when considering their backscatter electron microscopy work as specimen irradiation damage could have had an adverse effect on some of the results. Their use of a Faraday Cup to standardise the beam current at the higher accelerating voltages used in the study may not ensure a low electron beam dosage rate, especially given their relatively high beam current relative to previous work [80]. Consequently, slow irradiation damage to the samples could have resulted, possibly biasing the findings.

In summary, significant changes in osteoarthritic bone tissue have been documented. In some cases, these presented prior to gross *in situ* cartilage damage and were at least coincident with histopathological symptoms. There is still contention regarding the increase or decrease of tissue mineralisation due to presence of the disease. However, this is quite likely to be a direct result of the lack of quantitative disease severity assessment. Results are stated without explicit definition of the stage of progression of the disease. One hypothesis of this present work is that the progression of this disease could occur in a number of predetermined finite stages, with each stage of progression exhibiting independent pathological symptoms either physically or biochemically within both *in situ* tissues. Hence, characteristic OA symptoms may not be absolute but could be transient in nature and change as a function of disease progression. This would most likely occur as a result of a changing biological or mechanical environment as the *in situ* tissues are initially affected and subsequently endeavour to compensate as predicted by Wolff's Law.

Unlike the mineralisation situation, little contention exists regarding the significant decrease in localised tissue stiffness repeatedly observed. Addi-

tionally significant changes to osteoblast-like cells and their products points to serious fundamental changes in the material. OIM work looking at the main altered product, the homotrimer, offers much insight into the likely deleterious effect that this tropocollagen mutation could have on the overall strength of the resulting mineralised tissue, as evidenced by thinner and poorly aligned mineral crystals *in vivo*. In light of the obvious importance of the organic constituent of the bone composite, this present work attempted to quantitatively assess the organic matrix of the trabecular tissue samples using high pressure liquid chromatography (HPLC). Collagen quantity and quality were investigated by quantification of the collagen content and the mature forms of the non-enzymatic collagen crosslinks, based on the hypothesis that presence of the homotrimer's detrimental effect would present in the level of either type 1 collagen and/or its associated crosslinks.

2.5 Nanoindentation

Mechanical characterisation of the bone tissue samples was carried out using a technique known as nanoindentation. In simple terms, nanoindentation is an evolution of the basic mechanical engineering hardness test. This test involves probing a sample using a diamond tipped indenter and quantifying the resulting impression left on the material's surface. From this measurement, the sample hardness or resistance to plastic deformation can be assessed. Nanoindentation involves a similar idea but advances the technique through the use of recent improvements in measurement technology and indentation theory.

Nanoindentation involves an axisymetric indenter of arbitrary profile being driven into a material's surface. The material directly beneath the indenter tip deforms both plastically and elastically. The tip is then unloaded, resulting in recovered elastic deformation as it is removed from the surface. A permanent residual impression is left on the sample's surface (Figure 2.20) but unlike conventional hardness testing, the impression is not assessed vi-

sually. Instead, load and corresponding displacement data are recorded as a function of time throughout the testing phase. From these measurements, mechanical characteristics of the material can be derived at the point of tip unloading. Hardness and elastic modulus are the most commonly derived mechanical characteristics but fracture toughness can also be determined using nanoindentation.

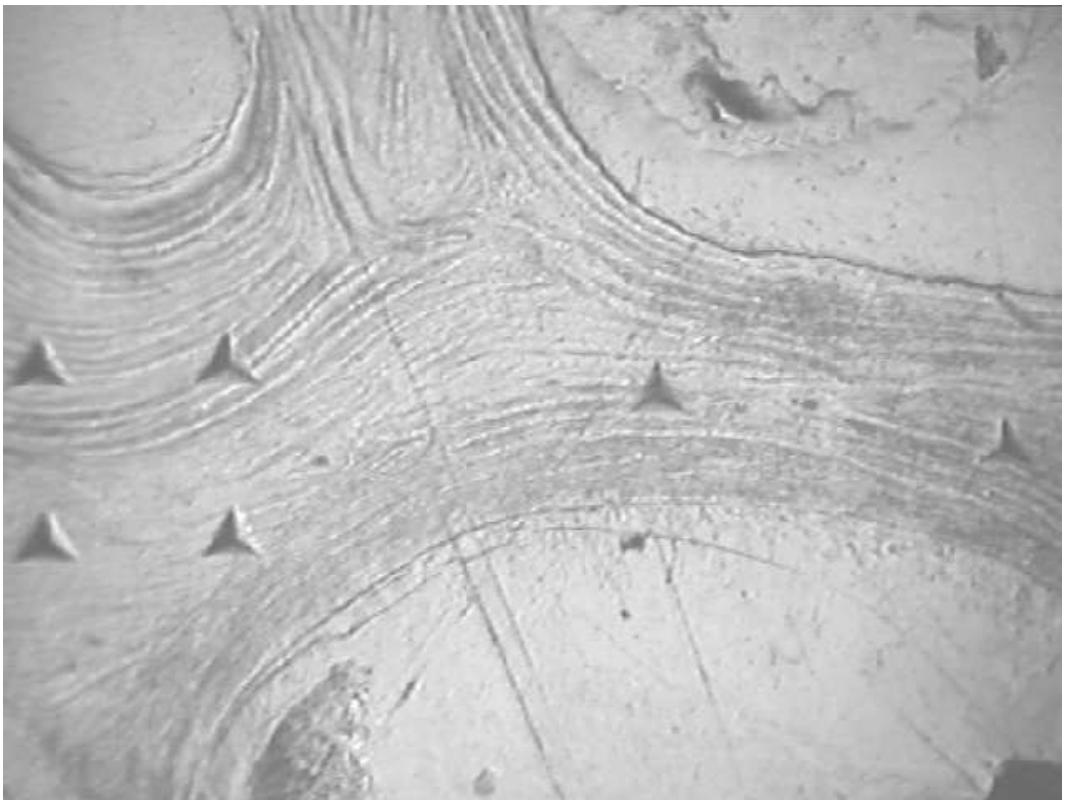

Figure 2.20: Indentations performed on a trabecular bone sample within the embedding medium (PMMA).

2.5.1 Theory

A typical load versus displacement curve resulting from a standard nanoindentation protocol can be seen in Figure 2.21. The three most important quantities that can be measured using the load vs. displacement curve are: the maximum load, P_{max}, the maximum displacement, h_{max}, and the elastic unloading stiffness, $S = dP/dh$. The accuracy of the derived mechanical characteristics depend strongly on the measurement quality of these experimental parameters [81]. The fundamental relationships used to determine hardness and elastic stiffness are:

$$H = P/A \tag{2.2}$$

where P is the load and A is the projected contact area at that corresponding load, and:

$$E_r = \frac{\sqrt{\pi}}{2\beta}\frac{S}{\sqrt{\mathrm{A}}} \tag{2.3}$$

where E_r is the reduced modulus of contact and β is a constant dependent on the indenter geometry. The reduced modulus is used to account for elastic displacements occurring in both the indenter and the sample during indentation. A second expression for the reduced modulus allows the determination of the actual modulus of each of the respective materials to be calculated once the reduced modulus has been determined. This expression is given in Equation 2.4.

$$\frac{1}{E_r} = \frac{1-\nu^2}{E} + \frac{1-\nu_i^2}{E_i} \tag{2.4}$$

The indenter geometry constant, β, for the Berkovich indenter tip has been empirically determined to be 1.034. From Equations 2.2 and 2.3, it is clear that the contact stiffness, S, and contact area, A, must be determined for each indentation to facilitate calculation of the indentation hardness and stiffness.

Determining the contact stiffness, S, involves forming an expression for the load, P, in terms of the displacement, h, during the unloading phase of the indentation and differentiating this expression. It has been shown

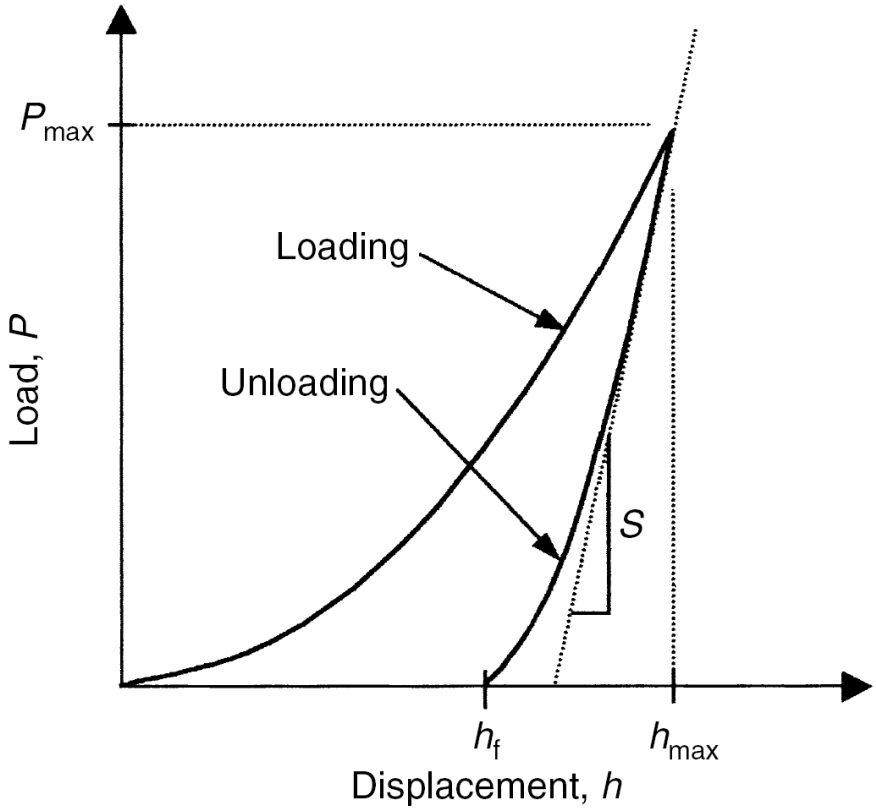

Figure 2.21: Typical load versus displacement curve for a typical nanoindentation. [16]

empirically that a power law expression produces the best fit but only for the upper portion of the unloading curve. This power law expression is normally of the form:

$$P = \alpha(h - h_f)^m \tag{2.5}$$

where α and m are power law fitting constants. By evaluating the differentiated form of this expression at the maximum displacement, h_{max}, we can determine the contact stiffness, S, given in Equation 2.6.

$$S = dP/dh \tag{2.6}$$

Determining the contact area involves evaluating an empirically derived indenter area function for the indenter tip used throughout the experimental procedure. This contact area is a function of the contact depth, h_c and can be expressed mathematically as Equation 2.7. h_c is the difference between the total depth, h, and the sink-in depth, h_s (Equation 2.8). These terms are explained schematically in Figure 2.22.

$$A = f(h_c) \tag{2.7}$$

$$h_c = h - h_s \tag{2.8}$$

Using an expression for h_s, we can substitute into and rearrange Equation 2.8 to give Equation 2.9:

$$h_c = h - \epsilon \frac{P}{S} \tag{2.9}$$

where ϵ is a indenter geometry constant. This allows us to empirically calibrate an area function for the specific indenter tip.

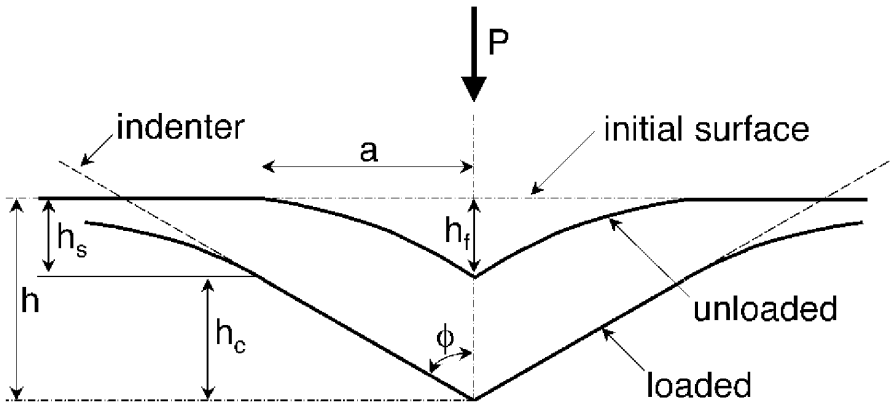

Figure 2.22: Contact geometry during indenter loading and unloading. [16]

2.5.2 Continuous Stiffness Measurement (CSM)

Recent advances in nanoindentation techniques have further improved the measurement of mechanical characteristics. Dynamic or Continuous Stiffness Measurement (CSM) has made it possible to measure stiffness and hardness continuously as a function of indentation depth instead of assessing the material only at the point of tip unloading. This has not only improved the measurement capabilities but has also significantly simplified the indenter area function calibration procedure. CSM testing is accomplished by superimposing a small force oscillation on the force signal and assessing the corresponding amplitude and phase of the displacement signal using a frequency-specific amplifier. To ensure modelling accuracy, the design of the system is kept relatively simple, with a schematic shown in Figure 2.23. As previously discussed, the calculation of hardness and stiffness is facilitated by the determination of the contact stiffness, S. The contact stiffness of a standard nanoindentation test is determined by calculating the slope of the load versus displacement data during the unloading portion of the test. This allows the determination of the contact stiffness at the maximum penetration depth only. The CSM method facilitates the continuous measurement of the contact stiffness throughout the entire process.

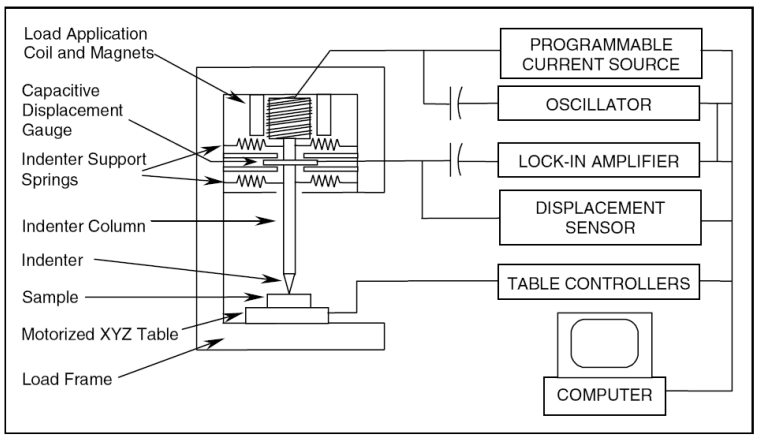

Figure 2.23: Schematic of nanoindenter indentation head.

The accuracy of this method is determined by its ability to accurately model the dynamic response of the nanoindentation equipment. Consequently, the material's dynamic response can be isolated from the total response. Motion is restricted to one dimension, allowing accurate representation of the system as a simple harmonic oscillator and analysed using simple second-order differential equations. By application of Newton's second law of motion and the summation of the forces on the system, an expression for the model can be written as:

$$m\ddot{z} + D\dot{z} + Kz = F(t) \tag{2.10}$$

where z is the indenter displacement and K is an equivalent stiffness term, comprised of the contact stiffness, S, the machine load-frame stiffness, K_f and the support springs stiffness, K_s and can be written as:

$$\left(K = \frac{1}{S} + \frac{1}{K_f}\right) + K_s \tag{2.11}$$

The term, D, is the system damping rate, comprised of both the damping rates of the indenter head and the sample, written as:

$$D = D_i + D_s \tag{2.12}$$

$F(t)$ can be written in its equivalent form:

$$F(t) = F_o e^{i\omega t} \tag{2.13}$$

This form of the expression has a particular solution for the resulting displacement, z, of the form:

$$z(t) = z_o e^{i(\omega t - \phi)} \tag{2.14}$$

In real terms, these equations tell us that the displacement at the indenter head will oscillate at the same frequency as the force, ω, but lags behind by a phase angle, ϕ. This phase angle can be calculated by the substitution of

the displacement solution (equation 2.14) and the expression for F (equation 2.10) into equation 2.10, giving:

$$\left|\frac{F_o}{z_o}\right| = \sqrt{(K - m\omega^2) + (\omega D)^2} \tag{2.15}$$

and

$$\tan\phi = \frac{\omega D}{K - m\omega^2} \tag{2.16}$$

These two equations can be solved simultaneously for K and D, resulting in an expression for the stiffness and damping rate of the contact. These can be written as:

$$S = \left[\frac{1}{\frac{F_o}{z_o}\cos\phi - (K_s - m\omega^2) - \frac{1}{K_f}}\right] \tag{2.17}$$

and

$$D_s\omega = \frac{F_o}{z_o}\sin\phi - D_i\omega \tag{2.18}$$

Consequently, knowing the machine parameters (K_f, m, K_s and D_i), setting the excitation frequency (ω) at the beginning of each experiment and measuring the displacement amplitude (z_o), phase angle (ϕ) and excitation amplitude (F_o), numerical quantities for contact stiffness S and damping term $D_s\omega$ can be calculated relatively easily. Once S has been determined in this manner, the techniques described previously can be employed to calculate elastic stiffness and hardness as a function of penetration depth.

A major advantage with this technique, specifically applicable to the field of biomechanics, is the reduction of time-dependent plasticity and thermal drift effects at high frequencies [16]. It also allows more accurate determination of the initial point of contact and has the obvious advantage of measuring mechanical characteristics as a function of depth below the sample surface, averaged up to the specified depth of nanoindentation. A typical load versus displacement CSM curve and resulting graph of stiffness as a function of penetration depth in healthy trabecular bone are shown in Figures 2.24 and 2.25.

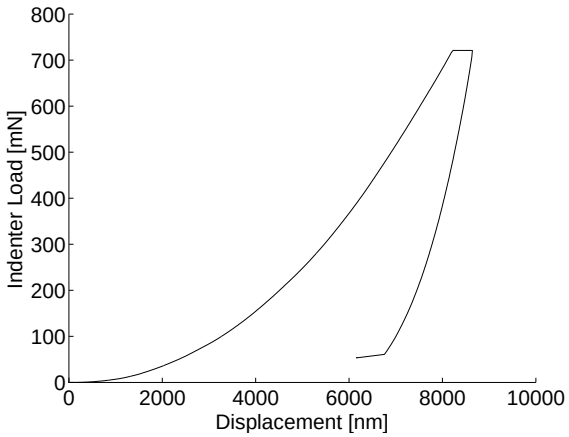

Figure 2.24: Indentation load as a function of indenter displacement into subchondral trabecular bone sample.

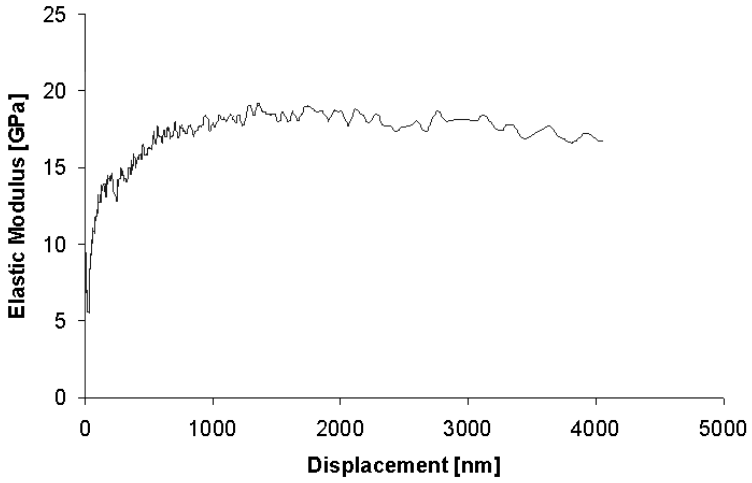

Figure 2.25: Typical elastic modulus versus indentation depth curve for bone.

2.5.3 Calibration and Tip Selection

To facilitate accurate nanoindentation protocol and data analysis, several machine calibrations were performed. Localised changes in measured displacement due to thermal effects, machine compliance and tip wear were

accounted for to reduce their effects on measured raw data and subsequent material characterisation calculations.

Thermal Drift

Thermal drift is an experimental artifact which manifests itself continuously during nanoindentation testing within the nanoindentation apparatus [82]. Measured displacements can vary, even when constant applied loads are maintained. These displacement fluctuations occur as a result of small amounts of expansion or contraction within the sample and/or the testing apparatus itself. Such variations will obviously affect the measured displacements, leading to reduced experimental accuracy. This thermal drift rate can vary quite dramatically over a short period of time and therefore was assessed for each nanoindentation. The thermal drift calibration technique is based on the idea that, at low constant applied loads, the only variation in measured displacement is due to thermal expansion or contraction. Time-dependant creep effects are minimised and a thermal drift rate can be calculated from the displacement data at this low, constant applied load.

Thermal drift assessment is performed at the end of each test by reducing the applied load to approximately 10% of the maximum applied load. This applied load is then held for a sufficient length of time, usually 100 seconds. During this time, load is controlled while the measured displacements are carefully recorded as a function of time. An example showing the result of such a test for fused quartz is shown in Figure 2.26. In this example, a drift rate of approximately 0.31 nm/s was measured. Once a thermal drift rate has been calculated, it describes the amount of displacement that occurs every second due to thermal effects (units given as nm/s). This allows experimental displacement data, throughout the entire measured range, to be adjusted to account for thermal drift. This removes the effect of thermal drift rate on the displacement data by subtracting the amount of thermal drift that occurs at each particular time increment from the raw displacement data at that point.

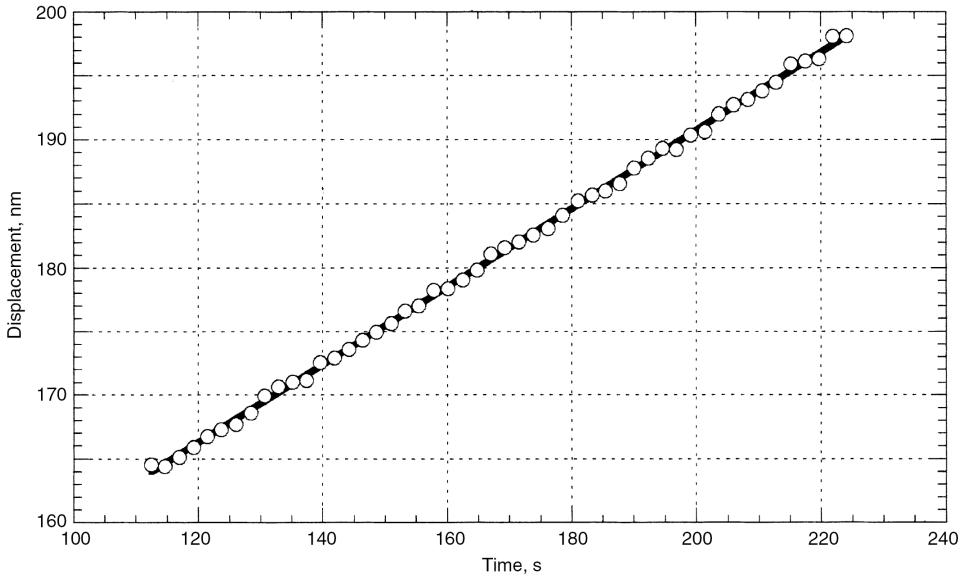

Figure 2.26: Thermal drift as a function of time due to constant applied load. [17]

An example of the effect of thermal drift rate correction on experimental displacement data can be seen in Figure 2.27.

Machine Compliance

Machine compliance is defined as the portion of measured nanoindentation test compliance that can be attributed to the machine apparatus itself. All displacements measured using a commercial nanoindentation testing machine result from three main compliance components: sample compliance, indenter tip compliance and machine compliance. Indenter tip compliance is minimised by selecting a suitable indentation tip material such as diamond, whose high elastic modulus and hardness minimise the contribution to total measured compliance [16]. However, a specific calibration procedure is required to remove the influence of machine compliance on measured displacements.

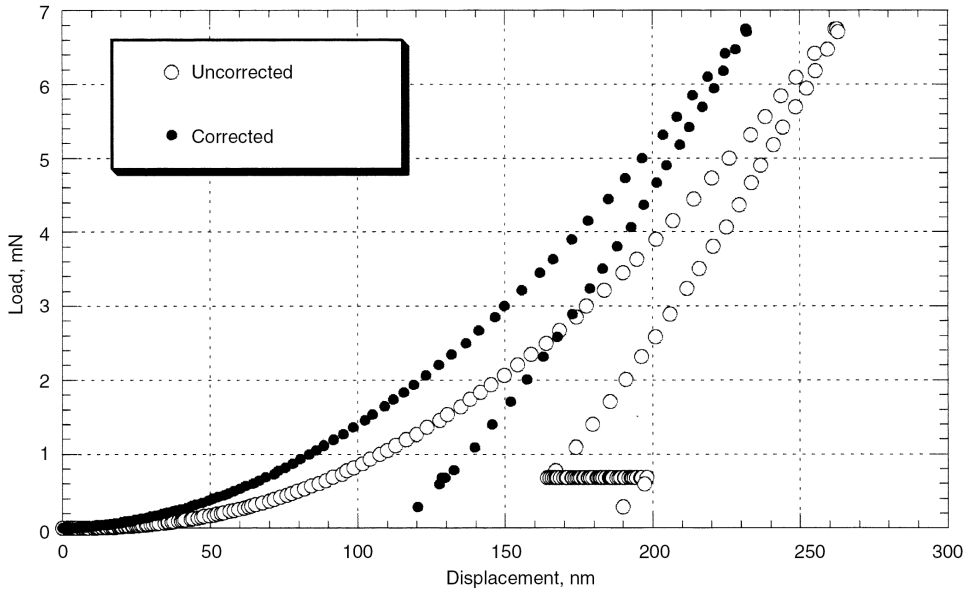

Figure 2.27: Effect of thermal drift on load versus displacement data. [17]

Under certain circumstances, machine compliance can contribute significantly to the total measured compliance during testing and must, therefore, be considered during analysis [17]. Such a situation arises when contact stiffness values approach the machine's stiffness value. An example of the effect of machine compliance correction is shown in Figure 2.28. At the loads shown, the contact stiffness represents approximately 10% of the machine stiffness and machine compliance becomes a significant consideration. If, in spite of this relatively high load, the effect of machine compliance is ignored (by assuming the machine compliance tends towards a value close to infinity, say $K_m = 1 \times 10^{30} N/\text{m}$ where $K_m = 1/C_m$), the corresponding effect on the load-displacement data can be clearly seen in the displacement drift shown in Figure 2.28. This graph highlights the effect of choosing an infinite value of machine compliance compared with choosing its actual value, $K_m = 6.8 \times 10^6 N/\text{m}$. Significant changes to the raw experimental data result. Consequently, any derived material characteristics will also be misinterpreted. Once the machine compliance, C_m, has been determined, the

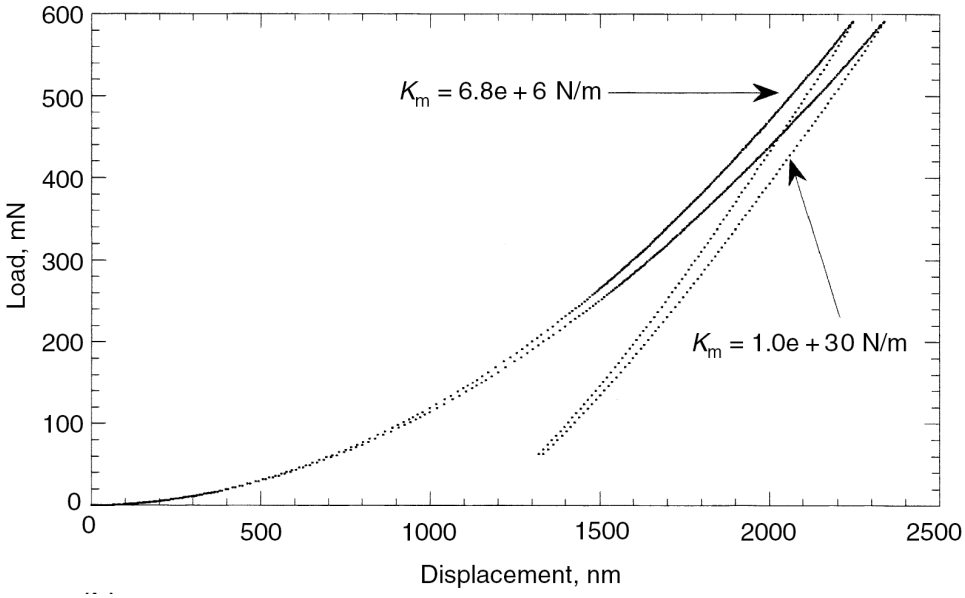

Figure 2.28: Effect of compliance calibration on measured load versus displacement data. [17]

machine displacement occurring due to this compliance, h_m, can be calculated for any specified load, P, using the Equation 2.19.

$$h_m = C_m P \tag{2.19}$$

This portion of the displacement can be subtracted from the total measured displacement at each increment, removing the influence of machine compliance on the test displacement data. To determine the compliance, the machine and contact are modelled as springs in series with additive compliances. We can define a total measured compliance, C_t, as:

$$C_t = C_s + C_m \tag{2.20}$$

where C_s is the elastic compliance of the indenter-sample contact. By definition, compliance is the inverse of contact stiffness ($C_s = 1/S$). Hence, Equation 2.20 can be rewritten using Equation 2.3 as:

$$C_t = \frac{\sqrt{\pi}}{2\beta E_R} \frac{1}{\sqrt{A}} + C_m \tag{2.21}$$

By equating this expression with the equation of a line and plotting C_t versus $A^{-1/2}$, the intercept point can be determined and the value at this point gives the machine compliance, C_m.

In practical terms, the calibration procedure to determine the machine compliance is an iterative one and is achieved by making a series of indentations at large depths where the ideal area function of the indenter geometry (A=$24.5h^2$) is expected to apply. This will facilitate a simpler subsequent determination of the area functions for the performed indentations. It is first assumed that C_m=0 and the load-displacement data are corrected according to Equation 2.21. The data are then analysed using Equations 2.5, 2.6, 2.7 and 2.9. The intercept point of the plot of C_t versus $A^{-1/2}$ will now yield a different estimate of C_m. This procedure is repeated until adequate convergence in C_m is obtained.

Area Function

The area function calibration is required to accurately describe the contact geometry, and consequently the contact area during indentation but is especially important for small contact depths and pyramidal indenters. Subtle deviations from assumed geometrical perfection near the indenter tip can have a significant effect on the measured properties. This is exaggerated with the use of pyramidal indenters which exhibit tip blunting with use [17]. The calibration theory involves a series of indentations performed on a material of well-known elastic properties. A material is required which exhibits no pile-up and is free from surface contaminants and oxides that could influence the near-surface elastic properties. For these reasons, fused silica is commonly used.

The basic assumption throughout the area function calibration is that the material's elastic modulus is independent of depth and does not exhibit pile-up. The span of indentation depths used throughout the calibration range from the smallest possible to the largest possible depth within the depth range of interest. A suitable number of indentations are performed within

a chosen region of interest (ROI). The collected data are then corrected to account for the machine compliance before the contact stiffness and contact depths are calculated using Equation 2.6 and 2.9. By rearranging Equation 2.3 into the form shown in Equation 2.22, the contact areas for all calibration tests performed can then be determined.

$$A = \frac{\pi}{4}\left(\frac{S}{\beta E_R}\right)^2 \tag{2.22}$$

The tip's area function is determined by plotting contact area, A, as a function of contact depth, h_c. This representative curve can be fitted to give a mathematical expression for the area function. A general form of this expression is given by Oliver *et al.* [16] and is shown in Equation 2.23.

$$A = C_0h^2 + C_1 + C_2h^{1/2} + C_3h^{1/4} + \ldots + C_8h^{1/128} \tag{2.23}$$

The initial term, C_0, represents the ideal tip geometry for the chosen indenter. For Vickers, Berkovich and Cone indenter tips, this ideal area function is $A = 24.5h^2$. The subsequent function constants ($C_1 \ldots C_8$) take account of deviations from this ideal geometry due to tip blunting.

Tip Geometry

The Berkovich indenter is one of the most frequently used pyramidal indenters in nanoindentation work, particularly in mineralised tissue nanoindentation analysis [83, 84, 85, 86, 87, 88, 89, 41]. It offers many advantages over its pyramidal and spherical alternatives, the most important being the high manufacturing standard possible relative to other tip geometries. The Berkovich, being a three-sided pyramid as opposed to the four-sided Vickers, can be ground to a point ensuring self-similar geometry at small scales. The chisel edged contact seen in Vickers tips can cause its small scale geometry to differ from the geometry seen at larger indentation depths. The Berkovich is also the preferred choice over spherical indenter tips due to the difficulty in obtaining high quality spheres from hard, rigid materials. It should be noted however, that even if suitable spherical indenters were available at this small

scale, the stresses produced by a spherical indenter tip would differ significantly from pyramidal tips, making them more suited to analysis of elastic deformation and the elastic-plastic transition. Investigations into these types of contact regimes were of little interest with regard to the scope of the work presented in this thesis.

The choice of indenter geometry is therefore determined by the mechanical characteristics of interest. Sharp indenters have a distinct advantage when examining viscoelastic or strain rate dependent materials as they result in a characteristic strain that is constant irrespective of load and displacement. This makes strain rate regulation much simpler. Sharper pyramidal indenters, such as the cube-corner indenter tip, will obviously result in greater characteristic strains and are most commonly used to initiate cracking in a sample, for example in fracture toughness investigations. For spherical indenters, the characteristic strain constantly changes as the indenter penetrates the material. For the reasons outlined, the Berkovich was the indenter tip of choice for this present work.

Sample Pile-Up

Sample pile-up is a phenomenon observed in some materials whereby the plastic deformation that occurs forces the plastically deforming material beneath the indenter tip to lift up around the rigid indenter. This is a phenomenon associated with sharp indenters, such as the Berkovich, and elastic-plastic contact mechanics. A schematic of this phenomenon is shown in Figure 2.29. Quantitatively, specimen pile-up results in an increased contact area which is not taken into account by the indentation analysis techniques used. This results in overestimated elastic moduli and hardness values. Careful examination of the bone samples revealed sink-in phenomenon only, shown schematically in Figure 2.30. This phenomenon does not cause an analysis problem for the experimental work conducted here on trabecular bone. The analysis procedures used in interpreting material indentation with pyramidal

indenters are based entirely on elastic models of indentation contact which account for this sink-in phenomenon.

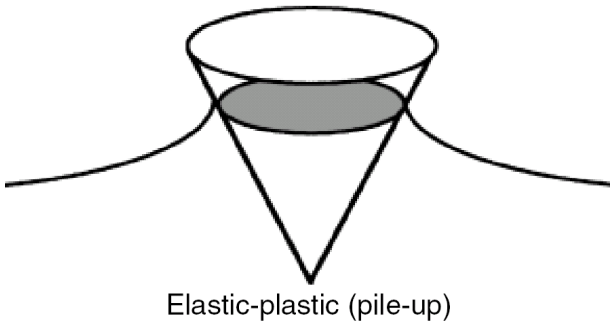

Figure 2.29: Schematic showing an exaggerated representation of pile-up as a result of a typical indentation. [17]

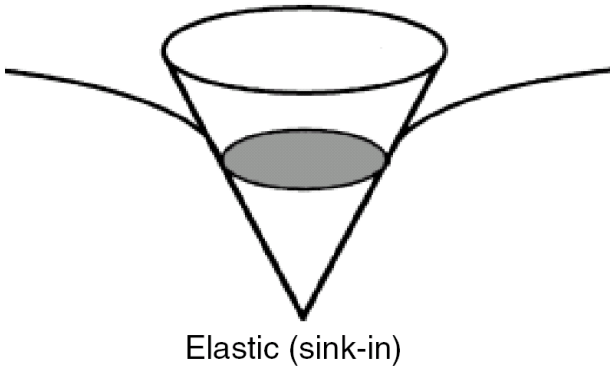

Figure 2.30: Schematic showing an exaggerated representation of sink-in as a result of a typical indentation. [17]

2.6 Nanoindentation of Mineralised Tissue

A significant body of work has accumulated dealing with the mechanical properties of bone assessed by nanoindentation. Numerous tissue types have been investigated but the most important difference between contemporary assessments using nanoindentation concerns the material preparation protocol employed. Three main types of test protocol are commonly applied to bone tissue; (i) wet testing with specimen embedded in a non-infiltrating medium (e.g. epoxy resin) (ii) dry testing with specimen embedded in a non-infiltrating medium (iii) dry testing with specimen embedded in an infiltrating medium (e.g. PMMA).

The importance of the applied test protocol lies in the absolute values of tissue mechanical properties measured. This was demonstrated quantitatively by Bushby *et al.* in 2004 [41]. They examined equine cortical bone tissue and measured the relative effect of tissue dehydration and subsequent PMMA embedding on their test samples. They found an artificial increase in the recorded nanoindentation stiffness results of dehydrated samples (between 10 and 30%) relative to wet, unembedded samples. Subsequent embedding of the tissue in PMMA after dehydration resulted in an artificially increased tissue stiffness, much greater in magnitude (≈66 to 74%), relative to healthy, wet, unembedded samples. In absolute terms, the average stiffness of wet, unembedded, equine cortical bone tissue was 11.2 ± 2.8 GPa. Dry, unembedded samples returned an average value of 12.5 ± 3.4 GPa while dry PMMA-embedded samples exhibited an average tissue stiffness of 19.5 ± 2.7 GPa. Consequently, interpretation of any nanoindentation work on bone must take the method of material preparation into consideration. The protocol adopted throughout this present work involved the third method described i.e. dry testing of PMMA-embedded bone tissue.

2.6.1 Wet, Non-infiltrated Bone Tissue

Epoxy resin in an unadulterated form is a relatively viscous substance prior to polymerisation and hence, makes a suitable, non-infiltrating embedding medium for bone tissue. Samples prepared and tested using this protocol resemble *in vivo* conditions most closely. Human cortical and cancellous bone from varied anatomical locations have been examined. Average osteonal bone properties from numerous locations have been measured with stiffness values ranging from 13 to 22 GPa [89]. Corresponding osteonal hardness was also quantified and found to range from 0.3 to 0.7 GPa [89]. The same study also looked at interstitial tissue and trabecular bone and found stiffness ranges for these tissues to vary between 13-25 GPa and 7-16 GPa respectively. Hardness ranges for these samples followed a similar pattern. Interstitial hardness was found to range from 0.4 up to 0.75 GPa while trabecular hardness varied from 0.25 to 0.55 GPa. A subsequent study using an identical experimental rig and set-up [84] found almost identical values, the only difference being an improved narrowing of the tissue property value range. However, concerns regarding the consistency of moisture level within irrigated tissue samples using a similar custom irrigation system were expressed by Rho and Pharr [90], possibly explaining the overall variation in values seen in the studies conducted by Zysset *et al.* [89] and Hoffler *et al.* [84].

2.6.2 Dry, Non-infiltrated Bone Tissue

The use of non-infiltrating embedding and subsequent testing of dry bone tissue is a protocol predominantly employed by a nanoindentation research group that was previously headed by Dr. Jae-Young Rho in the Department of Biomedical Engineering in the University of Memphis. In 1997, this group examined human cortical and cancellous bone, taken from tibiae and vertebrae respectively [85]. Average tissue properties were measured in the longitudinal direction in these samples, aged 57 and 61 respectively. As in the wet, non-infiltrating studies [89, 84], osteonal, interstitial and trabecular

tissues were individually assessed. The average osteonal, interstitial and trabecular tissue stiffness' were found to be 22.5 GPa, 25.8 GPa and 13.4 GPa respectively. Hardness followed the same trend with average tissue values of 0.614 GPa for osteonal tissue, 0.74 GPa for interstitial tissue and 0.47 GPa for trabecular tissue.

In a subsequent study carried out by the same research group in 1999 [86], examinations focused on human cortical bone, specifically from the femoral diaphysis. The study examined the tissue properties (stiffness and hardness) as a function of increasing distance from the central Haversian canal in cortical structures. Osteon stiffness and hardness were found to vary between 17-22.7 GPa and 0.49-0.74 GPa respectively. Interstitial stiffness and hardness were elevated, exhibiting a range of 24.2-26.8 GPa and 0.72-0.86 GPa respectively. Further work on this tissue type proved extremely interesting as a significant lack of correlation was found to exist between tissue properties at the microstructural level and sample age. This study replicated earlier work by producing a similar range of tissue stiffness and hardness values [87].

2.6.3 Dry, Infiltrated Bone Tissue

The earliest nanoindentation work on dry, infiltrated bone tissue was conducted by Turner *et al.* in 1999 [83]. This study focused on human cortical and cancellous bone taken from the femoral head of a healthy 65 year old donor. Nanoindentation results were compared with acoustic microscopy measurements made within the same samples at coincident locations. Cortical bone was assessed in both the longitudinal and transverse directions and trabecular tissue stiffness was found to lie within the range of stiffness values defined by longitudinal and transverse bone stiffness. Longitudinal cortical bone tissue stiffness was found to be 23.45 $\pm$ 0.21 GPa on average, with transverse cortical bone exhibiting an average stiffness of 16.58 $\pm$ 0.32 GPa. As mentioned, trabecular tissue stiffness was found to lie between these two values, specifically 18.14 $\pm$ 1.7 GPa.

Ferguson *et al.* [39] examined human cortical subchondral bone from the femoral heads of donors ranging from 55 to 89 years of age. A spherical indenter tip was used throughout this study because of the study's singular interest in the tissue stiffness. An average tissue stiffness of between 18.75 and 19 GPa was reported. Interestingly, Bushby *et al.* [41] used both a Berkovich tip and a spherical indenter tip in a study conducted the following year [41] and reported that indenter tip shape did not have a significant effect on the measured tissue stiffness for the load and depth range they examined using their specific tip geometries. The most recent work involving this test protocol was conducted by Gupta *et al.* in 2005 [88]. This investigation focused on human cortical subchondral bone, isolated from the patellae of 39 to 54 year old donors. A tissue stiffness and corresponding hardness of 17-18 GPa and 0.6 GPa respectively were reported.

This present work employs the use of dry, infiltrated bone tissue samples for various reasons. The most important reason for embedding the samples was the necessity to support the trabecular network during the polishing procedures employed. It also simplified sample handling significantly, although this alone did not determine my choice. Dehydrated samples were preferred in spite of the consequent effects on measured mechanical properties outlined in the previous two sections. This choice was made as a result of the previous investigators' [90] concerns regarding the ability to ensure constant sample hydration levels throughout the empirical work. A custom irrigation setup would be required, significantly complicating the experimental procedures. This coupled with sample hydration concerns governed my choice of sample hydration.

In summary, this thesis is the first of its kind to specifically examine human trabecular subchondral bone, isolated from the tibial end of the knee joint. Additionally, the pathological effect of OA on such a tissue, using the methods employed throughout this present work has not been published previously and is of significant scientific interest. This study is also the first to employ a new nanoindentation analysis technique, namely continu-

ous stiffness measurement (CSM) to investigate OA subchondral trabecular bone tissue properties at this scale in human tissue. The literature reviewed establishes a realistic contemporary range of quantitative expected values based on tissue type, location and sample preparation. Additionally, a relative relationship has been established between the results reported by this study and those published.

2.7 Quantitative Backscatter Electron Imaging

Quantitative Backscatter Electron Imaging (QBEI) is a Scanning Electron Microscope (SEM) technique which facilitates composition-based analysis of primarily conductive materials such as metal, although the technique has been adapted to facilitate examination of non-conductive organic samples, such as mineralised bone tissue. The SEM is a particle beam instrument that produces high energy electron beams and examines the interactions between these incident electrons and a specimen of interest. Limitations inherent within the normal light microscopy technique resulted in the need for more powerful microscopes, capable of significantly higher magnification and resolution. The wavelength of light limits the maximum magnification and resolution of light microscopes to approximately 2000 times and 0.2 μm respectively. The invention of the SEM allowed significantly higher magnification and resolutions of the order of 500,000 times and less than 0.001 μm respectively.

The SEM functions essentially in an identical manner to a light microscope but uses electrons instead of light. A schematic of a basic SEM can be seen in Figure 2.31. The electrons are created using an electron source of some kind (usually a thermionic electron gun) and are accelerated towards the specimen using a positive electrical potential. The electron beam is focused using a series of apertures and magnetic lenses, allowing precision adjustments of the final beam surface diameter or 'spot size'. Interactions between the electron beam and the sample occur within a finite sample in-

teraction volume. It is these interactions and their effects that are detected and used to form images displaying the information of interest. A number of different interactions can occur within the sample, such as production of X-rays, secondary electrons and auger electrons. The most important with regard to this present work are backscattered electrons.

There are a number of significant problems regarding the use of the SEM and organic or thermally fragile sample specimens. Radiation damage due to the electron beam can significantly alter the state of the imaged specimen. There are numerous effects that can occur during the imaging process which alter the material to such an extent as to invalidate any quantitative as-

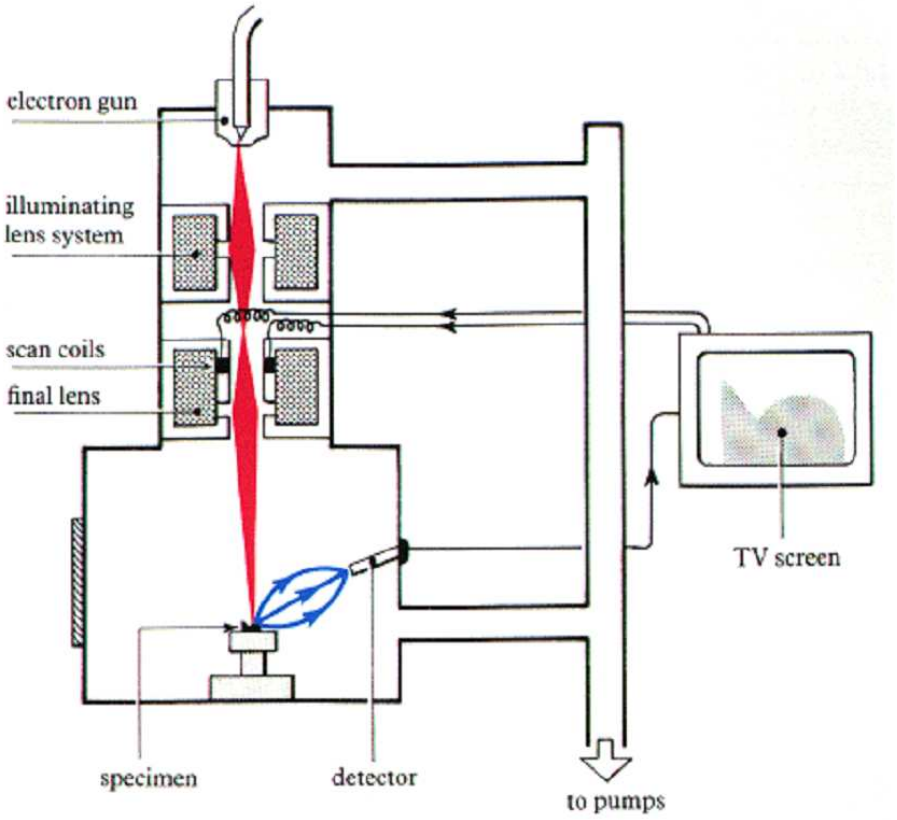

Figure 2.31: Schematic illustrating the basic components and function of a Scanning Electron Microscope (SEM).

sessments using the technique. These changes include heating, electrostatic charging, radiolysis, displacement damage, sputtering and hydrocarbon contamination [91], all of which significantly alter the intrinsic nature of the sample and consequent measured properties. Radiation damage is of particular importance when relatively high accelerating voltages are used. Increases in accelerating voltages result in an increased electron beam energy and consequent increases in sample damage. Due to the nature of this study which involved altered accelerating voltages, relatively high beam energies and electron beam sensitive mineralised samples, radiation damage and its control was of paramount importance to ensure error-free quantitative assessment of pathological changes to tissue mineralisation. Consequently, a comprehensive assessment of the electron beam theory and techniques was required.

2.7.1 QBEI of Mineralised Tissue

Electron beam interactions have been employed in numerous investigations into the compositional nature of mineralised biological tissues over the last two decades. Direct comparisons between all these investigations is not possible due to the inherent nature of electron beam imaging. The image grey level (GL) of a homogenous elemental material varies, in spite of constant atomic density, depending on the variable machine settings, usually optimised for image clarity. The image brightness and contrast, also known as the offset level and the gain level controls of the signal respectively, alter the imaged GL of a material with constant atomic density. For quantitative measurements using this technique, some form of brightness and contrast calibration must be employed to ensure reproducibility of compositional measurements.

Two calibration procedures have been extensively employed throughout the majority of current literature utilising the QBEI technique. Both techniques calibrate the GL scale but as a result of different calibration standard materials, direct comparisons between their measurements are not possible. The first calibration procedure was developed by Professor Alan Boyde, pre-

viously of the Hard Tissue Research Unit of the Department of Anatomy and Developmental Biology, University College in London. The technique was detailed in 1995 [92] and is essentially based on the use of two distinct calibration materials to define a specific GL range. Two novel polymers (thermoset dimethacrylate esters) were developed based on the reaction of halogenated phtalic acids and glycidal methacrylate [92].

A second calibration technique was developed by Professor Paul Roschger based in the Ludwig Boltzmann-Institute of Osteology, Vienna and is described in detail in his 1995 publication [80]. This technique used less complicated calibration materials, namely pure carbon and aluminium. Additionally, by using Energy Dispersive X-ray Analysis (EDX) at corresponding locations on the same tissue samples, corresponding mineralisation values were measured, in terms of weight percentage calcium (wt% Ca). This facilitated the calibration of GL results in terms of this more commonly adopted method of mineralisation assessment. This offers a distinct advantage over the method proposed by Boyde *et al.* and has been successfully employed in a number of bone tissue investigations [92, 93, 94, 39].

Quantitative backscatter electron imaging (QBEI) has been predominantly employed in the investigation of human bone tissue [39, 88, 92, 93, 94, 80, 19, 95, 96, 97] with notable exceptions [75, 98, 99, 100]. Human femoral heads were first examined using Roschger's calibration technique in 1995 [80]. Specifically, Roschger *et al.* looked at trabecular bone tissue. They found a strong linear correlation between GL and wt% Ca. The range of mineralisation values recorded for healthy trabecular bone from these samples was between 18 and 26 wt% Ca. In a subsequent study on human trabecular bone from transiliac biopsies [19], a much smaller range of mineralisation measurements were published (21 to 23 wt% Ca). In 2001, Roschger *et al.* published a paper [95] looking at both cortical and cancellous iliac bone from postmenopausal women. A similarly tight range (21 to 22 wt%Ca) was found. Most importantly, in a study conducted in 2003 [96], bone from various anatomical sites, ethnic backgrounds, gender and age ranges were

investigated. No significant differences were found in mineralisation based on ethnicity, skeletal site, gender or age. However, significant differences were evident when pathological samples were investigated. Effectively, bone mineralisation density distribution (BMDD) is constant in healthy human adult bone tissue. This reinforces the importance of this technique in mineralisation assessment, particularly with regard to pathological investigation. Grabner *et al.* [75] used this technique to investigate the osteogenesis imperfecta mouse model (OIM) while Ferguson *et al.* [39] examined osteoarthritic human subchondral cortical bone from the femoral heads of late-stage OA samples, finding a significant decrease in average mineralisation level. For these reasons, the methods of Roschger *et al* have been used in this present work. The detailed implementation is described in Section 2.7.4.

2.7.2 Theory

The theory behind backscatter electron interactions is based on a fundamental law of physical interaction between atomic particles. When an electron passes close to an atomic nucleus, it may be attracted to its opposite charge. If this occurs, an electron can change direction by an angle, α. α can vary anywhere between 0^0 and 180^0. This deflection angle is known as the scatter angle and its magnitude depends primarily on two things; (i) how much energy the electron possesses and (ii) how close it passes to the nucleus. When this occurs, an electron-specimen interaction occurs.

Electron-specimen interactions can be split into two main groups. The first is inelastic scattering. This tends to occur when the incident electron energy is high and the specimen has a medium to low atomic number. The electron will penetrate the sample surface and tend to lose a large amount of its kinetic energy as a result of sub-surface interactions. This energy is absorbed by the specimen and will normally result in the emission of electrons from within the sample. These inelastic emissions include X-ray emission, cathodeluminescence, secondary electrons, auger electrons and transmitted electrons. The second type of interaction, elastic scattering, is of primary

concern within this study. Elastic interactions tend to occur when the incident electron energy is relatively low and the sample has a high atomic number. Initial interactions will have a pronounced effect on electron trajectory and hence, fewer tend to occur. Therefore these elastic collisions do not reduce the kinetic energy of the incident electron as much as inelastic collisions and result in much larger scatter angles. These collisions originate within the sample, specifically below the sample surface and are therefore capable of providing useful information about the specimens composition and crystal structure nondestructively. A schematic showing some of the common electron specimen interactions is shown in Figure 2.32.

Backscatter electrons produce composition-based images due to their relationship with sample atomic density. For a given constant beam energy and a sample possessing a relatively low atomic number, the incident electron beam will penetrate deep into the specimens surface. This results in a large percentage of incident beam electrons remaining within the interaction volume. These electrons will undergo a large amount of subsurface collisions, each of

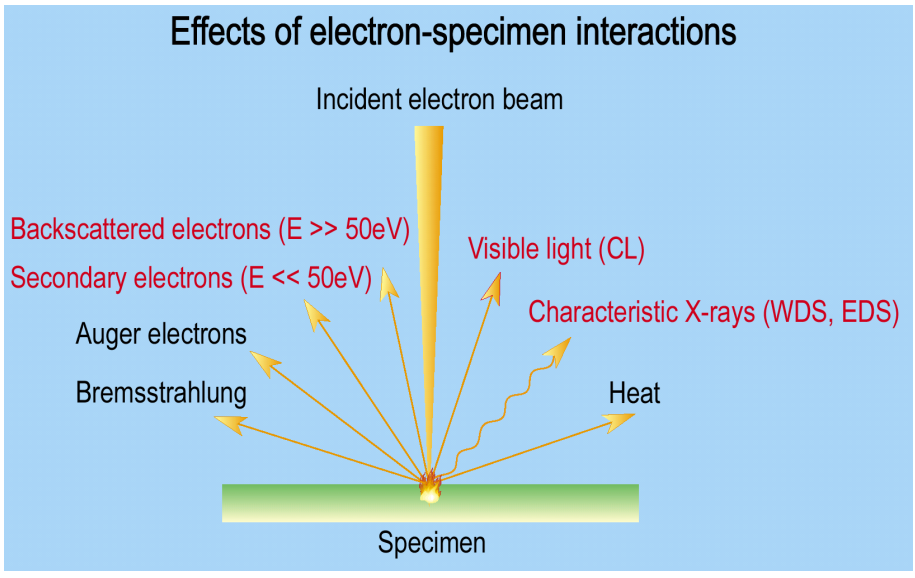

Figure 2.32: Common electron specimen interactions due to an incident electron beam.

which decreases their kinetic energy by a finite amount. A large proportion of these electrons will not possess sufficient energy to escape after these subsurface interactions and hence the amount of backscattered electrons detected is low. In samples possessing a relatively high atomic number, incident electrons are less likely to penetrate as deeply into the specimen, resulting in a greater proportion of high energy backscattered electrons. This effectively means that the amount of backscattered electrons is inherently linked with the atomic density of the material being examined.

A backscatter yield (η) can be defined and is commonly referred to as the backscatter coefficient. This coefficient is equal to the number of backscattered electrons divided by the total number of incident electrons on the specimen at a given time interval and is written mathematically as Equation 2.24:

$$\eta = \frac{\eta_{BSE}}{\eta_B} \tag{2.24}$$

It has been shown empirically that this backscatter coefficient (η) varies monotonically with the specimen atomic number (Z) of a pure element for Z numbers within the low atomic number range (approximately less than 20) [18]. Due to the imaging of more complex compositions, it becomes necessary to define a mean weighted backscatter coefficient, $\overline{\eta}$ shown in Equation 2.25 [18].

$$\overline{\eta} = \sum_{i=1}^{n} C_i \eta_i \tag{2.25}$$

In simple terms this mean, the weighted backscatter coefficient ($\overline{\eta}$) of a composite material, is related to the backscatter coefficient of each of the individual constituents. An expression for the mean atomic Z number ($\overline{Z}$) was also derived and is given by Equation 2.26:

$$\overline{Z} = \frac{\sum(NAZ)}{\sum(NA)} \tag{2.26}$$

For a composite material, the mean backscatter coefficient is linearly related to the mean atomic number once the atomic elements are homogenously distributed on an atomic scale, as is the case with bone [80].

Using electron detectors that collect backscattered electrons, a backscatter image can be formed which represents the intensities of the backscattered electrons collected. These intensities are linearly related to atomic density so the image reflects the atomic density of the imaged specimen. An example of this effect can be seen in Figures 2.33 and 2.34. Both figures show the same alumina-nickel composite material. The secondary electron image reflects surface topography, similar to the type of image seen using normal light microscopy but at a greatly increased magnification level (Figure 2.33). This image illustrates the grain boundary structure and shows the material to be apparently uniform. The backscatter image, seen in Figure 2.34 obviously reflects the composition of the material instead. Here the atomically denser nickel shows up as a phase with a brighter image intensity.

This property is extremely useful for polyphase materials as we have seen. In samples consisting of a single phase, the BSE image will exhibit a uniform intensity with no contrast. In polyphase materials, such as the alumina-nickel composite shown in Figures 2.33 and 2.34, the local Z number and consequently the backscatter coefficient (η) vary from phase to phase. The intensity level is quantified using the grey level (GL) scale where brighter GLs represent areas of increased atomic density. For mineralised tissue, a comprehensive protocol based specifically on the use of this method in the examination of mineralised tissue has been developed and successfully implemented in both healthy and pathological bone tissue [80, 100, 19, 95, 96]. This method is described in more detail in Section 2.7.4.

2.7.3 Depth-Specific Imaging

Unlike secondary electrons which originate from the surface of a sample specimen, backscatter electrons originate from a specific emission volume within the sample [18]. The size of this interaction volume depends on the penetration depths of the sample incident electrons. Hence sampling volume varies with two SEM variables, accelerating voltage and probe diameter, as well as three material parameters, namely morphology, composition and crystal

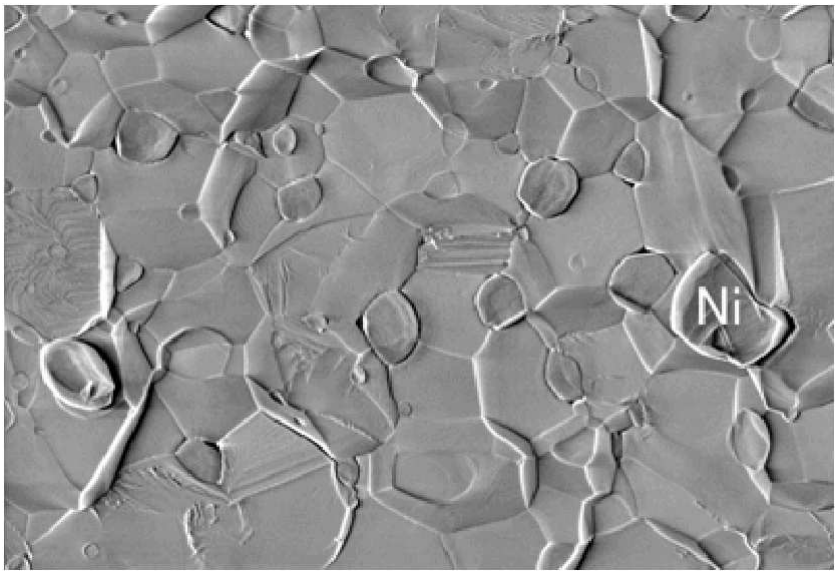

Figure 2.33: Image of alumina-nickel composite viewed using secondary electron emission.

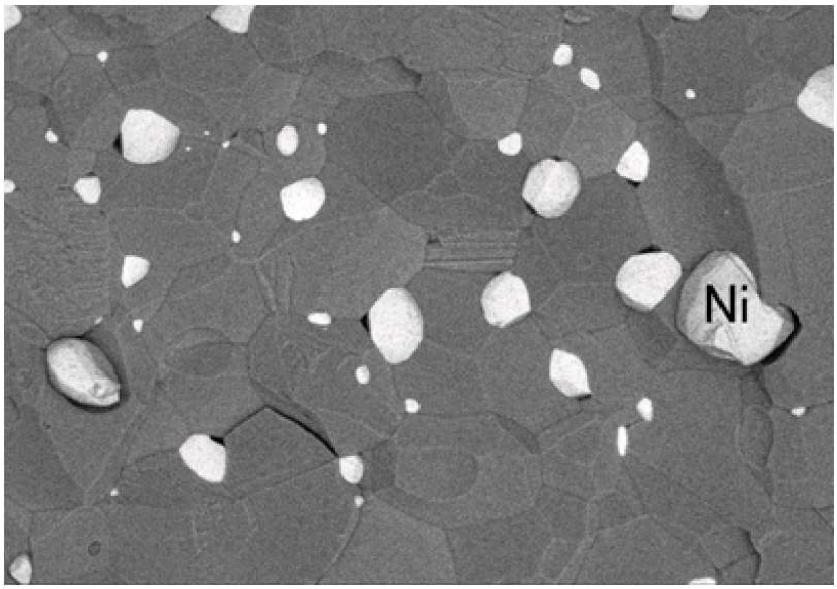

Figure 2.34: Image of alumina-nickel composite viewed using backscatter electron emission.

structure [18]. The relationship between accelerating voltage and penetration depth of incident electrons has been extensively studied. The incident beam range, defined as the greatest depth within which the incident electrons can penetrate has been empirically determined and is described in Equation 2.27.

$$R = \frac{75E_0^{5/3}}{\rho} \tag{2.27}$$

where E_0 is the beam energy in keV, R is the penetration range in nm and ρ is the density of the specimen in g/cm^3. The schematic shown in Figure 2.35 illustrates the relative escape depth of backscattered electrons compared with the electron beam range and various forms of specimen emissive interactions. However, the incident beam range is larger than the depth from which backscattered electrons can escape. This depth has been found to vary from as little as a third of the incident beam range [101] to as deep as half [102]. For this reason, coupled with the relationship of backscatter intensity with average elemental Z number, the backscatter image contains information about the interior of the specimen rather than the surface.

By varying the accelerating voltage, it is therefore possible to vary the interaction volume from which the composition based information originates. Much work has been conducted within this specific field of QBEI research, specifically in the study of layered semiconductor materials [103, 104, 102, 105]. However, there are limitations with this technique which particularly complicate tomographic research. Due to the nature of the electron interaction volume, it is difficult to isolate particular planes of interest below the surface for analysis. By their nature, increased electron interaction volumes include compositional and morphological information averaged across the entire BSE escape depth. Hence, isolated imaging or assessment of individual subsurface layers such as those seen in semiconductive materials can be extremely difficult. However, when examining materials that represent a constant bulk material with a compositional distribution varying with depth, altering the interaction volume offers a powerful quantitative insight into how the materials composition changes throughout its depth.

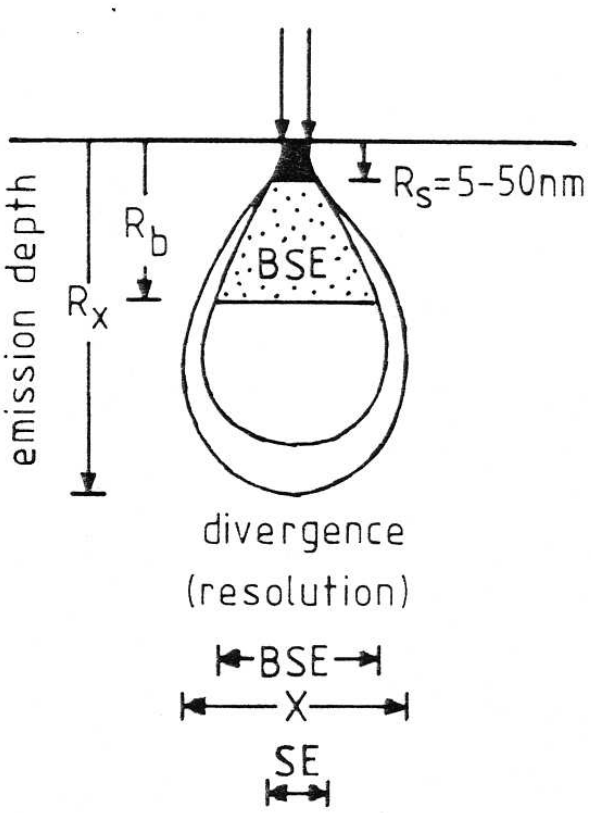

Figure 2.35: Comparison of different emission depth penetration ranges for typical electron beam interactions. [18]

Each measurement represents the average composition of the complete backscatter electron (BSE) interaction volume at a specified accelerating voltage (see Figure 2.36). In a material with a linearly increasing density as a function of depth, the difference between measurements conducted at two different accelerating voltages represents the change in average density between two different BSE interaction volumes. Hence, this method will identify changes in the composition of a material as a function of depth but will tend to underestimate the magnitudes of these changes. Any large change in density in the new material encompassed by the larger BSE interaction

volume will not be as obvious due to the averaging effect of the measurement.

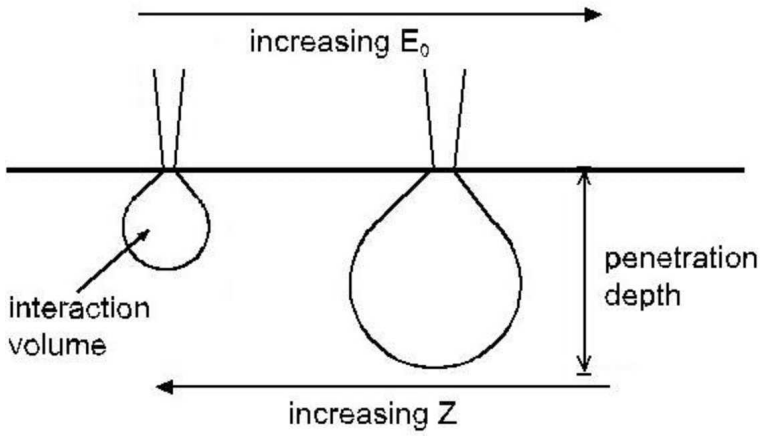

Figure 2.36: Interaction volume as a function of accelerating voltage.

2.7.4 Quantitative Calibration

As illustrated in Figures 2.33 and 2.34, backscatter electron imaging highlights clear, qualitative differences between the compositions of two separate materials. Each pixel within a backscattered electron image represents the average atomic density at that point, measured as a grey level intensity (GL). The grey level intensity scale ranges from 0 GL (or absolute black) to 255 GL (absolute white). For the study of osseous tissue, where measures of bone mineralisation and composition are known determinants of strength, compositional assessment using a scale common to the analysis of this tissue is vital. A suitable technique to accomplish this was initially developed in 1995 by Roschger *et al.* [80], successfully employed in many subsequent analyses of mineralised tissue [100, 19, 95, 96] and used throughout this present work.

Their method involved imaging areas of healthy bone tissue samples using a novel backscatter electron imaging technique [80]. Briefly, the GL scale was calibrated by imaging two pure element standards, carbon and aluminium,

and altering the brightness and contrast in realtime until the carbon standard returns a GL value of 25 ± 1 and aluminium returns a value of 225 ± 1. This calibration was checked every 15 to 20 minutes. Sample testing was performed using this standardised GL scale, with GLs subsequently converted to wt% Ca values. This involved the quantitative assessment of pure osteoid (defined as 0 wt% Ca) and pure hydroxyapatite (defined as 39.86 wt% Ca), measuring their corresponding GL values and extrapolating a linear relationship between the two points, as described in Roschger *et al.* [80]. A graph representing these calibration measurements is shown in Figure 2.37.

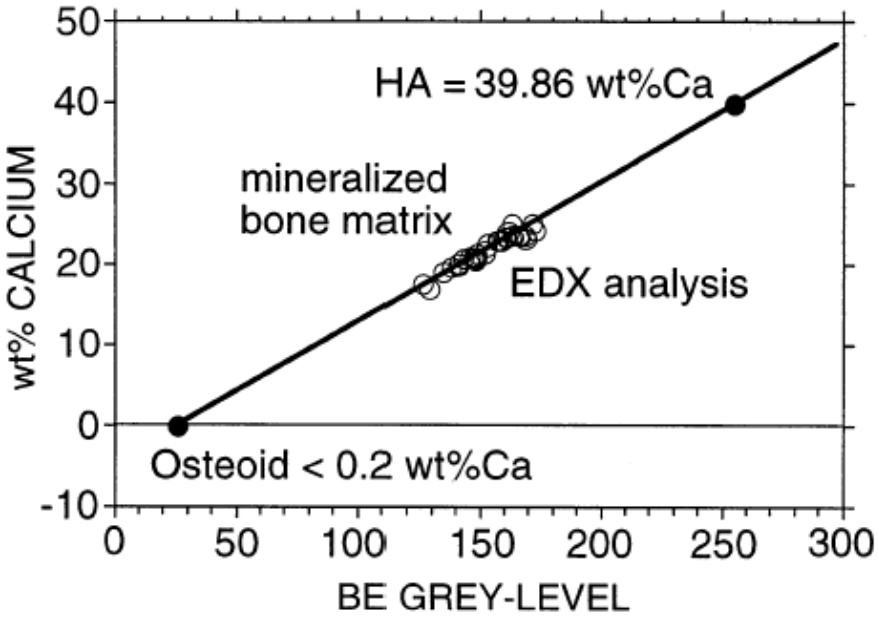

Figure 2.37: Linear relationship between QBEI grey levels and wt% Ca. [19]

2.7.5 Beam Damage

Specimen damage (surface irradiation damage) caused by the incident electron beam is of particular importance in biological and polymeric specimens as they are particularly sensitive to electron beam interactions. There are a number of common ways in which an electron beam can adversely affect organic samples during examination. Some of these effects include heating, electrostatic charging, ionisation damage (radiolysis), displacement damage, sputtering and hydrocarbon contamination. The worst radiation damage occurs in organic solids. Radiolysis effectively breaks down chemical bonds, causing a loss of sample crystallinity or a change in composition. Localised increases in temperature can also render an organic sample more susceptible to such damage. Specimen damage is also dependent on beam current, probe size and exposure time [91]. Electron dosages are usually kept as low as possible by limiting exposure times while the current, and consequently the probe size, are kept constant using a Faraday cup. The analysis required incremental increases in incident beam energy to increase the electron interaction volume in order to obtain depth-specific data [104]. An unwanted side effect of these increased beam energies is an increased probe current [106] and decreased probe size at each energy increment, leading to an increased dosage rate in spite of the beam current being kept at a constant value. The net effect of this increased beam energy on the samples was irreversible specimen damage. This damage can be seen in Figure 2.38 as a bright, square patch towards the top left of the backscatter image. Subsequent light microscopy images were taken of these areas. The light microscope image corresponding to the backscatter image seen in Figure 2.38 can be seen in Figure 2.39. It is clear by comparing both images that this was not an imaging or charging artefact. The exact nature of the damage could not be discerned and was beyond the scope of this present work but appeared to be tissue radiolysis. Its effect on the sample's composition measured using the QBEI technique was to artificially and irreversibly increase the measured atomic density of this region. This would obviously invalidate the quantitative nature of this

study and a technique to reduce this damage was developed. The process by which this damage occurred in the samples was unknown and beyond the scope of this study but based on the possible forms of radiation damage described in previous studies [91], it was likely that it was not electrostatic charging, hydrocarbon contamination or electron beam sputtering. Probable damage mechanisms included atomic displacement, electron beam heating and/or radiolysis.

Atomic Displacement

If the electron beam energy exceeds a material-specific energy threshold value, high angle elastic scattering can displace atomic nuclei to interstitial lattice positions and thereby degrade the crystalline structure of the material.

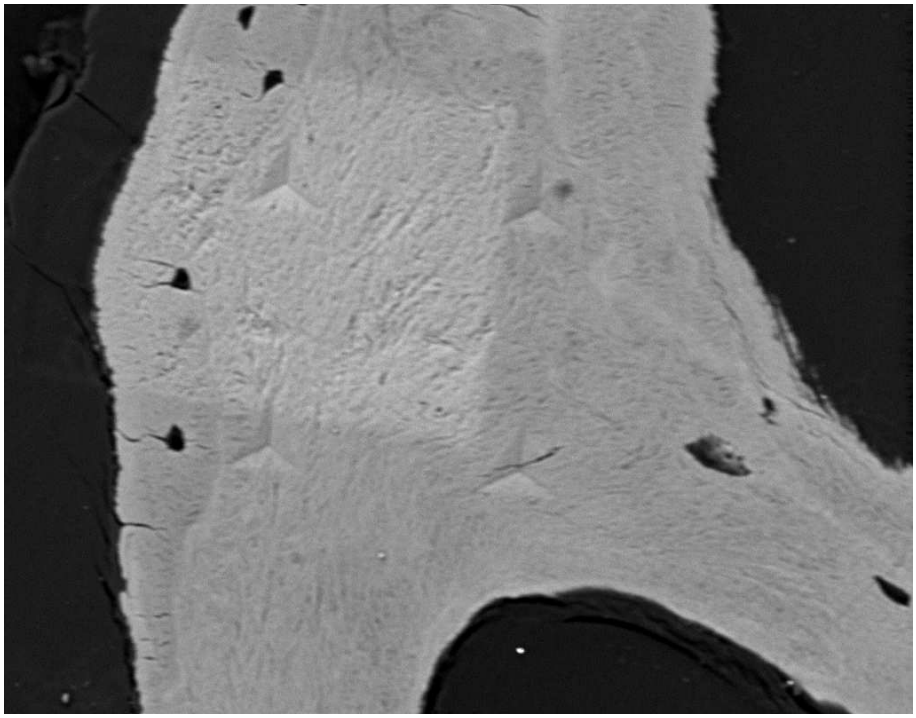

Figure 2.38: QBEI image of a trabecular bone sample exhibiting irreversible specimen damage in the form of a 'bright' patch.

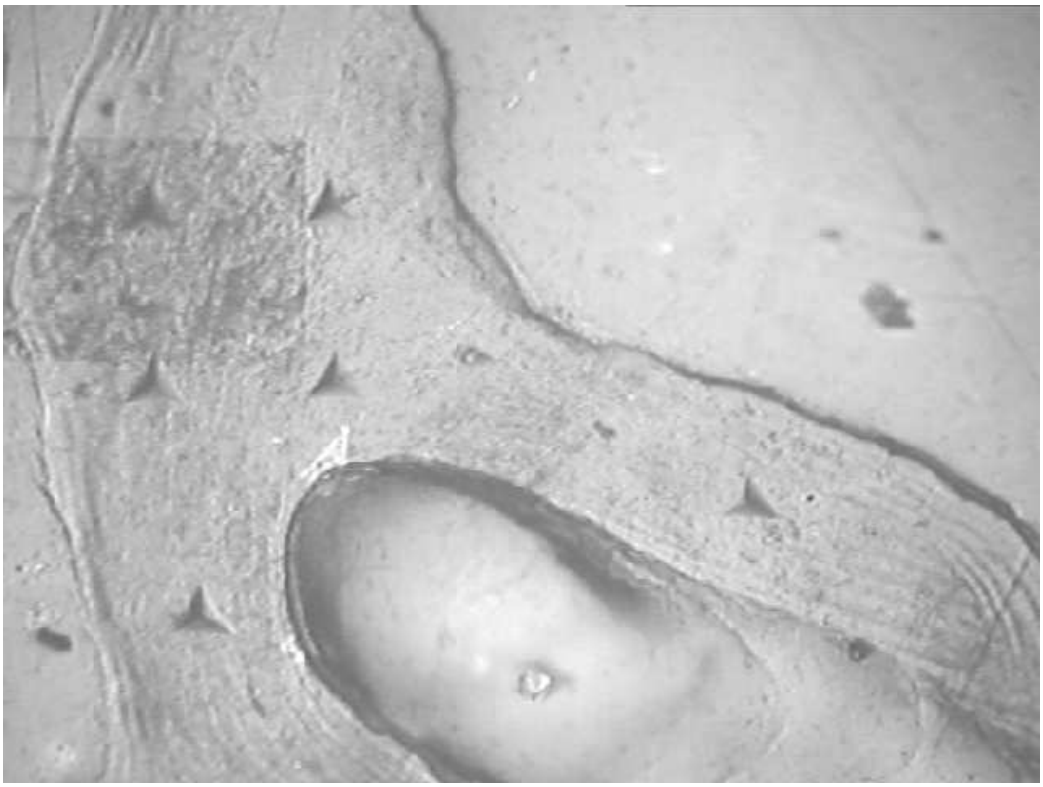

Figure 2.39: Corresponding light microscope image of the damaged region in Figure 2.38.

Electron Beam Sputtering

Occurs at the surface where electron displacement energy is lower due to the fact that surface electrons are free to leave the surface, as opposed to being forced into interstitial space. This process is analogous to atomic displacement, whereby a threshold energy value must be exceeded for the process to occur.

Electron Beam Heating

Arises due to energy transfer between the inelastically scattered electron beam electrons and sample electrons. This process can result in thermal degradation or melting where appropriate.

Electrostatic Charging

Charging at high incident electron beam energies can result in the creation of a mechanical force. Depending on the inherent strength and/or coincident sample damage due to electron beam heating, significant sample damage can occur.

Hydrocarbon Contamination

This is the inverse of mass loss, whereby hydrocarbon molecules present are polymerised by incoming or outgoing electrons, resulting in the deposition of hydrocarbon based contaminants on the sample surface, consequently obscuring the SEM image and consequent material data.

Radiolysis

Radiolysis occurs most easily in organic materials containing low strength atomic bonds, such as hydrogen and Van der Waals bonds. Electron excitation occurs within each affected molecule in the sample but subsequent de-excitation may not return the molecule to its original state. Once this occurs, the electron bond is broken and a loss of crystallinity occurs due to the shift in molecular arrangement. This process is dependent on a critical electron dose (electron exposure)

2.7.6 Novel Damage Reduction Technique

It is accepted that damage is dependent on dosage rate or electron exposure rate [91]. It was therefore vital to keep the electron dosage as low as possible. Dosage rate $[C/cm^2]$ is a product of incident current density and exposure time. However, the SEM used throughout this present work was not equipped with a Faraday Cup, which allows the regulation of beam current. Previous researchers, using only one beam energy throughout their analyses, have utilised a Faraday Cup to standardise the beam current at their chosen accelerating voltage [19, 92]. This standardises the effective dosage

per scanned area, for constant beam energy, facilitating interassay comparison. However, this method of calibration is insufficient when analysing a fragile specimen at different accelerating voltages since the beam current increases as a direct result of the increased accelerating voltage. The second side effect resulting from the increased accelerating voltage is a decreased beam diameter. To compensate for the former, the Faraday cup is used to lower the beam current. However, this simply decreases the beam's diameter further. Decreasing the beam diameter has the overall effect of increasing the dosage rate at this elevated accelerating voltage. The protocol developed in this present work calibrates the overall electron dosage rate instead of concentrating specifically on the beam current. This allows regulation of the effective electron dosage, by altering both the beam current and beam diameter together until the dosage rate is at an acceptably low level. The procedure for calibrating the sample electron dosage was developed using an *in situ* X-Ray detector and employing Energy Dispersive X-ray analysis (EDX). The number of X-Rays detected is measured in counts per second and denoted CPS.

The CPS is equivalent to the rate of X-Rays produced by inelastic scattering at the sample surface per second [106]. Therefore, for a material of constant bulk composition, the CPS rate can be used as a relative measure of mean energy transfer rate to the sample and consequently a relative dosage measure as the operating parameters are altered. The CPS is dependent on a number of factors but assuming no changes to the sample or its setup were made, the only parameters of concern are accelerating voltage, probe size and probe current. Using the measured CPS value, a method for standardising the relative dosage at each beam energy increment was developed and used throughout the duration of this study. The CPS calibration value was determined empirically. For this experimental work, determination of this calibration value involved imaging a carbon standard, the material with the lowest backscatter coefficient used throughout the work, at 15keV (the lowest accelerating voltage used throughout the course of the experiments). The

SEM's spot size was then adjusted until the lowest acceptable CPS value was reached while imaging the carbon standard at 15keV. The lowest acceptable CPS value was defined as the lowest spot size setting that resulted in constant image brightness and contrast, once the offset and gain level controls were kept constant. This value was found to be approximately 5900 CPS for the carbon standard at 15keV. This calibration was performed whenever the accelerating voltage was altered. Since this CPS calibration was always performed before the GL calibration, it only affected the sample dosage rate and could not interfere with the GL calibration step. Obviously, every time the accelerating voltage was altered, the dosage calibration was repeated, as was the wt% Ca calibration, in order to allow quantitative assessment of the mineralised tissue. This has a distinct advantage over the Faraday cup by ensuring dosage-controlled QBEI, performed at multiple accelerating voltages, while examining mineralised tissue samples.

Chapter 3

Materials and Methods

3.1 Materials

3.1.1 Sample Origins

This study examined early-stage OA bone tissue and age-matched healthy controls taken from human knee joints. Donors were sourced by the Orthopaedic Research Laboratory, Aarhus University Hospital, Aarhus, Denmark [107, 108, 109, 110]. All donors used throughout this study were Caucasian with ages spanning approximately two decades, from 61 to 85 years of age, with cause of death due to either trauma or acute disease. Twenty-two samples in total were harvested from both male and female donors, 12 OA and 10 healthy samples. One tibia was taken from each donor for excision of bone samples. Both medial and lateral samples were taken from each donor, all from the proximal tibiae. All excision work was conducted post-mortem. All groups were assessed both clinically and histologically. The control group was found to exhibit no macroscopic damage to the cartilaginous surfaces and presented no metabolic disease. OA group cartilage damage was defined macroscopically as degenerated fibrillated cartilage and confirmed histologically. OA group cartilage damaged tibiae exhibited visual degeneration with slight fissures in the superficial zone of the medial

condyles. The lateral condyles presented no visual symptoms of the pathology. These findings were confirmed histologically by looking for cell clusters in the superficial zone and testing for reduced safranin O staining. Further descriptive analysis of the sample's degree of pathological severity was conducted clinically using the Mankin scoring system. This system is detailed in Table 3.1. In the samples used throughout this present work, samples defined as healthy did not have a Mankin score higher than 2. OA sample Mankin scores ranged from 1.5 up to 7.0, with medial sample values no lower than 3.0. Lateral samples from samples exhibiting OA within the medial compartment did not exhibit a Mankin score of greater than 3, the average value being 1.7. This presented an opportunity to investigate bone tissue changes in lateral samples showing no significant evidence of cartilage damage due to OA.

Table 1
Histological scoring system

Parameter	Grade	Description
Articular cartilage structure	0	Normal
	1	Surface irregularities
	2	1–3 Superficial clefts
	3	>3 Superficial clefts
	4	1–3 Clefts extending to the middle zone
	5	>3 Clefts extending to the middle zone
	6	1–3 Clefts extending into the deep zone
	7	>3 Clefts extending into the deep zone
	8	Clefts extending to zone of calcified cartilage

Table 3.1: Mankin scoring system grades [20]

One sample was chosen from each site (medial or lateral) at random from a choice of between six or seven possible sites within each proximal tibial plateau. Post-hoc analysis of the control samples was performed to confirm that the moduli of the bone samples were unrelated to the sampling site within each compartment.

3.1.2 Sample Preparation

Trabecular bone situated between the articular cartilage cortical base and the epiphyseal plate was defined as subchondral trabecular tissue. Sample preparation was carried out by the Erasmus University Rotterdam. Samples were cored from both the medial and lateral sides of the joint using a 7.5 mm diameter trephine core. During the removal of tissue, the core was always perpendicular to the cartilaginous surface. Trabecular sections, 1 mm in thickness, were removed from below the articular bone plate of each core using an EXACT diamond precision band saw while under constant irrigation. Marrow and fatty deposits were subsequently removed using a soft water jet. Each 1 mm thick, 7.5 mm diameter trabecular section was then cut along the major x and y axis to produce four wedge-shaped sections. One section from each sample was used for this study while the other sections were sent to alternate research institutions for analysis. After all cutting procedures were completed, all samples were immediately placed in sealed plastic tubes containing physiological saline and stored at -20^{0}C until the embedding procedure.

3.1.3 Embedding Procedure

Samples were thawed prior to the embedding procedure. Sample embedding was carried out by the Erasmus University Rotterdam. Polymethylmethacrylate (PMMA) was chosen as the embedding material and is an infiltrating embedding medium often used for mineralised tissue analysis. Sample dehydration, necessary for the embedding procedure, was conducted using a graded series of alcohol solutions, summarised in Table 3.2. There were four increasing concentration levels used successively for a total of 192 hours, resulting in complete dehydration of the samples. The samples were then immersed in a solution of alcohol mixed with acetone, with a 1:1 concentration by volume for 48 hours. Acetone was a requirement for the polymerisation of the PMMA resin. Finally, the samples were introduced to a solution con-

Solution	Time
70% Alcohol	48 hours
80% Alcohol	48 hours
90% Alcohol	48 hours
100% Alcohol	48 hours
100% Alcohol\Acetone (1:1)	48 hours
Plastic and Softener	48 hours

Table 3.2: Embedding procedure and alcohol concentrations.

taining the MMA plastic and a softener. The samples were left for 48 hours in this final solution, resulting in complete polymerisation of the infiltrating monomer.

Once embedded, the sample surfaces were polished initially using a wet silica carbide paper grinding procedure. Samples were polished by hand using a polishing wheel equipped with 1000 grade silica-carbide paper under constant irrigation and then subsequently using the finer 2400 grade silica-carbide polishing paper. Further polishing of the sample surfaces was required before mechanical or compositional characterisation could be performed. Extremely smooth surfaces are a prerequisite for nanoindentation and QBEI. This subsequent polishing was conducted using alcohol-based diamond polishing solutions with progressively decreasing diamond grit sizes. Alcohol was used to ensure no damage was introduced during the polishing process. Use of aqueous lubrication during the grinding or polishing of methacrylate-embedded bone tissue has been shown to introduce permanent tissue damage, in the form of bone ultracracks [111]. Each sample was subjected to approximately ten minutes polishing using the 9 μm grit size polish, followed by another ten minutes using 6 μm grit size. Final polishing using 3 μm and 1 μm grit sizes was performed for approximately four minutes and one minute respectively. Once completed, each sample was viewed under

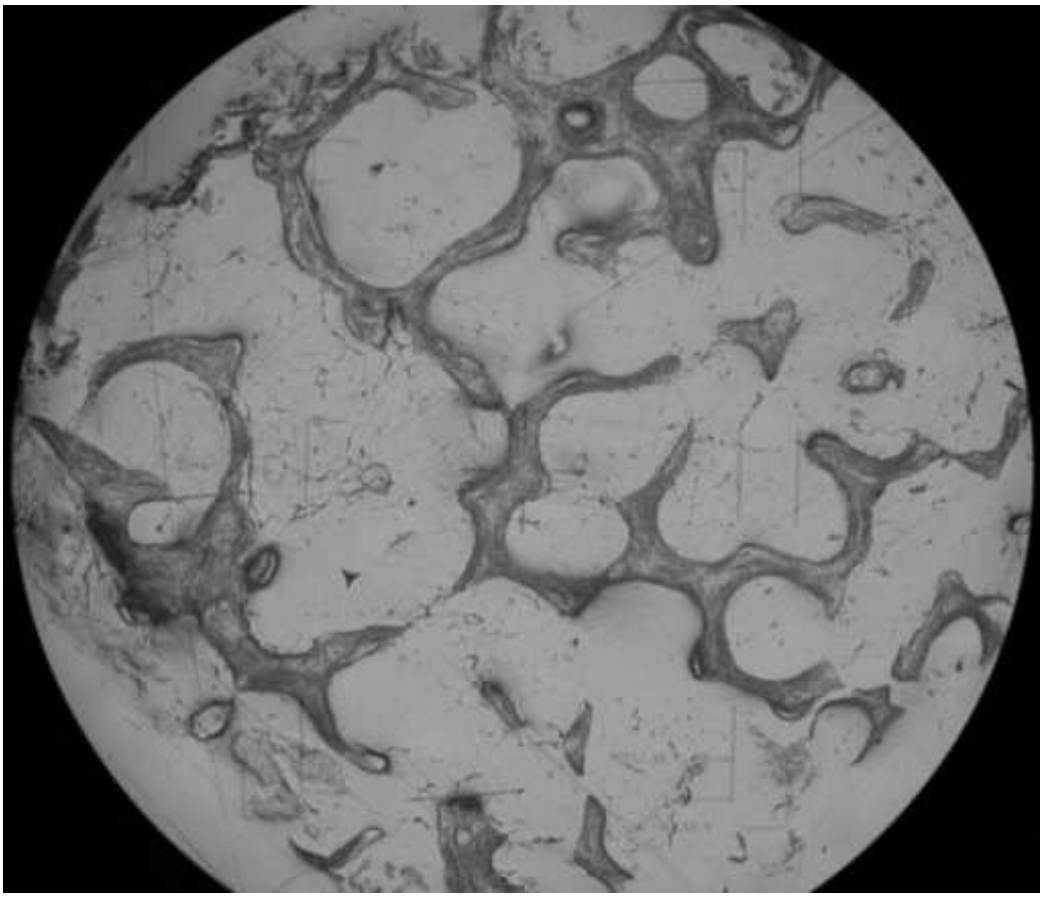

Figure 3.1: Trabecular bone sample map cross-section through a typical trabecular network.

a microscope and a digital image was captured, resulting in bone sample maps, used throughout the testing stage to mark and subsequently identify nanoindentation tests for analysis (Figure 3.1).

3.2 Nanoindentation Setup

All nanoindentation experiments were carried out in a temperature controlled environment at room temperature (approximately 23^0C). A Nanoindenter XP (MTS Systems), equipped with high performance vibration isolation and

CSM capability, was used throughout the duration of this present work (Figure 3.3). The Nanoindenter XP offered load and displacement resolutions of 0.05 μN and 0.01 nm respectively. The indenter tip chosen was an Accu-Tip (TM) Berkovich diamond indentation tip, with defined elastic modulus of 1141 GPa and a Poisson's ratio equal to 0.07. The Berkovich geometry was chosen for its relatively flat profile, ensuring low tip stresses and the reduced likelihood of indenter-induced specimen cracking during indentation. An ideal Berkovich geometry exhibits a total included angle of 142.3^0 and a half angle of 65.35^0. Prior to any bone specimen testing, the nanoindenter was first calibrated by evaluating the indenter tip contact area using a fused silica sample standard. Using a calibration method supplied with the nanoindenter Testworks software, ten CSM indentations were performed on the silica standard (E_{Si}=72 MPa) and the coefficients required to describe the contact area function were determined.

Samples were temporarily bonded to an aluminium sample stage insert supplied with the nanoindenter using a cyanoacrylate-based adhesive. The sample stage insert (with sample *in situ*) was then placed in the sample stage (Figure 3.2). Its vertical position within the stage is adjustable. Protocol requires that the sample surface be a defined distance away from the indenter tip. The sample surface was adjusted to the correct level before the indentation proceeded. Incorrect positioning can cause the indenter to overestimate the distance between the sample surface and the indenter tip. This can lead to catastrophic failure due to indenter impact with the sample surface. Once the sample surface plane position was set, the stage was placed in the nanoindenter rig (Figure 3.3) and the sample surface was imaged using an *in situ* camera linked to the integral light microscope lense. The microscope focus was then adjusted to give a visually optimal image, resulting in high contrast between trabecular bone tissue and the surrounding infiltrating embedding medium. Figure 2.20 is an example of such an image.

Prior to the start of the loading procedure, certain experimental parameters were set to facilitate CSM analysis of the samples. A suitable Poisson's

Figure 3.2: Sample stage with bone sample, aluminium standard and fused silica standard inserted.

ratio for the test samples of 0.3 was chosen based on previous literature [112, 83, 85, 87, 89] and a validation study [113]. The Young's Modulus and Poisson's ratio for the Berkovich diamond indenter tip were input. A maximum depth of 4 μm was chosen to correspond with the maximum possible depth of examination examined using the subsequent QBEI mineralisation analysis procedure. A constant strain rate target of 0.05/s was applied throughout and a surface approach velocity of 10 nm/s was specified. A small dynamic oscillation, 45Hz in magnitude, was imposed on the force signal throughout the load cycle. A harmonic displacement target of 2 nm was also set prior to the beginning of the load cycle. A minimum acceptable drift rate of 0.8 nm/s was also specified prior to testing. This prohibits the start of

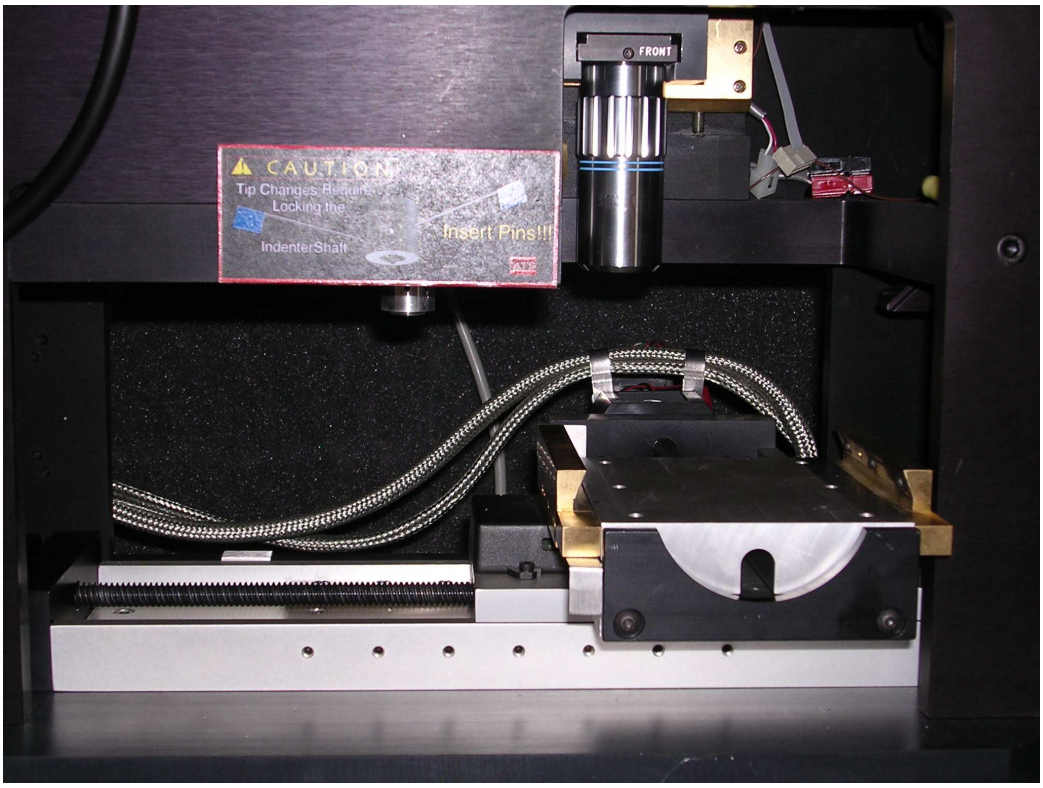

Figure 3.3: Nanoindenter XP apparatus with sample stage removed.

any indentation before the drift rate reaches an acceptably low level, defined by the user.

3.2.1 Procedure

The Continuous Stiffness Measurement (CSM) load cycle was used throughout during sample testing. The CSM experimental protocol used was a load-controlled indentation procedure, allowing a constant target strain rate to be set for the duration of each test. Required indentation parameters were chosen based on a previous validation study by Brady *et al.* [113]. Elastic modulus and hardness were calculated continuously within the software as a function of depth (Figures 3.5 and 3.6) from the load and displacement data (Figure 3.4).

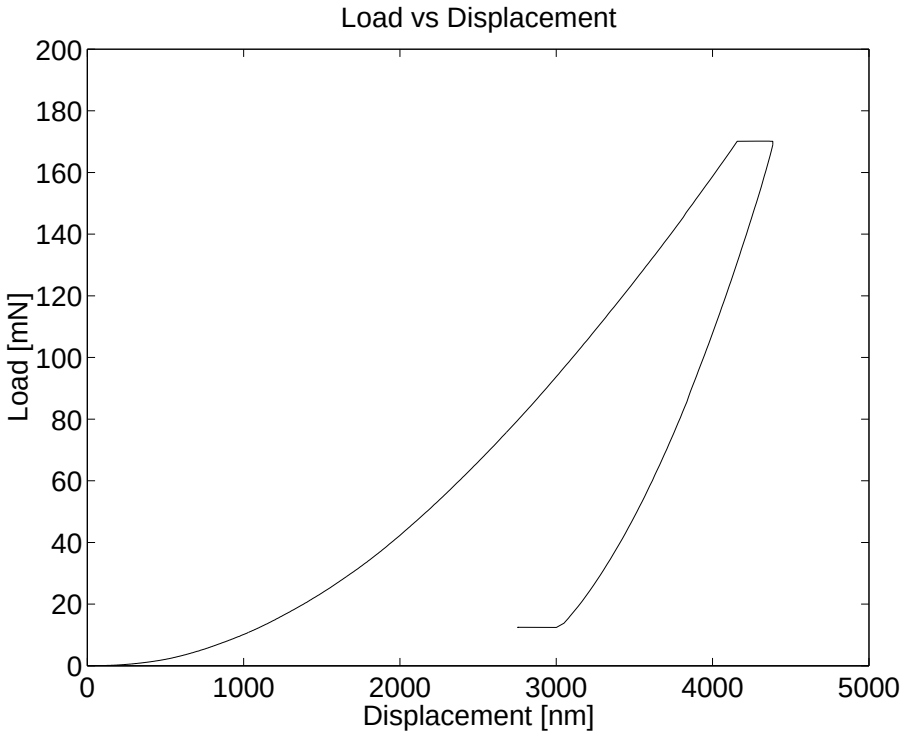

Figure 3.4: Indentation load as a function of indenter displacement into subchondral trabecular bone sample.

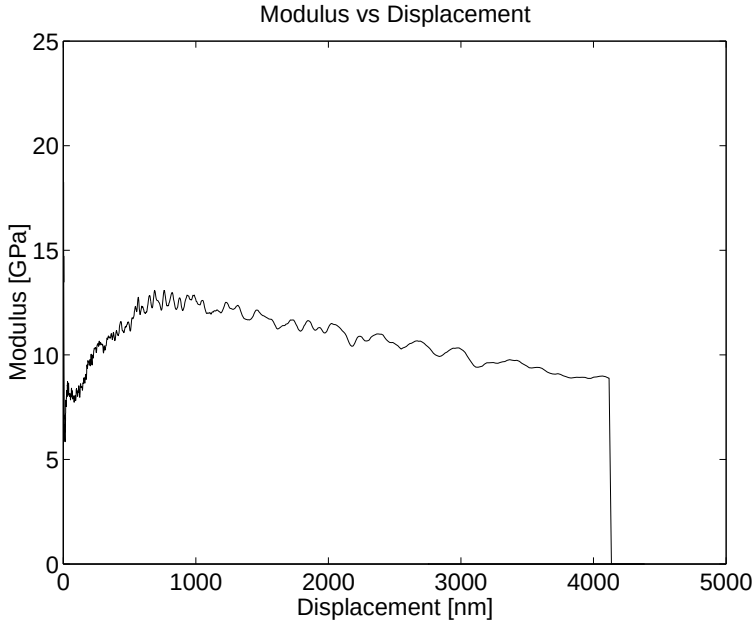

Figure 3.5: Indentation modulus as a function of indenter displacement.

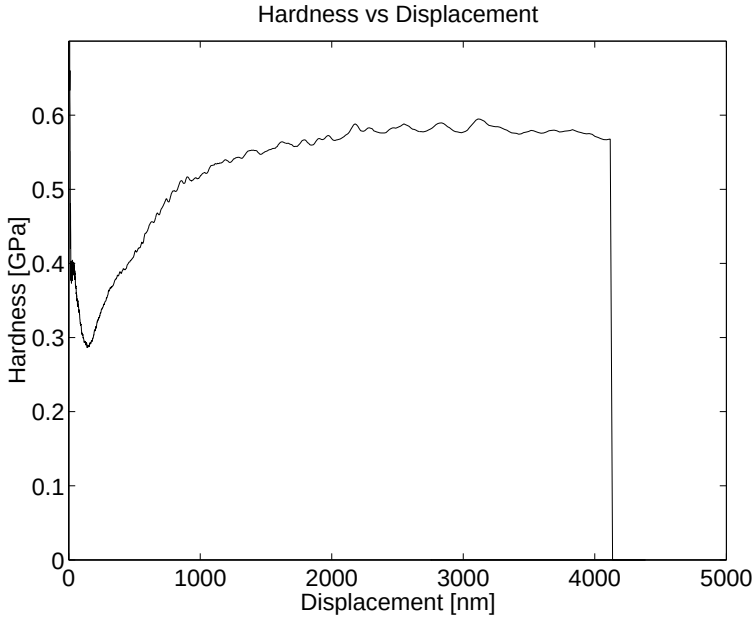

Figure 3.6: Indentation hardness as a function of indenter displacement.

Suitable target areas were chosen based on their microstructure, viewed through the light microscope attached to the apparatus. Coordinates for each target area were saved within the indentation program, ensuring no two indentation locations, performed using a Berkovich tip, would be closer than 20 to 30 times the maximum indentation depth [17]. In this study, indentations were at least 80 μm apart. Approximately 100 indentations were performed on each sample, except when sufficient suitable trabecular material was unavailable. Every attempt was made, prior to indentation, to ensure that the chosen locations were deep enough to accommodate the penetration depth of the indenter and the resulting stress fields at maximum load. Subjective analysis of each indentation site was performed with partially transparent indentation sites avoided. Partial transparency or translucence of a bone sample site under light microscopy indicated an extremely thin section and resulted in unsuccessful nanoindentations. An additional negative indication of insufficient depth of material presented as the gradual disappearance of tissue along the length of an individual plate or strut. This occurred when the orientation plane of an individual strut or plate was oblique with regard to the plane of sample sectioning. An example of this can be seen in Figure 3.7.

The load versus displacement data seen in Figure 3.4 consisted of a constant ramp from zero load to a maximum load specified by the required indentation depth of 4 μm. This maximum load was between 200mN and 250mN depending on the sample tested. This maximum load was then held constant for a period of 90 seconds to allow viscoelastic creep displacements to dissipate before the unloading cycle began. This period was chosen based on preliminary analysis of creep effects in nanoindented bone tissue [113]. The load was then linearly ramped down to approximately 10% of the maximum load and held for a further 90 seconds. This facilitated the quantification of thermal drift influences throughout the testing phase. Finally, the load was decreased to zero and the indenter tip was removed from the specimen surface. A total of 2,957 indentations were attempted, of which 2,250 were

Figure 3.7: Trabecular bone sample showing insufficient depth of material, imaged using light microscopy with specimen embedded in PMMA.

completed successfully. The loss of 707 indentations was due to unforseen errors occurring during the test procedure and the test software declaring the indentation as invalid. Examples of such errors included incorrect surface detection, localised sample roughness and indentation on subsurface pores or cracks.

3.2.2 Analysis

Once testing was completed, each sample was examined using the *in situ* light microscope. Each indentation was located using the sample map and its image was saved for subsequent surface analysis and data evaluation.

Indentations that had been successfully performed but were located on, or sufficiently close to, the embedding medium or surface abnormalities were discounted from subsequent statistical analysis. An example of this situation can be seen in Figure 3.8. This decreased the number of valid indentations from 2,250 to 1,968. Further removal of erroneous raw data was performed using the QBEI method as described in Section 3.3.2. After visual analysis of the indentation sites using light microscopy and QBEI images, results from each indentation test were exported into a Microsoft Excel file using an in-built function within the Nanoindenter-supplied Testworks (TM) software. These excel files were then imported into Matlab using a novel script I developed specifically for this purpose. Raw experimental data for each indentation were then extracted using another novel Matlab script developed

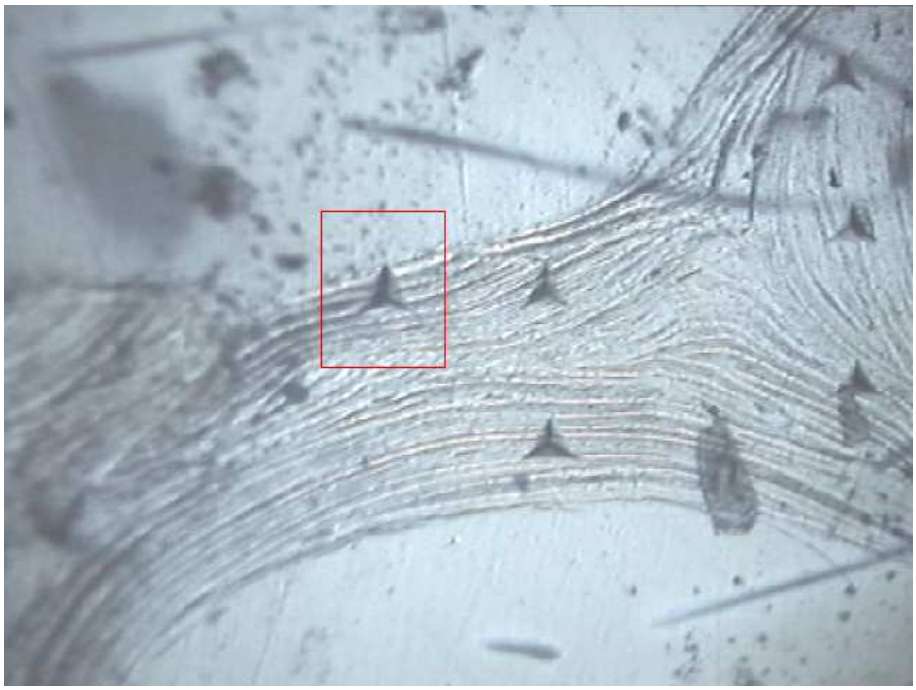

Figure 3.8: Indentation set showing indentations performed close to embedding medium. Left-most indentation deemed too close to sample edge.

during this present work. Modulus, hardness, load, displacement, harmonic contact stiffness and time were all recorded and saved from each test. Relevant data plots were created and stored. These plots were used to manually check the intrinsic surface detection result for each test, ensuring no error in surface detection occurred. Incorrect surface detection can lead to erroneous material characteristic calculation errors. They were also used to ensure no additional erroneous events occurred throughout the indentation process that had been unaccounted for using the two visual methods mentioned previously. Examples of such events would include real-time disturbances to the apparatus during testing, such as a vibrational disturbance or machine surge. Each plot included nine subplots illustrating important experimental parameters plotted against each other. These plots were used for qualitative data post-processing only. A typical example is shown in Figure 3.9 while the entire collection is contained in the appendix CD-rom attached to this thesis.

3.3 QBEI Setup

Samples were mounted on individual SEM mounting stubs using adhesive carbon discs. Quick-drying silver paint was placed around the circumference of the samples edge, ensuring continuity of the paint layer between sample embedding resin and the underlying aluminium SEM stub. Figure 3.10 shows the amount of conductive paint required for charge-free imaging. Silver paint was used in addition to the conductive carbon discs to ensure no charge-up effects were present during sample imaging. Extreme care was taken to ensure no contamination of the bone sample embedded within the medium. Samples were sputter-coated with carbon using a Bio Rad (Microscience Division) Carbon Coater Model TB500 prior to any experimental work in the SEM. This thin layer of carbon particles is a prerequisite for SEM analysis of organic, non-conductive samples such as bone or other biological samples. Electron conduction improves the flow of electrons away

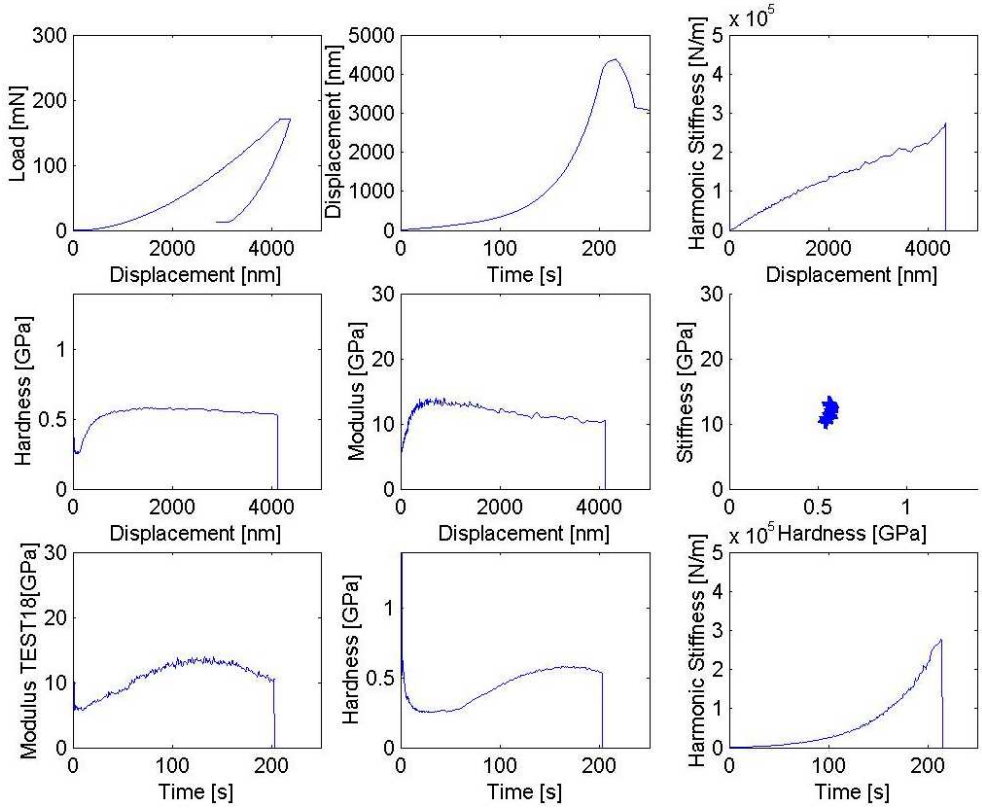

Figure 3.9: Typical plots of major experimental parameters as a function each other.

from the incident point of contact between the electron beam and sample surface, reducing thermal effects or damage to the sample. Carbon sputtering, and hence electron conduction, was mainly used to reduce specimen charging. Over time, the negative charge due to the retained incident electrons builds up until incident electron-sample interactions are detrimentally affected by the considerable repulsive negative spot charge. Once coated, all samples were placed in air tight containers and stored at room temperature until tested. Figure 3.10 shows a typical sample, bonded to an aluminium stub and prepared for SEM analysis.

Figure 3.10: Embedded trabecular bone sample mounted on aluminium SEM stub with silver paint placed around the circumference.

3.3.1 QBEI Procedure

Quantitative backscatter electron imaging (QBEI) was carried out using a JEOL JSM-5410 LV Scanning Electron Microscope (SEM). A conventional backscattered electron detector (paired semiconductor type; JEOL), as supplied with the JEOL JSM-5410 LV microscope, was employed. The accelerating voltages used spanned the total range of values available using the

JEOL JSM-5410 SEM, specifically from 15kV to 30kV in 5 kV steps. Using the equation detailed in Chapter 2, Section 2.7.3, the penetration range in mineralised tissue corresponding to the employed accelerating voltages were calculated. This defined the range of examination depths possible throughout the course of this study.

The SEM's optimal working distance was 20 mm. The instrument used for X-ray detection was a Phoenix-Pro X-ray Microanalyser System for the SEM (EDAX Incorporated, USA). This system is based in a Si(Li) type SEM detecting unit with super ultra thin window for detection of all elements down to and including beryllium. Resolution is 133eV or better, measured at MnKα, 1000CPS and with the time constant 100 microseconds. Peak to background is 20,000:1 or better and the active detector area is 10 mm^2. Data processing was carried out by a dual Pentium PC workstation running Windows NT4 operating system. The software package used was the EDAX Particle/Phase Analysis software package. The X-ray detector geometries were as follows: working distance = 20 mm, tilt angle = 0^0, take-off angle = 20^0. The spot size or probe diameter was calibrated using a novel electron dosage calibration technique, described in detail in Section 2.7.6. Briefly, it involves setting the CPS value of a carbon standard to a known low-dosage value of 5,900 CPS prior to testing. This CPS calibration was performed every time the accelerating voltage was altered. The GL values were calibrated using the technique published in Roschger *et al.* [80]. Two pure element standards were used to calibrate a linear GL reference scale, whereby pure carbon displays a weighted GL_{mean} of 25 $\pm$ 1 when imaged and pure aluminium exhibits a GL_{mean} = 225 $\pm$ 1. This allows quantitative comparison between different scanned areas in terms of the calibrated GL scale. These calibrations were checked every five to six scans using the pure element standards to ensure that instrument instability-induced deviations were prevented from affecting GL measurements. The backscatter images were formed in real time and captured digitally using an integral analog digital conversion system. An image resolution of 1,024 x 800 pixels per scanned

area was chosen when capturing images for analysis. The sample magnification used while imaging the specimens was set to 500x, which equates to a spatial resolution of less than 0.4 μm. Each high-resolution scan required approximately eight to ten seconds to perform. From this point on, two different protocols were employed. The first involved the assessment of the novel dosage calibration to evaluate the quantitative improvement in damage reduction due to employing the novel technique. The second protocol was concerned only with pathological assessment.

Damage Analysis

For sample damage analysis, the backscatter images of unindented human trabecular subchondral bone samples were formed in real time and captured digitally using an integral analog digital conversion system. An image resolution of 1024 x 800 pixels per scanned area was chosen when capturing images for analysis. The sample magnification used while imaging the specimens was set to 500x, which equates with a spatial resolution of less than 0.4 μm. For each damage assessment scan, a suitable ROI was selected. Once chosen, this single specified ROI was captured twenty consecutive times as a high-resolution image. This resulted in an approximate total exposure time per ROI of 160 to 200 seconds. Each image was saved with reference to its scan number for subsequent image analysis. These damage rate measurements were then used to investigate the effect of the novel imaging protocol on sample irradiation damage. For a given ROI, the mineralisation histogram data were overlaid on top of each other. Sample damage manifested as an artificial increase in measured GL. Hence, the quantitative effect of damage done to a specific ROI was seen as a drift in mineralisation histogram plots for a specific ROI. An example of this can be seen in the results Chapter in Figure 4.67. Additionally, the mean effective damage rate was also calculated. This involved plotting the peak histogram GL against the respective sample scan number. This allowed quantification of damage rates for each test. An example of this can be seen in the results Chapter in Figure 4.64.

Damage rates were investigated at both extremes of accelerating voltages used throughout this present work. At 15keV, the damage rate of this novel protocol (low spot size, CPS $\simeq$ 5900) was compared with the damage resulting from a visually optimum dosage rate (high spot size, CPS $\simeq$ 19,000), highlighting the sensitivity of bone to electron beam damage. At 30 keV, the novel protocol was compared with a constant machine spot size value, set at 15 keV (CPS $\simeq$ 5900) and held constant as the accelerating voltage was increased to 30 keV, resulting in a CPS $\simeq$ 19,000. This effective dosage rate is representative of the lowest calibrated damage rate possible without an *in situ* EDX machine or Faraday cup. A more detailed discussion of this protocol is given in Section 4.6.2 in Chapter 4. These images were saved and raw histogram data were extracted and imported into Matlab for the required graphical and statistical analysis.

Pathological Assessment

For pathological assessment, backscatter images of nanoindented ROIs were formed in real time and captured digitally using an integral analog digital conversion system. An image resolution of 1024 x 800 pixels per scanned area was chosen when capturing images for analysis. The sample magnification used while imaging the specimens was set to 500x, which equates to a spatial resolution of less than 0.4 μm. Nanoindentation sets were located using reference images containing identifiable landmarks and a high quality backscatter picture of the set was captured. Once chosen, the specified ROI was captured once as a high-resolution image and exposure time was kept to a minimum as QBEI protocol suggests. This resulted in an approximate total exposure time per ROI of 8 to 10 seconds. These images were saved and raw histogram data were extracted and analysed using a custom image analysis script developed in Matlab. This procedure was repeated for every successful indentation within each bone sample. The whole procedure was repeated four times, increasing the accelerating voltage each time by 5keV from an initial value of 15keV up to 30keV.

3.3.2 Analysis

Once QBEI testing was completed, each QBEI image was examined individually. As was the case with nanoindentation pictures, the QBEI pictures were closely examined to ensure no indentations had been performed on subsurface inhomogeneities such as pores or cracks. Any nanoindentations performed on unseen subsurface defects (detected using QBEI) were discounted from statistical analysis of the data. This procedure reduced the number of completely valid indentations from 1,968 to 1,338. After visual inspection of the QBEI data, images resulting from the damage analysis protocol were imported into Matlab and analysed using a custom script developed specifically for the analysis stage. Analysis plots were created for each sample. This involved overlaying the ROI histograms of each scan on top of each other, highlighting any damage that arose. Peak GL values and full-width half-maximum (FWHM) values were calculated for each scan and plotted as a function of scan number, demonstrating the rate of change of the peak GL for a specified ROI.

After irradiation damage assessment, images of the performed nanoindentations were examined using custom image analysis software developed in Matlab. Every indentation within the backscatter images was selected manually (Figure 3.11, top left indent) and a ROI of 50 μm squared was drawn around the indentation centre (see Figure 3.12) with an average length along each nanoindentation side of approximately 20 μm. This ROI was then thresholded to remove peaks at both extremes of the GL intensity histogram. The effect of the topographical changes due to nanoindentation on the quantified GL histogram was of interest and consequently investigated. It was hypothesised, due to the inherent lack of topographical information associated with QBEI, that the effect of the nanoindentation would have little effect on the histograms peak GL value. This was found to be true (no statistical difference due to nanoindentation topography, p=0.87). Hence, for simplicity of analysis, ROIs were analysed with the topographical artifacts

included as they were found to have no significant effect on the measured peak GL value.

The peak GL value was then calculated, along with the Full Width at Half Maximum (FWHM) value for the ROI histogram. A normal Gaussian distribution curve, created using the peak height and FWHM of each distribution, was then overlayed on the resulting histogram, for subsequent analysis of histogram skewness and kurtosis (Figure 3.13). This information was saved for subsequent statistical analysis and comparison with corresponding nanoindentation results for each ROI.

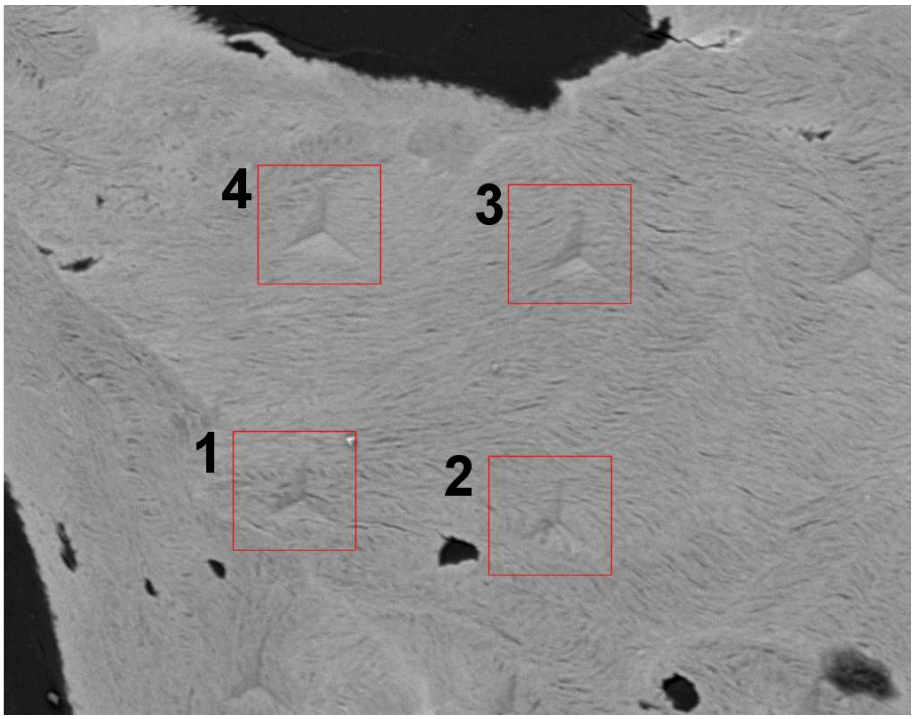

Figure 3.11: Backscatter image of trabecular bone. Nanoindentations are denoted 1 to 4 anti-clockwise from bottom left.

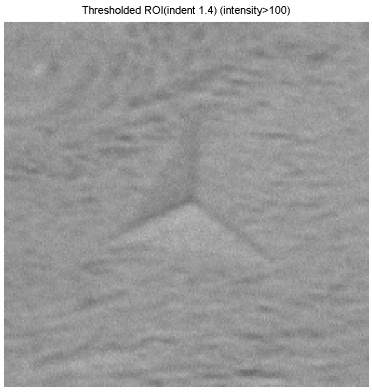

Figure 3.12: Selected ROI around nanoindentation 4 from Figure 3.11.

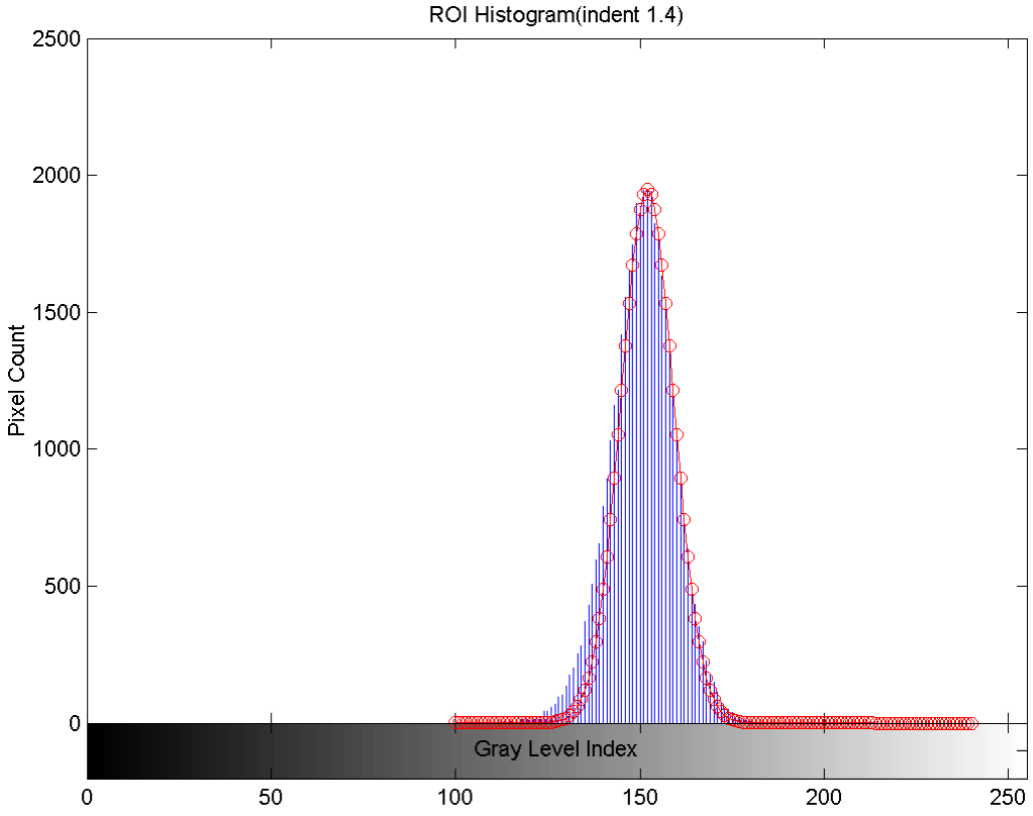

Figure 3.13: Gaussian curve fitted to histogram data from the nanoindentation shown in Figure 3.12.

3.4 Chromatography

Chromatography encompasses a group of empirical methods used to separate extremely small quantities of complex mixtures with very high resolution. Modern chromatography is frequently used for the detection of quantities as small as nanograms of a sample material. The basis for all types of chromatography is the partition of sample compounds between a stationary phase material and a mobile phase which flows over or through the stationary phase in question. Many forms of chromatographic analysis exist and their application is dependent on the molecular state of the specific phase of interest. Examples of these techniques include gas, liquid, thin layer and supercritical fluid chromatography. This study focused on the use of liquid chromatography, specifically high pressure liquid chromatography.

Liquid chromatography is conducted using chromatographic columns. These consist of a column of particulate material, such as silica or alumina. A solvent or mobile phase is passed through at low pressure, facilitating one of two possible methods of separation, (i) adsorption (liquid/solid) or (ii) partition (liquid/liquid). The sample is dissolved within the mobile phase prior to application to the column. Once applied, the mobile phase elutes the sample through the column, allowing components to separate based on adsorption or partition methods. Liquid chromatographic analysis resolution can be significantly improved through the use of smaller column packing particulate material. Higher pressure are required to force the mobile phase through such tightly packed columns, hence the development of high pressure liquid chromatography.

3.4.1 High Pressure Liquid Chromatography

When a material is non-volatile or thermally fragile (such as collagen), high pressure liquid chromatography (HPLC) is particularly applicable. However, choice of sample detection method is more restricted relative to other chromatographic techniques, such as gas chromatography. Detection is limited mostly to spectroscopic methods, which are particularly suitable with regard to this study due to the fact that collagen crosslinks are naturally fluorescent. Traditional chromatography employs a polar stationary phase surface and a non-polar solvent. Reverse-phase chromatography reverses this setup and is particularly suited to large non-volatile biomolecules, such as collagen crosslinks. Due to the non-polar nature of the particulate surface, the chief mechanism of retention is dispersion forces. Highly polar components are eluted the quickest while weakly polar components are retained the longest.

The mobile phase can be altered to manipulate the interactions between the sample and the stationary phase. There are several types of mobile phase compositions but the two of interest throughout this study were isocratic and gradient mobile phases. Isocratic elutions involve the elution of compounds through the use of a constant mobile phase composition. Compounds within the mobile phase begin migration at onset but will migrate at a different rate, resulting in distinct component elution rates. Gradient elution works by increasing the concentration of the mobile phase during the elution run. Using this method, migration rates can be adjusted for either faster or slower elution rates, depending on the specific compound of interest. Resolution can also be improved relative to isocratic methods but at the cost of a more complicated chromatographic protocol. Isocratic elution methods are usually employed in quality control sample runs where a single analyte of interest has been extensively characterised and the sample is being run to confirm its identity and quantity.

As previously mentioned, detection and quantitation methods in HPLC depend on the sample in question. No sensitive, universal detector currently exists. The only universal bulk property HPLC detector is the refractive

index detector which cannot be used in gradient elutions, requires extremely precise temperature control and can be as much as 1000 times less sensitive than sample specific detectors. Due to the inherent nature of collagen crosslinks, which fluoresce naturally, fluorescence detectors are used. Fluorescence detectors are among the most sensitive types of detection method currently available. They work by exciting the fluorescent nature of a sample through the use of light at a specific wavelength and subsequently capturing the emitted fluorescent light at a specific wavelength, distinct from the excitation value. A simple schematic diagram is shown in Figure 3.14, illustrating the most important parameters within a fluorescence detector output used to characterise a typical chromatographic elution. In such an elution, separated components differ from each other only in their residence time in or at the stationary phase, referred to as retention. The total retention time (t_{r_1} or t_{r_2} in Figure 3.14) is the time required by a sample component to migrate from column inlet to column end. The parameters described in Figure 3.14 in the first peak shown are $w_{1/2}$=peak width at half height and w=band width of the peak. Peak symmetry is measured at 10% of the total peak height. These symmetry parameters A and B are a measure of the proportion of the peak on each side of the maximum peak value. t_0=the dead time of a column. t_{R_1} and t_{R_2} are the retention times of components one and two respectively. Consequently, t'_{R_1} and t'_{R_2} are the net retention times of components one and two respectively.

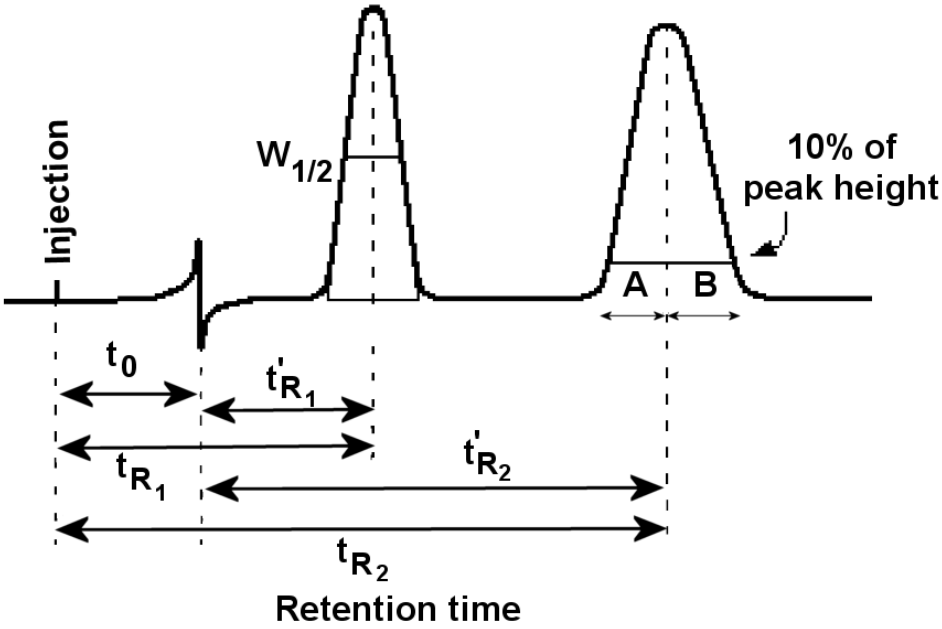

Figure 3.14: Sample chromatogram illustrating the most important parameters used to characterise a separation (Mackery-Nagel Inc)

.

3.4.2 Chromatographic Quantification

The amount of a specific component within a mobile phase is measured as it exits the column and passes through the detector. In modern systems, the detector signal is usually fed into a digital or analogue recorder. From this a plot of signal strength versus time is produced (Figure 3.14). The peak area for an eluting component is proportional to the quantity of material detected. Identification of the compound is based on the retention time of a specific sample peak. Digital processing of the signal facilitates the automatic mathematical integration of the sample peak area. Chromatogram baselines can be set automatically or manually input by the operator. However, absolute quantification of a standard of unknown quantity requires the use of sample standards. The amount of fluorescence detected must be calibrated using a similar substance of known composition and quantity. External or internal

standards may be used, using either peak height or peak area as calibration variables.

External Standard

Multiple standards are run outside the mobile phase. The peak heights or areas are plotted versus the quantities or concentrations of the standards used. A major source of error using this method is the reproducibility of the standard injection used, particularly if injections are made manually.

Internal Standard

Sample standards are run within the mobile phase. The internal standard is added to the sample prior to analysis. The standard compound must be sufficiently similar to the elution component of interest but must not overlap on the chromatogram. The standard must be readily separated from any sample compounds run. This method of calibration removes the possibility of quantification error due to inherent changes in the injected volume.

3.4.3 Setup

The method employed to quantify mature bone collagen crosslinks was a simplified form of that reported in a study conducted in 1997 and subsequently in 1998 [114, 115]. Briefly, the HPLC assay was developed for both pyridinium and pentosidine crosslinks in mature collagen from a variety of connective tissue crude hydrolysates. The original method reported in the above mentioned articles involved a simple two step isocratic assay using a reverse phase column. The simplification employed throughout the course of this present work involved the removal of the second step which is exclusively concerned with age-related pentosidine crosslinks.

Sample Preparation

Healthy bovine bone tissue samples (20mg) were used throughout the preliminary investigation stage. Each sample was hydrolysed in an oven using 800 μl of 6M HCL for twenty hours in 5ml glass vials with PTFE-lined screw caps. The oven temperature was set at 110^0C. After hydrolysation, samples were transferred to 5ml eppendorf tubes and dried using a speed vac SC110. After drying was completed, dehydrated samples were dissolved in 50 μl of distilled water for every mg of mineralised tissue hydrolysed. At this point, the internal standard was added to the sample solution at a concentration of 10 nmol/ml. The internal standard used throughout was pyridoxine or vitamin B_6.

The final preparation stage involved the dilution of the sample solution five-fold in a solution of 0.5%(v/v) Heptafluorobutyric acid (HFBA) in 10%(v/v) acetonitrile. From this diluted sample, 50 μl was injected into the HPLC system. This resulted in 200 μg of mineralised tissue applied to the column along with 100pmol pyridoxine in every run.

3.4.4 Chromatographic Run

The chromatographic runs were completed using an Alltech column. (Prior to each run, the column was washed with 0.1%(v/v) HFBA in 75%(v/v) acetonitrile for ten minutes and subsequently equibrilated with 0.15%(v/v) HFBA in 24%(v/v) methanol. Elution of the sample and internal standard was conducted at ambient temperature at a flowrate of 1ml/min in one isocratic step: time 0-17 min 0.15%(v/v) HFBA in 24%(v/v) methanol. Fluorescence was monitored using a programmable fluorometer at an excitation wavelength of 295 nm and an emission wavelength of 400 nm.

3.4.5 Results

Results from this Section of the study were inconclusive. Reservations regarding the stability of the apparatus were of major concern. Initial preliminary chromatographic runs containing only the internal standard in identical concentration to that outlined in the protocol were unrepeatable. Approximately fifty to one hundred attempts, under the direct supervision of a resident biochemist, were conducted over a number of months to no avail. After exhaustive testing, it appeared to be an unresolvable apparatus problem. Misalignment of the fluorescence detector was suspected and calibration was not conducted within a time frame that would have allowed completion of this Section of the project.

3.5 Statistical Analysis

All statistical analysis was carried out using Matlab. Each of the main variables of interest, namely Young's modulus, hardness and mineralisation level were assessed using three-factor Analysis of Variance (3-way ANOVA) at each of the four predetermined depths of interest, namely 1, 2, 3 and 4 μm below the sample surface. These depths were chosen in order to correspond with the depth-specific mineralisation analysis using QBEI. The three factors of interest were disease (healthy or OA), site (medial or lateral) and gender (male and female). Based on the outcome of this analysis and the presence of factor interactions, the effect of the primary factor, disease, was investigated as a function of the secondary factors (gender and site) and the results are detailed in the following Chapter. All analyses and comparisons conducted were repeated for each of the four depths of interest below the sample surface. Specifically, significant differences in individual sample groups' mechanical variables and composition due to the presence of OA were investigated (i.e. effect of pathology on medial, lateral, male and female properties). This highlighted any specific differences in the effect of the pathology on different samples sites and genders.

The effect of the disease on the relationship between modulus and hardness was also investigated for all groups, in order to investigate the possibility of an altered elastic-plastic relationship in the tissue as a result of the onset of the disease. Mineralisation changes due to presence of the pathology were also investigated. All comparisons were conducted using Analysis of Variance (ANOVA) techniques. One, two or three-way ANOVA was performed where necessary and corresponding p values accompany all the aforementioned comparisons.

Chapter 4

Results

4.1 Population Analysis

Initial statistical analysis of the complete data set was required for data comparison purposes throughout the assessment of experimental results. Three-factor ANOVA was used to determine the presence and magnitude of dependent effects between the three factors of interest, namely disease, gender and site. Disease was the primary factor of interest. Three-factor analysis was conducted for all three experimentally assessed properties. Table 4.1 presents the samples numbers by factor. Tables 4.2, 4.3 and 4.4 present the ANOVA data, specifically the p values indicating the presence, or lack thereof, of statistically significant factor interactions.

		Male	Female	Total
Medial	**Healthy**	n=2	n=2	n=4
	OA	n=5	n=2	n=7
Lateral	**Healthy**	n=4	n=2	n=6
	OA	n=1	n=4	n=5

Table 4.1: Total samples numbers divided by factor.

Source: Stiffness	p value
Disease	0.6938
Gender	0.5081
Site	0.0645
Disease*Gender	0.3073
Disease*Site	0.0086
Gender*Site	0.0001
Disease*Gender*Site	< 0.0001

Table 4.2: Three-factor ANOVA of nanoindentation stiffness data. * indicates factor interaction.

Source: Hardness	p value
Disease	0.8258
Gender	0.4774
Site	0.5225
Disease*Gender	0.0597
Disease*Site	0.6849
Gender*Site	< 0.0001
Disease*Gender*Site	0.0003

Table 4.3: Three-factor ANOVA of nanoindentation hardness data. * indicates factor interaction.

Source: Mineralisation	p value
Disease	< 0.0001
Gender	< 0.0001
Site	0.956
Disease*Gender	< 0.0001
Disease*Site	< 0.0001
Gender*Site	< 0.0001
Disease*Gender*Site	0.035

Table 4.4: Three-factor ANOVA of QBEI mineralisation data. * indicates factor interaction.

The average material stiffness measured by nanoindentation in either healthy or diseased samples was not found to be significantly affected by gender (p=0.31) but was significantly affected by site (p=0.009). Hardness results were not significantly affected by either gender (p=0.06) or site (p=0.68) while mineralisation data were found to be significantly affected by both gender (p<0.0001) and site (p<0.0001). These statistical results influence the presentation of results throughout this Chapter. Stiffness measurements of male and female samples can be combined but medial and lateral sample sites must be considered separately. Hardness values were independent of gender or site while mineralisation results must be split into gender and site specific groups when describing the effect of the disease. Mineralisation density levels were found to be dependent on both gender and site and were analysed accordingly. However, further analysis revealed that this was due to an artefact present in the results found at an examination depth of 1 μm deep. Results recorded at the remaining examination depths (2, 3 and 4 μm depth) showed no mineralisation density dependance on gender, a result found previously in healthy tissue [96]. Consequently, for the purpose of simplicity, gender specific mineralisation density results are not included in the main body of the thesis. Mineralisation results were considered only based on disease and site, as was the case with tissue stiffness analysis. However, gender specific results are included in an attached appendix Section.

It should also be noted that the measurements described within this Chapter represent average mechanical or compositional properties of the examined tissue up to the specified depth, including all material from the surface down to the specified depth of indentation. The results describe relative changes in the material's stiffness and mineralisation as a function of indentation depth. They do not represent mechanical strength of the two-dimensional plane at the stated depth of indentation. All tissue material up to and including that at the depth of indentation contribute to the overall measurement at the point of maximum indentation depth. The overall effect of this consideration on the reported results is to underestimate any observed

relative changes in tissue properties between successive examination depths. Hence the depth-specific results reported are a conservative measure of relative tissue property changes between successive examination depths as a function of increasing depth below the trabeculae indentation surface.

A final consideration, previously described in detail in Chapter 3, Section 3.1.1, is reiterated regarding the effect of the difference in medial and lateral sample symptoms. All tissue samples taken from the medial sides of sample tibiae presented clinically-defined macroscopic damage to the overlying cartilaginous tissue, while the lateral samples did not.

4.2 Mechanical Assessment

The following subsections within Section 4.2 describe the elastic stiffness and hardness results of nanoindentations performed on both the healthy and early-stage OA bone samples described in Chapter 3. Each subsection presents the data resulting from the continuous stiffness measurement (CSM) analysis of nanoindentations performed at specific depths of interest which correspond to mineralisation measurements assessed at the same backscatter electron penetration depth. These results describe how the material's mechanical properties change due to the pathology in both medial and lateral sites. Only site specific results are presented within the stiffness results. No gender specific results are included in the stiffness results due to the lack of a statistically significant (p>0.05) disease-gender interaction. Three-factor ANOVA analyses performed on the sample population only returned significant factor interaction between incidence of the disease and sample site. The results of this analysis can be seen in table 4.2.

4.2.1 1 μm Indentation Depth

Medial Stiffness

The results illustrated in Figure 4.1 represent the effect of the clinically-defined, early-stage pathology on medial tissue samples up to 1 μm below the sample surface. A significant decrease in trabecular subchondral bone tissue was seen in early-stage OA samples. In relative terms, presence of the disease results in an average drop in tissue stiffness of approximately 4% relative to healthy controls.

Lateral Stiffness

The change observed in the average localised tissue stiffness value in the non-presenting lateral samples at an indentation depth of 1 μm was opposite in direction but similar in magnitude to the medial samples at a similar depth. Presence of early-stage OA in trabecular subchondral sample resulted in a significant increase in tissue stiffness. The magnitude of this increase represented an increase above average healthy sample values of approximately 3%. This change is shown in Figure 4.2.

	Healthy	**OA**	**p**
Medial E [GPa]	17.54±0.53	16.79±0.35	**p**<0.05
Lateral E [GPa]	16.53±0.24	17.08±0.43	**p**<0.05
H [GPa]	0.6704±0.011	0.6599±0.014	**p**=0.826

Table 4.5: Healthy versus OA medial result summary (1 μm).

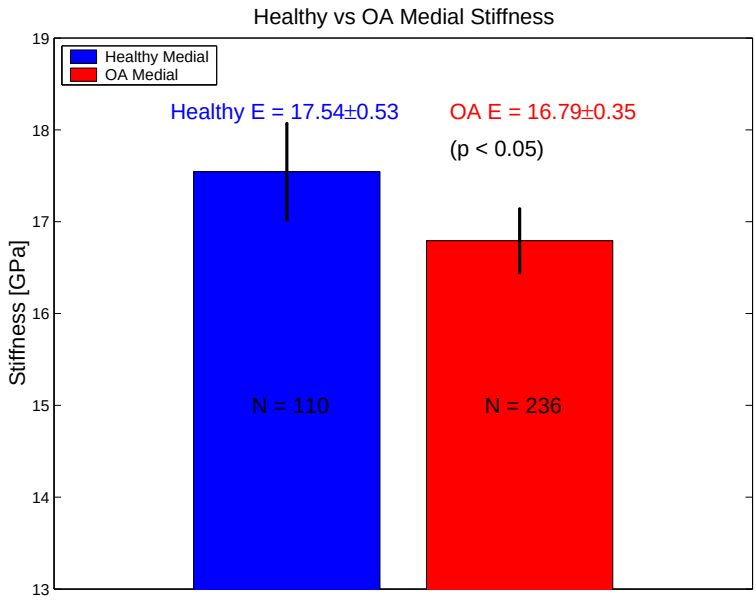

Figure 4.1: Healthy versus OA medial average sample stiffness with 95% confidence intervals (1 μm).

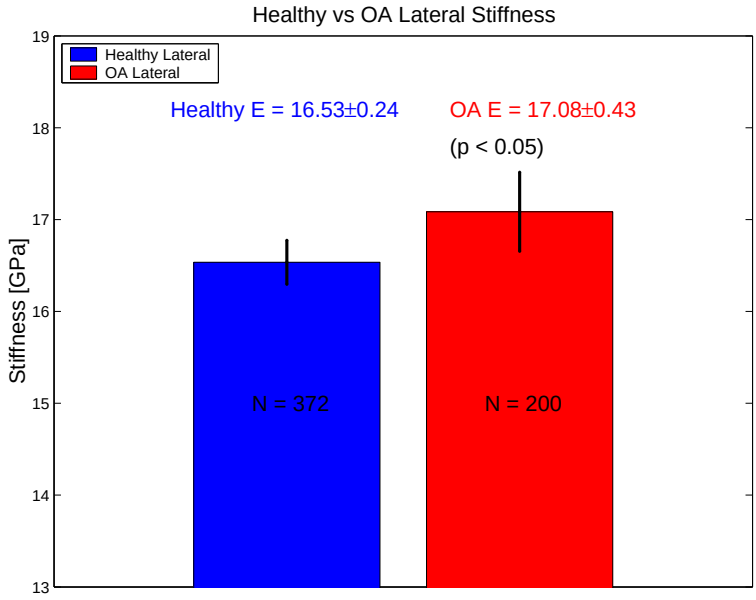

Figure 4.2: Healthy versus OA lateral sample stiffness with 95% confidence intervals (1 μm).

Hardness

The average tissue hardness of diseased trabecular samples were assessed at this depth and were altered relative to their healthy counterparts. The average magnitude of this decrease in tissue hardness due to OA was approximately 10.5 MPa, corresponding to a percentage decrease relative to healthy controls of 1.6%. However, this decrease was not statistically significant, as would be expected based on such a small drop in average hardness value. This is illustrated graphically in Figure 4.3. However, no difference in response was seen between site or gender. Average hardness values were decreased in OA samples relative to healthy controls.

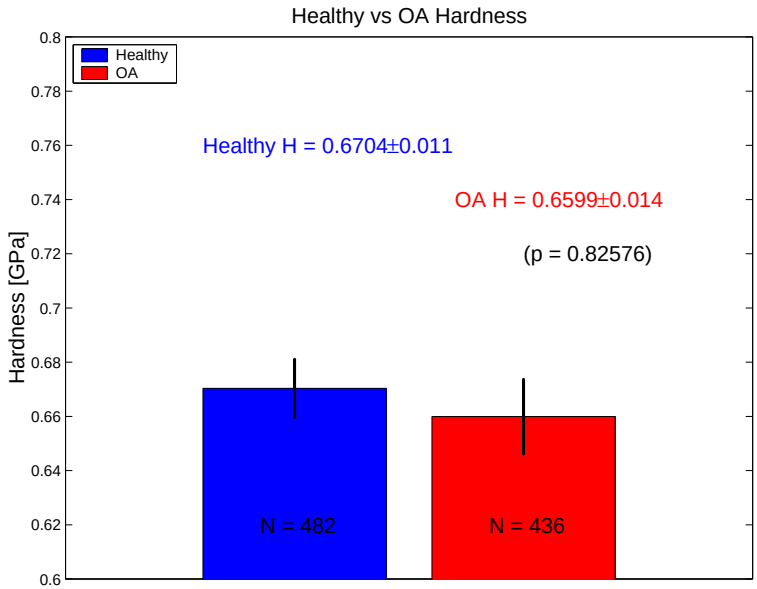

Figure 4.3: Healthy versus OA sample hardness with 95% confidence intervals (1 μm).

Medial E/H Relationship

The relationship between the measured localised stiffness and hardness was examined as a function of disease (Healthy or OA). This ratio is often used to capture changes in the ratio of elastic and plastic deformation. Corresponding stiffness and hardness results from both healthy and OA tissue were plotted and linear regressions were determined. Altered elastic/plastic response was defined as a statistically significant difference in either the slope of the regression line or elevation of the linear regression trend lines y intercepts. Figure 4.4 shows the scatter plot of stiffness versus corresponding hardness data for healthy and OA medial samples. A decrease in the OA sample trend line slope was seen (Figure 4.5) but was not statistically significant (p>0.05). The y intercept difference between the OA trend line and corresponding healthy regression was also non-significant.

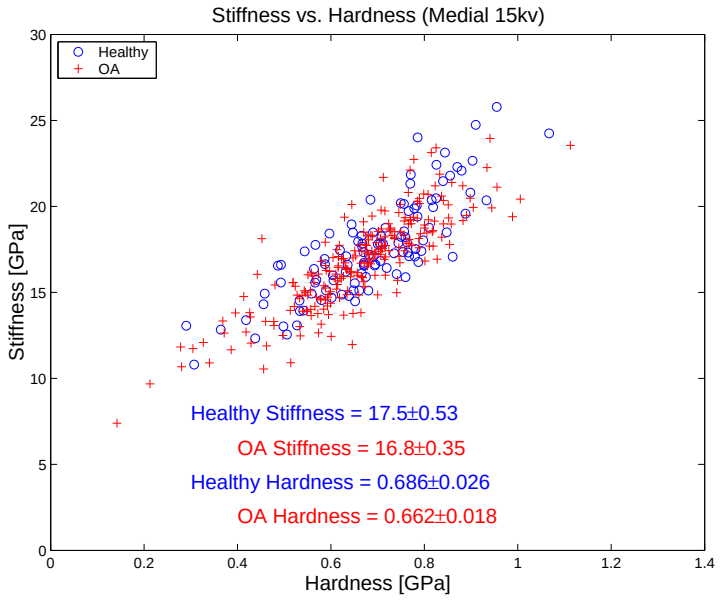

Figure 4.4: Scatter plot of stiffness versus hardness in medial samples (1 μm).

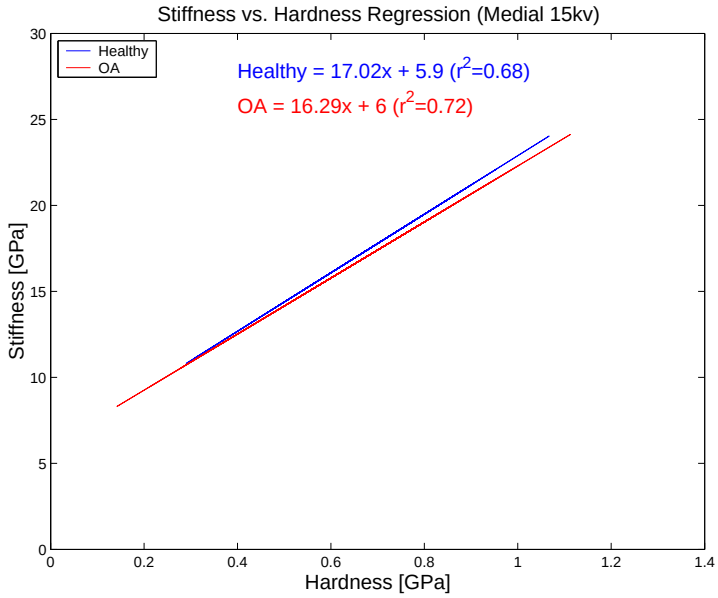

Figure 4.5: Linear regression of stiffness versus hardness in medial samples (1 μm).

Lateral E/H Relationship

The relationship between the tissue stiffness and corresponding tissue hardness was also investigated in healthy and OA lateral samples. A similar result to the medial samples was found. An increase (as opposed to the decrease seen in medial samples) was observed in the slope of the OA sample trend line but was not significantly different to the corresponding healthy regression line (p>0.05). No statistically significant difference was seen in the trend line y intercept elevation relative to the healthy y intercept value. Hence, the relationship between the two was not significantly altered by the presence of the disease. These results can be seen in Figures 4.6 and 4.7.

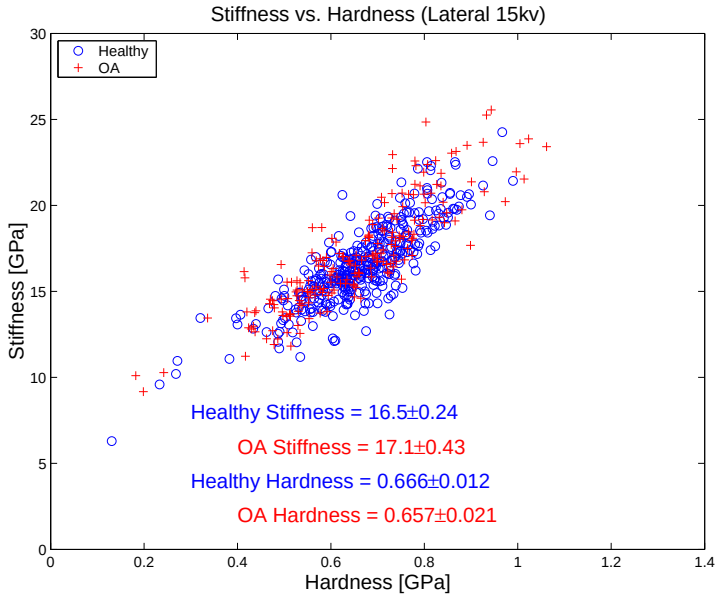

Figure 4.6: Scatter plot of stiffness versus hardness in lateral samples (1 μm).

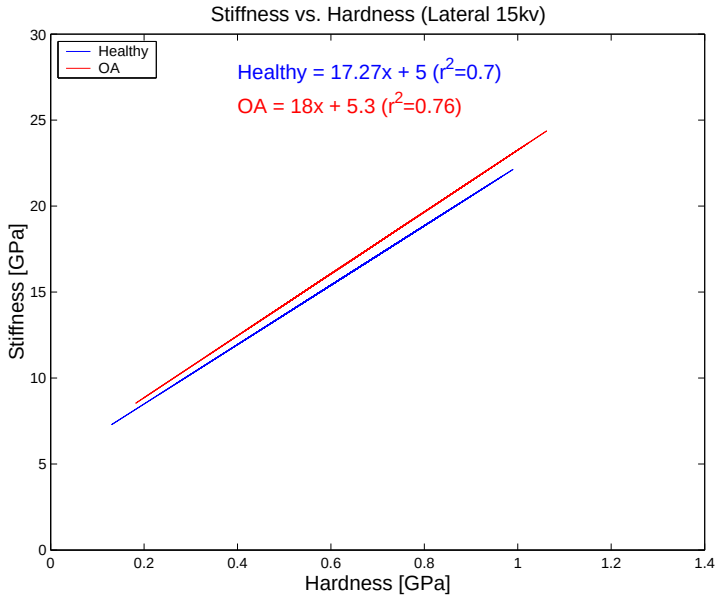

Figure 4.7: Linear regression of stiffness versus hardness in lateral samples (1 μm).

4.2.2 2 μm Indentation Depth

Medial Stiffness

The results illustrated in Figure 4.8 represent the effect of the clinically-defined, early-stage pathology on medial tissue samples at an indentation depth of 2 μm below the sample surface. A significant decrease in trabecular subchondral bone tissue was seen in early-stage OA samples, as previously observed at a depth of 1 μm. In relative terms, the disease results in an slightly greater average percentage drop in tissue stiffness in comparison with the medial results at the previous examination depth, approximately 5% relative to healthy controls.

Lateral Stiffness

Changes observed in the localised tissue stiffness values of non-presenting lateral samples at the 2 μm depth were similar in magnitude but opposite in direction to those seen in the medial samples, as was the case at an indentation depth of 1 μm. Presence of early-stage OA in trabecular subchondral samples resulted in a significant increase in tissue stiffness. The magnitude of this increase represented an increase above average healthy sample values of approximately 5.5%. This change is shown in Figure 4.9 and was increased relative to the recorded decrease in lateral samples at the previous examination depth.

	Healthy	**OA**	**p**
Medial E [GPa]	16.99±0.46	16.1±0.3	**p**<0.05
Lateral E [GPa]	15.9±0.23	16.78±0.38	**p**<0.05
H [GPa]	0.6854±0.009	0.672±0.012	**p**=0.822

Table 4.6: Healthy versus OA result summary (2 μm).

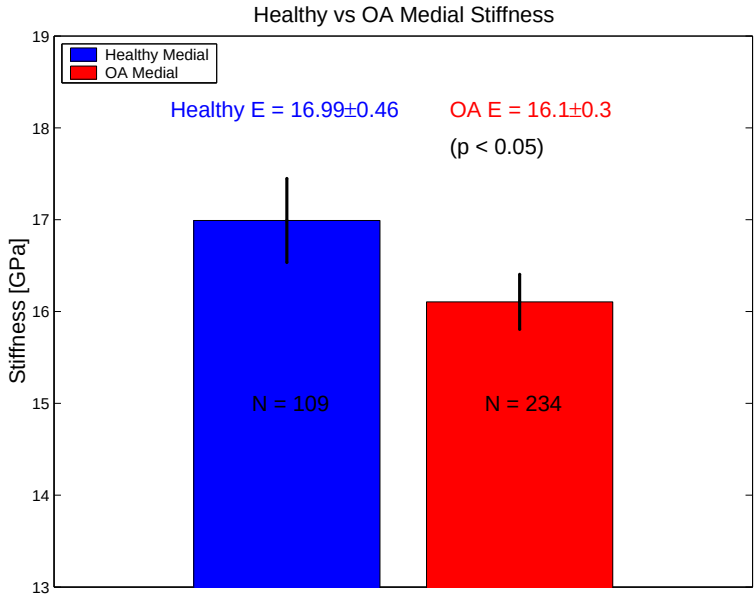

Figure 4.8: Healthy versus OA medial sample stiffness with 95% confidence intervals (2 μm).

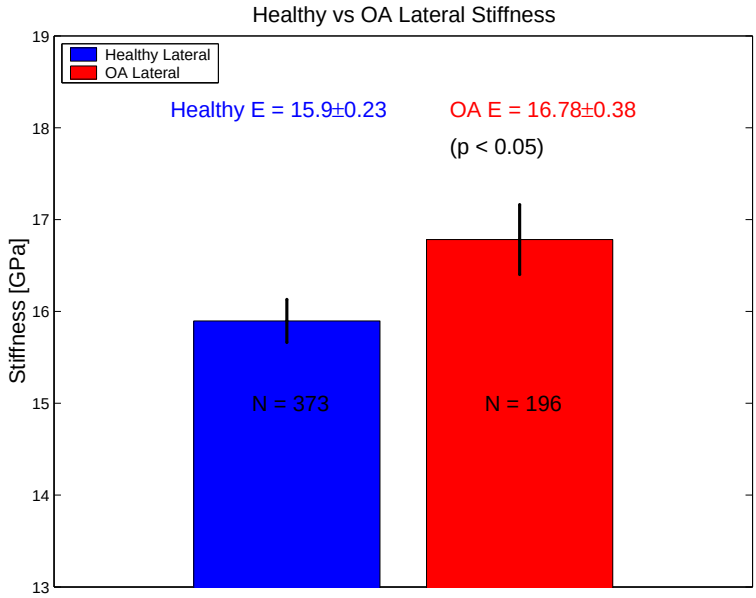

Figure 4.9: Healthy versus OA lateral sample stiffness with 95% confidence intervals (2 μm).

Hardness

The average hardness value was decreased in OA samples relative to healthy controls. However, this decrease was not statistically significant, as was the case at the 1 μm indentation depth. The average measured decrease in tissue hardness due to OA was approximately 13.4 MPa, corresponding to a percentage decrease relative to healthy controls of 2%. This is illustrated graphically in Figure 4.10.

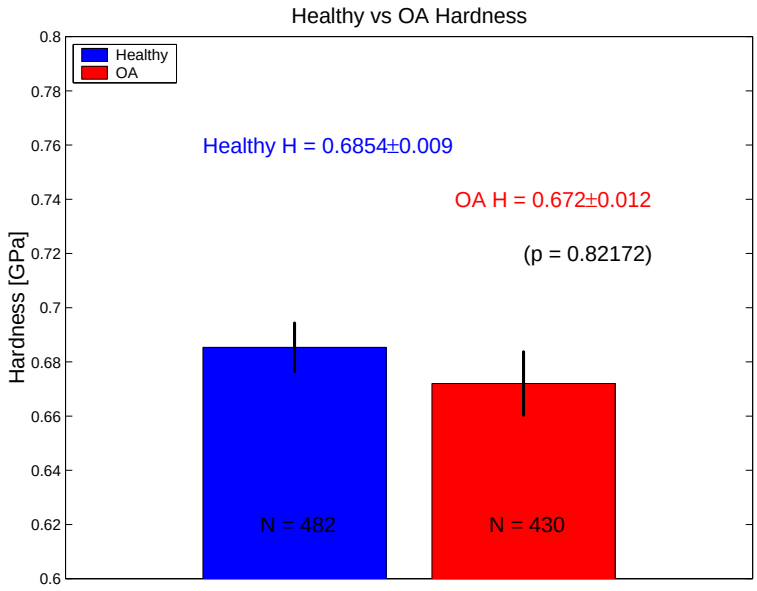

Figure 4.10: Healthy versus OA sample hardness with 95% confidence intervals (2 μm).

Medial E/H Relationship

Figure 4.11 shows the scatter plot of stiffness versus corresponding hardness data for healthy and OA medial samples. An increase in the OA sample trend line slope relative to the healthy trend line was seen, as opposed to the decrease seen at an indentation depth of 1 μm, but was not statistically significant. The decreased y intercept value of the OA trend line was also non-significantly different to the corresponding healthy trend line (p>0.05). These results can be seen in Figure 4.12.

Lateral E/H Relationship

The relationship between the tissue stiffness and corresponding tissue hardness was investigated in healthy and OA lateral samples. A similar result to the medial E/H relationship at 2 μm was found. An increase was observed in the slope of the OA sample trend line relative to its corresponding healthy lateral trend line but was not statistically significant (p>0.05). No statistically significant difference was seen in the trend line y intercept elevation value either (p>0.05). Once again, the relationship between the two was not significantly altered by the presence of the disease, resulting in an unaffected elastic/plastic deformation response in early stage OA. These results can be seen in Figures 4.13 and 4.14.

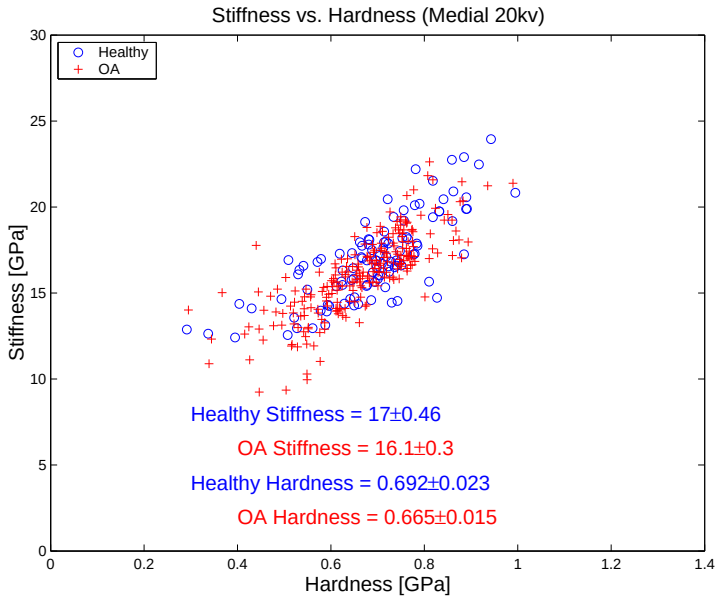

Figure 4.11: Scatter plot of stiffness versus hardness in medial samples. (2 μm).

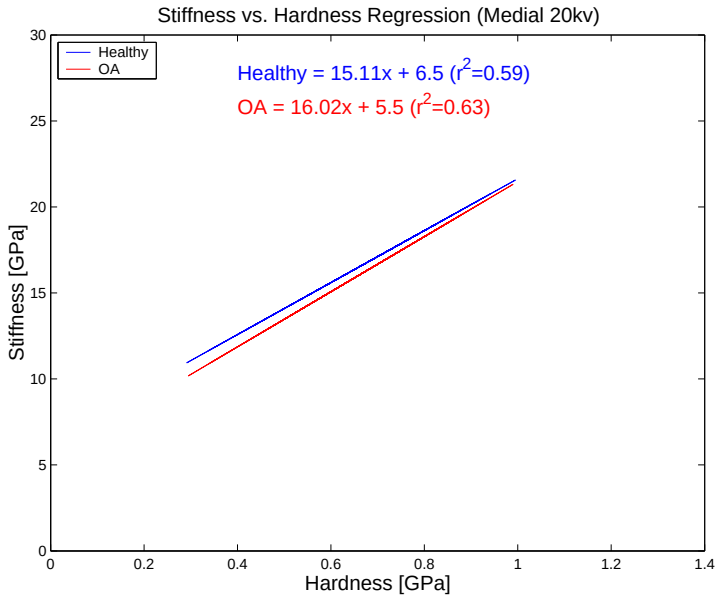

Figure 4.12: Linear regression of stiffness versus hardness in medial samples. (2 μm).

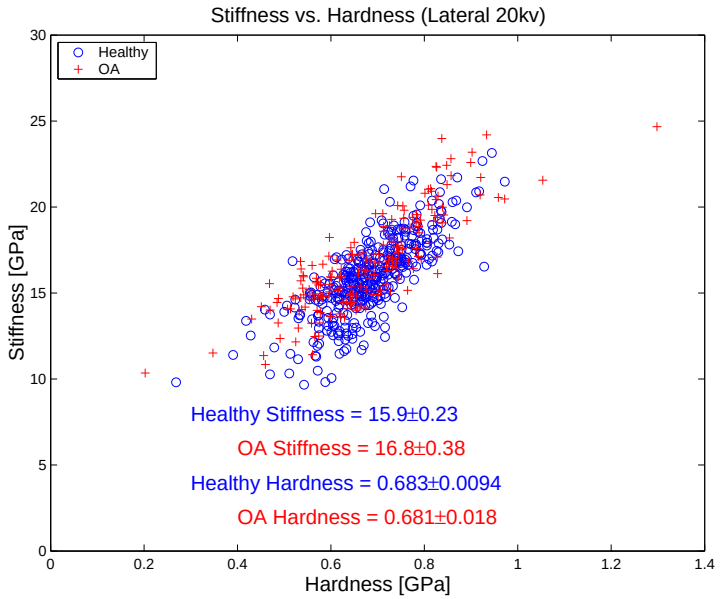

Figure 4.13: Scatter plot of stiffness versus hardness in lateral samples. (2 μm).

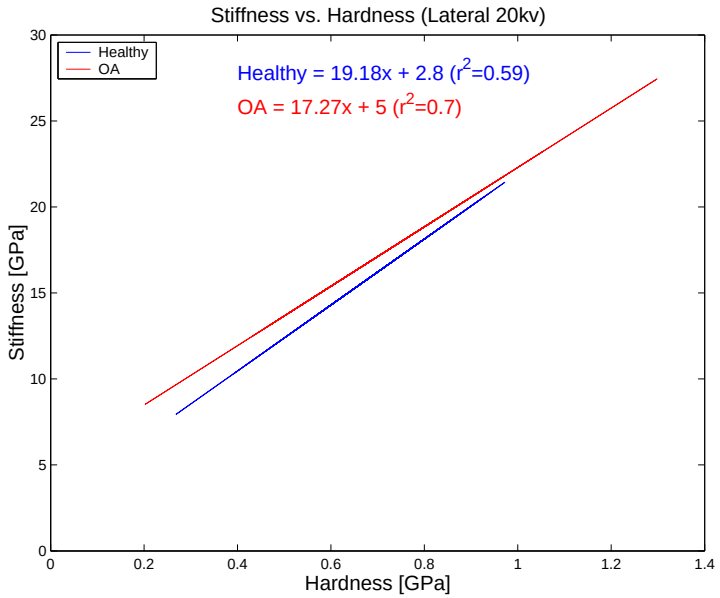

Figure 4.14: Linear regression of stiffness versus hardness in lateral samples. (2 μm).

4.2.3 3 μm Indentation Depth

Medial Stiffness

The results illustrated in Figure 4.15 represent the effect of the clinically-defined, early-stage pathology on medial tissue samples at an indentation depth of 3 μm. A significant decrease in trabecular subchondral bone tissue was again seen in early-stage OA samples ($p<0.05$), as seen previously in medial tissue samples at examination depths of 1 and 2 μm. In relative terms, the disease results in an average drop in tissue stiffness of a slightly larger magnitude than before, 7% relative to healthy controls.

Lateral Stiffness

Changes observed in the localised tissue stiffness values of non-presenting lateral samples were opposite in direction but similar in magnitude relative to medial samples at 3 μm, as was also the case at indentation depths of 1 μm and 2 μm. Presence of early-stage OA in lateral trabecular subchondral samples at 3 μm resulted in a significant increase in tissue stiffness. The magnitude of this increase represented an increase above average healthy sample values of approximately 7.5%. This change is shown in Figure 4.16.

	Healthy	OA	p
Medial E [GPa]	16.4±0.42	15.46±0.29	**p**<0.05
Lateral E [GPa]	15.23±0.25	16.2±0.36	**p**<0.05
H [GPa]	0.6818±0.008	0.671±0.011	**p**=0.604

Table 4.7: Healthy versus OA result summary (3 μm).

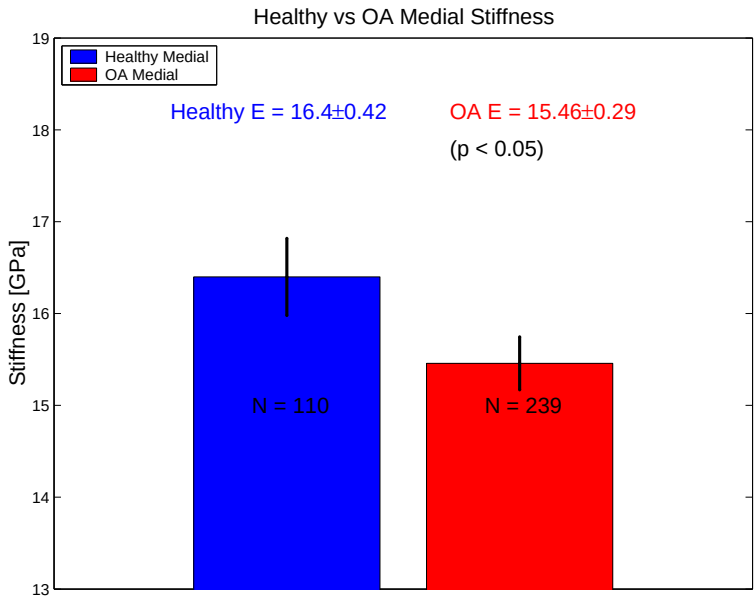

Figure 4.15: Healthy versus OA medial sample stiffness with 95% confidence intervals (3 μm).

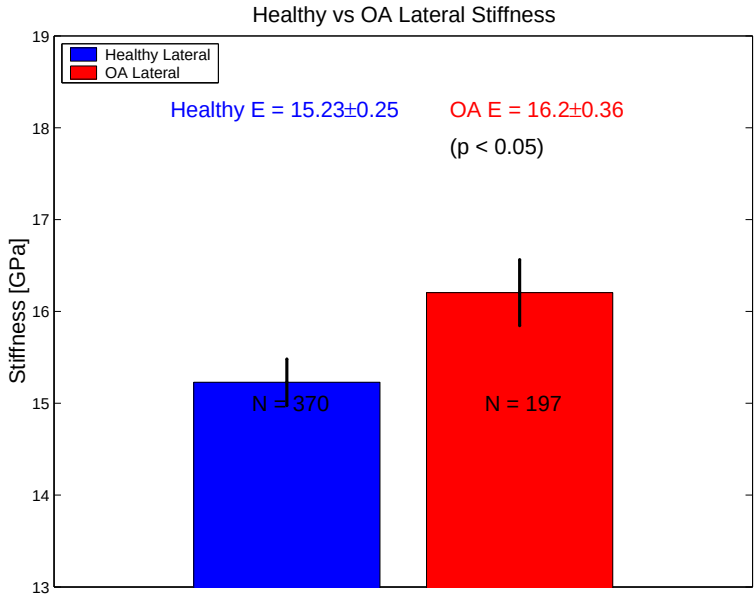

Figure 4.16: Healthy versus OA lateral sample stiffness with 95% confidence intervals (3 μm).

Hardness

The average hardness value was decreased in OA samples relative to healthy controls as before. However, this decrease was not statistically significant, as was the case at the 1 μm and 2 μm indentation depths. The average measured decrease in tissue hardness due to OA was approximately 13.4 MPa, corresponding to a percentage decrease relative to healthy controls of 2%. This is illustrated graphically in Figure 4.17.

Medial E/H Relationship

Figure 4.18 shows the scatter plot of stiffness versus corresponding hardness data for healthy and OA medial samples at 3 μm below the sample surface. An increase in the OA sample trend line slope over the healthy regression slope was seen, shown in Figure 4.19, but was not statistically significant. The y intercept elevation difference of the OA trend line was also non-significant when compared with its corresponding healthy trend line.

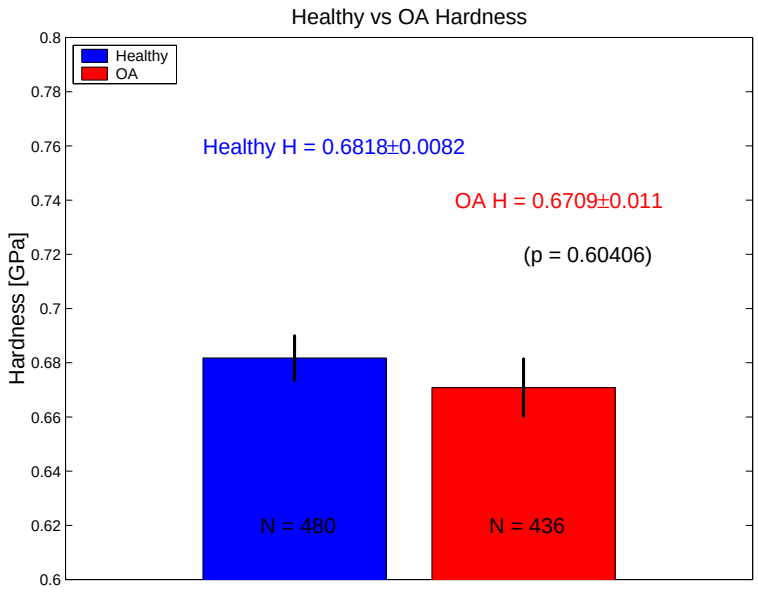

Figure 4.17: Healthy versus OA sample hardness with 95% confidence intervals (3 μm).

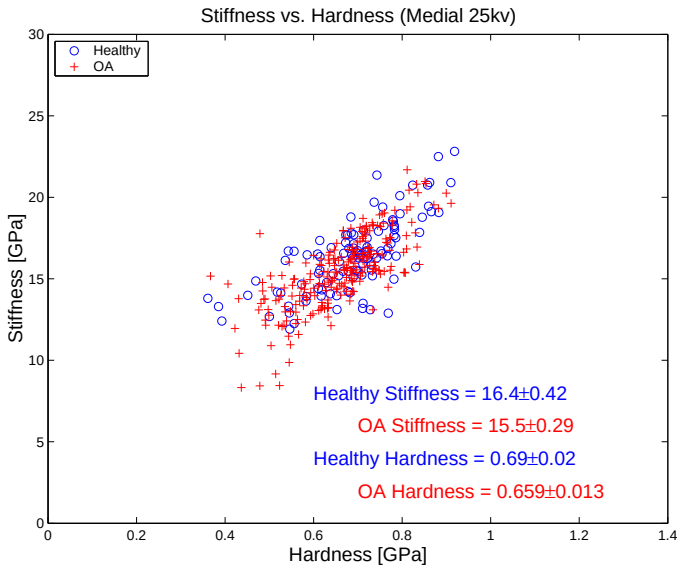

Figure 4.18: Scatter plot of stiffness versus hardness in medial samples. (3 μm).

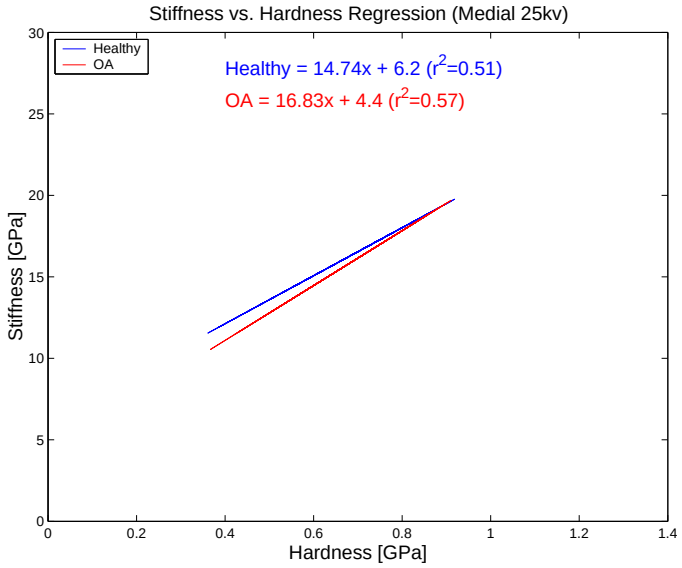

Figure 4.19: Linear regression of stiffness versus hardness in medial samples. (3 μm).

Lateral E/H Relationship

The relationship between the tissue stiffness and corresponding tissue hardness was investigated in healthy and OA lateral samples. A similar result to the medial samples was found. An increase (as opposed to the decrease seen in medial samples) was observed in the slope of the OA sample trend line relative to the slope of the healthy trend line but was not statistically significant. No statistically significant difference was seen in the trend line elevation either. Once again, the relationship between the two was not significantly altered by the presence of the disease. These results can be seen in Figures 4.20 and 4.21.

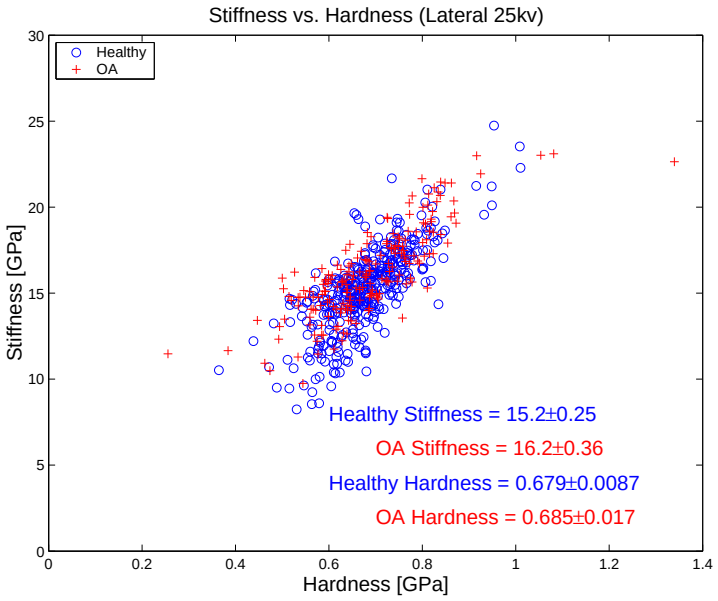

Figure 4.20: Scatter plot of stiffness versus hardness in lateral samples. (3 μm).

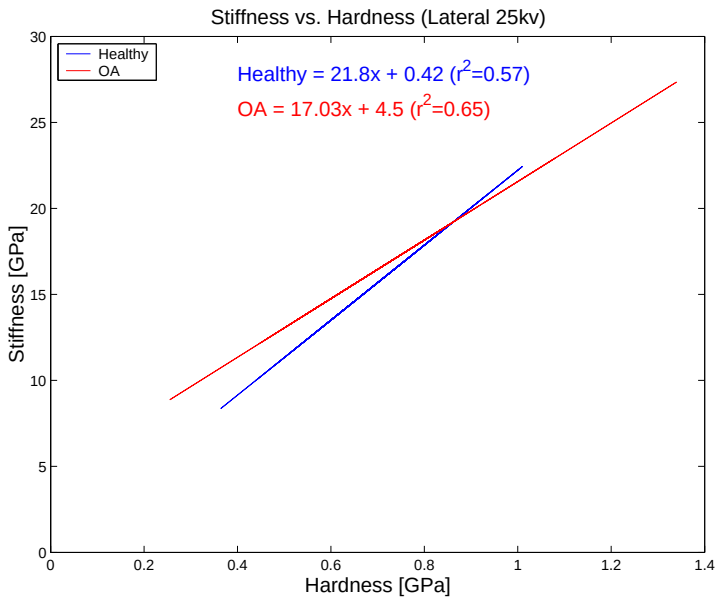

Figure 4.21: Linear regression of stiffness versus hardness in lateral samples. (3 μm).

4.2.4 4 μm Indentation Depth

Medial Stiffness

The results illustrated in Figure 4.22 represent the effect of the clinically-defined early-stage pathology on medial tissue samples at an indentation depth of 4 μm. A significant decrease in trabecular subchondral bone tissue stiffness was seen again in pathological samples ($p<0.05$), also seen at depths of 1 μm, 2 μm and 3 μm. In relative terms, the disease results in an average drop in tissue stiffness of similar magnitude to the drop seen at an indentation depth of 3 μm, approximately 7% relative to healthy controls.

Lateral Stiffness

Changes observed in the localised tissue stiffness values of lateral samples were opposite in direction but similar in magnitude relative to medial samples at this depth. This trend was seen at all previous indentation depths.

The presence of early-stage OA in trabecular subchondral sample resulted in a significant increase in tissue stiffness ($p<0.05$). The magnitude of this increase represented an increase above average healthy sample values of approximately 7.4%, identical to the change seen at the previous indentation depth of 3 μm. This result is shown in Figure 4.23.

	Healthy	OA	p
Medial E [GPa]	15.84±0.43	14.81±0.29	**p**<0.05
Lateral E [GPa]	14.6±0.26	15.68±0.37	**p**<0.05
H [GPa]	0.675±0.008	0.667±0.01	**p**=0.453

Table 4.8: Healthy versus OA result summary (4 μm).

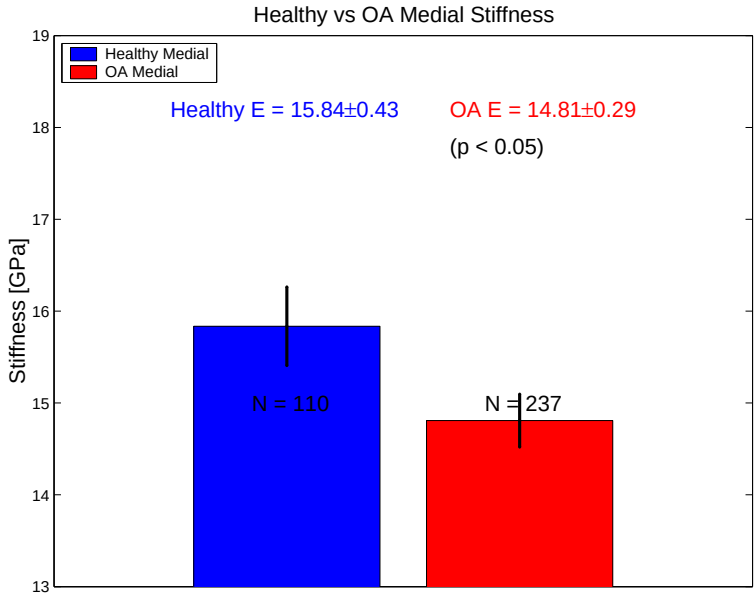

Figure 4.22: Healthy versus OA medial sample stiffness with 95% confidence intervals (4 μm).

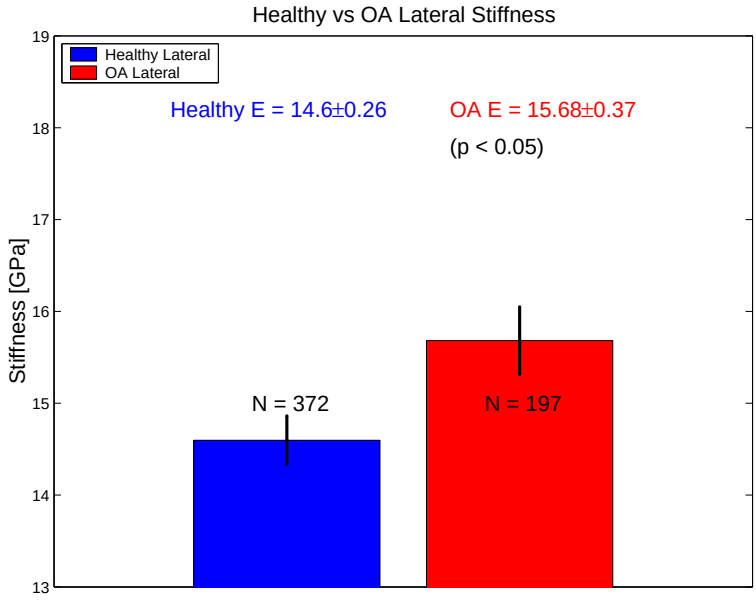

Figure 4.23: Healthy versus OA lateral sample stiffness with 95% confidence intervals (4 μm).

Hardness

The average hardness value was decreased in OA samples relative to healthy controls, as before. However, this decrease was not statistically significant, as was the case at the 1 μm, 2 μm and 3 μm indentation depths. The average measured decrease in tissue hardness due to OA was approximately 8.3 MPa, corresponding to a percentage decrease relative to healthy controls of 1%. This is illustrated graphically in Figure 4.24.

Medial E/H Relationship

Figure 4.25 shows the scatter plot of stiffness versus corresponding hardness data for healthy and OA medial samples at 4 μm below the surface. An increase in the OA sample trend line slope relative to the healthy medial regression was seen but was not statistically significant. The elevation decrease of the OA trend line was also non-significant (Figure 4.26).

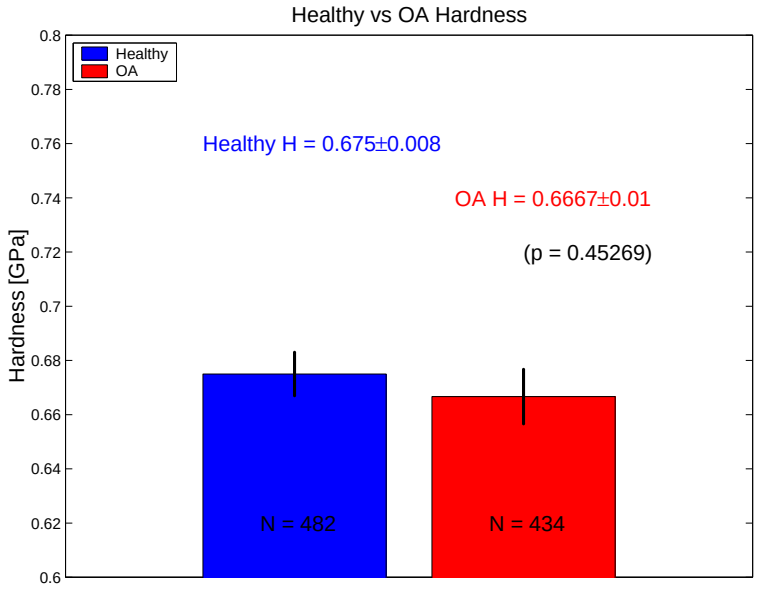

Figure 4.24: Healthy versus OA sample hardness with 95% confidence intervals (4 μm).

Lateral E/H Relationship

The relationship between the tissue stiffness and corresponding tissue hardness was investigated in healthy and OA lateral samples. A similar result to the medial samples was found. An increase was observed in the slope of the OA sample trend line relative to the healthy trend line but was not statistically significant. No statistically significant difference was seen in the trend line elevation either. Once again, the relationship between the two was not significantly altered by the presence of the disease. These results can be seen in Figures 4.27 and 4.28.

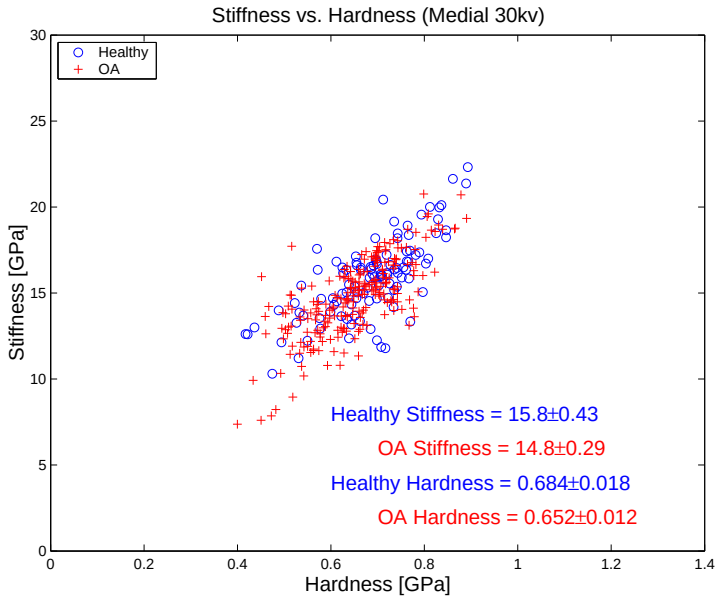

Figure 4.25: Scatter plot of stiffness versus hardness in medial samples. (4 μm).

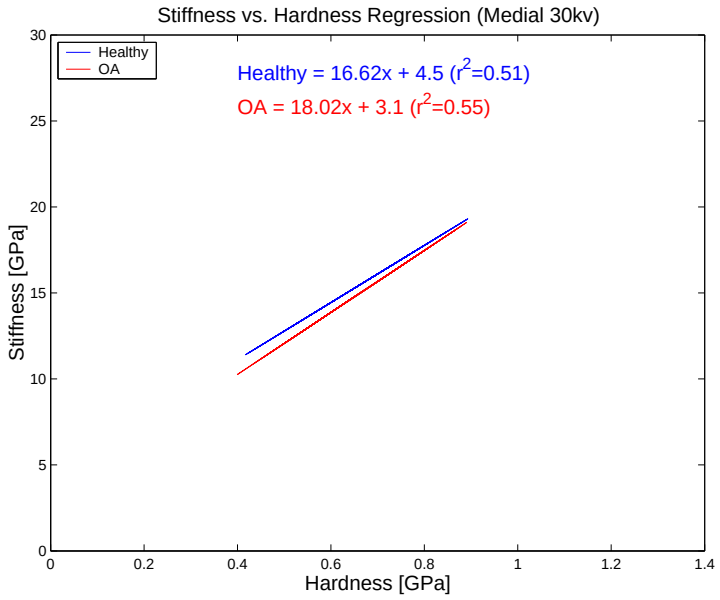

Figure 4.26: Linear regression of stiffness versus hardness in medial samples. (4 μm).

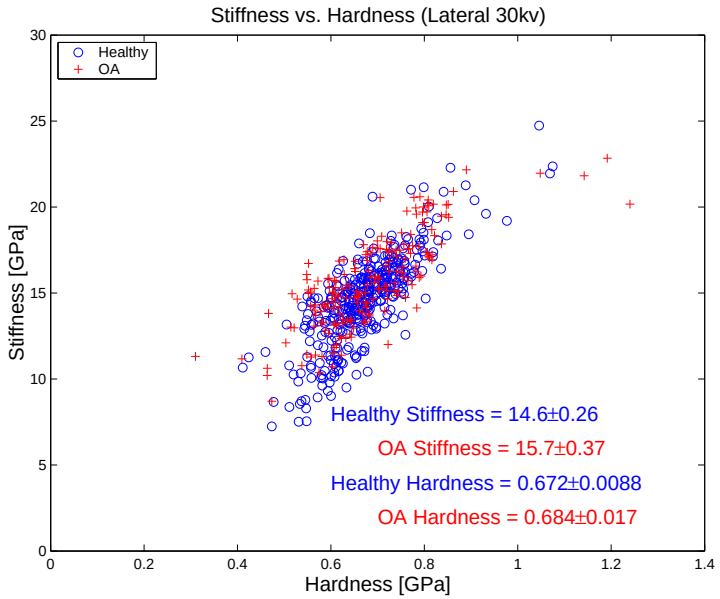

Figure 4.27: Scatter plot of stiffness versus hardness in lateral samples. (4 μm).

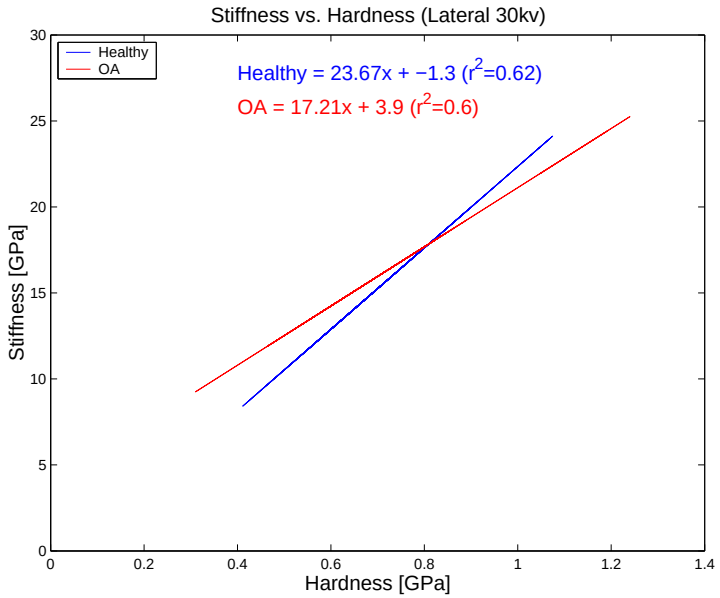

Figure 4.28: Linear regression of stiffness versus hardness in lateral samples. (4 μm).

4.2.5 Depth-Specific Behaviour

Stiffness

By combining all mechanical property data acquired throughout the experimental stage, a number of interesting depth-related trends were observed. Localised tissue stiffness was seen to decrease as a function of increasing indentation depth. This decrease was seen in both healthy and OA samples, as well as in both medial and lateral sample sites (Figures 4.30 and 4.31). The decreases observed became statistically significant ($p<0.05$) between indentation depths separated by as little as between 1 μm and 2 μm. Presence of the disease did not appear to significantly alter the relationship between stiffness and indentation depth. However, presence of the disease did result in a statistically significant change in localised tissue stiffness at all depths and sites examined.

The exact nature of these changes differed between sites. Medial samples, where cartilage damage was indicative of early-stage OA, exhibited a significant decrease in stiffness due to OA at all examination depths. Lateral samples presented an opposite response to the disease, specifically a statistically significant increase in stiffness due to OA at all depths examined. Table 4.9 compares the average indentation stiffness at the initial test depth, 1 μm, with subsequent depths, indicating statistical significance where applicable. The results are presented schematically in Figures 4.30 and 4.31 with Figure 4.29 illustrating the scale of such indentation depths relative to the thickness of a standard trabecular strut.

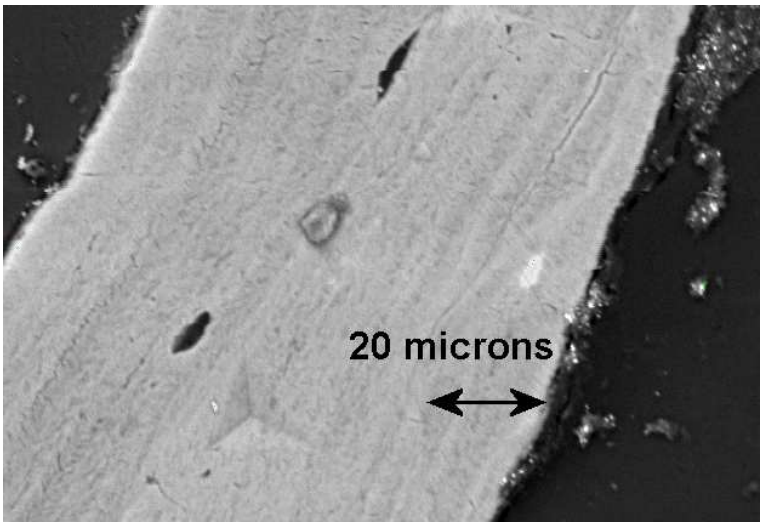

Figure 4.29: Comparative image of bone sample highlighting the extent of indentation depth relative to trabecular thickness.

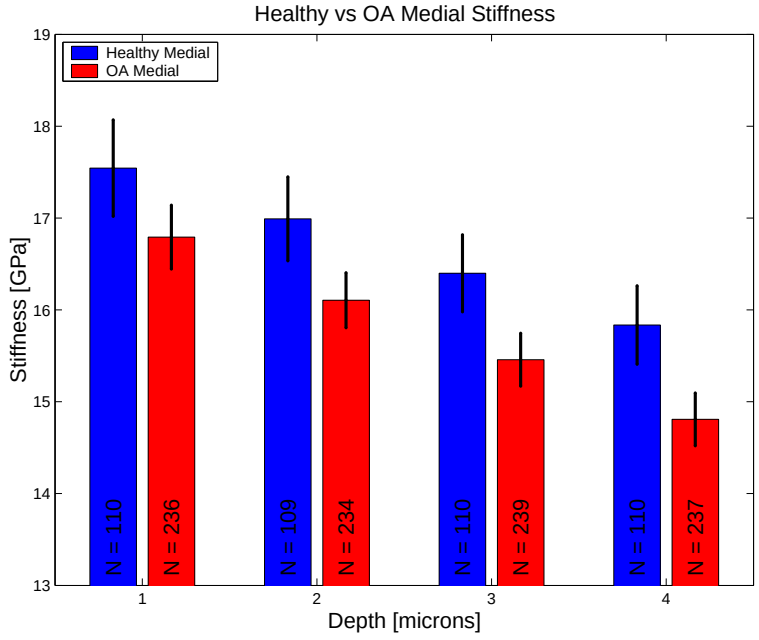

Figure 4.30: Medial stiffness as a function of indentation depth in healthy and OA tissue.

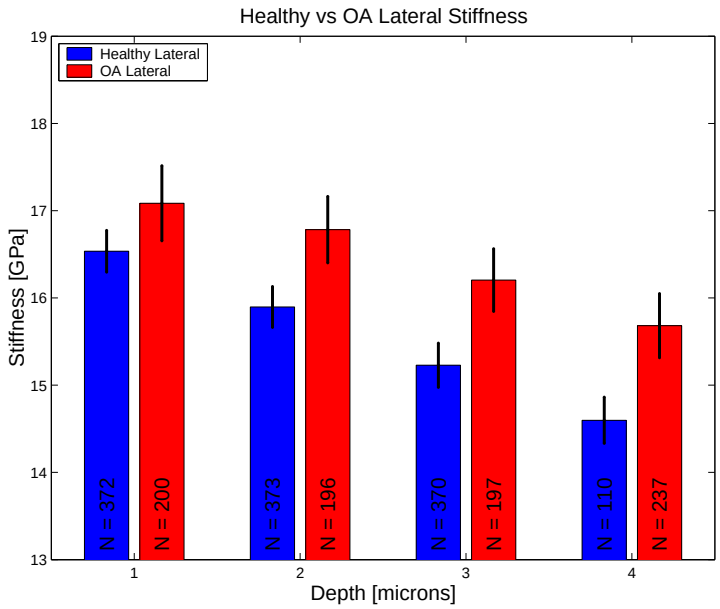

Figure 4.31: Lateral stiffness as a function of indentation depth in healthy and OA tissue.

Indentation Depth	Stiffness [GPa]			
	Healthy		OA	
	Medial	Lateral	Medial	Lateral
1μm	17.54	16.53	16.79	17.08
2μm	16.99	15.9 **	16.1 **	16.78
3μm	16.4 **	15.23 **	15.46 **	16.2 **
4μm	15.84 **	14.6 **	14.81 **	15.68 **

Table 4.9: Average stiffness values as a function of indentation depth. ** indicates statistical significance ($p<0.05$) relative to the 1 μm value.

Hardness

Sample hardness exhibited no significant change in magnitude due to increases in indentation depths. The presence of the pathology also had no significant effect on this relationship although a consistent trend of decreasing average OA hardness relative to the healthy controls was seen. This can be seen in Figure 4.32. Table 4.10 compares the average indentation hardness at the initial test depth, 1 μm, with subsequent depths.

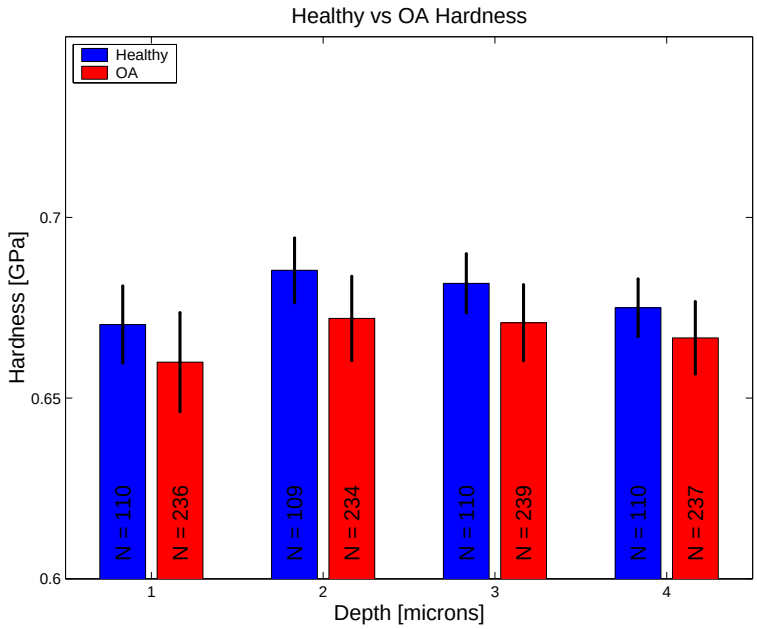

Figure 4.32: Hardness as a function of indentation depth in healthy and OA tissue.

Indentation Depth	Hardness [GPa]	
	Healthy	OA
1μm	0.670	0.660
2μm	0.685	0.672
3μm	0.682	0.671
4μm	0.675	0.667

Table 4.10: Average hardness values as a function of indentation depth.

Stiffness/Hardness Ratio

Although no statistically significant differences were evident when stiffness was compared to corresponding hardness values at each individual examination depth, a particularly interesting effect was seen when the E/H relationship was assessed as a function of examination depth. Plotting E/H as a function of increasing examination depth gives a quantitative measure of how the material's elastic/plastic relationship changes throughout the examined depth range. Figures 4.33 and 4.34 show the results in both medial and lateral samples. These plots were created by plotting the slope of the linear regression approximation of the E/H data at each individual depth (Figures 4.5, 4.7, 4.12, 4.14, 4.19, 4.21, 4.26 and 4.28) as a function of increasing examination depth. In real engineering terms, the E/H ratio gives a quantitative measure of the overall relationship between the elastic and plastic deformation response of an investigated material. Changes in this relationship reflect an inherently altered elastic and/or plastic response within an examined material. Changes in the E/H ratio of a material reflect altered proportions of elastic and plastic deformation given the total applied deformation.

When the slopes of the stiffness versus hardness linear regression fits were plotted as a function of examination depth for the medial tissue samples, no statistically significant difference was observed between healthy and OA E/H trends (Figure 4.33). In contrast, the lateral samples presented a stark and

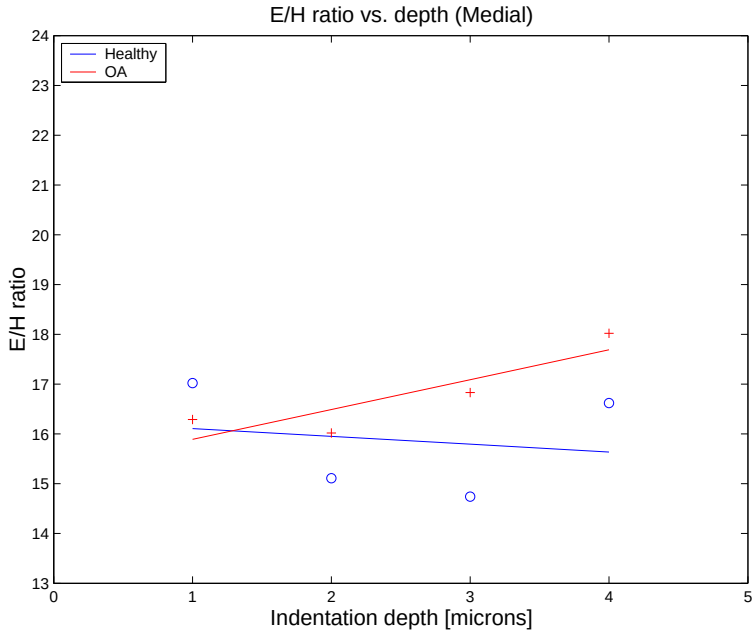

Figure 4.33: Medial stiffness/hardness ratio as a function of increasing examination depth.

significant difference between the healthy and OA E/H trend lines, specifically lateral controls showed an increase in the E/H ratio as a function of increasing examination depth (Figure 4.34).

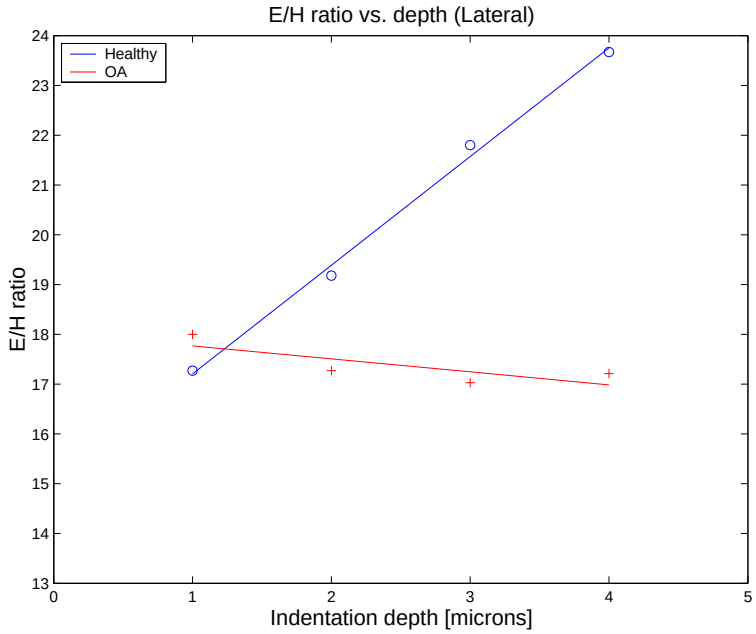

Figure 4.34: Lateral stiffness/hardness ratio as a function of increasing examination depth.

4.3 Mineralisation Assessment

The following sections describe the inorganic mineralisation results of the backscatter SEM analysis (QBEI) performed on both the healthy and early-stage OA bone samples described in Chapter 3. Each Subsection within Section 4.3 presents the data resulting from QBEI analysis of all indentations performed throughout the nanoindentation phase of experimental work at a specific depth of interest. Mineralisation measurements corresponding to all four nanoindentation depths are included, facilitating direct comparison at each examination depth. These results describe how the material's inorganic composition changes as a function of indentation depth and as a function of pathology incidence. It should be noted that the measurements represent average mineralisation of the tissue up to the specified indentation depth and describe relative changes in the material's composition as a function of BSE escape depth. They do not represent mineralisation of the two-dimensional

plane at the depth specified. All tissue material up to and including that at the depth of examination contribute to the overall measurement at the point of maximum BSE escape depth. This is similar to the nanoindentation tests and therefore allows for direct correlation.

4.3.1 1 μm Indentation Depth

Medial

The effect of the presence of early-stage OA on mineralisation in all sample subgroups was investigated. Bone samples taken from the medial sides of donor tibiae were studied and the results are summarised in Figure 4.35. OA bone samples showed a significantly increased mineralisation level relative to healthy controls ($p<0.05$). The average increase due to the presence of the disease was 2% in magnitude, as shown in the corresponding figure.

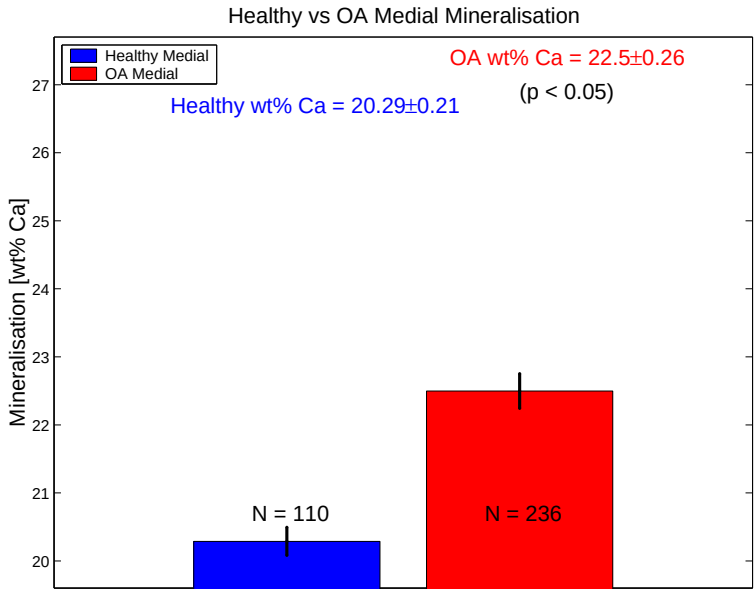

Figure 4.35: Healthy versus OA medial mineralisation assessed by QBEI at 15keV with 95% confidence intervals.

Lateral

Lateral samples also exhibited disease-related changes, found to be statistically significant, but were much smaller in magnitude than their medial counterparts. Healthy lateral mineralisation was similar in magnitude to healthy medial mineralisation, if slightly elevated ($p<0.05$). Early-stage OA lateral samples presented a statistically significant mineralisation increase ($p<0.05$), of approximately 0.5 wt% Ca in magnitude (Figure 4.36).

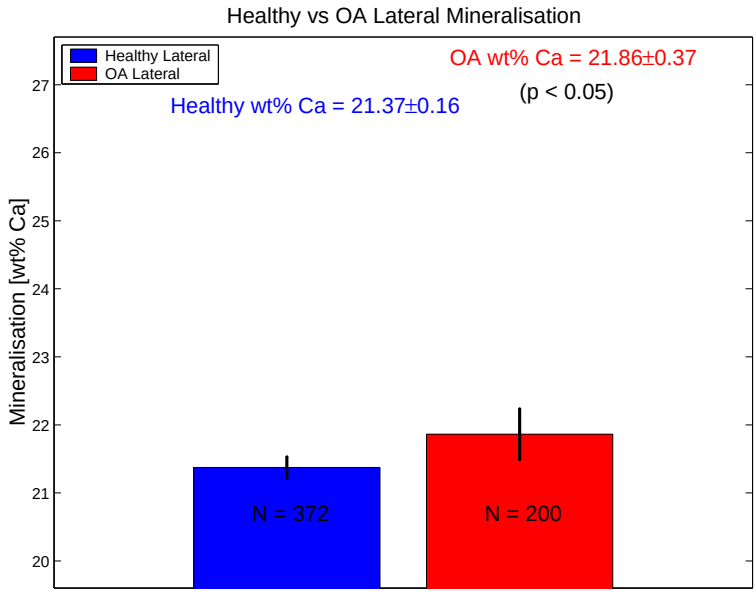

Figure 4.36: Healthy versus OA lateral mineralisation assessed by QBEI at 15keV with 95% confidence intervals.

4.3.2 2 μm Indentation Depth

Medial

At the increased BSE escape depth resulting from an increased accelerating voltage of 20keV, changes occurring within deeper subsurface layers of trabecular samples could be examined. An accelerating voltage of 20keV corresponds with an approximate BSE escape depth of 2 μm in human bone. The presence of early-stage OA in medial samples examined at this escape depth resulted in a significantly increased tissue mineralisation level ($p<0.05$). The magnitude of both healthy and OA mineralisation levels was increased relative to samples analysed at an examination depth of 1 μm. OA resulted in an approximate 2.3 wt% Ca increase in medial mineralisation, as shown in Figure 4.37.

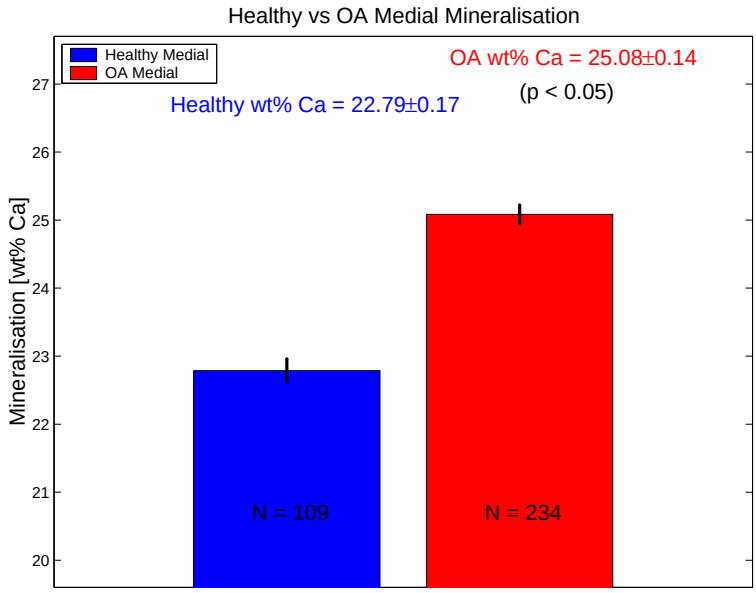

Figure 4.37: Healthy versus OA medial mineralisation assessed by QBEI at 20keV with 95% confidence intervals.

Lateral

Unlike the previous depth of examination (1 μm), presence of the disease in lateral samples resulted in a significantly decreased mineralisation level relative to healthy controls ($p<0.05$). OA samples exhibited on average a decrease in mineralisation of approximately 1.2 wt% Ca in magnitude, as shown in Figure 4.38.

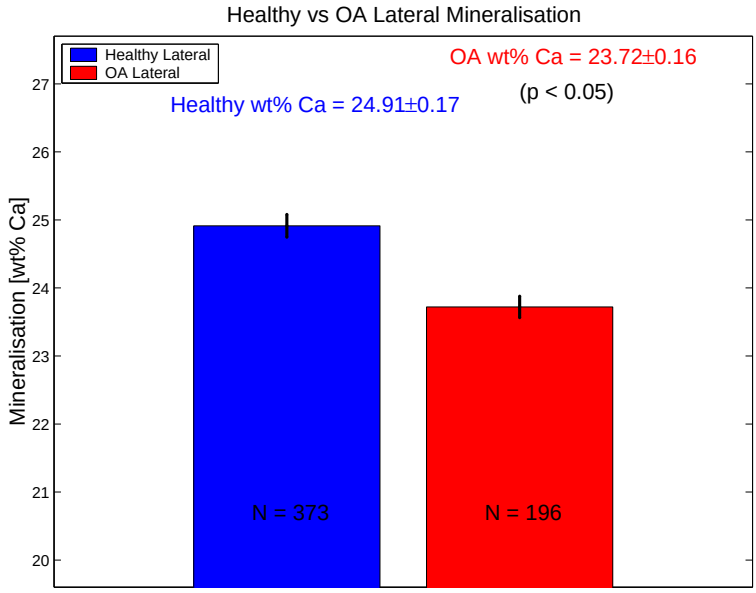

Figure 4.38: Healthy versus OA lateral mineralisation assessed by QBEI at 20keV with 95% confidence intervals.

4.3.3 3 μm Indentation Depth

Medial

Quantification of the mineralisation of medial samples at this depth of examination resulted in a similar trend to those seen previously in medial samples. Presence of the disease resulted in a significant increase in the average mineralisation level ($p<0.05$), although the magnitude of this increase was considerably smaller than previously observed ($\approx$ 0.8 wt% Ca). This decreased difference between healthy and OA mineralisation is largely due to an increasing average healthy mineralisation relative to an approximately unchanged OA mineralisation. This result is shown in Figure 4.39.

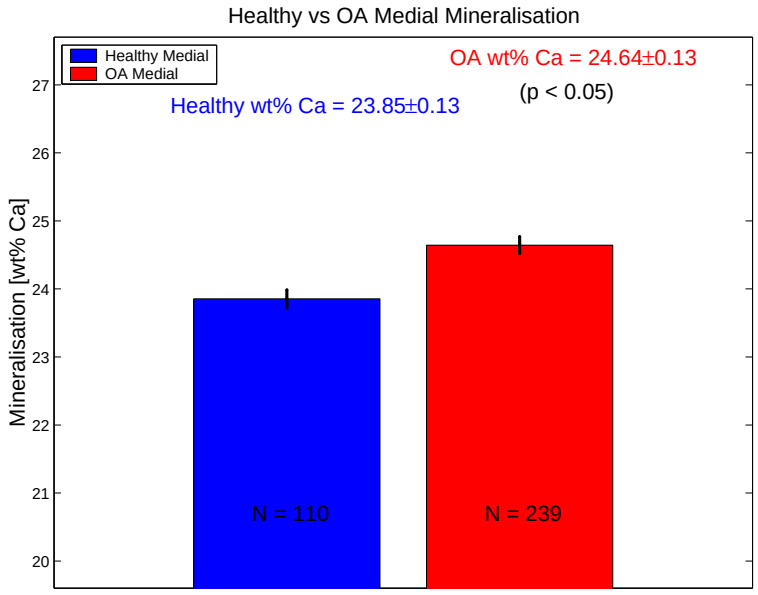

Figure 4.39: Healthy versus OA medial mineralisation assessed by QBEI at 25keV with 95% confidence intervals.

Lateral

Lateral samples exhibited a statistically significant decrease in average mineralisation due to the presence of the pathological condition ($p<0.05$). As was the case with all samples examined at this examination depth so far, the magnitude of the effect of OA on mineralisation level was considerably decreased when compared with the diseases effect at a shallower examination depth. The average decrease in lateral mineralisation was approximately 0.5 wt% Ca and is shown in Figure 4.40.

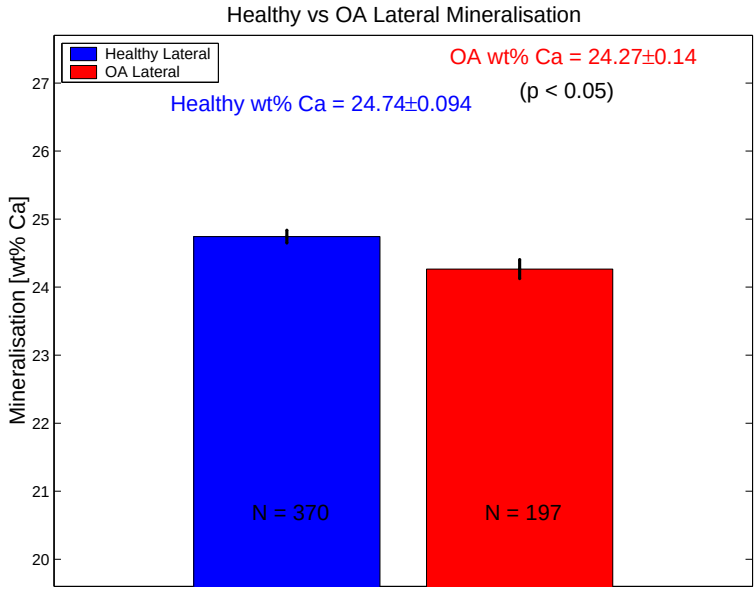

Figure 4.40: Healthy versus OA lateral mineralisation assessed by QBEI at 25keV with 95% confidence intervals.

4.3.4 4 μm Indentation Depth

Medial

Examination of tissue mineralisation at this examination depth resulted in similar trends to those seen at previous depths. The trend of decreasing magnitudes also continued at this examination depth. The average mineralisation of medial samples was significantly increased ($p<0.05$) but in real terms, a considerable reduction in the magnitude of this change occurred. The average increase was only 0.7 wt% Ca compared with the previous increases in medial mineralisation due to OA (see Figures 4.35, 4.37 and 4.39. The current increase in mineralisation is illustrated in Figure 4.41.

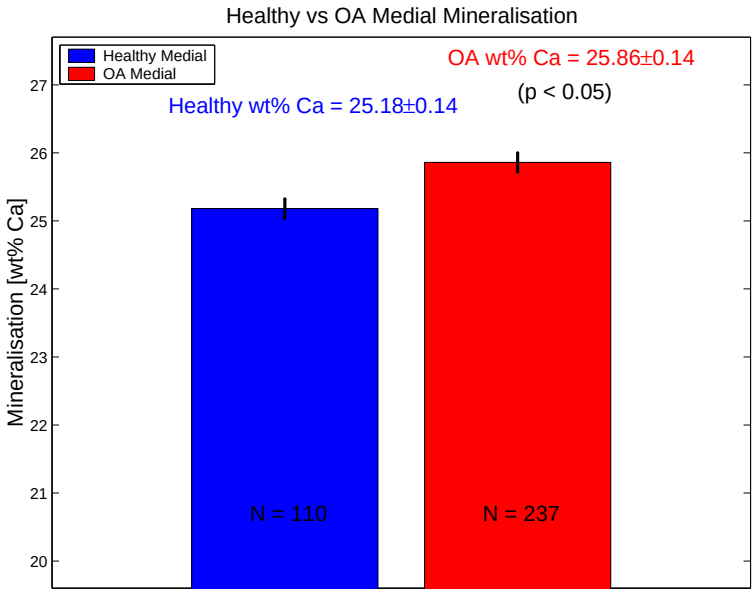

Figure 4.41: Healthy versus OA medial mineralisation assessed by QBEI at 30keV with 95% confidence intervals.

Lateral

A significant decrease in average mineralisation was seen in the OA lateral samples relative to their corresponding healthy controls ($p<0.05$). In reality, this change was much smaller than that seen at previous examination depths. This is illustrated in Figure 4.42.

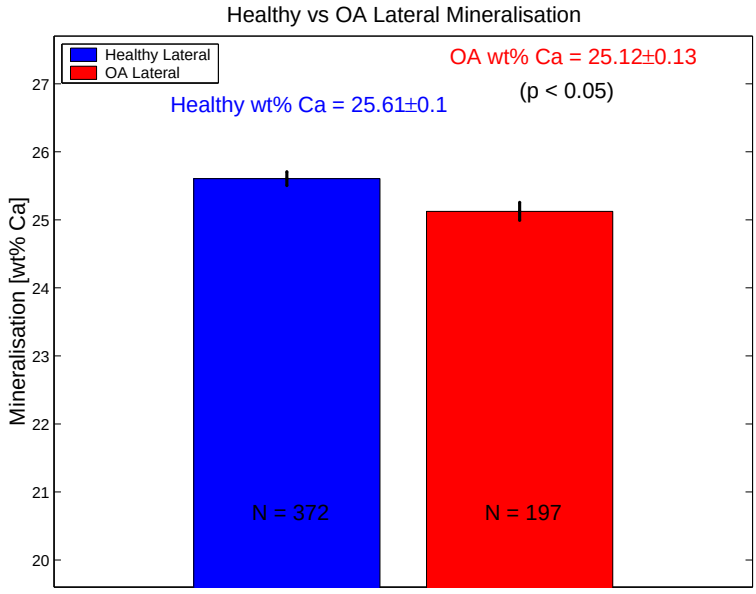

Figure 4.42: Healthy versus OA lateral mineralisation assessed by QBEI at 30keV with 95% confidence intervals.

4.3.5 Depth-Specific Behaviour

By combining all the acquired mineralisation data acquired throughout the QBEI SEM analysis, a number of interesting depth-related trends were observed. To summarise the results, medial samples exhibited a ubiquitous increase in mineralisation due to presence of the disease. Lateral samples exhibited an opposite response to the disease at all examination depths with the exception of the surface layer. At examination depths of 2, 3 and 4 μm, lateral samples from diseased donors present a significantly decreased mineralisation level. At the surface, the samples exhibit a significant increase, mirroring the situation seen at all examination depths in the medial symptomatic samples

Medial

Medial samples showed a ubiquitous increase in average mineralisation level at all indentation depths examined. The largest difference in mineralisation level was seen at the shallowest depth. Mineralisation increases, due to OA at the four examined depths, were found to decrease in magnitude as a function of increasing depth (Figure 4.43). It was clear from the data that the depth-specific method developed was valid. Both increases and decreases in average mineralisation as a function of examination depth were seen, highlighting the ability of this method to accurately represent subsurface mineralisation changes.

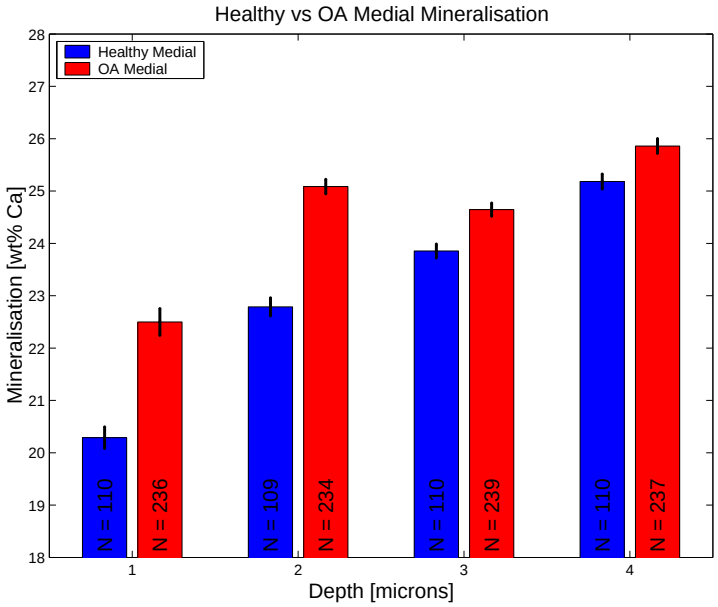

Figure 4.43: Medial mineralisation as a function of indentation depth in healthy and OA tissue with 95% confidence intervals.

Lateral

On average, lateral mineralisation level changes due to OA were opposite in magnitude when compared with medial mineralisation changes. However, the surface layer was exceptional by exhibiting an identical response to that seen in the medial samples (i.e. increased mineralisation due to OA). With the exception of this surface layer, presence of OA resulted in a significant decrease in average lateral mineralisation level. As in the medial samples, changes in the magnitudes of mineralisation differences due to OA decreased as a function of increasing examination depth. (Figure 4.44).

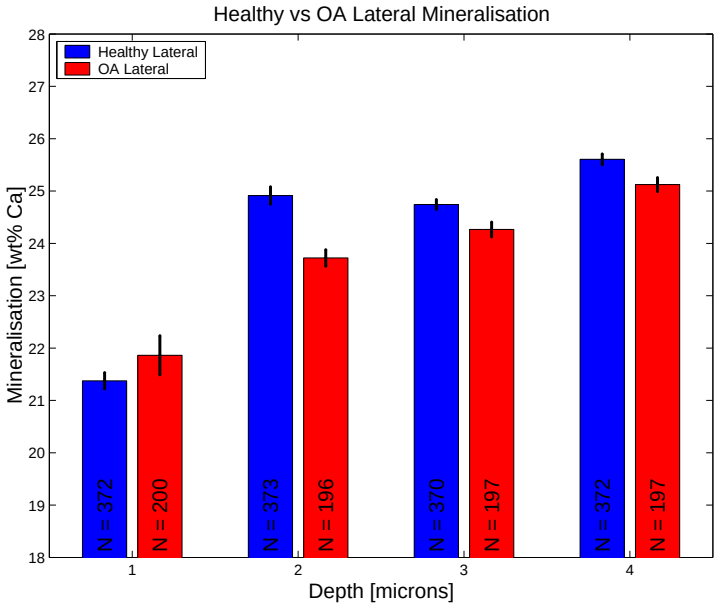

Figure 4.44: Lateral mineralisation as a function of indentation depth in healthy and OA tissue with 95% confidence intervals.

4.4 Mechanical/Mineralisation Relationship

Part of the hypothesis of this present work is that there is a link between mechanical properties and the constituent materials and that this link might explain the changes observed due to OA. Significant changes were observed in both mechanical properties and mineralisation. The results are presented in the following sections.

4.4.1 1 μm Indentation Depth

Medial Stiffness and Mineralisation

The data summarised in Figure 4.45 reflect the results of the medial group. Presence of early-stage OA symptoms resulted in a significantly increased mineralisation level. These samples showed a corresponding significant decrease in stiffness ($\approx$ 0.7 GPa). No strong significant linear relationship

exists between stiffness and mineralisation for this group in either healthy or OA samples. Of interest, however, is that healthy bone achieved a higher stiffness with a lower mineralisation level when compared with OA samples. Consequently, the increased mineralisation in OA samples had no apparent mechanical benefit. This was consistent for all medial data (Figures 4.45, 4.49, 4.53 and 4.57).

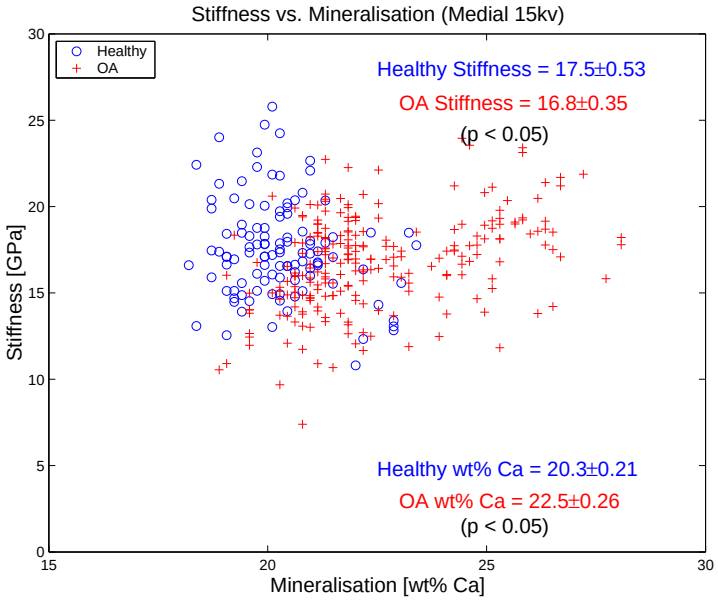

Figure 4.45: Healthy and OA stiffness versus mineralisation in medial tissue samples (1 μm depth).

Medial Hardness and Mineralisation

Medial hardness results and their relationship with corresponding mineralisation levels were distinct from the stiffness results. No significant difference in the average hardness value was found in spite of a significant increase in mineralisation (Figure 4.46). Similar to the medial stiffness, the hardness data indicated that healthy bone maintained its hardness with less mineral than OA bone. This is consistent for all medial data (Figures 4.46, 4.50, 4.54 and 4.58)

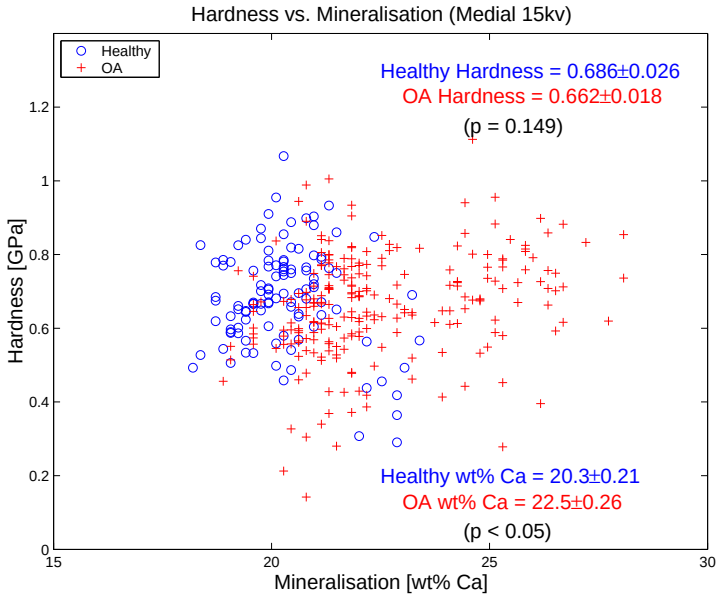

Figure 4.46: Healthy and OA hardness versus mineralisation in medial tissue samples (1 μm depth).

Lateral Stiffness and Mineralisation

Lateral samples exhibited a significantly increased average tissue stiffness relative to their corresponding healthy controls. A corresponding significant decrease in average mineralisation level, albeit small in real terms was also seen at this depth. This data can be seen in Figure 4.47 and it is clear, as was the case in the medial samples, that no strong linear relationship exists between lateral stiffness and mineralisation. A unique situation was observed at this depth of examination with regard to the relative effect of the disease on tissue mineralisation. At three out of the four examination depths, presence of early stage OA resulted in a significantly decreased average mineralisation level. At this depth (1 μm), this trend was reversed, resulting in a significant increase in average mineralisation level due to presence of OA. Of particular interest was the fact that this unique scenario mirrored that seen in medial samples which exhibit a more developed stage of the disease. Consequently, these results may be the first indication of a shift in the devel-

opment of the disease in the lateral, non-presenting sites, capturing a change in mineralisation profile towards that seen in the symptomatic medial samples. No corresponding change was seen in the stiffness data, indicating that the mineralisation level may be the primary marker of disease initiation.

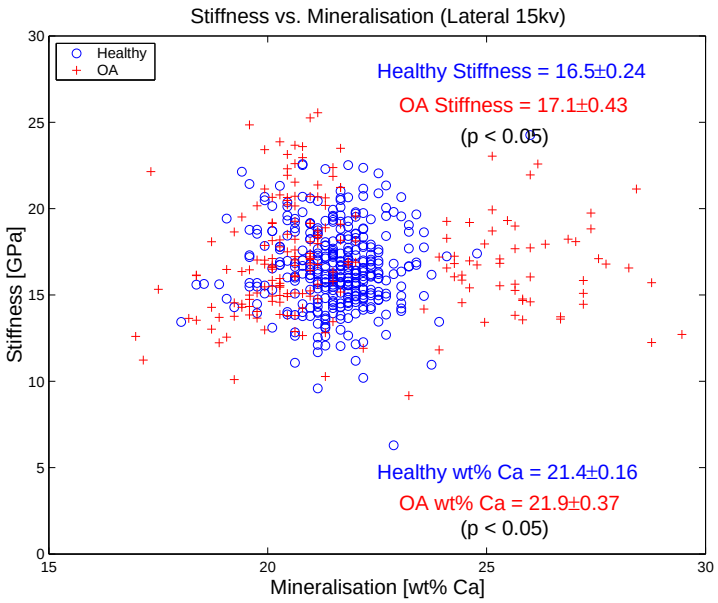

Figure 4.47: Healthy and OA stiffness versus mineralisation in lateral tissue samples (1 μm depth).

Lateral Hardness and Mineralisation

At this initial depth of examination, lateral tissue hardness results and their corresponding relationship with average mineralisation level were similar to their medial counterparts. As seen in the lateral stiffness results at this depth of examination, no significant decrease in average tissue hardness was seen. Conversely, a statistically significant decrease in average tissue mineralisation level was observed. The plots and corresponding values and statistical p values can be seen in Figure 4.48. As was the case with the lateral stiffness findings at this examination depth, the significantly increased mineralisation level had no apparent benefit with regard to average tissue hardness.

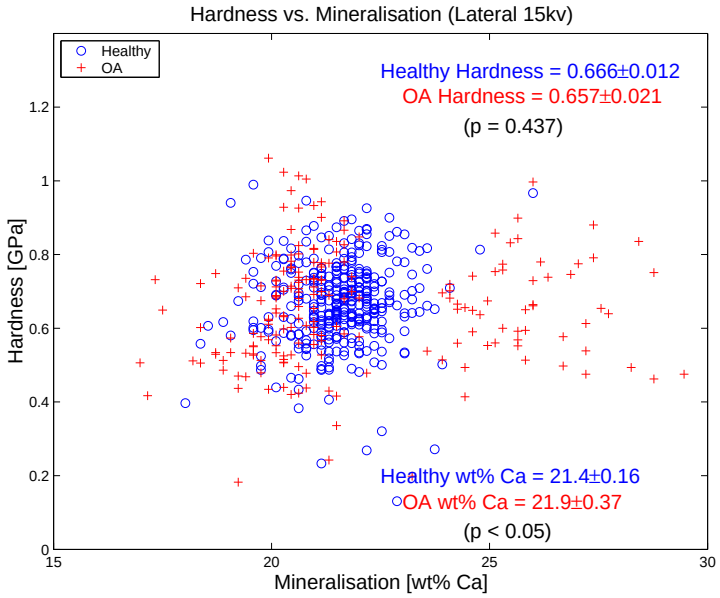

Figure 4.48: Healthy and OA hardness versus mineralisation in lateral tissue samples (1 μm depth).

4.4.2 2 μm Indentation Depth

Medial Stiffness and Mineralisation

At the second specified depth of examination, a statistically significant increase in average tissue mineralisation level was seen in samples displaying evidence of early-stage OA. A corresponding statistically significant decrease in average tissue stiffness was also seen in these samples. This mirrored the scenario seen at the previous examination depth, specifically that healthy bone tissue was achieving a higher average tissue stiffness with a lower mineralisation level relative to OA samples. The increased mineralisation level in OA samples had no apparent benefit with regard to mechanical stiffness. Additionally, as at the previous examination depth, no strong linear relationship between the two properties was observed in either healthy or OA samples. These results can be seen in Figure 4.49.

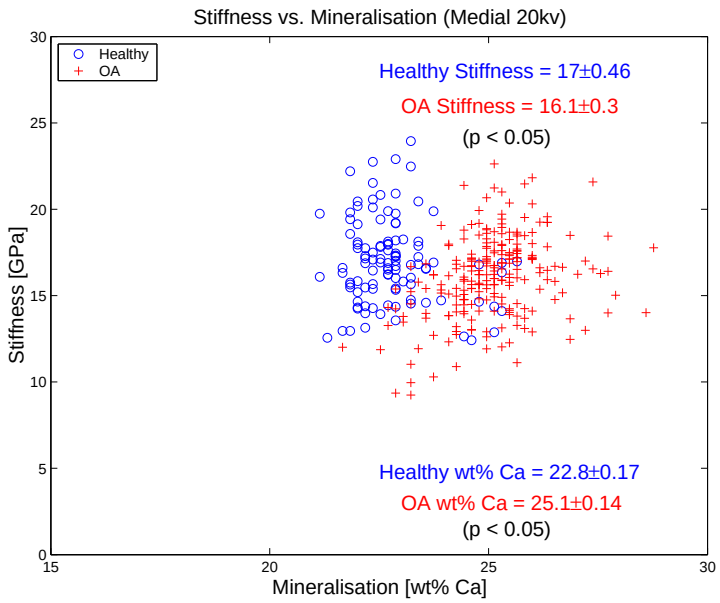

Figure 4.49: Healthy and OA stiffness versus mineralisation in medial tissue samples (2 μm depth).

Medial Hardness and Mineralisation

At an examination depth of 2 μm, a significant decrease in average tissue hardness was seen in OA samples. A corresponding mineralisation increase was seen, also found to be statistically distinct from the healthy control value (Figure 4.50). This reflects the situation seen in the stiffness results at this examination depth, as would be expected given the dependent relationship between tissue stiffness and hardness. Consequently, as was the case with the medial stiffness results at this depth, the increased mineralisation level in OA samples appeared to offer little mechanical benefit with regard to tissue hardness. Healthy tissue achieved a greater average tissue hardness than OA samples with a lower mineralisation level.

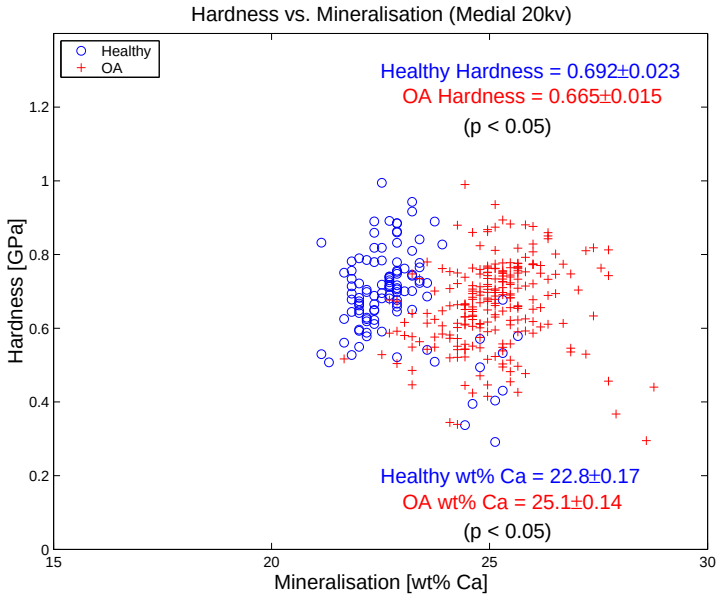

Figure 4.50: Healthy and OA hardness versus mineralisation in medial tissue samples (2 μm depth).

Lateral Stiffness and Mineralisation

In the lateral samples at an examination depth of 2 μm, a statistically significant increase in tissue stiffness was observed due to implicit presence of the disease, as seen at the previous examination depth. However, the average mineralisation value was affected by presence of the disease in an alternate fashion to the mineralisation seen in the overlying layer. A significant decrease in stiffness was observed, approximately 1 GPa in magnitude, as opposed to the significant increase seen in lateral samples at the initial examination depth. This resulted in a reversed trend to that seen at the 1 μm examination depth. In early stage lateral samples at a depth of 2 μm, OA samples achieved a higher average tissue stiffness with a lower average mineralisation level, relative to healthy tissue (Figure 4.51). This trend was seen at all subsequent depths in lateral samples. Once again, no distinct linear relationship was observed between stiffness and mineralisation.

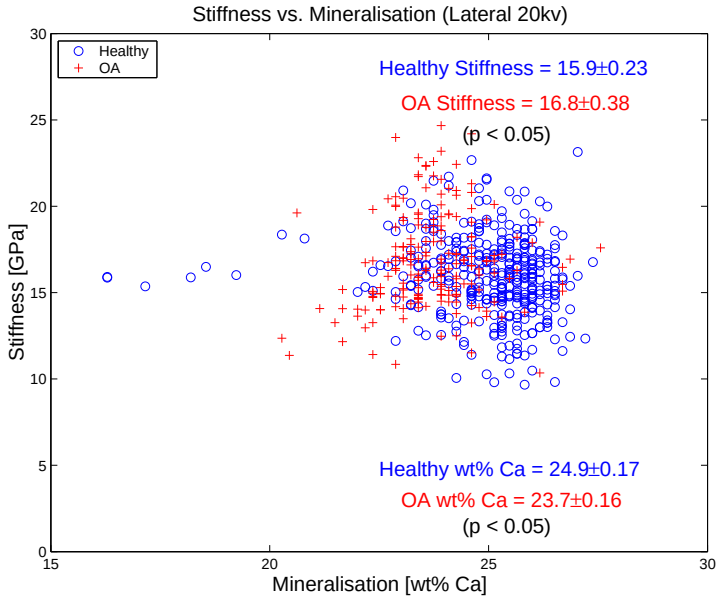

Figure 4.51: Healthy and OA stiffness versus mineralisation in lateral tissue samples (2 μm depth).

Lateral Hardness and Mineralisation

The average OA tissue hardness recorded in the lateral samples at this examination depth did not differ significantly from the healthy control value. Of particular interest was that this was found to be true despite a significantly increased tissue stiffness seen in the lateral stiffness results at this examination depth. In addition to this, the average OA mineralisation level was decreased in the OA lateral samples relative to healthy controls at this depth of interest. Consequently the observed average decrease in mineralisation level had no apparent effect on corresponding average tissue hardness in lateral trabecular samples (Figure 4.52).

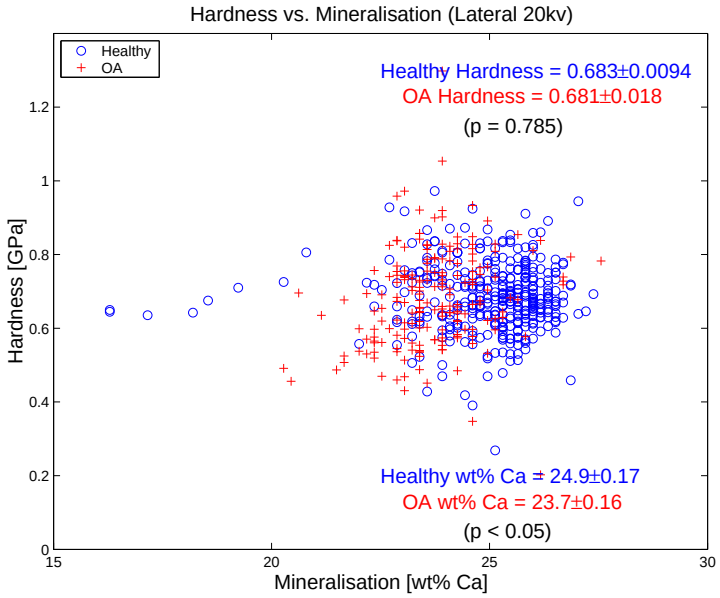

Figure 4.52: Healthy and OA hardness versus mineralisation in lateral tissue samples (2 μm depth).

4.4.3 3 μm Indentation Depth

Medial Stiffness and Mineralisation

Presence of early-stage OA in the medial samples examined at this depth resulted in a significantly decreased average tissue stiffness. Corresponding average mineralisation was found to be statistically increased relative to healthy medial controls. This trend was identical to those seen at shallower examination depths in the medial samples. Healthy samples achieved a higher average stiffness with a lower average mineralisation level (Figure 4.53). Consequently, the increased average mineralisation level in OA samples did not result in any mechanical benefit to the tissue.

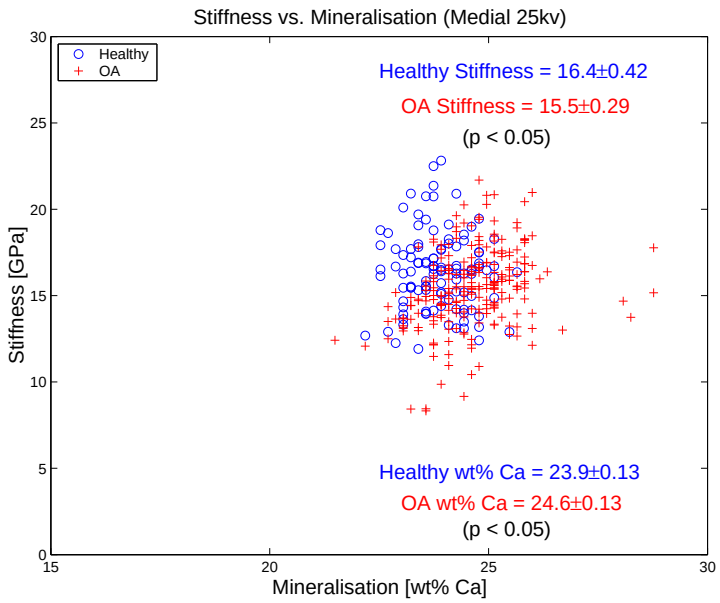

Figure 4.53: Healthy and OA stiffness versus mineralisation in medial tissue samples (3 μm depth).

Medial Hardness and Mineralisation

Hardness results assessed using medial samples at this examination depth were similar to medial results recorded at previous depths. A significant decrease in hardness was seen in the early-stage OA samples, while a significant increase in mineralisation was also observed (Figure 4.54). This trend was identical to the situation seen in the medial stiffness results at this examination depth, as might be expected given the relationship between tissue stiffness and hardness. Healthy samples achieved a greater average hardness value with less mineralisation than their OA counterparts. The increased average mineralisation level in OA samples did not result in any apparent mechanical benefit to the tissue.

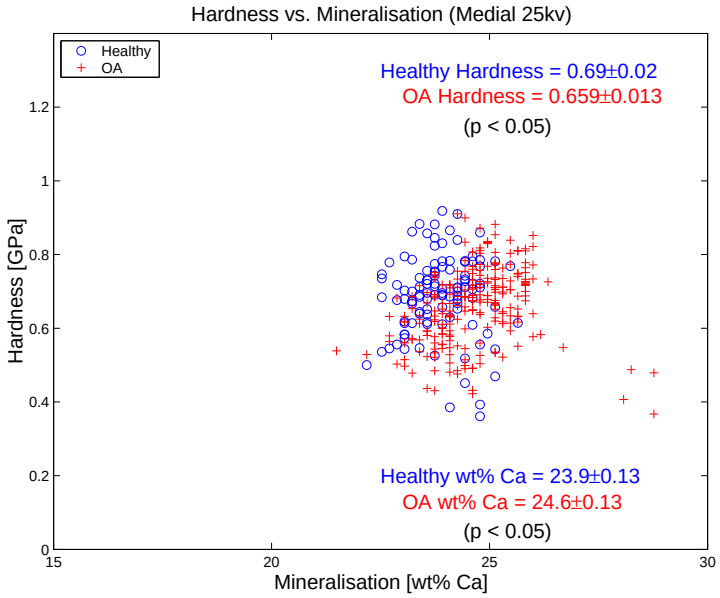

Figure 4.54: Healthy and OA hardness versus mineralisation in medial tissue samples (3 μm depth).

Lateral Stiffness and Mineralisation

Lateral samples, in contrast to the medial samples examined at this examination depth exhibited a statistically significant increase in average tissue stiffness, as well as a significantly decreased average mineralisation level (Figure 4.55). This trend was identical to that seen in lateral samples at the previous examination depth of 2 μm. In the earliest stage of the disease, a higher tissue stiffness is achieved, relative to healthy controls. This was seen in spite of a lower corresponding average OA mineralisation level relative to the control value.

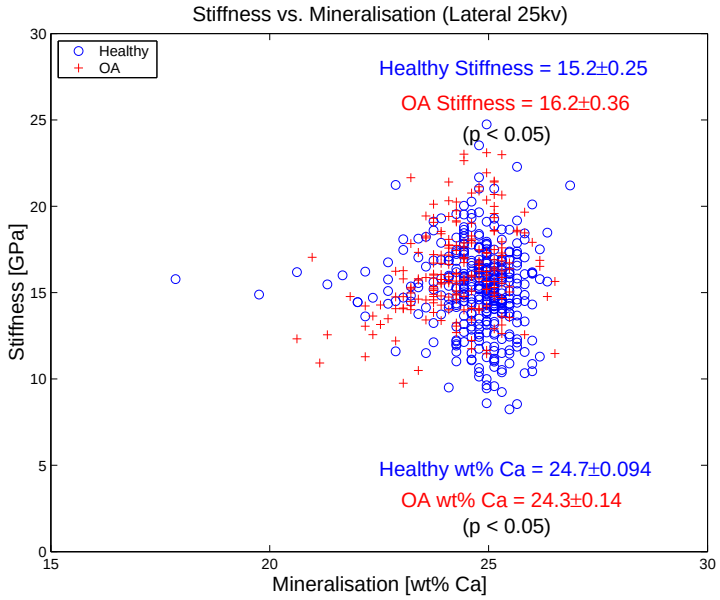

Figure 4.55: Healthy and OA stiffness versus mineralisation in lateral tissue samples (3 μm depth).

Lateral Hardness and Mineralisation

Lateral tissue samples showed no significant change in average hardness at this examination depth but did exhibit a small but significant decrease in mineralisation (Figure 4.56). This trend was similar to that seen in hardness assessments performed on lateral samples at the previous examination depth of 2 μm. Hardness appeared to be relatively unaffected in the early stages of the disease relative to healthy controls and the corresponding stiffness results. The average decrease in mineralisation level did not have an apparent mechanical consequence with regard to the average tissue hardness, unlike the situation seen in stiffness assessments of the same samples.

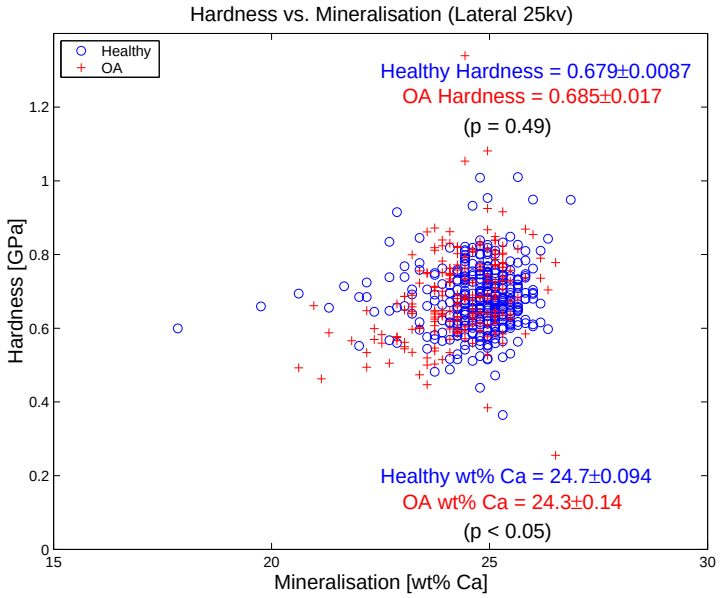

Figure 4.56: Healthy and OA hardness versus mineralisation in lateral tissue samples (3 μm depth).

4.4.4 4 μm Indentation Depth

Medial Stiffness and Mineralisation

At an examination depth of 4 μm, the average recorded medial stiffness was reduced in early-stage OA samples ($p<0.05$) relative to healthy controls. Mineralisation was significantly increased but this increase relative to healthy controls was smaller in magnitude than seen at previous examination depths. The relationship between stiffness and mineralisation at this examination depth mirrored the trend seen at all previous depths in medial samples. Healthy controls achieved a greater average stiffness with a lower average mineralisation level than their OA counterparts (Figure 4.57).

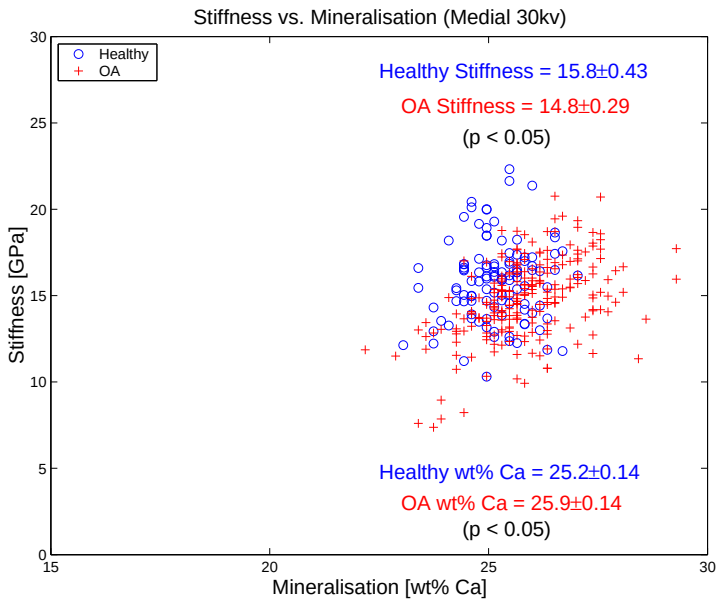

Figure 4.57: Healthy and OA stiffness versus mineralisation in medial tissue samples (4 μm depth).

Medial Hardness and Mineralisation

In Medial tissue samples, the recorded average tissue hardness was significantly reduced relative to healthy controls, while average mineralisation level was statistically increased relative to healthy controls. However, the magnitude of this change was quite small in real terms as seen at previous depths of examination. As before, this observed trend of significantly decreasing average hardness and increasing mineralisation level was identical to that seen in the stiffness data at this examination depth and the stiffness and hardness data for medial samples at all previous examination depths. The results concerning medial tissue hardness and mineralisation at this examination depth are plotted in Figure 4.58.

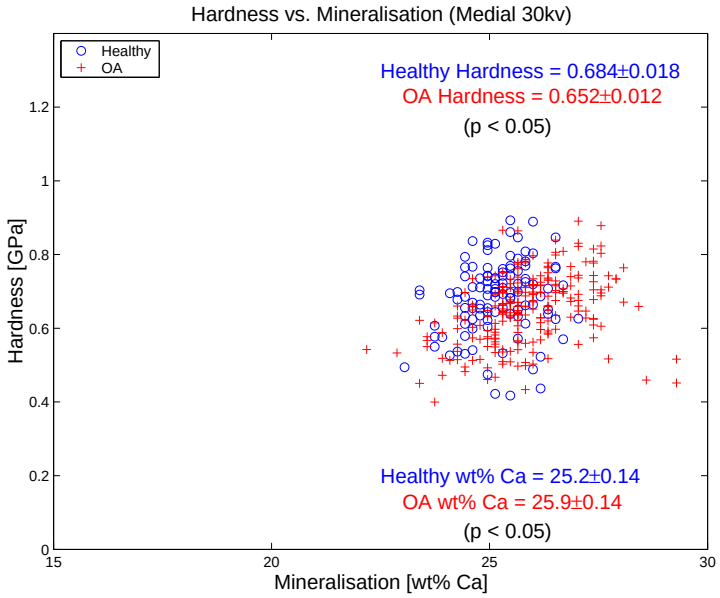

Figure 4.58: Healthy and OA hardness versus mineralisation in medial tissue samples (4 μm depth).

Lateral Stiffness and Mineralisation

The average recorded lateral tissue stiffness at this examination depth was significantly increased due to the presence of early-stage OA. Mineralisation level was seen to significantly decrease relative to healthy controls but this change was relatively small in magnitude (Figure 4.59). As seen previously in lateral samples at the previous two examination depths, the relationship between the average tissue stiffness and mineralisation level was reversed relative to the same relationship seen in medial samples. OA samples achieved a significantly greater average stiffness with a lower mineralisation level then their healthy counterparts.

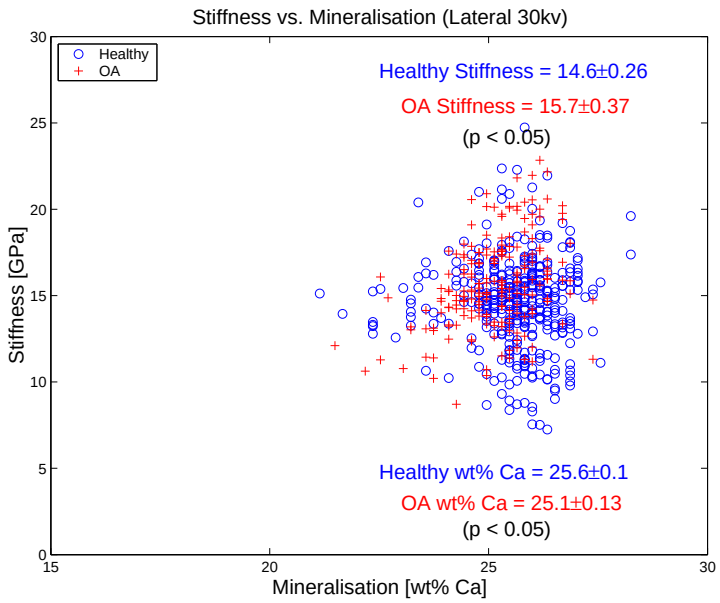

Figure 4.59: Healthy and OA stiffness versus mineralisation in lateral tissue samples (4 μm depth).

Lateral Hardness and Mineralisation

At this final depth of examination, average tissue hardness of lateral samples was not significantly altered relative to healthy controls due to implicated presence of OA. Mineralisation on the other hand was significantly decreased, as shown in Figure 4.60. This trend was identical to those seen previously in the hardness assessments of lateral healthy and OA samples, with the exception of the initial examination depth of 1 μm. Consequently, the recorded decrease in average mineralisation level did not have any apparent effect on the corresponding tissue hardness of either healthy or OA bone tissue for the examination depths of 2, 3 and 4 μm.

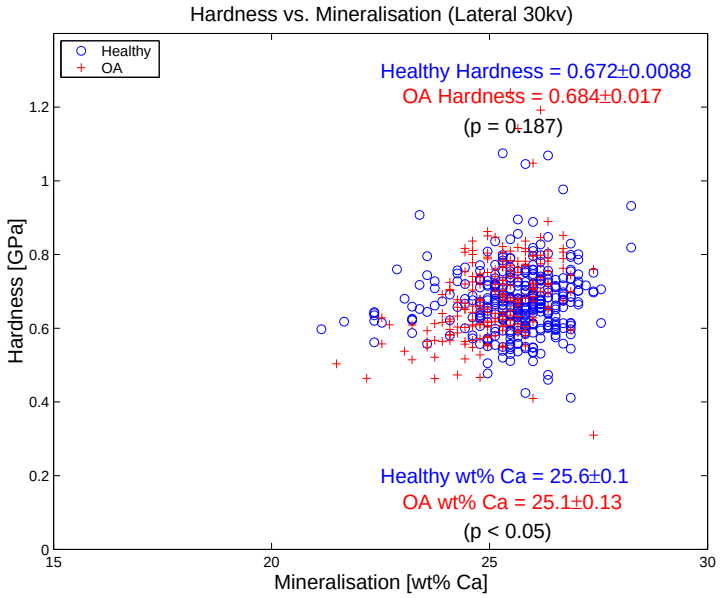

Figure 4.60: Healthy and OA hardness versus mineralisation in lateral tissue samples (4 μm depth).

4.4.5 Depth-specific Behaviour

The results illustrated in Figures 4.61 and 4.62 reveal the effect of early-stage OA on the stiffness versus mineralisation relationship as a function of depth below the samples surface.

Medial

When the paired data were sorted based on both diseased state (healthy or OA) and sample site of origin (medial or lateral), medial samples exhibited the relationship seen in Figure 4.61. Considering medial tissue mineralisation, it was obvious from Figure 4.61 that a statistically significant difference in average tissue mineralisation was seen at all examination depths due to the presence of early-stage OA symptoms. This was obvious from the relative separation of the healthy and OA data scatter, in blue and red respectively in Figure 4.61. It was evident that the average tissue mineralisation increased

as a function of examination depth at each specific depth increment. It was also noted that the magnitude of the recorded mineralisation elevations, due to the pathology, decreased at each depth increment. This was clearly seen as a decrease in the separation of the healthy and OA data scatter sets, denoted by the colours blue and red respectively in Figure 4.61.

Changes to the tissue stiffness as a function of depth were markedly different. In the medial samples, the early-stage OA stiffness values were found to be significantly decreased relative to average healthy values at all depths. This finding is visually represented in Figure 4.61 as the difference between the 'Healthy' and 'OA' stiffness trend lines drawn along the 'Examination Depth' axis. It was also obvious that, independently, both healthy and OA medial stiffness decrease as a function of examination depth. This is illustrated as the decreasing slopes of each respective regression. It is clear from the figure that the observed changes in the tissue stiffness as a result of the pathology are substantially smaller than the corresponding changes observed in mineralisation. It was also noted that unlike the mineralisation data, the average magnitude of the stiffness changes, as a function of depth, remained approximately constant throughout the range of depths examined, in both healthy and OA samples. Of additional interest was the fact that OA mineralisation levels in adjacent examination depths were seen to both increase and decrease relative to each other, independently validating the depth-specific protocol.

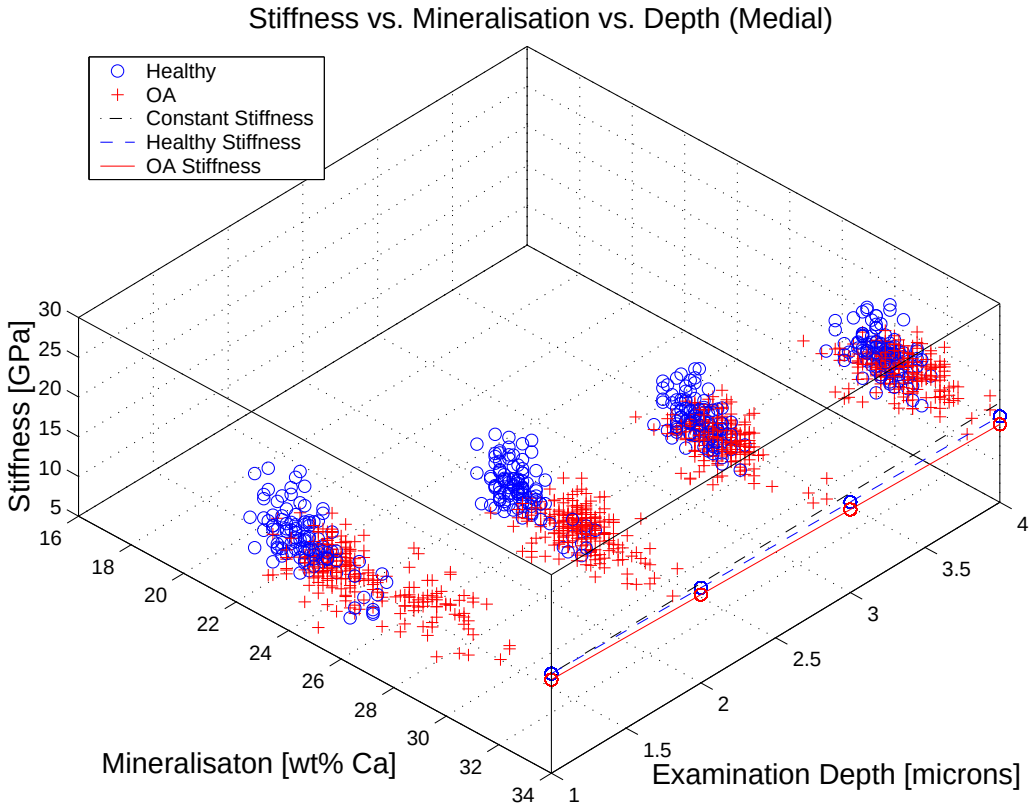

Figure 4.61: Healthy and OA stiffness versus mineralisation as a function of examination depth (Medial).

Lateral

The lateral samples presented distinct results from their medial counterparts. As before, average mineralisation decreased as a function of increasing examination depth below the surface, with the exception of the 1 μm indentation, due to the implied presence of the pathology. In lateral samples, the magnitude of this decrease in most pronounced at the shallowest depth (2 μm) but was significant nonetheless at all subsequent depths. As with the medial samples, the magnitude of this depression decreased as function of depth. The overall effect of the disease was reduced in the lateral samples examined. All depths show a significant change in average mineralisation level

but none were as large as those seen in the first two medial examination depths. Hence, significant overlap of the observed mineralisation range values was evident in the lateral result, visually apparent when Figures 4.61 and 4.62 were compared.

Average OA stiffness was found to be significantly elevated at all examination depths relative to healthy controls. Independent of this observation, both healthy and OA average tissue stiffness decreased as a function of increasing depth within the tissue. As seen in medial samples, the average magnitude of the lateral stiffness changes, as a function of depth, were approximately constant in both healthy and OA samples. It is clear that small but significant changes occurred in the lateral sites taken from OA patients with no physical lateral symptoms of the pathology. Stiffness is altered, as is mineralisation. However, large mineralisation changes are predominantly at the surface (as seen in Figure 4.62) and stiffness changes are opposite in magnitude relative to corresponding medial sample results. Additionally, as seen in the medial tissue, mineralisation levels in adjacent examination depths were seen to both increase and decrease relative to each other, independently validating the depth-specific protocol.

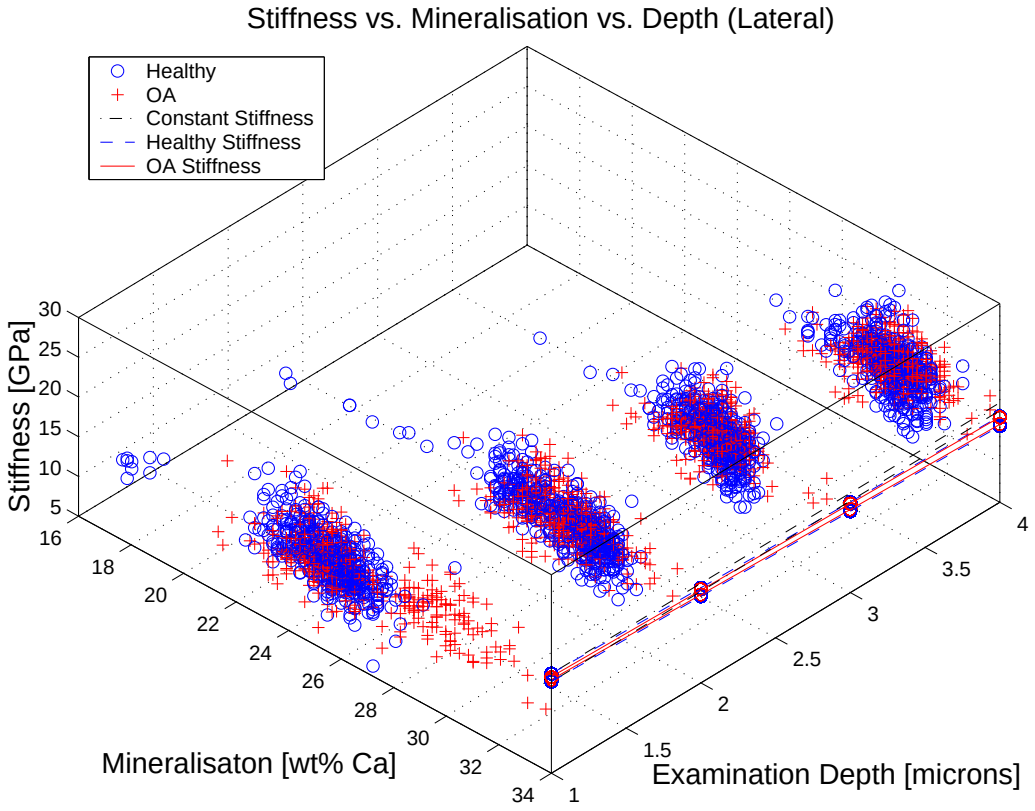

Figure 4.62: Healthy and OA stiffness versus mineralisation as a function of examination depth (Lateral).

4.5 Transverse Mechanical/Mineralisation Relationship

Nanoindentations performed in the transverse direction were isolated and analysed as a separate group to the entire sample population. This separate analysis was of scientific interest based on previous empirical evidence of the anisotropic nature of cancellous bone tissue strength assessed using nanoindentation [116]. No significant evidence of a preferential relationship between mechanical properties and corresponding mineralisation was seen in the purely transversely tested samples. This was true regardless of site or disease. The general observed trend throughout the transverse experiments was

a very weak correlation between localised mineralisation level and stiffness or hardness respectively. Regardless of tissue site or mechanical property (stiffness or hardness), OA samples presented a much stronger relative correlation with mineralisation at most examination depths, as seen by Ferguson *et al.* [39] but these were not statistically significant.

4.6 SEM Damage Calibration Results

The consequences of employing the novel dosage calibration technique developed during this investigation were quantitatively assessed. This provided a clear assessment of the advantages of the use of this technique when analysing electron beam sensitive materials, such as bone. The results detailed within this Section are divided into two parts; (i) experiments performed at 15KeV and (ii) experiments performed at 30KeV. The dosage calibration technique was evaluated at both accelerating voltages illustrating the advantages of employing the technique at both extremes of beam energy settings used throughout this present work, within which the majority of contemporary analyses are conducted [39, 88, 92, 93, 94, 80, 19, 95, 96, 97].

4.6.1 15keV Accelerating Voltage

This Section contains the results of the damage caused using an electron dosage calibration (CPS $\approx$ 5900) compared to the damage caused by using a visually optimum electron dosage setting (CPS $\approx$ 19,000). This comparison was performed at the lowest accelerating voltage commonly used during the analysis of mineralised tissue, 15keV. Five scan sites were tested within one of the healthy subchondral bone samples, employing the novel method of dosage calibration using an *in situ* EDX to standardise the CPS of a carbon standard. These were compared with five separate scan sites tested within the same sample using a visually optimum beam current. This was achieved by setting the beam current to a value just below that for image over-saturation (indicated by total image white-out). This setting would commonly be used

for visually optimal analysis, where specimen irradiation damage would be of little concern (i.e. dense, conductive materials). Figure 4.63 shows the results of the five tests using the novel dosage rate calibration. Each test involved 20 consecutive scans of the same trabecular region of interest (ROI). Each point in Figure 4.63 represents the peak histogram GL value of one of the five ROIs examined. The peak GL for each scan was recorded and then plotted as a function of its respective scan number. A linear regression line was drawn for each of the five samples, the slope of which represents the average rate of GL increase as a function of successive scan number or more simply as the average sample damage rate. Figure 4.64 shows the results of the experiments when a visually optimum dosage (beam current) was used. As in Figure 4.63, each regression represents the average damage rate for one of the five samples. Comparing the slopes of the linear regressions in figures 4.63 and 4.64 allows comparison of the respective damage rates incurred through the use of each dosage calibration method.

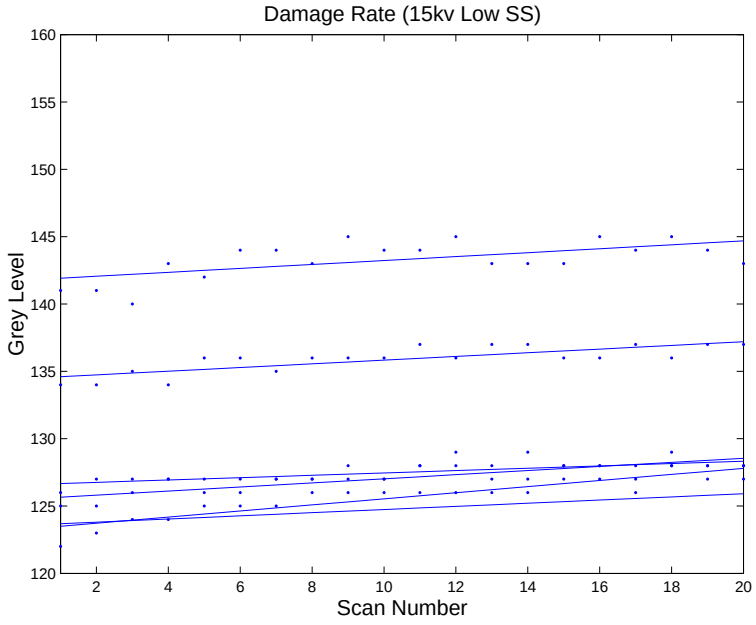

Figure 4.63: Histogram drift rates (Sample 1 to 5) using a novel CPS calibration (Low dosage setting) at 15keV.

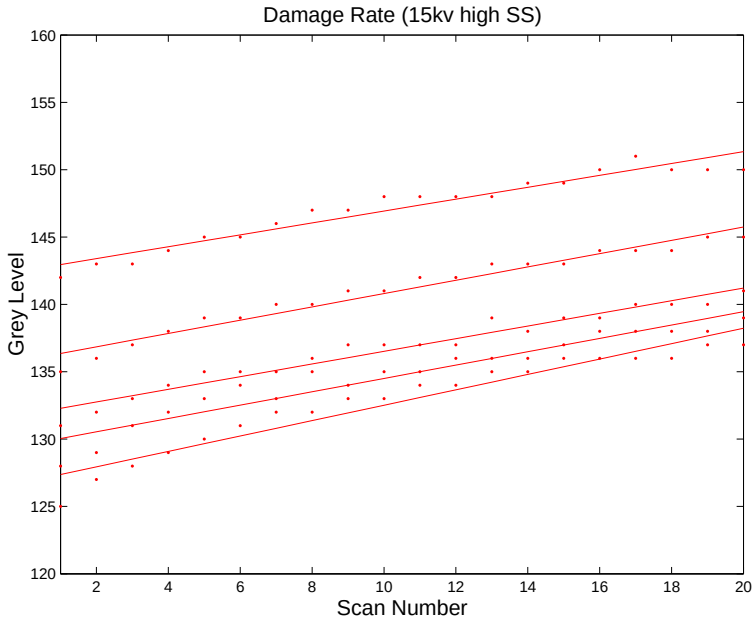

Figure 4.64: Histogram drift rates (Sample 1 to 5) using visually optimum calibration (High dosage setting) at 15keV.

The quantitative difference in damage rate is represented as a box plot in Figure 4.65. Figure 4.65 compares the slopes of both methods and highlights the statistically significant decrease in damage rate attained through the use of the novel calibration method. The actual effect that this specimen damage has on the GL intensity histogram measured is shown in figure 4.66 and figure 4.67. The number of pixels exhibiting a particular GL value plotted as a function of GL is known as an intensity distribution. The multiple histograms represented in each figure correspond to the scan numbers. Hence, each figure contains twenty histograms drawn on top of each other. This illustrates the histogram drift caused by a particular dosage setting. Figure 4.66 shows the drift in the GL intensity histogram for a trabecular ROI due to the novel dosage calibration technique. Figure 4.67 shows the drift due to imaging at a visually optimised dosage setting. Figure 4.66 and Figure 4.67 can also be used to capture any change in the histogram's Full Width at Half Maximum (FWHM) value as a function of exposure time. Changes

in the FWHM value of a constant region of interest (ROI) would represent a non-ubiquitous change in measured grey level and can only occur due to non-uniform specimen damage. No significant difference was seen due to either imaging method or exposure time. The purely horizontal drift of the histogram at each exposure increment highlights a constant FWHM as a function of exposure count.

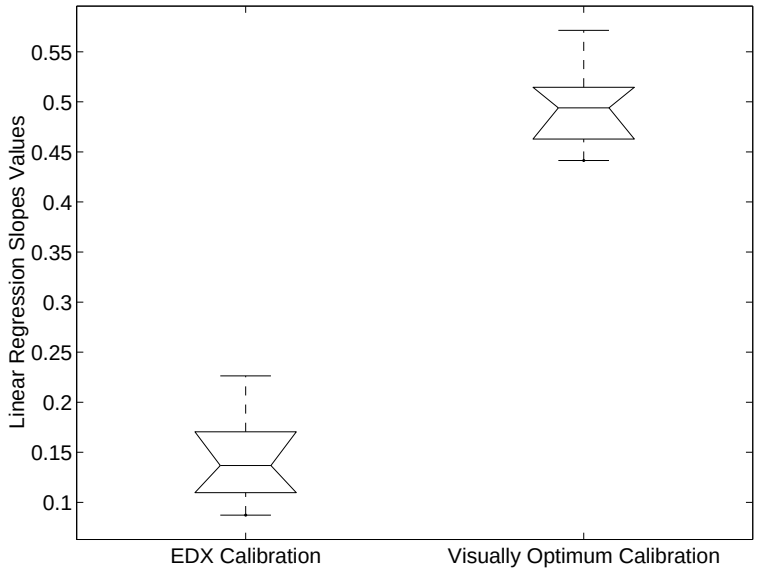

Figure 4.65: Boxplot illustrating linear regression slope values from figures 4.63 and 4.64 at 15keV.

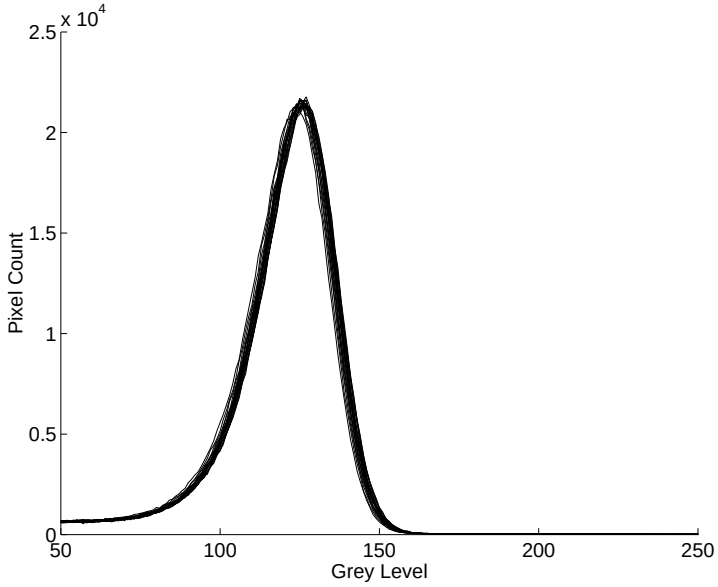

Figure 4.66: Histogram drift due to a novel CPS calibration (Low dosage setting) at 15keV.

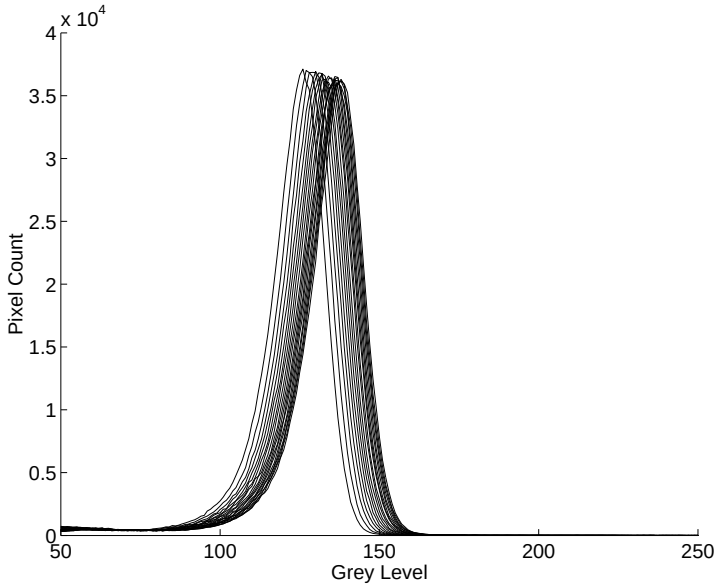

Figure 4.67: Histogram drift due to visually optimum calibration (High dosage setting) at 15keV.

4.6.2 30keV Accelerating Voltage

As machine accelerating voltage is varied across the operating range of values within a study, the actual probe current varies in spite of a constant machine spot size setting. As machine accelerating voltage is varied across the operating range of values within a study, the actual probe current at the sample varies, in spite of a constant machine spot size control setting. This results in an inherent relationship between spot size and accelerating voltage. Probe current is linearly related to spot size. Hence, the use of a Faraday cup allows the quantification of probe current and hence facilitates the setting of a constant current and consequent spot size at a specific accelerating voltage. Specimen irradiation damage is related to electron dosage, a parameter directly linked with both probe current and spot size. Hence, at a specific, constant accelerating voltage, a Faraday cup is an ideal method for standardising electron dosage and hence specimen damage.

Without the use of a Faraday cup, only the machine spot size setting can be held constant and consequently changes in the absolute spot size and probe current occur whenever the accelerating voltage is altered. When multiple accelerating voltages are used, this is not an adequate method for electron dosage, and consequently specimen damage, control. Altering the accelerating voltage has a unique effect on the relationship between probe current and spot size. As accelerating voltage is increased, probe current increases but spot size decreases. At this accelerating voltage, the normal relationship between probe current and spot size still applies but their absolute relationship is altered. Hence, for multiple accelerating voltage studies within the same samples, an alternative method for electron dosage, and hence specimen damage, must be employed.

To limit the damage incurred through the use of higher accelerating voltages (without the use of a Faraday cup) while maintaining experimental standardisation throughout all SEM scans, the lowest possible machine spot size value must be set and held constant throughout all testing. This value corresponds with the lowest machine spot size setting needed to achieve com-

plete image saturation for a given material of constant atomic composition. This is performed on the material within a given study which exhibits the lowest backscatter coefficient, for example a carbon standard. At the highest accelerating voltage employed the absolute spot size will have obviously increased but this value represents the lowest achievable standardised spot size set without the use of a Faraday cup. This Section compares the damage caused by the novel electron dosage calibration at 30keV (CPS $\approx$ 5900) with the damage resulting from a standardised constant machine spot size setting at an accelerating voltage of 30 keV.

This initial calibrated constant spot size was set as low as possible (CPS $\approx$ 5900 for carbon standard) at 15keV. The spot size setting control was then held constant as the accelerating voltage was increased, resulting in approximately 19,000 CPS at 30keV. This increase in CPS was due to the intrinsic relationship between accelerating voltage and electron beam spot size and probe current mentioned earlier [106]. Without an accurate method of measuring the beam current, this protocol would be the only method available to allow a researcher to standardise experiments performed at different accelerating voltages. Standardisation without a measure of probe current allows interassay comparisons but with an obvious cost to specimen integrity. The novel technique overcomes this inherent problem by calibrating the overall electron dosage experienced by the sample. This accounted for changes in both probe current and beam spot size as a function of accelerating voltage. Figures 4.68 and 4.69 compare the new novel calibration method at this increased accelerating voltage with the constant spot size setting, with each regression line representing the average damage rate.

The novel method employed at 30 keV offered a similarly low damage rate to the one observed when the calibration was used at an accelerating voltage of 15keV. Figure 4.70 uses a box plot to highlight the advantages of the new calibration relative to the constant spot size setting at the increased accelerating voltage. The method resulted in significantly decreased damage rates. This is illustrated by the small amount of drift seen in the intensity

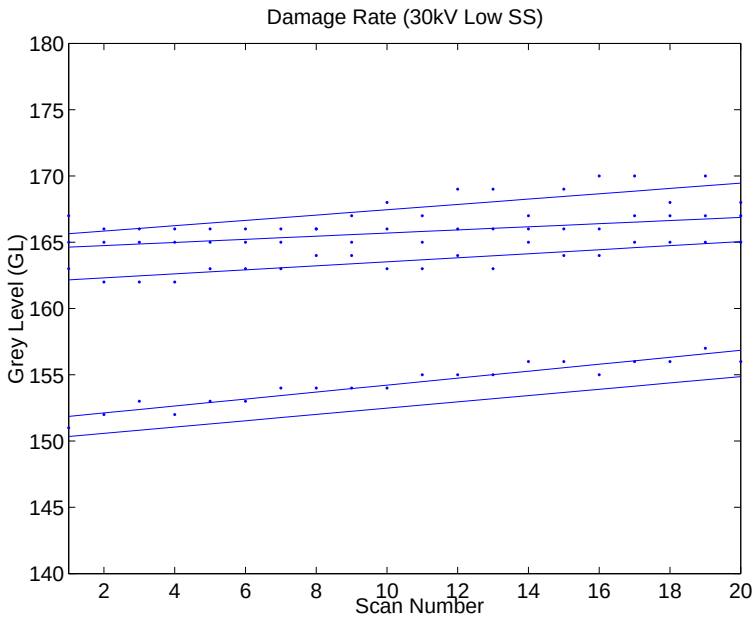

Figure 4.68: Histogram drift rate using a novel CPS calibration (Low dosage setting) at 30keV.

histogram drift (Figure 4.71) even after twenty consecutive exposures and exposure time. An example of the significant drift caused by electron dosage rates incurred through the lack of absolute sample spot size control at 30keV is shown in Figure 4.72. It should be noted that the initial grey level values are significantly higher for bone tissue when it is imaged at 30keV. This was due to a localised change in mineralisation as a function of depth below the sample surface. At 30keV, compositional information is originating from a greater depth below the sample surface where the material was compositionally different to the mineral composition in the overlying tissue.

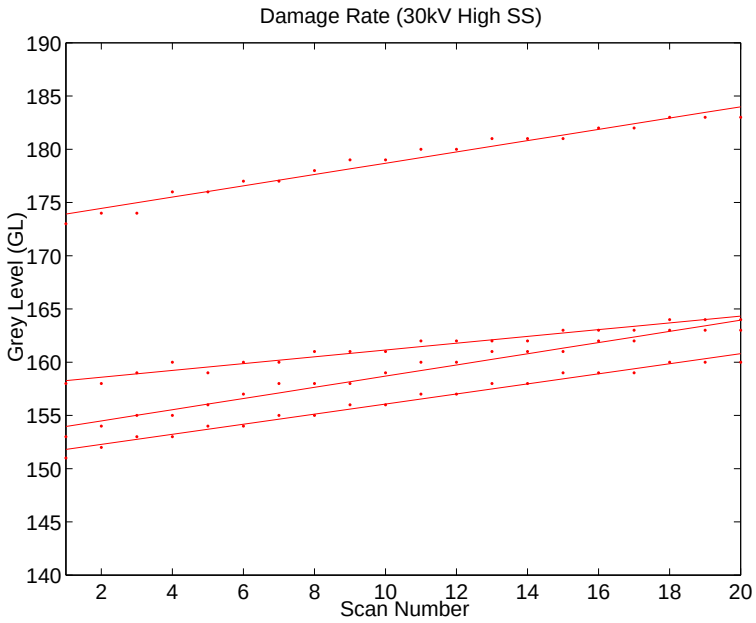

Figure 4.69: Histogram drift rate using constant spot size calibration (High dosage setting) at 30keV.

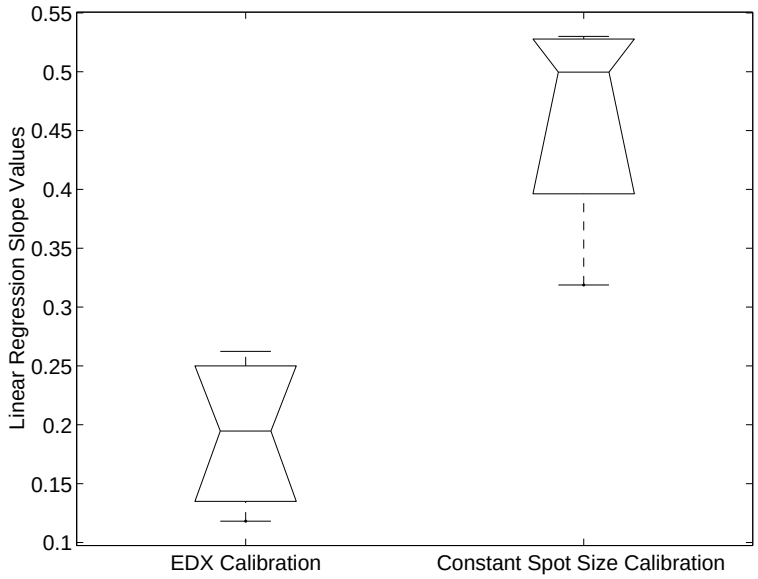

Figure 4.70: Box plot illustrating linear regression slope values from figures 4.68 and 4.69 at 30keV.

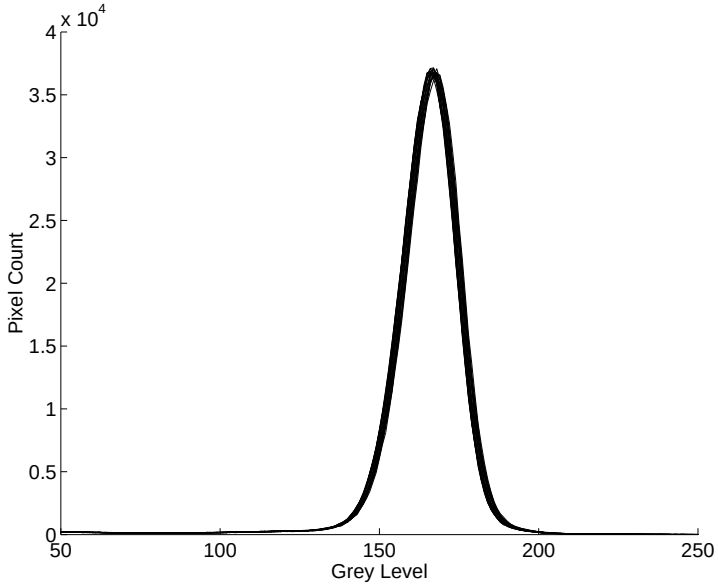

Figure 4.71: Histogram drift due to a novel CPS calibration (Low dosage setting) at 30keV.

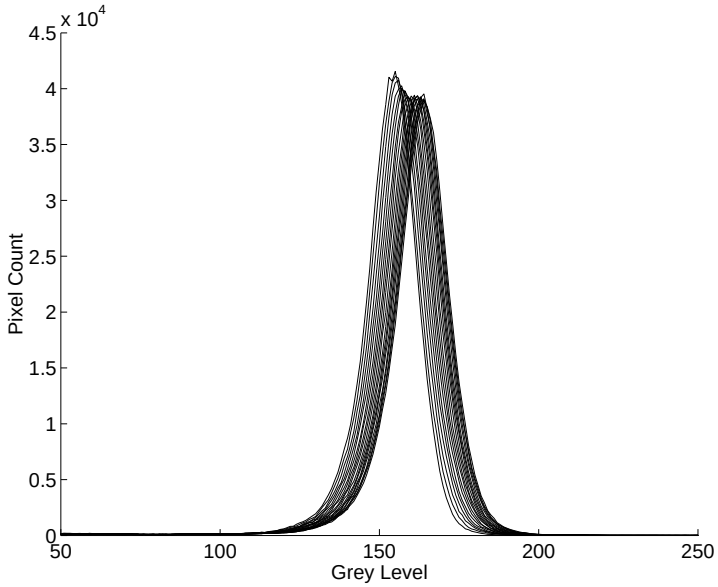

Figure 4.72: Histogram drift using constant spot size calibration (High dosage setting) at 30keV.

Chapter 5

Discussion

5.1 Population Analysis

5.1.1 Pathological Definition

The process of defining the severity of the disease's progression in the sample population used involved initially identifying and subsequently classifying the severity of cartilage damage in each tibial compartment, with subsequent confirmation through histological analysis of the samples [107]. This process is described in detail in Section 3.1.1. By initially quantifying disease severity and combining this information with subsequent mechanical and compositional analysis of the samples, a number of interesting and significant findings were revealed. Normal samples obviously showed no macroscopic cartilage damage in either lateral or medial tibial compartments. Diseased samples showed visual degeneration with slight fissures in the superficial zone of the medial condyle cartilage whereas the lateral samples did not. The lateral condyle cartilage surfaces were predominantly intact and defined as healthy tissue samples based on the Mankin scoring system employed. This was true for all samples used in this investigation. Assessment using the Mankin scoring system allowed quantitative definition of the severity of early-stage OA. This system is based purely on visual assessment of the cartilaginous surface.

The results of this OA severity quantification provided a unique opportunity to investigate the non-presenting lateral side of the diseased joints. Specifically it made it possible to discern whether or not changes had occurred within the subchondral bone tissue properties prior to any obvious changes in the overlying cartilage. The results showed conclusively that changes had occurred in both the tissue stiffness and mineralisation levels of the non-presenting lateral sides of the joints. This finding was interesting for a number of reasons but primarily due to important ramifications for the commonly accepted definition of OA. The classic definition of OA has been challenged in recent years, most successfully by a number of researchers using animal models [117, 118]. According to this classic definition of the disease, cartilage erosion or damage is the primary initiator of the disease. It was clear from the data in this present work that bone changes precede any gross damage to or loss of the overlying cartilage layer in human proximal tibial subchondral trabecular bone. It seems highly unlikely that any cartilaginous change, at the gross or tissue level, occurred prior to the observed subchondral tissue changes. It is reasonable to assume that any changes within the cartilaginous tissue, prior to subchondral bone changes, would not result in such a significant decrease in the tissue level stiffness of the bone. Furthermore, if such cartilaginous tissue changes were to result in the significant magnitude changes observed in subchondral properties, it seems highly unlikely that this would not also present as significant changes to the overlying macroscopic cartilaginous structure.

The results also highlight the extreme difficulty in defining this disease in absolute terms, particularly during initiation. Methods such as the Mankin scoring system are suitable for relative comparison but are obviously limited. However, conceptually, it is also difficult to imagine a more precise way to define the earliest stages of this disease. Without a clinical symptom, such as degenerated or damaged cartilage, how can onset of the disease be defined? Even if identification is possible prior to any obvious physical or clinical symptoms, sample harvesting would be difficult, if not impossible and

limited purely to animal models of the disease. The methods used in this present work facilitate the investigation of the early stages of the disease by taking advantage of the accepted progressive nature of the disease. The data indicated that in primary OA of the human knee, initiation of the disease within a proximal tibial compartment may have already occurred once its neighbour shows early-stage physical symptoms of the disease in the overlying cartilaginous tissue, defined using the Mankin scoring system. Therefore, by identifying early-stage primary OA symptoms in only one side of the tibial compartment of a joint and not within the adjacent compartment, isolation and assessment of this pre-symptomatic stage of the disease is possible. The discovery of this result is of major pathological significance. Having identified a pre-symptomatic stage of the disease and a method of isolating such tissue *in vitro*, subsequent work in this field is significantly advantaged. The ability to analyse pre-symptomatic tissue could yield a new early-stage pathological marker, possibly leading to the development of an early-stage diagnostic tool.

5.1.2 Data Pre-Processing

Data pre-processing conducted throughout the analysis of the experimental data resulted in some unexpected findings, specifically with regard to nanoindentation as a method of mechanical assessment. In particular, this phase of data analysis highlighted the unequivocal importance of post-nanoindentation review using both light and scanning electron microscopy. As mentioned in Section 3.2.1, a total of 2,957 nanoindentations were attempted on the relevant samples. Nanoindentation locations were chosen based on visual assessment of each proposed sample site. In spite of this, 707 nanoindentations failed to initiate, resulting in 2,250 successfully performed nanoindentations. Reasons for these failures included localised sample roughness or irregularities not completely removed by the extensive polishing procedures employed and impurities on the sample surface. Obviously due to a lack of test initiation, these attempts were discounted and had no effect on the overall results.

However, not all nanoindentations that successfully initiated were free from sample imperfection effects, unavoidable through sample preparation. Minor surface artifacts or inhomogeneities can influence the mechanical assessment without necessarily resulting in non-initiation of the nanoindentation procedure. For this reason, each individual nanoindentation was subsequently captured using an *in situ* light microscope and assessed in conjunction with the raw experimental data from the relevant nanoindentation tests. This data pre-processing is vital for correct interpretation of the experimental data and resulted in the removal of 282 nanoindentations, approximately 13% of the successfully initiated total of 2,250.

An additional data pre-processing stage was employed, taking advantage of the additional subsurface information available through the use of the quantitative backscattered images captured for each individual nanoindentation. Using these subsurface images in conjunction with the experimental raw data, nanoindentations affected by previously unseen subsurface defects were identified and removed from the analysis population. The amount of nanoindentations removed by this method was considerable, amounting to a total of 630 additional nanoindentations, approximately 28% the total successfully initiated nanoindentations. Both stages of the data 'clean-up' resulted in a final amount of 1,338 nanoindentations used in the results Section, approximately 60% of the successfully initiated 2,250 indentations.

The importance of this data clean-up was immediately apparent, due to the removal of approximately 40% of the supposedly successful nanoindentations (2250:1338). In quantitative terms, removal of these nanoindentations resulted in a significantly elevated sample stiffness mean. This was observed qualitatively as the removal of the outlying data points towards the lower end of the measured stiffness data. These subsurface defects were found to significantly decrease the measured stiffness of a given indent in a manner not appreciable by analysis of the raw load and displacement data alone. Rigorous examination of the indentation site and underlying integrity were required to validate such conclusions. The absolute effect of these excluded

outliers was quite small in magnitude ($\approx$ 2% decrease in measured mean stiffness) but could result in a decrease in average stiffness as large as 80% of the actual average sample stiffness in a single measurement, as seen in one of the samples. More importantly with regard to the significant changes seen in stiffness magnitudes throughout this present work, a 2% decrease is significant when presence of OA results in almost identical percentage changes in both medial and lateral samples (e.g. 3-4%). It is therefore vital that extreme caution should be exercised when examining pathological tissue or tissue deviating from normal composition or integrity. The artificially decreased average stiffness was a direct result of the aforementioned outliers being performed on sections of the bone samples exhibiting subsurface pores or irregularities. It follows that this effect would be more pronounced in heterogeneous samples, such as severe osteoporotic tissue. It should be stressed that without this method of post-experimental assessment, such deviations could be mistakenly attributed to natural tissue variation and significant pathological effects overlooked.

5.1.3 PMMA Embedding

All bone samples used throughout the course of this research were embedded in an embedding medium to facilitate both mechanical and compositional analysis. Due to the architecture of trabecular samples, macroscale support is required, primarily during the sample preparation phase. Embedding is also desirable when imaging organic samples using SEM analysis. However, use of such embedding mediums can alter the mechanical response of the tissue and therefore, consideration must be given to its effect on the recorded data and consequent measured mechanical properties. Due to the relative comparisons used throughout this present work comparing healthy and OA samples, quantifying the effect is not imperative with regard to the overall assessment of tissue changes in diseased samples. However, as a form of experimental validation it is obviously vital.

The material used throughout was polymethylmethacrylate or PMMA. PMMA's infiltrating nature has been extensively studied before by Bushby *et al.* and has been shown to artificially increase measured bone mechanical properties measured by nanoindentation [41]. Bushby *et al.* endeavored to quantify this effect and compared embedded samples with non-embedded controls to identify absolute tissue property changes specifically due to the embedding medium. Although the prevailing interest throughout this work has been the relative changes between healthy and OA tissue, the absolute nanoindentation values compared favorably with those of previous nanoindentation researchers. Absolute values for trabecular tissue are still disputed, with the typical range being empirically between approximately 2 and 14 GPa. However, the lower range of trabecular tissue values (<10 GPa) can be attributed to the techniques used to measure them. Values as low as these would normally arise from macroscopic testing methods, where architectural influences play a large part [119].

The best contemporary estimates of trabecular tissue stiffness (i.e.>10 GPa) are the result of nanomechanical testing of fresh, hydrated tissue, specifically research conducted by Zysset *et al.* [89]. By developing a novel apparatus to facilitate examination of fresh, wet, non-infiltrated human bone samples, Zysset *et al.* found fresh, wet trabecular tissue taken from unembalmed human femurs to exhibit an average tissue stiffness of approximately 11.4 GPa. Comparing this finding with that from Rho *et al.* [85], the approximate effect of sample dehydration can be approximated. Rho et al. [85] conducted research on dehydrated vertebral bone in a non-infiltrating mounting medium and found an average trabecular stiffness of 13.4 GPa. This finding coincided with work conducted by Bushby *et al.* [41]. They found that dehydration would artificially increase measured stiffness by approximately 30%. Rho *et al.* [85] measured the nanoindentation stiffness of trabecular tissue to be approximately 20% higher than those measured by Zysset et al. [89]. Differences in sample tissue site may account for the lack of precise agreement [120].

Additional to the effect of dehydration, Bushby *et al.* also examined the quantitative effect of PMMA embedding on average bone tissue stiffness [41]. Bushby and colleagues embedded their samples in the infiltrating medium, PMMA. They found an artificial increase in the measured nanoindentation mechanical properties. The magnitude of this increase was approximately 70%, changing a wet tissue modulus of approximately 11 GPa to about 19 GPa [41]. On average the stiffness results ranged from 16 to 18 GPa, which would initially seem high but in light of the previous findings mentioned, the values compare favorably with not only the work of other notable researchers using embedded tissue but also the work conducted on fresh, wet bone tissue when their correction factor is employed. The data lie well within the boundaries of expected embedded tissue moduli [85, 6, 86, 116, 87, 41, 89, 83, 84, 88, 39] and also confirms the small variation in trabecular tissue modulus, only consistently seen due to the relatively recent use of nanoindentation for the tissue level property assessment of mineralised tissues.

5.2 Nanoindentation Orientation

A method of random orientation testing was initially chosen, based on its distinct advantage of a non-preferential analysis of trabecular tissue at this level. Hence the range of measured nanoindentation stiffness and hardness would represent the complete range of intrinsic material stiffness and hardness in both healthy and OA subchondral trabecular bone, taken from medial and lateral sites within human tibiae. It became clear that this was not necessarily a requirement. The nanoindentations performed in a transverse direction and their corresponding QBEI resulted in the same overall range of tissue properties regardless. This is most likely due to the nature of the nanoindentation process. Mechanical properties are determined by displacing the material directly under the indenter tip in all three major axes (i.e. 3-D volumetric displacement in all directions).

If we assume that the results found at the extremities of the ranges of values recorded throughout this research represent the trabecular tissue level properties in the transverse and longitudinal directions, a relatively small range of trabecular stiffness values were recorded. The average lower range value of trabecular stiffness was approximately 14 to 15 GPa while the average higher range value was approximately 19 to 20 GPa. It should be noted that these are embedded samples and overestimate the actual tissue stiffness as seen quantitatively before [41].

5.3 Mechanical Properties

All nanoindentation measurements conducted throughout this research were performed by probing bone samples up to a specified maximum depth below the sample surface. As mentioned briefly in Chapter 4, these results report mechanical properties as a function of the measured depth below the surface at a number of specified examination depths. Specifically, the results report average mechanical values measured at four specific examination depths of interest, 1 μm, 2 μm, 3 μm and 4 μm.

The material properties reported at these specific examination depths reflect the average material response from the initial point of contact down to the specific depth reported. As such, changes in the material properties as a function of depth can be quantified but the technique tends to underestimate the magnitudes of these changes. This is a result of the contribution of all material, from the surface to the indentation depth, to the properties of interest (E & H). Hence, changes reported in the material properties due to disease, gender, site or indentation depth are conservative measures of the properties of the two-dimensional plane specified (e.g. 1 μm depth, 2 μm depth etc.). This effect does not affect the overall direction of the trends observed due to the presence of early-stage OA but simply understates the severity of its effect on intrinsic tissue strength at a given depth of interest.

5.3.1 Medial Stiffness

Healthy Samples

When the healthy group of samples taken from the medial sides of the sample population was examined, average stiffness was seen to decrease as a function of increasing indentation depth. The average stiffness within a depth of 1 μm below the sample surface was found to be 17.54 $\pm$ 0.53 GPa, with values of stiffness at depths of 2 μm, 3 μm and 4 μm equal to 16.99 $\pm$ 0.46 GPa, 16.4 $\pm$ 0.42 GPa and 15.84 $\pm$ 0.43 GPa respectively. These values compared favourably with findings of other researchers investigating healthy trabecular bone stiffness using nanoindentation. Turner *et al.* [83] measured an embedded trabecular stiffness of 18.14 $\pm$ 1.7 GPa using samples taken from human femoral condyles. Rho *et al.* [85] also examined trabecular samples taken from the thoracic vertebrae (T-12) of healthy human donors. They found an average embedded trabecular stiffness of 13.4 GPa. The difference between this finding and the current results is most likely due to tissue site variation and/or the different nature of the epoxy resin used.

As mentioned previously in Section 5.1.3, Bushby *et al.* [41] investigated the relative effect of testing cortical bone wet, dehydrated and embedded. When their estimated correction for the embedding effect was applied, the corrected results correlate very well with results of wet tested bone using nanoindentation conducted by other investigators [89, 84]. Zysset *et al.* [89] found a wet stiffness of approximately 12 GPa while Hoffler *et al.* [84] found the value for wet trabecular stiffness to lie somewhere between 8 and 14 GPa depending on sample origin, with distal radii showing the highest value and the fifth lumbar vertebra presenting the lowest value. It is also of interest to note that a study conducted on human knee patellar subchondral cortical bone tissue found an average cortical stiffness of approximately 20 GPa embedded in PMMA [88], marginally greater than these findings.

The results at subsequent depths could not be directly compared to those of other researchers due to the lack of published nanoindentation data on this

material. However, these deeper stiffness values did fall within the expected range for healthy human trabecular tissue. As mentioned briefly, intrinsic tissue stiffness was found to decrease as indentation depth increased. This result was in agreement with previous research conducted by Wang *et al.* on zebrafish bone using CSM nanoindentation. Wang *et al.* [121] also found a trend of decreasing stiffness as a function of increasing indentation depth. Similar studies have not been performed on human trabecular bone tissue. The magnitude of the change in stiffness from one depth to another were found to decrease in the results of this present work. However, when each incremental drop was expressed as a percentage decrease relative to the average stiffness value at the previous depth, a constant decrease of 3% was observed for each depth increment investigated.

Aside from the underestimation of mechanical property changes due to the inherent nature of the empirical technique used throughout the course of this study, the significant changes in average intrinsic tissue stiffness are more significant due to the fact that they occur over such a small depth range, particularly give the approximate size of a trabecular resorption cavity ($\approx$ 40 to 60 microns thick [122, 123]. An average lamellar layer is between three and seven microns and yet statistically significant differences are recorded within this range in healthy samples. This was quite likely due to the more random lamellar arrangement within trabecular tissue.

The ability to employ CSM methods to quantify tissue mechanical properties as a function of depth is a relatively new and expensive technique. Little empirical work has been conducted, aside from those mentioned here and the manufacturer's (MTS Systems) own calibration experiments. The work specifically described within the manufacturer's literature deals with two specific materials. In addition, this work investigated the properties of the supplied aluminium standard. By comparing these results, as well as those described by Wang *et al.* [121], with the manufacturer's work and conclusions, altered mechanical properties as a function of depth would not be expected in a homogenous bulk material. An example of such a mate-

rial is bulk plexiglass. Of particular interest with regard to the results was the calibration work conducted by the manufacturer on a nickel alloy layer (10 μm thick) on an aluminium substrate. Nanoindentation stiffness was found to decrease as a function of increasing penetration depth. The initial value reflected the value of the nickel alloy stiffness and as the penetration increased, the data recorded became more influenced by the presence of the relatively soft aluminium substrate. As would be expected for both these metallic materials, stiffness changes as a function of depth were mirrored by corresponding hardness changes across the nanoindentation depth range investigated. The work conducted on a supplied aluminium standard was also important with regards to result interpretation. Aluminium as a material produces a trend of decreasing stiffness and hardness as a function of depth, with a linear relationship between the two, in spite of being a homogenous bulk material. These findings have important implications for this present work when their conclusions are combined. The nickel alloy/aluminium substrate and pure aluminium exhibit a similar response as a function of depth across the indented depth range in spite of their intrinsically distinct microstructural construction. It can therefore be concluded that although the medial healthy sample stiffness results decrease as a function of depth, this does not necessarily indicate a specific change in composition. As observed in pure aluminium, this response could be an inherent material response in healthy subchondral bone, as opposed to altered layer properties throughout the examination depth. In addition to this, both materials exhibited a linear relationship between stiffness changes and corresponding hardness changes as a function of depth. This has major ramifications regarding the tissue level changes in the tissue samples that resulted in a subtle but significantly altered stiffness and hardness response due to presence of the disease (i.e. OA reduces medial tissue stiffness but does not significantly alter tissue hardness). The implications of this are discussed in Section 5.3.4.

OA Samples

When the results from medial samples showing evidence of early-stage OA were examined, a trend of decreasing stiffness as a function of increasing indentation depth was seen, identical to that seen in the medial healthy samples. As with the healthy medial samples, this decrease was smaller in magnitude with each incremental increase in indentation depth (Figure 4.30). However, when these drops in the magnitude of the tissue's stiffness were expressed as a percentage of the stiffness value at the previous indentation depth, a nearly identical scenario resulted. Each drop in average OA stiffness was approximately 4% in magnitude. The actual average stiffness within a depth of 1 μm below the sample surface was found to be 16.79 $\pm$ 0.35 GPa, with values of stiffness at depths of 2 μm, 3 μm and 4 μm equal to 16.1 $\pm$ 0.3 GPa, 15.46 $\pm$ 0.29 GPa and 14.81 $\pm$ 0.29 GPa respectively.

The main difference between the medial healthy and OA samples was a significant decrease in average intrinsic stiffness in OA samples relative to healthy controls. This was the case at all examination depths. Presence of early-stage OA, presented as damage to the overlying cartilage layer, resulted in a significant decrease in intrinsic subchondral trabecular bone stiffness. This result is similar to trends seen in the nanoindentation of PMMA-embedded subchondral bone taken from OA femoral heads, investigated by Ferguson *et al.* [39]. They did not see a significant decrease in the tissue stiffness but did see a definite trend of decreasing femoral subchondral stiffness in OA samples. The absolute values of their stiffness data also corresponded well with these results but tended to be marginally higher, possibly explained by variation due to sample site. Additionally, the results correspond with tests performed by Day *et al.* [107] on bulk samples from the same donor sites as the tissue used throughout this study, validating the protocols.

As was the case with the healthy medial samples, OA tissue properties changed significantly relative to healthy controls over the total range examined i.e. up to 4 μm. Of particular interest however was that these significant

changes in average tissue stiffness due to the disease were observed at an examination depth as small as 1 μm, confirming a significant small scale effect due to presence of the disease and supporting the idea that the effect of the disease at this stage of development is relatively ubiquitous in nature. This provides strong evidence for an intrinsic change in the nature of the material and also makes it difficult to explain changes in the bone mechanical properties due to the disease as secondary or reactionary to a breakdown in cartilage tissue, either micro- or macroscopically.

5.3.2 Lateral Stiffness

Healthy Samples

Bone tissue samples taken from the lateral sides of healthy human knee joints exhibited a similar relationship to their healthy medial counterparts with respect to indentation depth. Specifically, average tissue stiffness was seen to decrease as a function of increasing indentation depth. The average stiffness within a depth of 1 μm below the sample surface was found to be 16.53 $\pm$ 0.24 GPa, with values of stiffness at depths of 2 μm, 3 μm and 4 μm equal to 15.9 $\pm$ 0.23 GPa, 15.23 $\pm$ 0.25 GPa and 14.6 $\pm$ 0.26 GPa respectively. These values fall within the common range of accepted values for healthy trabecular tissue. Another similarity between the healthy medial and lateral samples is the percentage drop in stiffness, which was approximately 4% for each incremental increase in nanoindentation depth. Consequently, no difference in the magnitude of this characteristic decrease as a function of depth was seen between medial and lateral healthy samples, indicating a similar material response as a function of depth in both sites.

When the healthy lateral results were compared with their healthy medial counterparts, a statistically significant difference between the two was seen. Healthy lateral samples were found to exhibit a significantly decreased average tissue stiffness relative to the healthy medial samples at each examination depth. Day *et al.* [107] found a similar situation using bone samples from

the same population using a combination of finite element modelling and mechanical testing. Their method for assessing the intrinsic tissue modulus resulted in a non-significant, decreased lateral stiffness relative to the average medial value. Using nanoindentation, this present work found a statistically significant decrease between sites ($p<0.05$). This finding was unsurprising in healthy lateral samples due to the accepted normal human varus stance which tends to overload the medial tibial compartment. It would follow that this increased loading would result in an increased healthy medial tissue stiffness relative to the adjacent lateral compartment in the majority of a random sample population.

OA Samples

As with all previous groups, the relationship between stiffness and depth of indentation exhibited an identical trend of decreasing stiffness as a function of increasing examination depth. The average stiffness within a depth of 1 μm below the sample surface was found to be 17.08 $\pm$ 0.43 GPa, with values of stiffness at depths of 2 μm, 3 μm and 4 μm equal to 16.78 $\pm$ 0.38 GPa, 16.2 $\pm$ 0.36 GPa and 15.68 $\pm$ 0.37 GPa respectively. As seen in the healthy samples, the OA medial and lateral samples presented a percentage drop in stiffness as a function of depth, which was approximately 3% for each incremental increase in nanoindentation depth.

The lateral OA results exhibited an interesting and significant difference from the healthy lateral samples, especially when the medial situation is concurrently considered. OA lateral samples presented a significantly increased tissue stiffness relative to healthy lateral samples. As explained previously, lateral samples within this study did not exhibit damage to the overlying cartilaginous surface and if OA is inevitable in this compartment, as is commonly seen clinically, these lateral samples must represent an earlier stage of the disease not previously observed. Evidence of the presence of an early form of the disease is clear in the statistically significant alteration of tissue modulus, of similar magnitude to that seen in early-stage OA medial samples, albeit

opposite in direction. These results indicate a stage in the pathogenesis that occurs prior to cartilage damage and significantly affects the localised tissue stiffness within the trabecular subchondral bone. Of the two macrostructural forms of bone, namely cortical and cancellous, this present work hypothesised that any subtle changes that occur would most likely present in the cancellous bone due to the increased metabolism of the tissue. This is the first time these changes have been observed in the human model and they were observed within the cancellous tissue. However, it would be interesting to examine corresponding subchondral cortical structures for similar changes.

The significance of this finding is that it is the first statistically significant incidence of changes in the trabecular tissue modulus of human subchondral knee bone prior to damage to the overlying cartilage layer. The hypothesis of initial bone changes preceding cartilaginous damage during the early stages of the disease has been suggested by numerous authors, implied by a number of interesting research findings [29, 35, 32, 37] and strongly supported using animal models, most notably by Carlson *et al.* [117, 33]. The findings presented within this thesis prove conclusively that intrinsic bone tissue changes occur prior to large scale overlying cartilage damage. Although this work does not conclusively show that the overlying lateral cartilage tissue was completely free from evidence of OA on a cellular level, the findings suggest, as do those of previous studies, that the intrinsic tissue level bone changes are difficult to explain as secondary or reactionary to microstructural changes within the overlying cartilage. It seems highly unlikely that changes occurring in the *in-situ* cartilaginous tissue, resulting in an altered osteoblast phenotype and the intrinsic tissue stiffness changes seen here, would not present obvious macroscopic symptoms given the relatively delicate composition of cartilaginous tissue.

With regard to the alternate trends seen in clinically presenting medial OA samples and the non-presenting lateral OA samples, one could speculate that an earlier stage of the disease exists, previously unreported due to the inherent limitations of studying a disease which does not present clinically.

It was clear that a significant increase in average lateral tissue stiffness in OA samples occurred relative to healthy lateral controls. However, interpretation of this opposite trend in magnitude relative to the more developed instance of the disease seen in medial samples must consider changes seen in the tissue mineralisation. In the non-presenting lateral diseased samples, a greater tissue stiffness was achieved in spite of a significantly lower average mineralisation in these samples relative to healthy controls. This finding cannot be easily explained by the proposed presence of the type I homotrimer, given its reduced intrinsic strength [37] and very likely deleterious effect on the collagen/mineral interface. Additional speculation about its proposed effect on bone properties not specifically investigated within previous studies, such as impaired fibril formation and the nature of subsequent mineralisation, are also unable to explain the lateral OA results seen in this study. This invariably implicates another variable specifically during the non-presenting phase of the disease. It is possible, but unlikely, that the collagen/mineral bond is initially strengthened during this non-presenting stage of the disease, only to weaken as OA progresses, given the nature of the collagen changes seen in the later stages of disease development. It is therefore more likely, by deduction, to be an initial change in the organic matrix. Although predominantly type I collagen, the non-type I collagen components of the extracellular matrix (ECM) cannot be discounted. Previous studies involving soft tissue have implicated altered collagen proportions in changes in tissue stiffness [124]. Given the genetically distinct nature of the OA osteoblast seen in more advanced stages of the disease [32, 35], it is quite possible that this affects more than the type I collagen production exclusively. Initial changes could lead to subtle changes in the amounts of other osteoblast produced proteins in the ECM, having unexpected but significant increase on localised tissue stiffness, quickly overtaken by the drastically detrimental symptoms due to production of type I homotrimer.

5.3.3 Hardness

The hardness results were analysed statistically for significant factor interactions using three-factor ANOVA. Consequently, the results were not split into either medial and lateral or male and female compartments due to the non-significant interaction between disease and the two remaining factors (a) gender and (b) site.

Healthy Samples

Healthy samples were assessed using nanoindentation to determine tissue hardness information for each specified depth. The findings were quite different to their corresponding stiffness results. Average tissue hardness exhibited no discernable relationship with indentation depth. Hardness values were approximately constant, regardless of penetration depth. The average hardness within a depth of 1 μm below the sample surface was found to be 0.660 $\pm$ 0.014 GPa, with values of hardness at depths of 2 μm, 3 μm and 4 μm equal to 0.672 $\pm$ 0.012 GPa, 0.671 $\pm$ 0.011 GPa and 0.667 $\pm$ 0.01 GPa respectively. The lack of a distinct relationship between localised nanoindentation hardness and corresponding depth of indentation was of particular interest. This scenario differed from the corresponding stiffness relationship seen in this present work and corresponded with previous CSM nanoindentation work reported by Wang *et al.* [121]. Their study also found a significant decrease in nanoindentation stiffness with a corresponding approximately constant tissue hardness as a function of depth. Interestingly, their bone samples were not taken from human donors but from zebrafish. It was clear from the similarity between human bone tissue and zebrafish tissue response, and their corresponding distinction from the MTS calibration work on aluminium, silica and a nickel alloy on an aluminium substrate, that the lack of a distinct relationship between tissue stiffness and hardness as a function of depth is an inherent property of mineralised tissue. It is quite likely that this may be a direct result of the inherent porosity of the tissue and the change in tissue properties through densification.

As previously seen in the healthy stiffness results, the recorded hardness data correspond quite well with previous research in this area. Gupta *et al.* [88] examined subchondral cortical bone taken from human patellae and found an average hardness value only slightly greater ($\approx$ 0.717 GPa) than the results presented here. Since their mineralisation values were greater by a similar percentage, it would seem that trabecular and cortical tissue may not be significantly different at the tissue level. However, this is purely speculative as tissue origin site can vastly affect measured stiffness [84], as can lamellar orientation and these results highlight the lack of a strong linear relationship between nanoindentation hardness and bone mineralisation level. Ferguson *et al.* [39] also found very similar hardness results to this present work, approximately 0.650 GPa in magnitude for healthy cortical subchondral bone samples taken from human femoral heads. As was the case for the stiffness results, the values in this present work compared favourably with those conducted on wet tissue when a correction factor is applied, under the assumption that it applies to hardness as well. However, based on the findings highlighting a lack of strong correlation coefficient between stiffness and hardness (r^2 $\approx$0.5-0.7), it is likely to be a less accurate correction for nanoindentation hardness of mineralised tissue. Zysset *et al.* [89] found an average hardness of approximately 0.388 GPa for wet unembedded trabecular tissue taken from human femoral necks. Hoffler *et al.* [84] also tested wet trabeculae taken from numerous locations within the human body. They found trabecular tissue from the distal radius to exhibit a tissue hardness of approximately 0.500 GPa. Rho *et al.* [85] found a slightly lower average hardness value than these results with their embedded samples taken from the vertebra T-12. The found an average hardness value of approximately 0.470 GPa. As before, such variation is most likely due to site of sample origin [84].

It can be speculated that the lack of a strong linear relationship between nanoindentation hardness and mineralisation level (seen previously by Ferguson *et al.* [39]) is due to a shortcoming of the QBEI method. As seen in

many previous studies [39, 111, 80, 100, 19, 95, 96], QBEI is a very accurate method for the assessment of mineralisation level changes in bone. However, this alone does not capture all of the mineral changes responsible for inherent tissue strength, such as crystal size and geometry, two factors which are very likely to influence the inherent mechanical properties of the composite.

OA Samples

As was the case with the healthy hardness results in the previous Section, OA hardness analysis did not yield any discernable relationship between average OA tissue hardness and indentation depth. This was in contrast to the significant relationship observed between localised stiffness and indentation depth in all healthy and OA stiffness assessments.

OA hardness values were found to exhibit a trend of decreased magnitudes relative to the healthy samples. However, unlike the stiffness results, these differences were not significant at any of the chosen examination depths and were equivalent to approximately 1% to 2% reductions from the average healthy control values. Hardness values were found to stay effectively constant regardless of diseased state or indentation depth.

5.3.4 E/H Relationship

The observed E/H relationship was quite strong in absolute terms. The strongest relationships between stiffness and hardness were seen at the smallest depth of indentation and were not affected by either disease or sample site. The strongest regression coefficient was seen in lateral OA samples (r^2=0.76) but the remaining sample groups, namely healthy lateral and healthy and OA medial samples, exhibited similar regression coefficients at this initial 1 μm depth of indentation (r^2=0.7, 0.68 and 0.72 respectively).

The observed relationship between localised tissue stiffness and corresponding bone tissue hardness weakened as deeper examination depths were analysed. This was a result of their distinct relationship with indentation

depth, where hardness remained approximately constant throughout the examined depth range. The weakest correlation between the properties was found to be r^2=0.5 at a depth of approximately 4 μm below the indented surface. As previously discussed, site specific differences were observed in the stiffness results but not the hardness data. These differences did not affect the constant average E/H relationship measured in each sample site (as indicated by the almost identical slopes of the respective regression lines in Figures 4.5, 4.7, 4.12, 4.14, 4.19, 4.21, 4.26 and 4.28) but simply resulted in reduced constant E/H value in medial samples and an increased constant E/H value in the lateral samples due to presence of the disease.

For a material of known and constant composition, the tissue stiffness and hardness are strongly linked. This E/H ratio is a quantitative measure of the relationship between a material's elastic and plastic deformation behaviour. Consequently, disruption to this inherent relationship could indicate a change in a material's composition resulting in the altered behaviour. This is of particular relevance in composite materials. Most man-made and natural composites are combinations of two or more inherently different materials, resulting in mechanical properties somewhere in between those of each component individually. Alterations to the relative proportions of a composites constituents results in a situation similar to that observed in these samples. Small compositional changes usually result in a finely optimised set of materials properties. It is quite possible that a similar situation is occurring during early medial OA, resulting in a subtly tweaked tissue stiffness without any major effect on the corresponding hardness. It could be speculated that the quality of the collagen/mineral bond remains mostly intact but that the decreased homotrimic stiffness seen by previous researchers reduces the overall stiffness of the composite, as seen in the presenting medial samples, without reducing the corresponding hardness.

The lateral samples are another matter as the evidence of the homotrimer does not explain the significantly increased tissue stiffness. Hence, it is highly probable that a distinctive earlier stage in the disease exists and consideration

must be given to changes occurring in the individual constituents of the bone composite. Although the medial OA samples represented a more advanced stage of disease progression relative to the corresponding lateral samples, no statistically significant difference was seen between healthy and OA medial samples in the average E/H ratio across the range of examined depths. In isolation, this result implies a similar tissue elastic/plastic material response in both healthy and pathological bone tissue. In simpler terms, any effect on the observed mechanical characteristics of the tissue due to the presence of early-stage OA that were observed in this study did not preferentially alter either the elastic or plastic response of the medial tissue.

In contrast to this finding, lateral OA samples presented a significantly altered E/H response. In lateral OA samples, a statistically significant decrease in OA E/H ratio was observed relative to healthy controls as a function of increasing examination depth. This significantly altered elastic/plastic material response was unexpected due to the earlier stage of OA progression within these tissue samples and was indicative of a weaker dependence of elastic response on the material's plastic deformation in non-presenting lateral samples. In simplified terms, lateral samples showed a weaker link or bond between their elastic and plastic deformation response. In real terms, this implied that when the lateral samples were subjected to a specific amount of total deformation due to indentation, a larger than normal proportion of that total deformation could be made up of permanent plastic deformation, i.e. the samples would tend to deform in a preferentially plastic fashion relative to controls.

It can be hypothesised that this preference for plastic or permanent deformation, seen elsewhere as an increased tissue stiffness, could be quite detrimental to the overall behaviour of the tissue. Although increased stiffness at the macroscale is seen to be generally beneficial to the overall structure, the mechanical reasons for this stiffening at the macroscale can be inherently different to the stiffening processes occurring at the micron and nano level of examination. Lateral samples were found to be easier to deform plasti-

cally than elastically relative to controls, a result that could have serious microdamage or microcracking implications.

Of particular interest in light of this results was the medial samples lack of similar response. No significant difference in E/H ratio was seen as a function of increasing examination depth. Difficulty arises when speculating about this result in conjunction with other results of this study due to the progressive nature of the disease. Does the increased mineralisation density levels seen in medial samples reflect a reactionary response within the tissue as the disease develops? If so, is this the reason that the medial E/H ratio is so similar in both healthy and OA medial samples i.e. a return to some type of tissue normality? If so, it is very likely that this would be short-lived, with a return to elastic/plastic abnormality as the disease progresses and also to the clinically-observed tissue damage that occurs. What is implicitly clear is that regardless of the medial results, lateral samples showing no evidence of histological OA within the overlying cartilaginous tissue are fundamentally altered structurally relative to controls, providing definitive evidence of the inadequacy of the classic "wear and tear" definition of OA. Additionally, this result strongly points to the subchondral bone tissue as the primary instigator in this disease. This is based on the assumption that if changes occurred initially within the overlying cartilage that were severe enough to result in tissue level changes to the underlying subchondral bone tissue, it is highly unlikely that these cartilaginous changes would not present histologically in the cartilage structure.

5.4 Mineralisation

All quantitative backscatter electron image (QBEI) measurements conducted throughout the course of this research work were performed non-destructively by imaging carbon coated bone tissue at a number of predetermined accelerating voltages, namely 15, 20, 25 and 30 kV. The results show mineralisation as a function of depth below the sample test surface at a number of specified

examination depths. Specifically, the results report the average mineralisation values of individual nanoindentation sites at four specific depths of examination.

As was the case with the mechanical property measurements made using nanoindentation, the mineralisation results reported at these specific examination depths reflect the average mineralisation from the initial sample surface interaction down to the specific depth within the material specified. As such, changes in the mineralisation as a function of depth can be quantified but the technique tends to underestimate the magnitudes of these changes. This is a result of the contribution of all previous material imaged up to the examination depth specified. Hence, changes reported in the mineralisation due to disease, gender, site or examination depth are conservative measures of the properties of the two-dimensional plane specified (e.g. 1 μm depth, 2 μm depth etc.). This effect does not affect the overall direction of the trends observed due to the presence of early-stage OA but simply understates the severity of its effect on intrinsic tissue mineralisation at a given depth of interest. Additionally, this characteristic was identical in nature to the depth-specific nanoindentation characteristic described in Section 5.3. Consequently any comparisons between mechanical properties measured by nanoindentation and corresponding mineralisation measurements were complementary.

A significant advantage of this technique was highlighted within a study carried out by Roschger *et al.* in 2003. Bone mineralisation density distribution quantified using QBEI has been shown to be essentially constant in healthy adult human bone tissue. In contrast to this, significant changes in this mineralisation measurement was seen in diseased and clinically treated bone tissue [96]. Hence, its merit as a sensitive measurement technique for the identification and quantification of abnormal mineralisation changes is self-evident.

5.4.1 Medial Mineralisation

Healthy Samples

When the healthy medial samples were analysed, a strong relationship with examination depth was seen. Interestingly, the direction was opposite to that seen in the corresponding stiffness results. On average, mineralisation increased as a function of increasing examination depth in the healthy medial samples but not in every case. The magnitudes of these increases were not equal and tended to decrease as a function of increasing examination depth, with some exceptions. The average mineralisation value at an examination depth of approximately 1 μm was 20.29 $\pm$ 0.21 wt% Ca, with mineralisation values at depths of 2 μm, 3 μm and 4 μm equal to 22.79 $\pm$ 0.17 wt% Ca, 23.85 $\pm$ 0.13 wt% Ca and 25.18 $\pm$ 0.14 wt% Ca respectively.

The results compare favourably with existing research, conducted on healthy human trabecular bone tissue from varying sites. Roschger *et al.* [19] examined healthy trabecular bone taken from transiliac biopsies and found a range of mineralisation for the sample age range of 35 to 85 years of age. The range of values determined during their study was between 21 wt% Ca and 23 wt% Ca. Subsequently in 2003, Roschger *et al.* [96] examined healthy trabecular tissue taken from human patellae and femoral necks, finding an average mineralisation level of approximately 22 wt% Ca. Gupta *et al.* also used this technique to analyse cortical tissue taken from healthy human patellae. They found a mineralisation level between 22 wt% Ca and 23.5 wt% Ca.

The most significant result that arose from the investigation of mineralisation levels in healthy medial trabecular samples was the increased average mineralisation level as a function of increasing penetration depth. This result was significant when compared with corresponding tissue stiffness and hardness data. Tissue stiffness decreased as penetration depth increased while hardness stayed relatively constant. Considered speculation on this result returned three possible causes; (i) collagen (see lamellar) orientation (ii) col-

lagen/mineral interface and (iii) tissue age. Of the three, it was hypothesised that the most likely reason was due to collagen orientation changes as this would have little direct effect on measured mineralisation levels and could explain the lack of any major change in tissue hardness. Hence, the average mineralisation level could increase significantly with depth without a consequent increase in average tissue stiffness. The relationship would be further obscured if localised mineralisation quality were a factor. Irrespective of these concerns over the unusual relationship, relative changes due to the disease would still result in unequivocal evidence of the disease and its relative effect on each parameter in question.

OA Samples

When the OA medial samples were analysed, they showed a slightly different trend to that seen in the healthy medial samples. An overall increase in mineralisation as a function of increasing depth was seen as before with the exception at an examination depth of 2 μm. At this examination depth, the average mineralisation was larger than the mineralisation seen at the subsequent depth of 3 μm (Figure 4.43). The average mineralisation value at an examination depth of approximately 1 μm was 22.5 $\pm$ 0.26 wt% Ca, with mineralisation values at depths of 2 μm, 3 μm and 4 μm equal to 25.08 $\pm$ 0.14 wt% Ca, 24.64 $\pm$ 0.13 wt% Ca and 25.86 $\pm$ 0.14 wt% Ca respectively. These values could not be directly compared with previous OA human bone data but are slightly higher than the range of values expected of healthy human bone. The major importance of this observation is the validation of the novel calibration method. Both increases and decreases in localised tissue mineralisation can be detected below the surface of the examination plane non-destructively. The interpretation of this result in terms of the bone's microstructure is more difficult. Trabecular bone lamellae are not always parallel to the endosteum of the trabecular strut or plate. Hence, nanoindentations performed within a specified surface lamella structure may breach this lamellar boundary and pass into an adjacent lamella as the in-

dentation depth increases. This results in a level of randomness with regard to subsurface examination in these samples. Hence, deductions about the mineralisation gradient in healthy or OA trabecular bone are purely speculative. This was beyond the scope of this research but the advantage of this technique is obvious, especially when sample trabeculae are prepared and orientated along a specific axis.

The absolute magnitudes of the average OA medial mineralisation levels were also compared with the healthy medial results. Interestingly, at all examination levels, OA tissue showed a significantly elevated mineralisation level relative to healthy samples (Figure 4.43). Its corresponding effect on tissue stiffness was a significant decrease in tissue stiffness. The mineralisation result was similar to that seen in a murine model exhibiting a similar collagen defect. Grabner *et al.* [75] studied a form of Osteogenesis Imperfecta (OI) in the murine model, a form which results in the production of large amounts of type I collagen homotrimic molecules. They found a significantly increased mineralisation level as well as an increased tissue microhardness. Coupled with a significantly decreased homotrimic tensile strength seen in a study conducted by Misof *et al.* [76], they hypothesised that the increased mineralisation density was an attempt to compensate for the detrimentally affected mineral crystals observed by McBride *et al.* [66]. McBride and colleagues observed that mineral crystals isolated from the bone of this murine model were significantly thinner and less-well aligned than those seen in healthy controls. This tallies with the work by Bailey *et al.* and other studies conducted [37, 32, 35] and provides strong evidence that a genetically distinct tropocollagen may detrimentally affect the resulting mineralisation process.

5.4.2 Lateral Mineralisation

Healthy Samples

When the lateral results were examined, the findings were particularly interesting with regard to the medial sites. A similar situation to that seen in OA

medial samples was observed. Specifically, there was a significant trend of increasing mineralisation as a function of increasing examination depth with one exception. The average mineralisation value at an examination depth of approximately 2 μm was greater than the subsequent analysis depth of 3 μm. It was also observed that the healthy lateral samples exhibited a mineralisation range that tended towards the higher end of the mineralisation spectrum seen in both the healthy and OA medial samples. The average mineralisation value at an examination depth of'approximately 1 μm was 21.37 $\pm$ 0.16 wt% Ca, with mineralisation values at depths of 2 μm, 3 μm and 4 μm equal to 24.91 $\pm$ 0.17 wt% Ca, 24.74 $\pm$ 0.09 wt% Ca and 25.61 $\pm$ 0.1 wt% Ca respectively. These values were obviously elevated when compared with both the medial healthy samples from this present work and the research on healthy samples conducted by the relevant researchers [19, 96, 88].

As was the case with the medial healthy mineralisation results, corresponding tissue stiffness decreased as a function of increasing depth while the mineralisation increased on average. As before, it could only be postulated as to why this might have occurred. Changes in the lamellar, and consequently collagen, orientation may account for this observation. Likewise, relative tissue age on its own or combined with an alternating lamellar structure could also confuse the relationship. In spite of this, it is significant that the relationships were identical in nature and could hypothetically reflect a tissue specific relationship. It is additionally difficult to correctly interpret these findings due to the altered loading conditions experienced throughout the samples lifetime *in vivo*. Natural stance (e.g. varus or valgus stance) and physical level of activity result in naturally distinctive medial and lateral tissue properties. For these reasons, the healthy lateral samples should only be confidently compared to corresponding lateral OA samples. This should also be applied to the medial samples. Quantitative site to site comparisons and subsequent conclusions could be very misleading.

OA Samples

Lateral samples taken from OA donors exhibited a trend of increasing mineralisation as a function of increasing examination depth across the entire range of examination depths investigated (Figure 4.44). Interestingly, with the exception of the initial examination layer, OA lateral samples presented a significantly decreased average mineralisation level when compared with healthy lateral samples. This result was a reversal of the effect of the disease seen in medial samples, where presence of OA corresponded with a significant increase in mineralisation level relative to medial healthy sample levels. As mentioned, the exception to this was the initial layer of examination, approximately 1 μm below the prepared surface layer. The average mineralisation value at an examination depth of approximately 1 μm was 21.86 $\pm$ 0.37 wt% Ca, with mineralisation values at depths of 2 μm, 3 μm and 4 μm equal to 23.72 $\pm$ 0.16 wt% Ca, 24.27 $\pm$ 0.14 wt% Ca and 25.12 $\pm$ 0.1 wt% Ca respectively. Additionally, lateral OA mineralisation was significantly less than the mineralisation seen in OA medial samples.

It can be speculated that the lateral samples taken from joints diagnosed with early-stage OA of the medial compartment could be experiencing the effect of a previously unreported initial stage of disease onset, prior to overlying gross cartilage damage. The results clearly show significant alterations to both the intrinsic mechanical integrity and mineralisation level of the tissue samples in question. Due to the well-documented progressive and degenerative nature of the disease, eventual initiation of lateral side degradation within the examined OA joints would usually be assumed inevitable. This would be based on the assumption that an altered loading regime would be experienced within the damaged compartment, instead of a possible biological contamination or disease development within the lateral compartment. Damage due to such an altered loading regime would inevitably affect the weaker of the two *in situ* lateral tissues, namely the cartilaginous layer. In the OA lateral samples, no gross cartilaginous evidence of the pathology was observed but subchondral mineralisation deviations from healthy controls

were observed and are strong evidence of initiation of the pathology in the subchondral trabecular bone. The results show that this is definitively not a gross cartilage problem and hence favour the postulation that the disease is primarily biological in nature and not initiated by an altered joint loading condition. It can therefore be postulated that the observed increase in average mineralisation level seen in these OA medial samples was not the initial change that occurred in the development of the disease in these samples and consequently within the afflicted joint. Changes in the OA lateral sites show both increases and decreases in average mineralisation level compared with controls and all these changes occur before any physical damage was seen in the overlying cartilaginous tissue. These findings are strong evidence of not only disease initiation within the subchondral bone but also the ubiquitous and likely biological nature of the disease's mechanism within an affected joint.

As previously discussed in the OA results subsection of Section 5.4.1, from the combined work of this study and a number of notable previous investigations in a number of distinct fields, it can be speculated that primary OA initially affects the tissue by altering the phenotype of the tissue producing cells, the osteoblasts [35]. Consequently, all subsequent material produced by these genetically altered bone cells would be genetically distinct from normal products. This has already been seen in practice by Bailey and colleagues [48, 37]. Additionally, at some stage these genetically distinct osteoblasts would be likely to affect the *in situ* cartilage as seen by Westacott and colleagues [32]. However, for reasons discussed throughout this study, this is thought to be at least coincident with subchondral changes rather than prior as previously believed. Once OA bone cells are producing homotrimic tropocollagen, turnover rate is quite likely to be a major determinant of disease progression as it would be intrinsically linked to homotrimic proliferation throughout the tissue. The effect of the homotrimer is likely to be detrimental and has been seen to specifically result in thinner and less organised bone crystals in the OIM model [66]. This effect would be expected

given the tropocollagen residue-specific nature of the mineralisation process. Up to this point, the changes are a direct result of the disease and not a specific reaction by the body to the disease. After this, it can only be speculated as to the actual response that occurs. This is still a grey area. Both hypo- [34, 39] and hyper-mineralisation [20, 72, 75] have been observed in the past.

It was hypothesised for this study that this discrepancy was most likely due to the study of various undocumented stages of OA development within sample tissues in many studies. The results support this hypothesis strongly as this has occurred in the two sample groups exhibiting differing stages of disease development, the lateral and medial sides of the sample tibiae. Based on the findings of this study, it appears that the disease is either a two-stage condition or a composition of two or more distinct diseases. The latter is highly unlikely given that there is no empirical basis for this postulation within the published literature. It is more likely that the initial stage of the disease, seen in the lateral samples of this study, represents the initiation of homotrimic changes to the organic matrix. The subsequent stage of the disease's development can be seen in the medial samples and could correspond with the mass proliferation of the homotrimic tropocollagen throughout the tissue. This hypothesis is supported by the medial results, where the tissue stiffness is significantly decreased and the mineralisation level is correspondingly increased, postulated to be a compensatory mechanism for the weakened collagen substrate. However, the lateral sample results from this study do not apparently match the hypothesis, specifically that the observed lateral tissue changes represent a period closer to the initiation of the production of genetically distinct osteoblast and their consequent products and consequences. It is difficult to explain why the mineralisation level decreases while the tissue stiffness is elevated relative to controls. However, it is confidently believed that this is an accurate representation of the initial stages of primary OA development based on the lateral results at the initial depth of examination mirroring the situation seen in the more pathologically developed medial sites. The fact that the initial examination layer

mirrored the later stage medial samples corresponds with the currently accepted progressive nature of this disease. It can only be speculated as to why the mineralisation level decreased while the localised stiffness increased. It is reasonable to assume that the relatively simplistic hypothesis regarding the homotrimic molecule being entirely responsible for disease initiation does not capture the process accurately. The effect of a genetically distinct osteoblast and it consequently altered products was beyond the scope of this study but is likely to significantly affect the other components of the ECM and their subsequent developmental process (e.g. crosslinking profile in the case of collagen). The total effect of the homotrimer on the mineralisation process is also unknown and would require much subsequent investigation. However, this coupled with the likely altered crosslink profile is a prime suspect based on the intimate nature of the composite and collagen/mineral interface

5.5 Depth-Specific Behaviour

The characteristic responses as a function of examination depth, seen in the mechanical and mineralisation properties of all bone tissue samples examined within this present work, were of interest (Figures 4.30 and 4.31. Both tissue stiffness and mineralisation exhibited depth-specific trends which appeared to be artifactual. Tissue stiffness was found to decrease as a function of increasing examination depth below the sample's surface. This response was also observed by Wang *et al.* [121] in zebrafish bone samples using CSM nanoindentation. Considering calibrations conducted throughout this present work (and by the nanoindenter manufacturer) on metallurgical samples, knowledge of trabecular morphology and my knowledge of nanoindentation mechanics, it is extremely likely that this trend is an empirical artefact. It is postulated that subsurface deformation mechanics, such as plastic deformation or subsurface cracking below the indenter tip, could result in a trend of decreasing tissue stiffness as the nanoindentation process progressed in these samples.

The depth-specific characteristic mineralisation response was more intriguing (Figures 4.43 and 4.44). On average, mineralisation was found to increase as a function of increasing examination depth. It was unlikely that tissue mineralisation in the samples was actually changing over such a small depth of examination relative to the thickness of a lamellar layer (≈ 1 μm). Considering trabecular tissue morphology and the fact that mineralisation assessment was carried out after the nanoindentation process, it was initially hypothesised that sub-surface nanoindentation stress fields resulted in an artificial change in the density of the bone mineral within the examined ROI. However, when the work of Lloyd [18] was considered (i.e. backscatter coefficients do not change with changes in accelerating voltage in elements up to a Z number of approximately 20) in conjunction with our empirical findings at the 2 to 3 μm examination depths in both healthy and diseased tissue samples (i.e. decreased mineralisation as a function of increasing examination depth), it became more difficult to explain the depth-specific behaviour in mineralisation levels as artifactual occurrences. Unfortunately, the scope of this present study does not support any further speculations regarding these observed depth-specific artifacts.

5.6 Mechanical/Mineralisation Relationship

By combining the mechanical property data and corresponding mineralisation level results, no definitive relationship was recorded between either local stiffness or hardness and mineralisation level, site by site. This was true irrespective of the factors examined, namely disease (healthy or OA) and site (medial or lateral) as well as examination depth. With specific regard to the lack of a distinct relationship between localised stiffness and mineralisation, this result was unsurprising due to the randomness of nanoindentation test orientation throughout this study by design. No specific nanoindentation test orientation was applied at any stage throughout the study. In addition, the situation was compounded by the inherent nature of trabecular tissue non-

uniform lamellar orientation. Consequently the resulting randomness in the orientation of the collagen fibres would have had an effect on the properties measured throughout the tissue [125]. In spite of this, the investigation of a possible effect due to an applied preferential nanoindentation test orientation was of scientific interest in both healthy and OA samples. Consequently, this hypothesis was investigated using the existing data selected using an objective filtering system.

A number of previous researchers have found significant correlation between localised tissue stiffness measured by nanoindentation and local mineralisation levels in cortical subchondral bone tissue when tested within the transverse axes of the bone samples [88, 39]. Using the existing data, this relationship was investigated in both healthy and diseased samples. To ensure analysis of nanoindentations upon bone tissue lamellae exhibiting similar collagen/crystal plane orientation, only those nanoindentations within the total population performed transversely were subsequently analysed. The relationship was investigated, as before, by the analysis of matched pairs of transverse nanoindentations and corresponding QBEI scans. Transverse sections were selected by only including images of trabecular struts that did not branch into plates anywhere within the captured image. Consequently only nanoindentations performed along a trabecular strut were analysed.

Interestingly, no distinct relationship was observed between localised tissue stiffness or hardness and corresponding mineralisation in transversely indented subchondral human trabecular bone. This was the case regardless of the grouping factors of interest, namely disease, gender or site. It was concluded therefore that the lack of a relationship within the whole sample population was not related to the random orientation of performed nanoindentations, as previously speculated. Trabecular bone is a more heterogeneous structure at the tissue level when compared with cortical bone tissue. Trabeculae consist of fragmentary systems of superimposed lamellae with numerous intervening cement lines [13]. According to Currey [62], "At the lowest level, cancellous bone is usually made of lamellar, not woven bone.

However, the lamellae do not usually run parallel with the external surface of the trabecular struts and so they come out at the surface". Hence, the lack of a distinctive relationship between localised mechanical properties and corresponding localised mineralisation measurements is most likely due to the less homogeneous nature of trabecular bone microstructure.

This is supported by the work conducted by Ferguson *et al.* [39] on the subchondral layer immediately below the articular calcified cartilage (ACC) from human femoral heads. This work examined subchondral compact bone but the compact bone directly beneath the ACC resembles the less organised trabecular lamellar structure we observed and examined in these samples. They also found a lack of a distinct linear relationship between tissue stiffness and mineralisation level measured using QBEI. The lack of a distinct cortical organisation in their subchondral bone samples may explain their lack of a significant linear relationship between stiffness and mineralisation due to the physiological similarities of the examined tissue structure with trabecular bone. In contrast, their OA results showed a distinct drift towards a more linear relationship between the two properties but this was not mirrored in the findings of this present work.

The lack of a significant relationship between the localised mechanical properties and corresponding mineralisation level in OA samples was surprising given relevant contemporary investigations in this area, such as Ferguson *et al.* [39]. Their study found that healthy cortical subchondral tissue did not exhibit a strong relationship between mineralisation and stiffness measured by nanoindentation. However, in the case of the OA samples, a stronger relationship between the two was observed. Although this study found a similar trend, the correlation coefficients were too weak to definitively draw any conclusions about this empirical phenomenon in both healthy and OA bone. Unfortunately, the correlation coefficient results cannot be quantitatively compared with the study conducted by Ferguson *et al* [39]. They did not implicitly detail their correlation coefficient data. The most likely reason for the observed weakness of correlations in this study was the rel-

atively small sample number, resulting from isolation of purely transverse nanoindentations during the analysis stage. By random indentation location assignment, the majority of the nanoindentations were not performed on trabecular struts in a purely transverse orientation. Any ambiguity in the classification decision resulted in the non-inclusion of the nanoindentation in the transverse grouping. This resultantly small sample number was further compounded by the non-parallel nature of trabecular lamellae, ensuring that any nanoindentations performed transversely cannot be conclusively defined as 'purely transverse' in orientation.

The work conducted by Ferguson *et al.* [39] corroborates well with the more recent biochemical research on type I collagen homotrimer found in human OA bone femoral heads [37]. They found evidence of reduced intrinsic stiffness and reduced mineralisation in late-stage OA samples. Additionally they observed that the relationship between tissue stiffness and mineralisation level became more pronounced in the OA samples. This would seem surprising in the absence of a number of interesting contemporary investigations into the nature of OA collagen. Homotrimic collagen has been found to be intrinsically weaker than its healthy heterotrimic form [37] and mouse models of osteogenesis imperfecta (OIM) has shown evidence of an altered tissue mineralisation, exhibiting altered mineral crystal shapes and orientations [53]. It has also been observed that OA bone exhibits increased matrix deposition that tends to be hypomineralised [34]. This is unsurprising given the extremely specific nature of collagen post-translational modifications [8] and the matrix mineralisation process [10]. It can be hypothesised that at this level of tissue resolution, normal collagen may play a significant role in the determination of intrinsic tissue properties. This could explain the lack of a strong linear relationship between stiffness and mineralisation in healthy tissue samples. However, as the heterotrimic tropocollagen is replaced by its homotrimic counterpart, it is extremely likely that the organic substrate and mineralisation process will be detrimentally affected. This could explain the more linear relationship between the stiffness results and the level of

tissue mineralisation as the material's dependance on the mineral phase for intrinsic strength increases into late stage disease development. The scenario could only be this simple if the intrinsic mineral composition was unaffected directly. This has been shown to be the case. The mineral composition, quantified in the form of the Calcium:Phospate ratio (Ca/P ratio) was shown to be unaffected by the presence of late-stage OA [28, 126].

The findings reported here do not directly corroborate this hypothesis. Ferguson *et al.* [39] observed a decrease in both mineralisation level and tissue stiffness in late-stage OA samples from the femoral head. The results of this work present a significant decrease in OA tissue stiffness and a corresponding increase in OA mineralisation level in early-stage OA medial tibial samples. It can be speculated that the disagreement in terms of mineralisation level is primarily due to the early stage in the disease's development tested in this research. The findings do indicate an increased matrix deposition seen by Mansell *et al.*, presented as an increase in localised mineralisation level [34]. As before, the results exhibit some but not all of the symptoms evident in later-stage OA samples, possibly due to a heterogeneous distribution of homotrimic collagen in recently remodelled sections of the early-stage OA bone tissue. This speculation is further supported in absolute terms by the two main findings already mentioned, namely decreased tissue stiffness and a corresponding increase in mineralisation level and consequently bone metabolism. Based on the nature of the bone as an organic/inorganic composite made up of two intimately associated primary constituents (collagen and mineral), collagen and/or its intimate interaction with the mineral phase must be a significant initiator of this pathology in bone. Intrinsic tissue stiffness could only decrease in this compositionally-intact composite [28, 126] exhibiting an increased amount of mineral, if the other main constituent, collagen, is adversely affected.

The exact mechanism by which the pathology affects the tissue is still in contention and was beyond the scope of this research. However, from numerous investigations carried out on collagen and its interaction with the

mineral phase at the sub-nanostructure level [10, 52, 59, 11, 50, 51], it is extremely unlikely that normal mineralisation will occur on the substandard homotrimic collagen-based organic matrix substrate laid down by a genetically distinct osteoblast cell [35, 32]. The effect of the presence of this homotrimer is extremely significant with respect to mineralisation [53]. This collagenous substrate facilitates initial mineralisation of mineral crystals out of the surrounding extracellular matrix at specific centres of ossification. These are extremely specific and the presence of the third $\alpha 1$(I) chain, instead of the normal $\alpha 2$(I) chain, in the tropocollagen helix will significantly alter these points of attachment. Collagen crosslinking sites will also be significantly affected by this molecular change [42, 47]. The crosslinking process is extremely specific. Hence, the presence of the homotrimer results in a significantly decreased intrinsic tropocollagen strength and previous contemporary research has shown this to be a relatively large effect in terms the overall tissue strength [56, 43]. However, when OA tissue crosslinking was investigated, the levels did not appear to change as significantly as was previously expected [37]. It was found that the overall level of immature crosslinks significantly increased in OA tissue samples while the total mature crosslink content remained effectively unchanged. Additionally, pathologies such as osteogenesis imperfecta indicate that an apparently minor molecular change to the tropocollagen helix, as opposed to the crosslinking, can have drastic structural consequences [127]. Based on such current findings, it appears extremely likely to be a disease primarily concerning the interaction, or consequent lack thereof, between the tropocollagen fibrils and the intimately associated hydroxyapatite crystals.

5.7 Mechanical/Mineralisation Data Outliers

When the mechanical/mineralisation relationship data were examined, a particularly curious characteristic was observed (see Figure 4.45 up to Figure 4.60) in both the stiffness/mineralisation and hardness/mineralisation re-

sults. A small number of distinct outliers were observed specifically in the hardness/mineralisation data at the first three examination depths and in the stiffness/mineralisation data at examination depths of 2 and 3 μm. No characteristic trend was observed in these data. Both hyper- and hypo-mineralisation were observed in a small number of sample tests exhibiting nearly identical mechanical property values (Figures 4.51, 4.52, 4.53, 4.54, 4.55 and 4.56). Additionally, in an even smaller number of sample tests, altered mechanical properties were observed at sites exhibiting nearly identical mineralisation values (Figure 4.46).

It could only be hypothesised as to the cause of such observed data effects. Each outlier was assessed in terms of its location and testing order to elucidate any possible relationship between these erroneous sample tests and any possible cause or bias introduced into the testing procedures. No biasing relationship was found between any of these erroneous sample test data. Consequently, no suitable hypothesis was proposed in this present study to explain the outlying data. It was quite likely that some of these observations were due to nanoindentation of very thin or pre-damaged trabeculae segments (decreased mechanical properties in areas that exhibited normal mineralisation levels relative to the sample in question). The instances of normal mechanical properties exhibiting abnormal mineralisation levels relative to the sample population could not be explained. However, the amount of these outliers relative to the total sample population was quite small ($\approx$ 1-4%).

5.8 SEM Damage Calibration

A main aim of this part of the work was to develop a technique that utilises the inherent subsurface information generated by quantitative backscatter electron imaging conducted at various accelerating voltages. Specifically, a requirement was quantification of mineralisation levels in bone at predetermined depth increments below the sample's surface. The main advantage

of the novel technique is that, when combined with a mineralisation calibration technique such as Roschger *et al.* [80], quantitative, damage-free imaging across a range of accelerating voltages for a finite exposure time. Damage-free imaging cannot be guaranteed indefinitely due to the nature of the imaging technique but the technique presented in this present work offers a significantly increased damage-free exposure time when compared with current imaging protocols. This improvement over existing methods becomes much more significant at higher accelerating voltages. Aside from confidence that the measured mineralisation values are free of artificial drift due to sample irradiation damage, the technique offers significantly increased image resolution, due to the higher magnifications attainable without inducing catastrophic sample tissue damage. This has the obvious advantage of increasing the resolution of the acquired mineralisation data.

Use of the novel technique also allows investigation of changes in the tissue's mineralisation as a function of depth below the sample surface, non-destructively. Apart from depth-specific mineralisation data, the backscatter images were used as a method for validating corresponding nanoindentations performed on the bone samples. Subsurface pores, cracks and structural anomalies, invisible at the surface of the trabecular sample, were easily identified using this technique. Erroneous nanoindentation data, corresponding with indents performed on these subsurface artifacts, could be identified and excluded from analysis of the mechanical property data. The ability to isolate data variations due to architectural subsurface defects obviously improved the analysis of the material and ensured that any remaining variation in the recorded data was naturally occurring. The remaining valid nanoindentation data were then paired with corresponding mineralisation data. From the data, information about the relationship between the mechanical response of the bone samples and their corresponding mineralisation was examined as a function of depth below the sample's surface. Obviously, examining both the mechanical characteristics and mineral composition levels at the same scale

of analysis greatly improves the accuracy of the investigation (i.e. site specific paired data allowing correlation of mechanical properties and composition).

The dosage calibration results from the experiments performed at 15keV highlight the extreme sensitivity of mineralised tissues, such as bone, to the electron beam. Even slight changes in the beam current at this relatively low accelerating voltage can rapidly increase the rate of damage resulting from specimen imaging. As has been shown, the damage is not a charging artifact and is a permanent manifestation of composition alteration of the material. It is therefore vital for accurate, repeatable, quantitative analysis that this irreversible damage is stopped or at least rigidly controlled. The exact nature of the damage observed was not investigated during the course of this present work and was beyond the scope of this research. It is most likely a result of radiolysis, also described as chemical bond rupture.

The 30keV results highlight the damage that occurred when the machine spot size setting is held constant and the accelerating voltage is increased from 15keV up to 30keV. Increasing the beam energy will also increase the beam current and decrease the beam diameter. This increase in beam current was not recorded by the machine used throughout this study and would require a Faraday cup to quantify. It does however result in significant bone tissue damage. Use of a Faraday cup would obviously reduce the damage rate by facilitating the standardisation of beam current throughout the range of accelerating voltages used. However, it would not account for the increased damage rate resulting from the decreased beam diameter that occurs as the accelerating voltage is increased up to 30keV. The dosage calibration technique accounted for both changes (i.e. increased beam current and decreased beam diameter) by standardizing the effective dosage rate instead of using a Faraday cup to hold the experimental beam current constant as accelerating voltage was increased. As has been shown, it is vital to ensure this damage does not occur at any point throughout a quantitative study. Permanent specimen damage that occurs as a result affects the measured GL intensity and obviously destroys the GL calibration which facilitates interassay com-

parison, as well as allowing the investigation of the strength-composition relationship within the tissue.

Use of this technique, along with other similarly powerful analysis tools such as nanoindentation, has an obvious and practical advantage when analysing pathological tissue samples. Quantitative analysis on this scale, relating compositional and mechanical characterisation, can be used to elucidate subtle tissue-level changes in the material. Early stages in the progression of a disease can be more accurately and completely assessed, as well as investigations into the composition and nature of the relevant tissue below its surface. The ability to perform this function non-destructively has obvious advantages. Information resulting from such analyses would be of major relevance and benefit to both academic and clinical research.

Chapter 6

Conclusion

6.1 Main Results of the Thesis

The main aim of this thesis was to quantitatively investigate clinically-defined early-stage primary osteoarthritis in subchondral cancellous bone from human tibial plateaux, with specific focus on changes in the mechanical integrity of the tissue and the corresponding changes in the tissue's mineralisation level. The main conclusions of this study were as follows:

- Clinically-defined primary osteoarthritis (OA) in subchondral trabecular bone, harvested from medial compartments of human knee tibiae, results in a significantly decreased average tissue stiffness. No significant change in the tissue's hardness was observed but a significant increase in average mineralisation level was measured.
- Significant tissue level changes to both the average stiffness and mineralisation of tibial subchondral trabecular bone occur prior to clinically-evident, macroscale damage observed in the overlying cartilaginous tissue. This finding offers conclusive evidence that the classic 'wear' and 'tear' definition of osteoarthritis is an inadequate model of primary osteoarthritis in human knee joints.

- The observed changes due to the presence of non-presenting, early-stage osteoarthritis in lateral samples, specifically the increased intrinsic tissue stiffness, are difficult to explain as secondary consequences of an altered cartilaginous mechanical integrity. This observation further supports the contemporary hypothesis that changes in a primary OA-afflicted joint are not initiated by a disturbance in the mechanical equilibrium of the joint but instead, by a biological disruption within the organic matrix.
- The E/H relationship, across the range of depths examined, in medial early-stage OA samples was unaffected by the presence of the disease relative to controls. In contrast, non-presenting lateral samples taken from early-stage OA tibiae showed a statistically significant difference in this elastic/plastic deformation relationship within the depth of tissue examined. The tissue deformed preferentially plastically. In clinical terms, this would likely present as a slightly more brittle material, with increased susceptibility to microcracking or microdamage.
- At the tissue level, bone mineralisation is not as strong a determinant with regard to tissue stiffness or hardness, as previously assumed. Consequently, it is speculated that collagen and/or its intimate physical interaction with the mineral crystals must be a significant contributing factor to the tissue's intrinsic mechanical integrity, at this hierarchical level within bone.
- The novel quantitative backscatter electron imaging (QBEI) calibration technique, developed throughout the course of this thesis, facilitates depth-specific, damage-free QBEI of human cancellous bone tissue. This technique is suitable to be applied to similar mineralised tissues, sensitive to electron beam probing.
- Post-nanoindentation assessment using QBEI is a vital protocol required for accurate analysis of heterogeneous mineralised structures, such as human trabecular subchondral bone.

6.2 Future Work

The following recommendations regarding future work based on the subject of this thesis are outlined below:

- Significant changes to the tissue stiffness and mineralisation were observed in OA samples but were not significantly related. Future work should focus on the role collagen plays in this relationship at this structural level, specifically the type I collagen homotrimer [37].
- Tissue hardness was unaffected by the presence of the pathology, in spite of marked changes in the stiffness and mineralisation of the tissue. An explanation through subsequent empirical work in conjunction with the development of a suitable composite model of this hierarchical level of bone structure would significantly advance our understanding of the tissue.
- An earlier stage of the disease, previously unobserved within human bone tissue, was seen in this study. Additionally, the intrinsic stiffness and mineralisation changes due to the disease were similar in magnitude but opposite in direction relative to the clinically-observed, subsequent early-stage of the disease characterised using the Mankin scoring system. It remains to be determined why such a complete trend reversal occurs at the earlier, non-presenting stage of this disease.
- Changes occurring within OA tissue are predominantly reparative rather than destructive in nature. Additionally, the tissue has been shown to be intrinsically weakened. The identification of possible triggering events resulting in the observed increase in overall bone tissue metabolism is of vital importance. Are currently proposed bone metabolism triggering events, such as microdamage, involved in the onset or development of this disease, leading to a vicious circle of increased deposition of substandard homotrimic bone?

Bibliography

[1] Richardson M.L. http://courses.washington.edu/hubio553/totrad /scar/images/oashoulder.jpg. Internet, 1997.

[2] Eccles Health Science Library. http://medlib.med.utah.edu/webpath /jpeg3/bone150.jpg. Internet.

[3] A.D.A.M. Inc. http://z.about.com/d/arthritis/1/0/c/2/osteo.jpg. Internet.

[4] Murray R.K., Granner D.K., Mayes P.A., and Rodwell V.W. *Harper's Biochemistry*. Appleton and Lange, 24th edition, 1996.

[5] Gelse K., Pöschl E., and Aigner T. Collagens-structure, function and biosynthesis. *Advanced Drug Delivery Reviews*, 55:1531–1546, 2003.

[6] Rho J.Y., Kuhn-Spearing L., and Zioupos P. Mechanical properties and the hierarchical structure of bone. *Medical Engineering and Physics*, 20:92–102, 1998.

[7] Garland Publishing. Collagen schematic. Internet, 1998.

[8] Bailey A.J., Paul R.G., and Knott L. Mechanisms of maturation and ageing of collagen. *Mechanisms of Ageing and Development*, 106:1–56, 1998.

[9] Landis W.J., Hodgens K.J., Arena J., Song M.J., and McEwen B.F. Structural relations between collagen and mineral in bone as deter-

mined by high voltage electron microscopic tomography. *Microscopy Research and Technique*, 33:192–202, 1996.

[10] Landis W.J. The strength of a calcified tissue depends in part on the molecular structure and organisation of its constituent mineral crystals in their organic matrix. *Bone*, 16(5):533–544, 1995.

[11] Weiner S. and Traub W. Crystal size and organisation in bone. *Connective Tissue Research*, 21:259–265, 1989.

[12] Wagner H.D. and Weiner S. On the relationship between the microstructure of bone and its mechanical stiffness. *Journal of Biomechanics*, 25(11):1311–1320, 1992.

[13] Gray H. *Gray's Anatomy.* Longman Group Ltd., 35th edition edition, 1973.

[14] O'Kelly K.U. *On the microstructure and mechanical properties of cancellous bone.* PhD thesis, National University of Ireland, 2000.

[15] Hernandez C.J., Beaupré G.S., and Carter D.R. A model of mechanobiologic and metabolic influences on bone adaptation. *Journal of Rehabilitation Research and Development*, 37(2):235–244, 2000.

[16] Oliver W.C. and Pharr G.M. Measurement of hardness and elastic modulus by instrumented indentation: Advances in understanding and refinements to methodology. *Journal of Materials Research*, 19(1):3–20, 2004.

[17] Hay J.L. and Pharr G.M. *ASM Handbook Volume 8: Mechanical Testing and Evaluation (10th edition)*, volume 8, chapter Instrumented Indentation Testing, pages 232–243. ASM International, 10 edition, 2000.

[18] Lloyd G.E. Atomic number and crystallographic contrast images with the SEM: a review of backscattered electron techniques. *Mineralogical Magazine*, 51:3–19, 1987.

[19] Roschger P., Fratzl P., Eschberger J., and Klaushofer K. Validation of quantitative backscattered electron imaging for the measurement of mineral density distribution in human bone biopsies. *Bone*, 23(4):319–326, 1998.

[20] Anderson-MacKensie J.M., Quasnichka H.L., Starr R.L., Lewis E.J., Billingham M.E.J., and Bailey A.J. Fundamental subchondral bone changes in spontaneous knee osteoarthritis. *The International Journal of Biochemistry and Cell Biology*, 37:224–236, 2005.

[21] Creamer P. and Hochberg M.C. Osteoarthritis. *The Lancet*, 350:503–509, 1997.

[22] Peat G., McCarney R., and Croft P. Knee pain and osteoarthritis in older adults: a review of community burden and current use of primary health care. *Annals of the Rheumatic Diseases*, 60(2):91–97, 2001.

[23] Bedson J., Jordan K., and Croft P. The prevalence and history of knee osteoarthritis in general practice: a case-control study. *Family Practice*, 22(1):103–108, 2005.

[24] Straus Jr. W.L. and Cave J.E. Pathology and the posture of neanderthal man. *Quarterly Review of Biology*, 32(4):348–363, 1957.

[25] Lee T.C. and Taylor D. Bone remodelling: should we cry wolff? *Irish Journal of Medical Science*, 168(2):102–105, 1999.

[26] National Institute of Arthritis, Musculoskeletal, and Skin Diseases. Arthritis health publications. www.niams.nih.gov, 2002.

[27] National Institute of Arthritis, Musculoskeletal, and Skin Diseases. Question and answers about arthritis and exercise. www.niams.nih.gov, 2003.

[28] Grynpas M.D., Alpert B., Katz I., Lieberman I., and Pritzker K.P.H. Subchondral bone in osteoarthritis. *Calcified Tissue International*, 49:20–26, 1991.

[29] Dieppe P., Cushnaghan J., Young P., and Kirwan J. Prediction of the progression of joint space narrowing in osteoarthritis of the knee by bone scintigraphy. *Annals of the Rheumatic Diseases*, 52:557–563, 1993.

[30] Dequeker J., Mohan S., Finkelman R.D., Aerssens J., and Baylink D.J. Generalised osteoarthritis associated with increased insulin-like growth factor types I and II and transforming growth factor β in cortical bone from the iliac crest. *Arthritis and Rheumatism*, 36(12):1702–1708, 1993.

[31] Li B. and Aspden R.M. Mechanical and material properties of the subchondral bone plate from the femoral head of patients with osteoarthritis or osteoporosis. *Annals of the Rheumatic Diseases*, 56:247–254, 1997.

[32] Westacott C.I., Webb G.R., Warnock M.G., Sims J.V., and Elson C.J. Alteration of cartilage metabolism by cells from osteoarthritic bone. *Arthritis and Rheumatism*, 40(7):1282–1291, 1997.

[33] Mansell J.P., Tarlton J.F., and Bailey A.J. Biochemical evidence for altered subchondral bone collagen metabolism in osteoarthritis of the hip. *British Journal of Rheumatology*, 36:16–19, 1997.

[34] Mansell J.P. and Bailey A.J. Abnormal cancellous bone collagen metabolism in osteoarthritis. *Journal of Clinical Investigation*, 101(8):1596–1603, 1998.

[35] Hilal G., Martel-Pelletier J., Pelletier J.P., Ranger P., and Lajeunesse D. Osteoblast-like cells from human subchondral osteoarthritic bone demonstrate an altered phenotype *in vitro*. *Arthritis and Rheumatism*, 41(5):891–899, 1998.

[36] Li B., Marshall D., Roe M., and Aspden R.M. The electron microscope appearance of the subchondral bone plate in the human femoral head in osteoarthritis and osteoporosis. *Journal of Anatomy*, 195:101–110, 1999.

[37] Bailey A.J., Sims T.J., and Knott L. Phenotypic expression of osteoblast collagen in osteoarthritic bone: production of type 1 homotrimer. *The international Journal of Biochemistry and Cell Biology.*, 34:176–182, 2002.

[38] Bobinac D., Spanjol J., Zoricic S., and Maric I. Changes in articular cartilage and subchondral bone histomorphometry in osteoarthritic knee joints in humans. *Bone*, 32:284–290, 2003.

[39] Ferguson V.L., Bushby A.J., and A. Boyde. Nanomechanical properties and mineral concentration in articular calcified cartilage and subchondral bone. *Journal of Anatomy*, 203:191–202, 2003.

[40] Bank R.A., Verzijl N., Lafeber F.P.J.G., and TeKoppele J.M. Putative role of lysyl hydroxylation and pyridinoline cross-linking during adolescence in the occurrence of osteoarthritis at old age. *Journal of the Osteoarthritis Research Society International*, (10):127–134, 2002.

[41] Bushby A.J., Ferguson V.L., and Boyde A. Nanoindentation of bone: comparison of specimens tested in liquid and embedded in polymethylmethacrylate. *Journal of Materials Research*, 19(1):249–259, 2004.

[42] Gilham B., Papachristodoulou D.K., and Hywel T.J. *Will's Biochemical Basis of Medicine*. Butterworth Heinemann, 3rd edition, 1997.

[43] Oxlund H., Mosekilde Li., and Ørtoft G. Reduced concentration of collagen reducible cross links in human trabecular bone with respect to age and osteoporosis. *Bone*, 19(5):479–484, 1996.

[44] Wang X., Bank R.A., TeKoppele J.M., and Mauli Agrawal C. The role of collagen in determining bone mechanical properties. *Journal of Orthopaedic Research.*, 19:1021–1026, 2001.

[45] Wang X., Bank R.A., TeKoppele J.M., Hubbard G.B., Athanasiou K.A., and Agrawal C.M. Effect of collagen denaturation on the toughness of bone. *Clinical Orthopaedics and Related Research*, (371):228–239, 1999.

[46] Lowenstam H.A. and Weiner S. *On biomineralization.* Oxford University Press, 1989. p 144-157.

[47] Voet D. and Voet J.G. *Biochemistry.* John Wiley and Sons, 2nd edition, 1995.

[48] Bailey A.J. and Knott L. Molecular changes in bone collagen in osteoporosis and osteoarthritis in the elderly. *Experimental Gerontology*, 34:337–351, 1999.

[49] Gibson P.T. *Handbook of oceanographic winch, wire and cable technology.* National Science Foundation and the Office of Naval Research, 2000.

[50] Weiner S. and Traub W. Organisation of hydroxyapatite crystals within collagen fibrils. *FEBS Letters*, 206(2):262–266, 1986.

[51] Weiner S. and Price P.A. Disaggregation of bone into crystals. *Calcified Tissue International.*, 39:365–375, 1986.

[52] Ziv V., Wagner H.D., and Weiner S. Microstructure-microhardness relations in parallel-fibered and lamellar bone. *Bone*, 18(5):417–428, 1996.

[53] Fratzl P., Schreiber S., and Klaushofer K. Bone mineralisation as studied by small-angle x-ray scattering. *Connective Tissue Research*, 34(4):247–254, 1996.

[54] Ottani V., Martini D., Franchi M., Ruggeri A., and Raspanti M. Hierarchical structures in fibrillar collagens. *Micron*, 33:587–596, 2002.

[55] Bailey A.J., Sims T.J., Ebbesen E.N., Mansell J.P., Thomsen J.S., and Mosekilde Li. Age-related changes in the biochemical properties of human cancellous bone collagen: relationship to bone strength. *Calcified Tissue International*, 65:203–210, 1999.

[56] Knott L., Whitehead C.C., Fleming R.H., and Bailey A.J. Biochemical changes in the collagenous matrix of osteoporotic avian bone. *Biochemical Journal*, 310:1045–1051, 1995.

[57] Giraud-Guille M.M. Twisted plywood architecture of collagen fibrils in human compact bone osteons. *Calcified Tissue International*, 42(3):167–180, 1988.

[58] Ascenzi A. and Benvenuti A. Orientation of collagen fibres at the boundary between two successive osteonic lamellae and its mechanical interpretation. *Journal of Biomechanics*, 19(6):455–463, 1986.

[59] Weiner S., Arad T., Sabanay I., and Traub W. Rotated plywood structure of primary lamellar bone in rat: orientations of the collagen fibril arrays. *Bone*, 20(6):509–514, 1997.

[60] Marotti G. A new theory of bone lamellation. *Calcified Tissue International*, 53(Suppl 1):S47–S56, 1993.

[61] Ascenzi M.G., Ascenzi A., Benvenuti A., Burghammer M., Panzavolta S., and Bigi A. Structural differences between 'dark' and 'bright' isolated human osteonic lamellae. *Journal of Structural Biology*, 141:22–33, 2003.

[62] Currey J.D. *Bones: Structure and Mechanics.* Princeton University Press, 2002.

[63] Yamada K., Healey R., Amiel D., Lotz M., and Coutts R. Subchondral bone of the human knee joint in aging and osteoarthritis. *Osteoarthritis and Cartilage*, 10:360–369, 2002.

[64] Gevers G., Dequeker J., Martens M., Van Audekercke R., Nyssen-Behets C., and Dhem A. Biomechanical characteristics if iliac crest bone in elderly women according to osteoarthritis grade at the hand joints. *The Journal of Rheumatology*, 16(5):660–663, 1989.

[65] Miles C.A., Sims T.J., and Camacho N.P. Bailey A.J. The role of the $\alpha 2$ chain in the stabilisation of the collagen type I heterotrimer: a study of the type (i) homotrimer in the oim mouse tissues. *Journal of Molecular Biology*, 321:797–805, 2002.

[66] McBride Jr. D.J., Choe V., Shapiro J.R., and Brodsky B. Altered collagen structure in mouse tail tendon lacking the $\alpha 2$(I) chain. *Journal of Molecular Biology*, 270:275–284, 1997.

[67] Huznetsova N., McBride Jr D.J., and Leikin S. Osteogenesis imperfecta murine: interaction between type I collagen homotrimers. *Journal of Molecular Biology*, 309:807–815, 2001.

[68] Kundu B., Khare S.K., and Singh G. Role of polypeptides in the treatment and diagnosis of osteoporosis. *Peptides*, 20:523–537, 1999.

[69] Weinstein R.S. and Manolagas S.C. Apoptosis and osteoporosis. *American Journal of Medicine.*, 108:153–164, 2000.

[70] Taylor D., Hazenberg J.G., and Lee T.C. The cellular transducer in damage-stimulated bone remodelling: a theoretical investigation using fracture mechanics. *Journal of theoretical Biology*, 225(1):65–75, 2003.

[71] O'Brien F.J., Hardiman D.A., Hazenberg J.G., Mercy M.V., Mohsin S., Taylor D., and Lee T.C. The behaviour of microcracks in compact bone. *European Journal of Morphology*, 42(1-2):71–79, 2005.

[72] Miller L.M., Novatt J.T., Hamerman D., and Carlson C.S. Alterations in mineral composition observed in osteoarthritic joints of cynomolgous monkeys. *Bone*, 35:498–506, 2004.

[73] Knott L. and Bailey A.J. Collagen cross-links in mineralising tissues: a review of their chemistry, function and clinical relevance. *Bone*, 22(3):181–187, 1998.

[74] McBride Jr. D.J., Kadler K.E., Hojima Y., and Prockop D.J. Self-assembly into fibrils of a homotrimer of type i collagen. *Matrix*, 12(4):256–263, 1992.

[75] Grabner B., Landis W.J., Roschger P., Rinnerthaler S., Peterlik H., Klaushofer K., and Fratzl P. Age- and genotype-dependence of bone material properties in osteogenesis imperfecta murine model (oim). *Bone*, 29(5):453–457, 2001.

[76] Misof K., Landis W.J., Klaushofer K., and Fratzl P. Collagen from the osteogenesis imperfecta mouse model (oim) shows reduced resistance against tensile stress. *Journal of Clinical Investigation*, 100(1):40–45, 1997.

[77] Matsui H., Shimizu M., and Tsuji H. Cartilage and subchondral bone interaction in osteoarthrosis of human knee joint: a histological and histomorphometric study. *Microscopy Research and Technique*, 37:333–342, 1997.

[78] Patel V., Issever A.S., Burghardt A., Laib A., Ries M., and Majumdar S. MicroCT evaluation of normal and osteoarthritic bone structure in human knee specimens. *Journal of Orthopaedic Research*, 21:6–13, 2003.

[79] Messent E.A., Ward R.J., Tonkin C.J., and Buckland-Wright C. Tibial cancellous bone changes in patients with knee osteoarthritis. a short-

term longitudinal study using fractal signature analysis. *Osteoarthritis and Cartilage*, 13:463–470, 2005.

[80] Roschger P., Plenk Jr. H., Klaushofer K., and Eschberger J. A new scanning electron microscopy approach to the quantification of bone mineral distribution: Backscattered electron image grey-levels correlated to calcium kα-line intensities. *Scanning Microscopy*, 9(1):75–88, 1995.

[81] Oliver W.C. Alternative technique for analysing instrumented indentation data. *Journal of Materials Research*, 16(11):3202–3206, 2001.

[82] Fend G. and Nana A.H.W. Effects of creep and thermal drift on modulus measurement using depth-sensing indentation. *Journal of Materials Research*, 17(3):660–668, 2002.

[83] Turner C.H., Rho J., Takano Y., Tsui T.Y., and Pharr G.M. The elastic properties of trabecular and cortical bone tissues are similar: results from two microscopic measurement techniques. *Journal of Biomechanics*, 32:437–441, 1999.

[84] Hoffler C.E., Moore K.E., Kozlof K., Zysset P.K., Brown M.B., and Goldstein S.A. Heterogeneity of bone lamellar-level elastic moduli. *Bone*, 26(6):603–609, 2000.

[85] Rho J.Y., Tsui T.Y., and Pharr G.M. Elastic properties of human cortical and trabecular bone measured by nanoindentation. *Biomaterials*, 18:1325–1330, 1997.

[86] Rho J.Y., Zioupos P., Currey J.D., and Pharr G.M. Variations in the individual thick lamellar properties within osteons by nanoindentation. *Bone*, 25(3):295–300, 1999.

[87] Rho J.Y., Zioupos P., Currey J.D., and Pharr G.M. Microstructural elasticity and regional heterogeneity in human femoral bone of various

ages examined by nano-indentation. *Journal of Biomechanics*, 35:189–198, 2002.

[88] Gupta H.S., Schratter S., Tesch W., Roschger P., Berzlanovich A., Schoeberl T., Klaushofer K., and Fratzl P. Two different correlations between nanoindentation modulus and mineral content in the bone-cartilage interface. *Journal of Structural Biology*, 149:138–148, 2005.

[89] Zysset P.K., Guo X.E., Hoffler C.E., Moore K.E., and Goldstein S.A. Elastic modulus and hardness of cortical and trabecular bone lamellae measured by nanoindentation in the human femur. *Journal of Biomechanics*, 32:1005–1012, 1999.

[90] Rho J.Y. and Pharr G.M. Effects of drying on the mechanical properties of bovine femur measured by nanoindentation. *Journal of Materials Science: Materials in Medicine*, 10(8):485–488, 1999.

[91] Egerton R.F., Li P., and Malac M. Radiation damage in the tem and sem. *Micron*, 35:399–409, 2004.

[92] Boyde A., Jones S.J., Aerssens J., and Dequeker J. Mineral density quantitation of the human cortical iliac crest by backscattered electron image analysis: variations with age, sex, and degree of osteoarthritis. *Bone*, 16(6):619–627, 1995.

[93] Boyde A., Davy K.W.M., and Jones S.J. Standards for mineral quantitation of human bone by analysis of backscattered electron images. *Scanning*, 17(Supplemental V):V–6, 1995.

[94] Boyde A., Compston J.E., Reeve J., Bell K.L., Noble B.S., Jones S.J., and Loveridge N. Effect of estrogen suppression on the mineralisation density of iliac crest biopsies in young women as assessed by backscattered electron imaging. *Bone*, 22(3):241–250, 1998.

[95] Roschger P., Rinnerthaler S., Yates J., Rodan G.A., Fratzl P., and Klaushofer K. Alendronate increases degree and uniformity of mineralisation in cancellous bone and decreases the porosity in cortical bone of osteoporotic women. *Bone*, 29(2):185–191, 2001.

[96] Roschger P., Gupta H.S., Berzlanovich A., Ittner G., Dempster D.W., Fratzl P., Cosman F., Parisien M., Lindsay R., Nieves J.W., and Klaushofer K. Constant mineralisation density distribution in cancellous human bone. *Bone*, 32:316–323, 2003.

[97] Crofts R.D., Boyce T.M., and Bloebaum R.D. Aging changes in osteon mineralisation in the human femoral neck. *Bone*, 15(2):147–152, 1994.

[98] Bloebaum R.D., Skedros J.G., Vajda E.G., Bachus K.N., and Constantz B.R. Determining mineral content variations in bone using backscattered electron imaging. *Bone*, 20(5):485–490, 1997.

[99] Burr D.B., Miller L., Grynpas M., Li J., Boyde A., Mashiba T., Hirano T., and Johnston C.C. Tissue mineralisation is increased following 1-year treatment with high doses of bisphosphonates in dogs. *Bone*, 33:960–969, 2003.

[100] Roschger P., Fratzl P., Klaushofer K., and Rodan G. Mineralisation of cancellous bone after alendronate and sodium fluoride treatment: A quantitative backscattered electron imaging study on minipig ribs. *Bone*, 20(5):393–397, 1997.

[101] Graham Lawes. *Scanning electron microscopy and x-ray microanalysis*. Chichester : Published on behalf of ACOL by Wiley, c1987., 1987. page 316.

[102] Rau E.I. and Reimer L. Fundamental problems of imaging subsurface structures in the backscattered electron mode in scanning electron microscopy. *Scanning*, 23:235–240, 2001.

[103] Rau E.I. and Yakimov E.B. E-beam tomography of planar semiconductor structures. *Materials Science and Engineering*, B42:52–56, 1996.

[104] Niedrig H. and Rau E.I. Information depth and spatial resolution in BSE microtomography in SEM. *Nuclear Instruments and Methods in Physics Research B*, 142:523–534, 1998.

[105] Rau E., Hoffmeister H., Sennov R., and Kohl H. Comparison of experimental and monte carlo simulated bse spectra of multilayered structures and in-depth measurements in a sem. *Journal of Physics D: Applied Physics*, 35:1433–1437, 2002.

[106] Inc. JEOL USA. A guide to scanning microscope observation. Internet Booklet: http://www.jeolusa.com/sem/docs/index.html.

[107] Day J.S., Ding M., van der Linden J.C., Hvid I., Sumner D.R., and Weinans H. A decreased subchondral trabecular bone tissue elastic modulus is associated with pre-arthritic cartilage damage. *Journal of Orthopaedic Research*, 19:914–918, 2001.

[108] Ding M., Dalstra M., Linde F., and Hvid I. Changes in the stiffness of the human tibial cartilage-bone complex in early-stage osteoarthrosis. *Acta Orthopedica Scandinavica*, 69:358–362, 1998.

[109] Ding M., Danielsen C.C., and Hvid I. Bone density does not reflect mechanical properties in early-stage arthrosis. *Acta Orthopedica Scandinavica*, 72(2):181–185, 2001.

[110] Ding M., Odgaard A., and Hvid I. Changes in the three-dimensional microstructure of human tibial cancellous bone in early osteoarthritis. *Journal of Bone and Joint Surgery-British Volume*, 85-B:906–912, 2003.

[111] Roschger P., Eschberger J., and Plenk Jr. H. Formation of ultracracks in methacrylate-embedded undecalcified bone samples by exposure to aqueous solutions. *Cells and Materials*, 3(4):361–365, 1993.

[112] Reilly D.T. and Burstein A.H. The elastic and ultimate properties of compact bone tissue. *Journal of Biomechanics*, pages 393–405, 1975.

[113] Brady K. and O'Kelly K.U. Short term changes in the mechanical properties of wistar rat bone tissue due to osteoporosis. In Bedzinski R., Pezowicz C., and Scigala K., editors, *Proceedings of the 13th Conference of the European Society of Biomechanics.*, volume 4 of *1*, pages 384–385, 2002.

[114] Bank R.A., Beekman B., Verzijl N., de Roos J.A.D.M., Sakkee A.N., and TeKoppele J.M. Sensitive fluorometric quantitation of pyridinium and pentosidine crosslinks in biological samples in a single high-performance liquid chromatographic run. *Journal of Chromatography B*, 703:37–44, 1997.

[115] Bank R.A., Baybliss M.T., Lafeber F.P.J.G., Maroudas A., and TeKoppele J.M. Ageing and zonal variation in post-translational modification of collagen in normal human articular cartilage. *Biochemical Journal*, 330:345–351, 1998.

[116] Rho J.Y., Roy II M.E., Tsui T.Y., and Pharr G.M. Elastic properties of microstructural components of human bone tissue as measured by nanoindentation. *Journal of Biomedical Material Research*, 45:48–54, 1999.

[117] Carlson C.S., Loeser R.F., Jayo M.J., Weaver D.S., Adams M.R., and Jerome C.P. Osteoarthritis in cynomolgus macaques: a primate model of naturally occurring disease. *Journal of Orthopaedic Research*, 12:331–339, 1994.

[118] Carlson C.S., Loeser R.F., Purser C.B., Gardin J.F., and Jerome C.P. Effects of age, gender, and subchondral bone thickness on the severity of disease. *Journal of Bone and Mineral Research*, 11:1209–1217, 1996.

[119] Keaveny T.M., Borchers R.E., Gibson L.J., and Hayes W.C. Trabecular bone modulus and strength can depend on specimen geometry. *Journal of Biomechanics*, 26(8):991–995, 1993.

[120] Keaveny T.M., Morgan E.F., Niebur G.L., and Yeh O.C. Biomechanics of trabecular bone. *Annual Review of Biomedical Engineering*, 3(1):307–333, 2001.

[121] Wang X.M., Cui F.Z., Ge J., Zhang Y., and Ma C. Variation of nanomechanical properties of bone by gene mutation in the zebrafish. *Biomaterials*, 23:4557–4563, 2002.

[122] Eriksen E.F., Axelrod D.W., and Melsen F. *Bone Histomorphometry.* New York: Raven Press, 1994.

[123] A.M. Parfitt and B. Chir. Bone remodeling and bone loss: understanding the pathophysiology of osteoporosis. *Clinical Obstetrics and Gynecology*, 30:789–811, 1987.

[124] Burgess M.L., Buggy J., Price R.L., Abel F.L., Terracio L., Sameral A.M., and Borg T.K. Excercise- and hypertension-induced collagen changes are related to left ventricular function in rat hearts. *American Journal of Physiology*, 270(39):H151–H159, 2002.

[125] Martin R.B., Lau S.T., Mathews P.V., Gibson V.A., and Stover S.M. Collagen fiber organisation is related to mechanical properties and remodelling in equine bone. a comparison of two methods. *Journal of Biomechanics*, 29(12):1515–1521, 1996.

[126] Coats A.M., Zioupos P., and Aspden R.M. Material properties of subchondral bone from patients with osteoporosis or osteoarthritis by microindentation testing and electron probe microanalysis. *Calcified Tissue International.*, 73:66–71, 2003.

[127] Rauch F. and Glorieux F.H. Osteogenesis imperfecta. *The Lancet*, 363:1377–1385, 2004.